THE UNIVERSITY
of EDINBURGH

Structural Basis for the Rheology of Molten Chocolate

A Multi-Technique Approach

Iva Manasi

Doctor of Philosophy
The University of Edinburgh
March 2019

Abstract

Chocolate comprises a dense suspension of solids, mainly sucrose with cocoa and milk solids, in a continuous fat phase of cocoa butter stabilised by surfactants, namely lecithin (mostly phospholipid), and sometimes polyglycerol polyricinoleate (PGPR). The surfactants favourably affect the rheology of molten chocolate reducing energy cost during production. Lecithin reduces viscosity, however, undesirably increases the yield stress at high concentrations, whereas, PGPR is primarily used to reduce the yield stress. When combined, the viscosity and yield stress are reduced further than with either surfactant individually. Whilst this implies a modified inter-particle interaction, the molecular mechanism by which these modifications occur were previously poorly understood. This work provides a mechanism on the basis of molecular scale structural information for this co-operative rheological effect, opening up the potential to rationally select or design alternative surfactants and improve manufacturing of chocolate at a lowered fat content.

Small Angle Neutron (SANS) and X-rays (SAXS) Scattering show that lecithin and PGPR form micellar structures in triglyceride oil. Lecithin forms extended inverse cylindrical micelles that exhibit lamellar arrangements at high concentration or upon ageing. The addition of PGPR disrupts these ordered structures and decreases the aspect ratio of the cylindrical micelles. The adsorption of these micelles at the solid/fat interface leads to a modification of the inter-particle interactions which in turn changes the rheology.

The solid/fat interface in chocolate has been investigated using two complimentary model systems: a dense suspension of sucrose in triglyceride oil stabilised by lecithin and PGPR and an analogous model system based on an extended planar sucrose film. The model suspensions, comprising 65% w/w of sucrose in Glyceryl Triocotanoate (GTO) and Glyceryl Trioleate (TO) with 0.8% w/w total surfactant, exhibit similar rheology to molten chocolate and have been used to characterize the adsorption and structure of the interfacial surfactant films using SANS and SAXS. Varying the PGPR content whilst keeping the

total surfactant amount constant shows that the adsorbed surfactant interfacial film thickness increases with increasing PGPR fraction. In the lecithin rich suspensions the sucrose grains are in contact decorated by lecithin, giving rise to a fractal interface. On increasing the PGPR fraction the particles are pushed out of contact, resulting in a smooth particle interface. Spin Echo SANS studies show that sucrose-sucrose correlation length also increases, consistent with the picture in which the sucrose particles are pushed further apart for the surfactant compositions containing more PGPR.

A planar model system comprising a sucrose film spin-coated onto a silicon/silicon oxide substrate mounted into a flow cell has been used for Quartz Crystal Microbalance with Dissipation Monitoring (QCM-D) and X-ray and Neutron Reflectivity (XRR and NR, respectively) studies. Triglyceride oil containing lecithin and PGPR and their binary mixtures in the same molar concentration as chocolate has been flowed across the planar sucrose surface and the adsorption of the surfactants characterised using QCM-D. The adsorbed amount, found using the frequency shift, is comparable to the surfactant amount adsorbed in model suspensions found using small angle scattering. The dissipation shift increases with increasing PGPR fraction of the surfactant mixture, showing that the layers become more extended and diffuse. Structural details, investigated using NR and XRR, show that lecithin forms a compact phospholipid multilayer (5-7 monolayers) extending $\sim$10 nm and PGPR forms a solvated polymer layer of $\sim$30 nm. In binary mixtures the PGPR intercalates into the lecithin and the whole structure swells to $\sim$50 nm. Using these calculated thicknesses, the viscoelastic properties of the adsorbed surfactant films have been modelled by co-fitting the frequency and dissipation shift observed in QCM-D to the Voigt model. The interfacial surfactant structure and the viscoelastic properties of the interfacial films are then used to explain the role of different surfactants in the rheology of molten chocolate suspensions.

Based on this work we propose that lecithin layers reduce friction between sucrose grains, reducing the high-shear viscosity due to their high load bearing capacity whilst maintaining the fluid characteristic of the interfacial layer. The compact fractal interfacial layer implies that the sucrose grains are still sufficiently close in the suspension for Van der Waals adhesion to maintain a yield stress. PGPR incorporates into the lecithin layer, swelling it. This osmotically pushes the grains apart, decreasing Van der Waals interactions and reducing the yield stress giving the desired liquid-like flow.

Lay Summary

Surfactants are amphiphilic molecules, generally comprising a hydrophilic head-group and a hydrophobic tail. The presence of a polar and non-polar group means they can be used to stabilise immiscible dispersions of solids in liquid (suspensions) or of liquid in liquid (emulsions) by adsorption at the interface, modifying particle interactions. This leads to their use in various industries, e.g. food, cosmetics, paints and pharmaceuticals. In chocolate, surfactants are used to improve the flow properties (rheology) of the dispersion of sucrose, cocoa and milk solids in a continuous fat phase of cocoa butter. The rheology of molten chocolate at high and low shear stress (rubbing force) can be tuned by changing the compositional balance between different surfactants, enabling the molten chocolate to be formed into various shapes and composite structures. Making the chocolate flow more easily reduces the energy cost during production and allows the cocoa butter content required to achieve the desired flow properties to be lowered, reducing the most calorific and expensive constituent of chocolate. The way in which the surfactants modify the inter-particle interactions is poorly understood, hampering the rational search for alternative surfactants.

Commonly used surfactants in chocolate products are natural molecules like lecithin, primarily consisting of lipids, and in some cases polymeric surfactants like polyglycerol polyricinoleate (PGPR). They change both the viscosity (resistance to flow) and yield stress (the onset force required for the suspension to flow) of molten chocolate. To understand the structural mechanism controlling these rheological modifications, molecular resolution studies of these surfactant layers have been conducted. In our experiments crystalline sucrose accounts for the whole solid fraction and the fat is replaced with liquid triglyceride oil. Two model systems have been developed to investigate the solid/fat interface in chocolate:

- A dense model suspension of sucrose in triglyceride oil stabilised by lecithin and/or PGPR, which is discussed in the first half of the thesis. These suspensions exhibit rheological properties similar to molten chocolate (Chapter 2). In particular, lecithin and PGPR have the same effect on

the viscosity and yield stress as in chocolate. Structural investigations using x-ray and neutron scattering show micellar arrangements of lecithin and PGPR in triglyceride oil, detailed in Chapter 3. Adsorption of these aggregates at the sucrose/oil interface results in the interfacial surfactant films and are discussed in Chapter 4. Multiple scattering from these dense suspensions makes extracting detailed structural information from this data challenging.

- To circumvent the challenges caused by multiple (and isotropic) scattering from the suspensions, a planar model analogue for the sucrose/triglyceride interface has been developed by spin-coating crystalline sucrose films onto silicon. Adsorption of surfactants at the planar sucrose/triglyceride interface is discussed in Chapter 5 and detailed structural investigations of the adsorbed interfacial films using x-ray and neutron reflectivity are described in Chapter 6 and 7. This approach is equivalent to zooming in on a single sucrose/oil interface, allowing for more detailed structural information to be resolved in the direction perpendicular to the interface.

X-ray and neutron scattering measure the spatial inhomogeneities in a sample's scattering length density and thereby give structural details on the nano-scale. The physics behind these techniques have analogues in the scattering of light from dust resulting in a blue sky and reflection of light from oily films on puddles resulting in a rainbow of interference colours. As the wavelength of neutrons and x-rays is 500x smaller than light, the structures giving rise to these interference effects are 500x smaller, matching nicely to dimensions of the lipid molecules. X-rays interact with the electron density whereas neutrons interact with the nuclei, providing a way of seeing different molecular components. Reflection of neutrons is particularly useful as by introducing deuterium (heavy hydrogen) to produce isotopomers of the oils, the neutron refractive index of the oil can be tuned allowing various components to be matched out, similar to when a glass rod is seen to disappear when immersed in an oil of the same refractive index.

These studies have enabled the detailed structure of the interfacial surfactant layers to be determined. A microscopic mechanism for the rheology of molten chocolate is proposed whereby reduction in high-shear viscosity occurs due to compact lubricating lecithin layers, adsorbed at the sucrose/oil interface, that reduce frictional contact, similar to other lipid based lubrication. On the other hand, PGPR forms a solvated extended polymer layer which pushes the solid grains apart, causing a reduction in yield stress and leading to liquid-like flow.

Declaration

I declare that this thesis was composed by myself, that the work contained herein is my own except where explicitly stated otherwise in the text, and that this work has not been submitted for any other degree or professional qualification except as specified.

(*Iva Manasi, March 2019*)

To Mum and Dad, who taught me to always question.

The real point of honor is not to be always right. It is to dare to propose new ideas, and then to check them.

—Pierre-Gilles de Gennes

Acknowledgements

First and foremost, I would like to thank my supervisor, Dr. Simon Titmuss. His guidance and support throughout the last four years have been invaluable. I also thank my industrial supervisors, Annelie Verbon, MSc, and Dr. Isabella Van Damme at Mars Chocolate, who have provided useful insights into a complicated industrial system and have been supportive throughout this work. This work would not have been possible without funding from the EPSRC (EP/M506515/1) and Mars Chocolate, UK, as well as the use of the beamlines and offline facilities at the ISIS neutron source (Oxford, UK), the Institut Laue-Langevin (Grenoble, France), and the Diamond Light Source (Oxford, UK).

Thanks to all my colleagues at Edinburgh who have helped me at various stages along the way. In particular, Dan Hodgson and Elena Blanco for their help on all things related to the rheology of chocolate and Andrew Schofield for his help with anything chemistry related. I also thank Andy Garrie, Derek Low and Andrew Downie at the physics workshop who have made available custom-made flow cells for reflectivity experiments and other equipment, without which some of the experiments would have never been realised. I would also like to acknowledge the help of Dr. Juraj Bella, Department of Chemistry, with the NMR measurements and Prof. Vasileios Koutsos and Jake McClements, at CSEC, in obtaining the AFM images. I am also thankful to James Doutch, Jos Cooper, Nina Juliane Steinke, Luke Cliffton and Gavin Stenning at ISIS, STFC, UK, and Thomas Saerbeck at ILL, Grenoble, France for the invaluable support they have provided while using facilities at these institutes. Dr. Peixun Li at the ISIS Deuteration Facilities, UK and Dr. Tamim Darwish at National Deuteration Facilities, ANSTO, Australia provided the all-important deuterated triglycerides for the neutron measurements, and Prof. Phillip Whitfield at University of Highlands and Islands carried out the Lipidomics.

Many friends and comrades have fashioned this experience to be fun as well as educational. In particular, I would like to mention the backing of my friends, Sara, Parul, Laura and Ben who have motivated and encouraged me throughout the course of this work. Finally, I am immensely thankful to my family; to my parents and in-laws for their love and support throughout this work and beyond, and to my late grandmother who always showered unconditional love and care on me and contributed in my making. Last but not the least a big thank you to my husband, Kunal, for all the midnight discussions about various aspect of my PhD, his invaluable help with MATLAB and being my pillar of support throughout. This thesis would not have been possible without him.

Contents

List of Figures

List of Tables

Chapter 1

Introduction

1.1 Surfactants and Chocolate Rheology

Suspensions and emulsions are widespread in a variety of industries, including food, cosmetics, pharmaceuticals and paints. The systems comprise an immiscible solid, liquid or mixed phase dispersed in a continuous liquid phase often stabilised by surfactants. Surfactants, which are generally amphiphilic molecules comprising a hydrophilic and a hydrophobic part, adsorb at the interface of the polar/non-polar immiscible phases, reduce inter-particle interactions and stop the dispersion from coagulating [6]. This change in particle-particle interaction additionally modifies how the phases move past each other i.e. the rheology [7]. An example of one such system is chocolate: a dense suspension of solids (sucrose, milk solids, cocoa) in a continuous fat phase of cocoa butter stabilised by surfactants like lecithin and polyglycerol polyricinoleate (PGPR).

Different types of chocolate have been developed to suit the range of uses in the confectionery industry and demands of various markets. One of the challenges in manufacturing modern chocolates is how different shapes and composite structures are produced. To meet the specific product requirement the rheology of molten chocolate during production needs to be tuned. Moulding into bars requires chocolate that flows easily, i.e. has low viscosity, whereas for moulding Easter eggs, ease of spreading (low yield stress) is essential. Surfactants added in small quantities (<1%) can significantly change the viscosity and yield stress of molten chocolate, as shown in Figure 1.1 for sucrose in triglyceride oil (model

chocolate) suspension. The left panel of the figure shows 65% w/w sucrose in triglyceride oil suspension without any added surfactants. The mixture so formed is granular and does not flow. To this suspension 0.8% w/w lecithin (surfactant) is added to obtain a smooth flowing paste, as shown in the right panel of the figure. To achieve the same rheological properties ten times as much cocoa butter would need to be added [8, 9]. Therefore surfactants allow manufacturer to reduce the cocoa butter content, which is the most calorific and expensive constituent of chocolate.

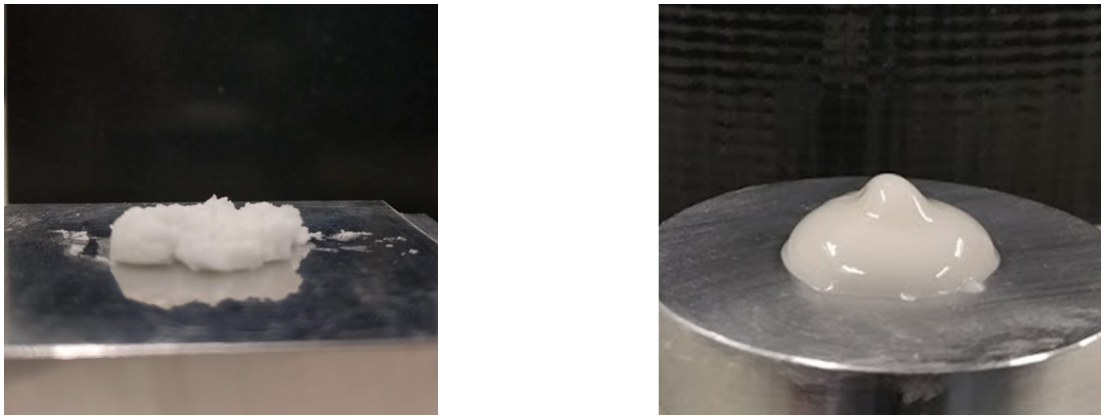

Figure 1.1 *The effect of surfactant on the flow properties of model chocolate (sucrose in triglyceride oil) suspensions. Left panel: 65% w/w sucrose in triglyceride oil suspension without any added surfactants forming a jammed granular paste. Right panel: Same concentration of sucrose in triglyceride oil suspension with 0.8% added lecithin forming a smooth flowing paste.*

It has been shown empirically that the rheological properties of molten chocolate at high and low shear stress can be tuned by changing the compositional balance between different surfactants [8–10]. For example, lecithin in small quantities (0.1-0.3%) reduces the viscosity of molten chocolate, but causes an increase in yield stress at higher concentration, whereas PGPR is primarily used for its ability to drastically reduce the yield stress. When used together they reduce both the viscosity and yield stress more than the effect of either of the two surfactants individually such that at particular ratios of lecithin to PGPR the viscosity is at a minimum and the yield stress vanishes. By using surfactants in appropriate ratios the flow properties of molten chocolate can be tuned to fit the confectionery requirement enabling production of different chocolate structures at reduced energy cost.

1.2 Aims and Motivation

The overarching aim of this work is to provide a structural basis for understanding the role that surfactants at the solid/fat interface play in determining the rheology of molten chocolate. This is fundamentally interesting as it provides an interaction mechanism between phospholipid and polymeric surfactants in a non-aqueous system and also industrially relevant as it enhances the understanding of chocolate rheology. By understanding how these thin surfactant films adsorb at the solid/fat interface modify particle-particle interaction, we gain useful insight into the role of lecithin and PGPR as rheology modifiers in chocolate. This is motivated by the industrial desire to find a natural replacement for the polymeric surfactant PGPR. Regulations restrict the total amount of additives that can be used in food products. In European Union the total quantity of artificial additives such as PGPR is restricted to below 0.5%. However, due to public perception, most chocolate manufacturers either do not use synthetic surfactants or use them in quantities <0.2%. By understanding the role of PGPR as a rheology modifier in chocolate, a natural alternative can be searched for on a rational basis, hopefully leading to chocolate with lower fat content and reduced cost during production.

An additional motivation that evolved during this work was to develop a methodology that married techniques such as x-ray and neutron scattering and reflectivity, that can only be accessed at central facilities, with lab based techniques, like tensiometry, QCM-D and lab based x-ray scattering.

1.3 Approach Used in the Thesis

In this work I have tried to understand the structural mechanism between surfactants in a complicated industrial system. To be able to discern these complex interactions I have used two main experimental approaches:

- Simplifying the industrial system by using models for the constituent components.

  Chocolate is a multicomponent system which makes it difficult to discern inter-particle interactions. The complexity of the system has been reduced in a step-by-step fashion. As a first step, the various suspended solid particles are replaced by milled crystalline sucrose, and the multi-component

cocoa butter is replaced by a single-component triglyceride oil. By choosing triglyceride oil, which is liquid at room temperature, molten chocolate could be studied at room temperature. These single component fat and solid phase are then used to make suspensions which are stabilised using the same surfactants that are used in commercial chocolate. To obtain more detailed information about the solid/liquid interface, a single planar sucrose substrate which can be used in flow cells through which liquid triglyceride oil is flowed has been used in addition to the suspensions which contain multiple interfaces. To gain further insight into the role of PGPR, measurement have also been made in which the multi-component lecithin has been replaced by a single phospholipid, POPC.

- Using multiple techniques self-consistently to unpick the way in which the different components interact with the interface and with each other, illustrated in Figure 1.2

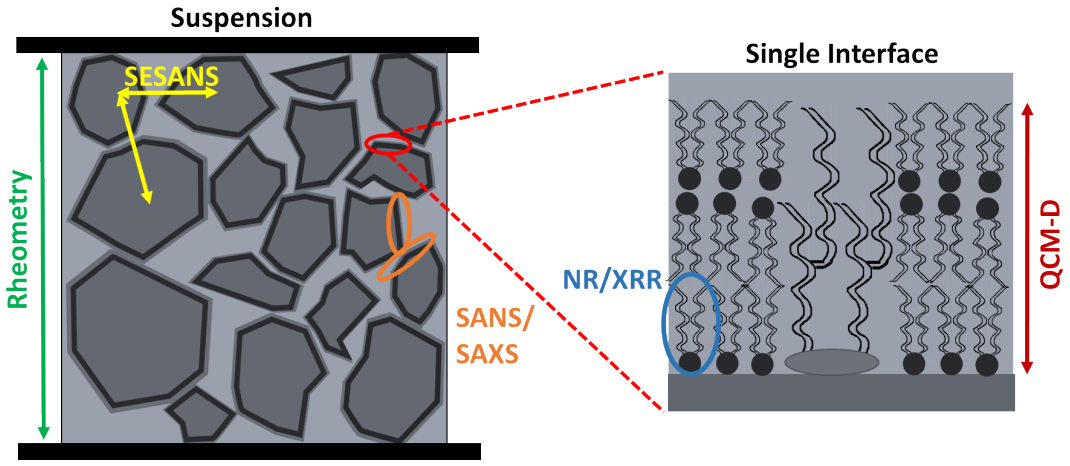

Figure 1.2 *A schematic showing the various techniques used to investigate model chocolate systems. Left panel: Techniques applicable to model chocolate suspensions. Right panel: Techniques used to investigate the planar model systems.*

Rheology is a bulk measurement technique, which gives average flow properties of the system as determined by the spatial correlation function of the particles. These inter-particle correlations are measured directly at the μm scale, size of the solid particles, using Spin Echo Small Angle Scattering (SESANS). In order to zoom in at the interfacial surfactant films which are on the nanoscale, $1 - 100$ nm, Small Angle Neutron and X-Ray Scattering (SANS and SAXS, respectively) have been used. To enhance the structural

details of the surfactant films measurements were done on the analogous planar model system. The adsorbed amount of surfactants, which are $\sim$mg/m^2, at the planar interface have been measured using Quartz crystal Microbalance with dissipation Monitoring (QCM-D), a sensitive technique that is able to measure such small added masses. Finally using Neutron and X-Ray Reflectivity (NR and XRR, respectively), the molecular level structural details of these surfactant films are studied. Table 1.1 summarizes the techniques, what they measure and the length scale of measurement.

Table 1.1 *Summary of techniques used to investigate model chocolate systems.*

Technique	System investigated	Aspect measured	Measurement scale
Rheometry	Suspensions	Flow properties[a]	Bulk technique , volume $\sim$ 1 cm^3
SESANS	Suspensions	Correlation function	$0.1 - 20$ μm
SANS/SAXS	Suspensions	Adsorbed amount and nature of interfacial films	$1 - 100$ nm
QCM-D	Planar	Interfacial adsorbed amount	$\sim$mg/m^2 [b]
NR/XRR	Planar	Structural detail of interfacial films	$1 - 100$ nm

[a] The flow properties are measured in terms of shear response of the system which are then converted to viscosity and yield stress
[b] This is typically the adsorbed amount for lipid monolayer which corresponds to a dry thickness of $\sim$1 nm.

The experimental investigations were performed using two triglycerides oils: the medium chain saturated Glyceryl Trioctanoate (GTO) and the long-chain unsaturated Glyceryl Trioleate (TO). GTO is cheap, is easily deuterated for neutron studies and is often used as a model for oil in food. This allowed us to study a large matrix of samples at multiple contrast. TO, which is perhaps more representative of the alkyl chain length and unsaturation in cocoa butter, but is more expensive and difficult to deuterate, has been used to study a subset of the large matrix in order to confirm the interaction are similar.

1.4 Neutron and X-ray Scattering

In this Ph.D. extensive studies have been carried out using Small Angle Scattering (SAS) and reflectivity of neutrons and x-rays. These are both scattering techniques based on the deflection of collimated radiation away from the straight trajectory after it interacts with structures that are on the length scale of the wavelength of the scattering radiation. The scattering occurs due to inhomogeneities in the material's density or the intrinsic scattering power of the constituent molecules. In order to investigate the surfactant structures at the nanometre length scale, neutrons and x-rays with wavelength of $1-10$ Å are used. X-rays interact with the electron density and neutrons interact with the nuclei[1] providing a means of seeing different molecular components. A brief overview of scattering theory is summarised here to better understand the mathematical formulation behind the analysis of the SAS and reflectivity data, discussed later. The discussion presented here is for elastic scattering of neutrons adapted from *Introduction to Small Angle Neutron Scattering and Neutron Reflectivity* by A. K. Jackson [3]. A more detailed discussion is available in *Introduction to Thermal Neutron Scattering* [11] and *Polymers and Neutron Scattering* [12]. The theory for x-rays scattering is the same apart from the fact that the nuclear scattering length and density is replaced by electronic scattering length and density [13, 14]. A summary comparing the two is presented to highlight the main differences.

1.4.1 Theory of Scattering

The neutron is a spin half sub-atomic particle exhibiting wave-particle duality. Due to its wave nature it is scattered by the nucleus (called nuclear scattering), an effect which can be used to probe structure of materials using techniques such as Small Angle Neutron Scattering and Neutron Reflectometry.

A collimated monochromatic beam of the radiation, neutrons or x-rays, with initial wave vector $\vec{k_i}$, is scattered from a particle, with scattered wave vector $\vec{k_s}$, as shown in Figure 1.3. In case of elastic scattering $|\vec{k_i}| = |\vec{k_s}| = k = 2\pi/\lambda$. For an incident plane wave travelling in z direction, with wave-function $\Psi_i = e^{ik_i z} =$

[1]The magnetic moment of the neutron can also interact with the magnetic moment of unpaired electrons giving rise to magnetic scattering. However, this is not relevant for non-magnetic soft matter structures and is therefore not discussed here

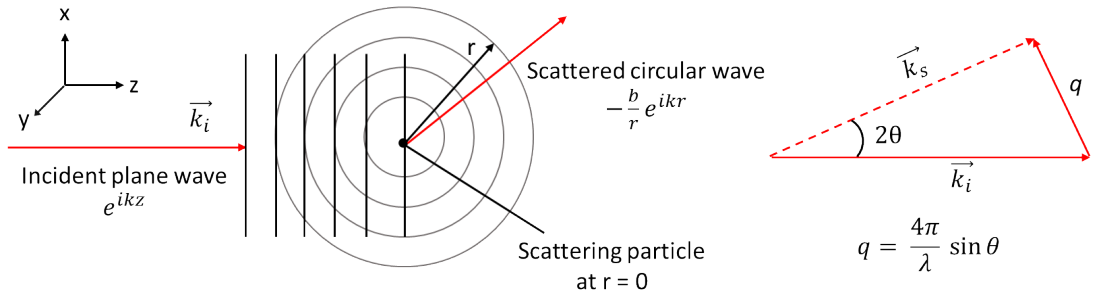

Figure 1.3 *Schematic showing the scattering of neutron (or x-rays) from an inhomogeneity in the sample. Adapted from [1]*

e^{ikz}, scattered from a rigid point particle[2], the scattered wave will be spherically symmetric, with wave function $\Psi_s = -\frac{b}{r}e^{ik_s r} = -\frac{b}{r}e^{ikr}$. For a 3-D assembly of scattering particles this becomes:

$$\Psi_s = -\sum_n \frac{b_n}{r} e^{i\vec{q}\cdot\vec{r}} \tag{1.1}$$

where b is the nuclear scattering length representing the interaction of the neutron with the scattering particle, r is the radial distance between the scattered neutron and interacting particle and $\vec{q} = \vec{k_s} - \vec{k_i}$ is the scattering vector (right panel of Figure 1.3).

Formally the neutron scattering length is a complex quantity with a real component that is dependent on the scattering power and an imaginary part that depends on absorption. However, in most cases the absorption co-efficient is negligible and the scattering length can be treated as a real quantity. The neutron scattering length of various elements varies randomly across the periodic table and also between isotopes of the same element [15] e.g. the coherent scattering length of hydrogen is -3.74×10^{-5} Å and deuterium is 6.67×10^{-5} Å. This allows isotopic substitution of hydrogen by deuterium to be used, to manipulate the scattering lengths in organic systems, whilst leaving the chemistry essentially unaltered. This effect of contrast variation is discussed with examples later.

In a scattering experiment, scattered neutrons or x-rays are measured as a function the scattering angle 2θ or the scattering vector q. From the scattering

[2]The assumption of the scattering particle as a point source can be justified as the radius of the nucleus ($\sim 10^{-15}$ m), which mainly scatters neutrons, is orders of magnitude smaller than the wavelength of the neutrons ($1 - 10$ Å) and the neutron interaction potential falls rapidly at distances beyond the nuclear radius [3].

triangle these are related as:

$$q = |\vec{q}| = 2k \sin\theta = \frac{4\pi}{\lambda} \sin\theta \tag{1.2}$$

Using Bragg's law, $\lambda = 2d \sin\theta$, this can be converted into an equivalent d-spacing for crystal lattice giving an indication of the length scale that can be probed using scattering at a particular q range.

$$\begin{aligned} d &= \frac{\lambda}{2\sin\theta} = \frac{2\pi}{q} \\ &\approx \frac{\lambda}{2\theta} \qquad\qquad \text{for} \quad \theta \ll 1 \end{aligned} \tag{1.3}$$

Small Angle Scattering, discussed in Section 3.4, and reflectivity, discussed in Section 6.2, probe structures ranging from 1-100 nm in the direction $\vec{q}$ by measuring small scattering angle in the range of 0.1-10°.

1.4.2 Scattering Cross-Section and Scattering Length Density

The scattering cross-section gives an indication of how strongly the radiation is scattered by the scatterer. For neutrons or x-rays, with incident flux Φ_0, scattered from a particle, the differential scattering cross-section is defined as:

$$\frac{d\sigma}{d\Omega} = \frac{I}{\Phi_0 d\Omega} \tag{1.4}$$

where I is the intensity (or count rate) of the scattered radiation measured by a detector that subtends a solid angle, $d\Omega$, positioned at a distance R from the scattering particle in direction θ, ϕ. Experimentally, the cross-section is measured and divided by the scattering volume to obtain the cross-section per unit volume. This measures the scattering cross-section per atom or per molecule. So dividing the above equation by total number of molecules in the system and using the scattered wave-function from Equation 1.1, the differential cross-section becomes:

$$\frac{d\sigma}{d\Omega}(\vec{q}) = \frac{1}{N} \left| \sum_{i=1}^{N} b_i e^{i\vec{q}\cdot\vec{r}} \right|^2 \tag{1.5}$$

The total scattering cross-section, σ_{tot}, is the sum of the coherent, incoherent and absorption cross-sections.

$$\sigma_{tot} = \sigma_{coh} + \sigma_{incoh} + \sigma_a \tag{1.6}$$

where, the coherent cross-section $\sigma_{coh} = 4\pi\langle b\rangle^2$, the incoherent cross-section $\sigma_{incoh} = 4\pi(\langle b^2\rangle - \langle b\rangle^2)$ and the absorption cross-section σ_a depends on the imaginary component of the scattering length, b.

When measuring large scale structures it is the scattering length averaged over a molecular component that is relevant for which we define a quantity scattering length density (SLD), ρ, as:

$$\rho = \frac{\sum_i^n b_i}{\overline{V}} \tag{1.7}$$

where b_i is the scattering length of the relevant atom and $\overline{V}$ is the volume containing n atoms[3]. As evident see from Equation 1.7, the SLD depends on the scattering power of the atoms and their distribution in a given volume, i.e. density.

1.4.3 Comparison with X-Rays

X-ray scattering follows the same formalism, with the exception that the neutron scattering length and density are replaced by the electronic scattering length and density of the material. As x-rays are scattered by the electron cloud surrounding the atom, the scattering power of atoms increases linearly with atomic number, and isotopes of the same material have identical x-ray scattering length which means techniques of contrast variation cannot be used. Due to scattering from the electron cloud, the assumption of point scatterers breaks down, and for x-rays the scattering intensity decreases with the increase in scattering angle. This is taken into account while reducing the data obtained from a scattering experiment.

The higher flux, especially with synchrotron radiation, and lower background achievable for x-rays, allows for measurement to higher q values than for neutron scattering, offering the potential for higher spatial resolution. Neutrons sources, reactor or spallation, give a range of wavelength between 2-20 Å whereas x-ray sources give well defined wavelength which results in higher q resolution using x-

[3]This is a valid description when the the scattering vector $q < 1/r^*$, where r^* is the distance over which the SLD is a constant. For water molecule this is ∼3 Å.

rays. Finally, since neutrons are not charged and only interact with atomic nuclei, they penetrate samples much more effectively than x-rays, which usually do not go much further than a millimeter deep, dependent on the adsorption by atoms i.e. the imaginary part of the scattering length density. Therefore, neutrons are more effective at probing buried interfaces.

1.4.4 Neutron and X-Ray Sources

The Small Angle Neutron Scattering (SANS) and Neutron Reflectivity (NR) experiments described in this thesis were conducted at either the neutron reactor source at the Institut Laue-Langevin (ILL), Grenoble, France, or at the neutron spallation source at ISIS, Oxford, U.K [16]. The reactor source at ILL produces a continuous flux of neutrons by nuclear fission from an uranium source. The spallation source at ISIS produces pulses of neutrons via nuclear spallation, in which accelerating protons collide with tungsten target; with the flux of neutrons produced being pulsed due to the pulsed nature of the synchrotron. The neutron beam produced at both sources is then passed through a moderator of either liquid hydrogen, methane, water or heavy water to obtain cold neutrons with lowered kinetic energy. This gives neutrons with wavelength in the range of $2 \leq \lambda \leq 20$ Å. After scattering from the sample the neutrons are collected using a ^{3}Helium detector with a very low intrinsic background level.

The Small Angle X-Ray Scattering (SAXS) and X-Ray Reflectivity (XRR) experiments described in this thesis were conducted at either the synchrotron source at Diamond Light Source, Oxford, U.K [17] or the lab based x-ray sources, Rigaku SmartLab [18] and XENOCS Nano-inXider SAXS/WAXS system [19] which use a Cu K-α source with wavelength 1.54 Å. At the Diamond Light Source, beams of intense light are produced by accelerating electrons around a synchrotron to generate electromagnetic radiation ranging in wavelength from x-rays to microwaves. The X-ray detectors are silicon pixel detectors called Pilatus detectors which detect the x-rays by converting them into electric signal by the photoelectric effect in silicon.

1.5 Structure of the Thesis

This thesis can be divided into two parts. The first half, Chapters 2-4, deals with model chocolate suspensions. In Chapter 2, I establish that model suspensions comprising sucrose in triglyceride oil exhibit rheology that is characteristic of chocolate. The effect of lecithin and PGPR on the rheological properties, specifically the viscosity and yield stress, of these model chocolate suspensions is also explored. In addition to lecithin, a single component model phospholipid is studied to establish a minimal model suspension for some of the structural investigations that follow. In Chapter 3, rheology and structural studies are carried out for solutions of the surfactants in triglyceride oil. This establishes how the surfactants interact in the triglyceride oil phase. Finally in Chapter 4, the adsorption and structural investigations of the surfactant thin films at the solid/liquid interface and their effect on inter-particle interaction is studied using SANS, SAXS and SESANS.

In the second part of the thesis, I zoom in on a single sucrose/triglyceride interface by developing an analogous planar model system that can be investigated with reflectivity techniques. The preparation and characterisation of the planar model system is discussed in the first half of Chapter 5. The relevance of this model interface to chocolate suspensions is then explored in the second half of this chapter by carrying out interfacial activity and adsorption studies for the surfactants. Detailed structural investigations of the surfactant thin films at the planar solid/liquid interface using Neutron and X-ray Reflectivity are then discussed in Chapter 6 and 7. Chapter 6 discusses the triglyceride oils at the sucrose interface and in Chapter 7 the effect of addition of lecithin and PGPR is explored. Based on these multi-technique investigations of the surfactant films at the solid/liquid interface in model chocolate systems, a structural model that explains the rheology of molten chocolate is proposed in Chapter 8.

Chapter 2

Model Chocolate Suspensions

2.1 Introduction

Model systems are widely used in soft matter physics to understand the details of various interactions. Real complex systems are simplified in a controlled manner such that relevant interactions are preserved and a well defined model system is constructed to understand the underlying physics. Chocolate is a dense suspension of solids, sucrose, milk and cocoa solids, in a continuous triglyceride fat phase of cocoa butter, containing lecithin and in some cases the polymeric surfactant PGPR. These surfactants are known to reduce the yield stress and viscosity of molten chocolate, which are both important in manufacturing chocolate. How the surfactants cause these modifications to the rheology of molten chocolate remains an open question. In this work we have developed both a suspension and a planar model system to understand the role of the surfactants, lecithin and PGPR, in modifying the rheology of molten chocolate. The suspensions are a minimal model of chocolate, where the sucrose replaces the multiple solid constituents but at a volume fraction comparable to that of the total solids in chocolate and a single component triglyceride oil phase replaces the multi-component cocoa butter. The planar system is constructed to zoom in on a single sucrose/triglyceride interface such that detailed structural investigations can be carried out using QCM-D, contact angle tensiometry and reflectivity.

In this chapter, sucrose in pure triglyceride oil suspensions are discussed as a

rheologically relevant model for molten chocolate, i.e. exhibiting flow properties similar to chocolate. In Section 2.2 the composition and rheology of molten model chocolate suspensions is discussed and the choice of suspended and continuous fat phase are detailed. In Section 2.3 the characterisation of various components used in our model system and the sample preparation for model chocolate suspensions are detailed. Thereafter, in Section 2.4, the rheological effect of lecithin, PGPR and their binary mixture is discussed. In addition to lecithin, a single component phospholipid, POPC, has been used and similar rheology studies were carried out for POPC, PGPR and their binary mixtures.

2.2 Model Chocolate Suspensions

The composition and rheology of chocolate plays an important part in understanding the relevant interactions in chocolate that control its flow properties. In order to use a model chocolate system to carry out detailed structural investigation, we need interactions similar to the one dominant in chocolate. In this section we detail the composition and rheology of chocolate and then use it for our choice for the components of the model system.

2.2.1 Composition of Chocolate

Chocolate is a dense suspensions which comprises $\sim$70% fine (90% of particles are $<$30 μm) solids; specifically sucrose, cocoa and milk solids, in a continuous fat phase of cocoa butter. Table 2.1 details the typical composition of milk chocolate as supplied by Mars Chocolate, UK in terms of the major components.

The solid particles in chocolate remain uncharged and are insoluble in the fat phase. Therefore, they can coagulate due to Van der Waals attraction [8]. To stop such a system coagulating the particle-particle attraction between the suspended particles needs to be reduced. For $0.1-10$ μm colloidal particles a repulsive steric stabilisation barrier of $5-20$ nm is required as attractive forces between colloidal particles are relatively long-ranged [20, 21].

In chocolate this is achieved by adding surfactants to this granular mixture of solids in fat whilst shearing, in a process called conching, to obtain a smooth flowing paste. The addition of surfactants modifies the flow properties of

Table 2.1 *Typical composition of milk chocolate.*

Ingredient	Weight percentage %	Density g/cm^3	Volume fraction
Non-cocoa solids [1]	70	1.45	0.60
Cocoa mass[2]	10	1.16	0.11
Cocoa butter	15	0.892	0.21
Milk fat	5	0.90	0.07
Surfactants[3]	0.8	1.034	0.01

[1] Non-cocoa solids consist of ∼65% sucrose with density 1.59 g/cm^3 and ∼35% skimmed milk powder with density 1.21 g/cm^3, giving it an average density of 1.45 g/cm^3.
[2] Cocoa mass consists of ∼55% fat with density 0.892 g/cm^3 and ∼45% solids with density 1.48 g/cm^3, giving it an average density of 1.16 g/cm^3.
[3] The surfactant used mostly is lecithin but sometimes a combination of lecithin and PGPR are used.

chocolate, as will be discussed in Section 2.4. To gain further insight into how surfactants stabilise the chocolate suspensions and modify its flow properties, we need to understand the physical interaction between the continuous fat phase and the suspended particles: sucrose, cocoa and milk solids. The complete chocolate system is too complex to study systematically, so a simpler model system that mimics the rheology and other physical properties is required. The suspended particles and the continuous fat phase are chosen such that the rheology and particle interaction in chocolate can be reproduced.

2.2.2 Rheology of Dense Suspensions

For suspensions of Brownian particles Newtonian behaviour is observed for dilute suspensions whereas a yield stress is observed for dense suspensions. However more complex flow properties are observed for suspensions of non-Brownian rigid particles, such as chocolate, governed by the volume fraction, particle size distribution, inter-particle interaction and solvent viscosity.

Suspensions of particles with repulsive interactions will not show a yield stress, in contrast to suspensions of Brownian particles, but will exhibit a characteristic shear thickening when the particles are pushed close to each other at high shear rates. The particles experience a shear-induced pressure upon being pushed

close to each other, which when exceeds a critical value P^* increases the friction coefficient between particles and the suspension shear thickens [22, 23]. These studies show that for suspensions of repulsive non-Brownian particles the flow develops complex behaviour due to the dependence of inter-particle friction co-effecient on the inter-particle pressure or applied mechanical stress.

In case of attractive particles, the flow behaviour is dominated by a characteristic yield stress, which occurs due to the adhesive forces between particles. This masks the shear thickening when the yield stress is greater than the onset shear thickening pressure P^* [24]. Once the adhesive constraints have been released, the systems often exhibit shear thinning, followed by constant high shear viscosity. Sometimes in the case of suspensions with low yield stress some shear thickening is additionally observed [25].

The underlying physics of dense suspensions of attractive particles is complex and there are various empirical models available to fit the shear rate dependence ($\dot{\gamma}$) of the shear stress (σ) for such systems [26]. The Bingham model, given by Equation 2.1, is an example of a simple model which can be used to explain the flow of a suspensions which exhibits a yield stress, σ_0, followed by Newtonian flow characterised by a high shear viscosity, η_{HS}.

$$\sigma = \sigma_0 + \eta_{HS}\dot{\gamma} \tag{2.1}$$

This model does not take into account shear thinning. The Casson model, given by Equation 2.2, is one of the most widely used models incorporating shear thinning into the rheology of food suspensions.

$$\sqrt{\sigma} = \sqrt{\sigma_{CA}} + \sqrt{\eta_{CA}\dot{\gamma}} \tag{2.2}$$

where σ_{CA} is the Casson yield stress and η_{CA} is the Casson high shear viscosity.

Chocolate exhibits complex rheological behaviour, as shown in Figure 2.1, with a yield stress followed by shear thinning and finally attaining a constant high shear viscosity, which is sometimes proceeded by shear thickening, typical of a suspension of attractive particles [8, 9].

The shear stress response and viscosity of the chocolate suspensions is fitted to the Casson and Bingham model, shown by the solid and dashed line in Figure 2.1

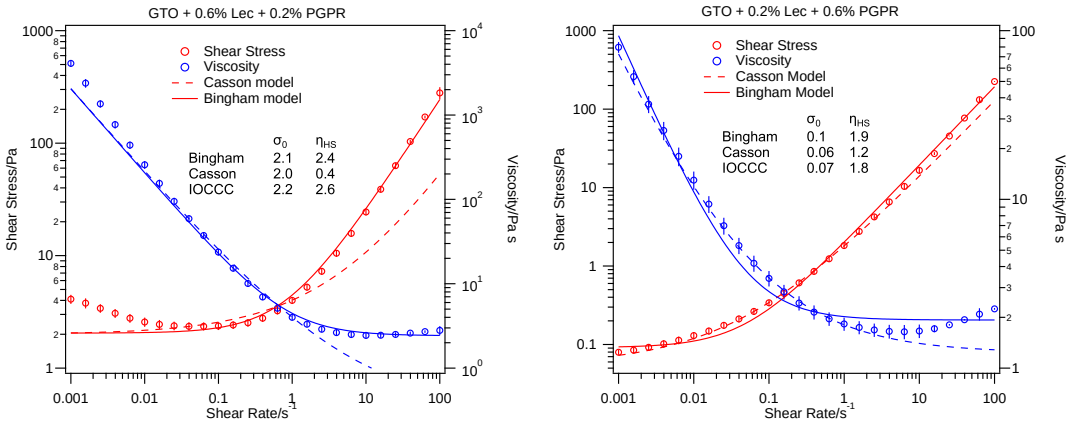

Figure 2.1 *Rheology of typical model chocolate suspensions. Left panel: Suspension with high yield stress and constant high shear viscosity. Right panel: Suspensions showing low yield stress followed by shear thinning and then shear thickening at high shear rates.*

respectively. Neither model fits the data perfectly. For the suspension with a high yield stress and constant high shear viscosity (right panel), the Bingham model provides a better fit, whereas suspensions with low yield stress fit better to the Casson model especially at low shear rates. However, the Casson model doesn't fit the data at high shear rates and the value for high shear viscosity obtained from the Casson model is much lower than the observed value. In addition to these models, the International Office of Cocoa Chocolate and Sugar Confectionery (IOCCC) suggests that another measure of the yield stress is the value of shear stress at a low shear rate (0.01 s^{-1}) and of the high shear viscosity is the measured viscosity at a high shear rate (30 s^{-1}). The values for yield stress obtained using the 3 different methods are consistent with one another within the error of the measurement, however the value of high shear viscosity is the same for the Bingham model and the IOCCC recommended model but the Casson model underestimates the high shear viscosity. For this reason, the Bingham model had been used throughout the thesis to fit the rheology of model chocolate suspensions and the values for yield stresses and high shear viscosities are obtained using the Bingham model.

As can be seen from the left hand panel of Figure 2.1, for shear rates <0.01 s^{-1} the stress response of the sample increases with decrease in shear rate. This could be due to the curve being double valued or that steady flow was not achieved at

low shear rates.[1] The sample was checked for steady state flow, using a variable in the TA output file, and only the shear rate data where steady state was attained has been plotted here onwards.

In addition to steady state shear response of the chocolate suspensions, another measure of the yield stress of the system is is provided by the oscillatory yield stress. In this method, an oscillatory stress of increasing amplitude in applied and the viscoelastic response of the material is measured by recording the viscous modulus, G″, and the elastic modulus, G′. The oscillatory yield stress, σ_{osc}, is the value of the applied oscillatory stress at which G″ becomes greater than G′. This is the stress at which the particle-particle correlations in the sample is destroyed and the response becomes fluid like. This provides another measure of the yield stress of the system and is generally of the same order of magnitude as the steady state yield stress. In the case of dense suspensions of attractive particles a difference between oscillatory and steady state yield stress can be observed with $\sigma_0 > \sigma_{osc}$ by up to an order of magnitude. This arises due to two different processes involved in yielding: breaking of the nearest neighbour bonds measured by the oscillatory yield stress, and breaking of the topology (or particle cage) measured by the steady state yield stress [27]. Despite the difference in magnitude of the two yield stresses, changes in inter-particle interactions are reflected in the oscillatory and steady state shear stress similarly as the nearest neighbour interaction also governs topological behaviour. Therefore, both the oscillatory and steady state yield stress provide a measure to study the inter-particle interactions in a suspensions of attractive particles.

2.2.3 Model Chocolate System: Choice of Various Phases

To find a rheologically relevant model for chocolate suspensions to investigate the effect of surfactants, the flow behaviour of the model suspensions needs to be qualitatively matched to that of chocolate; exhibiting the characteristic rheology of dense suspensions of attractive particles as discussed in Section 2.2.2. This can be done by suitably choosing the suspended particles and continuous phase as these are the main constituents governing inter-particle interaction apart from the surfactants, thereby defining a minimal model suspension for molten chocolate.

[1] The stabilisation routine for these measurements waited for 3 successive measurements to be within 5% of one another taken over a period of 10 s or a maximum of 120 s before taking measurements. So for $\dot{\gamma}<0.01$ s^{-1} with a wait of 120 s, the sample may or may not have attained steady state flow.

Suspended Particles

The suspended particle phase could be replaced by chemically inert spherical glass spheres as used by Hugelshofer [28] or by milled sucrose, which is already a major component of chocolate, as used by Vernier [8]. The glass beads are spherical and the surface chemistry can be tuned to allow different interactions to be studied, which could simplify experiments, whereas, sucrose in oil system with surfactants is closer to the actual chocolate system and therefore the interactions are more relevant.

Arnold *et al.* [29] explored the effect of lecithin on the rheology and inter-particle interaction for sucrose/oil suspensions and glass/oil suspensions. They used two types of oil for their comparison, namely soybean oil and a medium chain triglyceride (MCT). Their studies showed that both the dispersed and the continuous phase had an effect on the properties of the suspension. For both oils the addition of lecithin to sucrose suspensions showed a reduction in viscosity, which is consistent with observations for chocolate. For glass suspensions in soybean oil there was an increase in viscosity on addition of lecithin whereas in MCT there was a decrease. These results agree with Vernier's experiments on sugar in Triolein and Hugelshofer's results on glass beads in a mixture of medium chain triglycerides (Akomed R).

In order to study the inter-particle interaction between sucrose or glass spheres and oil, Arnold *et al.* performed AFM force-distance experiments. The experiments were done in oil using a cantilever tip modified by attaching sucrose or glass beads using a two-component epoxy glue and the substrate was prepared by gluing glass splinters or crystallising sucrose in Petri dishes. The detachment force between sugar crystals in soybean oil was found to be approximately 2.7±1.6 nN. Their results indicate that adhesive forces dominate the interactions between sugar particles dispersed in oil. Addition of lecithin was found to reduce the force required to separate the adhering of sucrose crystals by approximately 10-30% compared to the force required without the presence of lecithin. For glass beads in oil they found that the inter-particle interactions are much smaller and not influenced by lecithin. These results indicate some big differences between inter-particle interactions between sucrose in oil and glass sphere in oil.

The differences in rheology and inter-particle interaction suggest that in general glass spheres, even though they can provide more tunable interactions and are easier to study, are not suitable as a model for the suspended particles in chocolate

systems. For this reason, it was decided not to pursue glass beads in oil as a model system in this work. Rheological measurements on sucrose/sunflower oil systems done by the Poon group [10, 30] show that for a 65% w/w suspension flow properties similar to that of chocolate, i.e. a yield stress followed by shear thinning regime and finally a constant high shear viscosity, are obtained. Sucrose particles in oil are a suitable model to mimic the inter-particle interaction and rheology of chocolate and were used for further work in this PhD.

Continuous Fat Phase

The next choice is that of the continuous fat phase. Cocoa butter mainly comprises triglycerides of fatty acid with saturated and unsaturated alkyl chains with 16-18 carbon atoms; the majority of fatty acid tails being derived from palmitic acid, stearic acid and oleic acid. Table 2.2 [31] shows the fatty acid composition of cocoa butter. As cocoa butter is a natural product it also comprises mono and diglycerides and other surface active components which can obscure detailed structural investigation. Therefore, we decided to use a continuous phase fat of pure oil. It is desirable that the continuous fat phase is a liquid at room temperature as this means molten model chocolate can be obtained at room temperature. Another desirable feature of the oil phase is that it contains saturated fatty chains as this allows for easier deuteration of the molecule for neutron scattering and reflectivity studies (discussed later).

It has been shown by various studies [8, 10, 29, 30] that sucrose suspensions in both long chain and medium chain triglycerides mimic rheology of molten chocolate and can be used. The oils used in these studies were industrial oils e.g. sunflower oil, soybean oil which have a broad distribution of fatty acid chains and also contain additional surface active components, which is not desirable from the point of view of trying to discern the effects of surfactants in model chocolate, so in this Ph.D. high purity ($\geq$99%) single component oils have been used.

A starting point for each investigation was to measure the steady state and oscillatory rheology, using the method described in Section 2.3.5, of our minimal model chocolate suspensions formulated from 65% w/w sucrose in various pure oils using the method described in Section 2.3.4. The oils used were pure Glyceryl Trioctanoate (GTO), Glyceryl Trioleate (TO), Glyceryl Trioleate doped with 35%

Table 2.2 *Fatty acid and triglyceride composition of cocoa butter.*

	carbon and bonds	Percentage
	Fatty acid	
Stearic (S)	C18:0	34-35
Oleic (O)	C18:1	33-34
Palmitic (P)	C16:0	26-27
Linoleic (Lo)	C18:2	2-3
Arachidic (A)	C20:0	1
Palmitoleic (Po)	C16:1	<1
Other		<1
	Triglyceride	
POP	C16:0 C18:1 C16:0	16-18
POS	C16:0 C18:1 C18:0	40-43
SOS	C18:0 C18:1 C18:0	23-25
POO	C16:0 C18:1 C18:1	2-4
SOO	C18:0 C18:1 C18:1	3-5

w/w Glyceryl Tributyrate (TO + TB)[2], Glyceryl Tripalmitate (TP) and Glyceryl Trioleate doped with 25% w/w Glyceryl Tripalmitate (TO + TP)[3], and the non triglyceride oil Tetradecane (TD), commonly used as a model food oil. The surfactant concentration in these studies were kept at 0.6% w/w lecithin and 0.2% w/w PGPR, as this is a relevant surfactant ratio when lecithin and PGPR are used in combination in chocolate.

As can be seen from Figure 2.2, the rheology of 65% w/w sucrose suspensions in all triglyceride oils show the typical model chocolate behaviour exhibiting a yield stress, followed by shear thinning before reaching a Newtonian plateau. The exact value of yield stress and high shear viscosity depends on the oil used, but the qualitative behaviour is the same and representative of chocolate rheology. The data fits well to the Bingham model and the values for viscosity and yield stress obtained from the model are summarised in the annotation of the figure.

[2]TO is unsaturated and therefore cannot be easily deuterated.Dopin of TO with either deuterated TP or deuterated TB (which is a constituent of butter) provides a method of introducing neutron contrast that is much cheaper than deuterating TO. Suspensions of sucrose in these oil mixtures were studied to confirm that their rheology matched that of molten chocolate.

[3]TP is solid at room temperature so the rheology and preparation of suspensions in TP & TO+TP is done at 80°C. To compare these to TO at room temperature

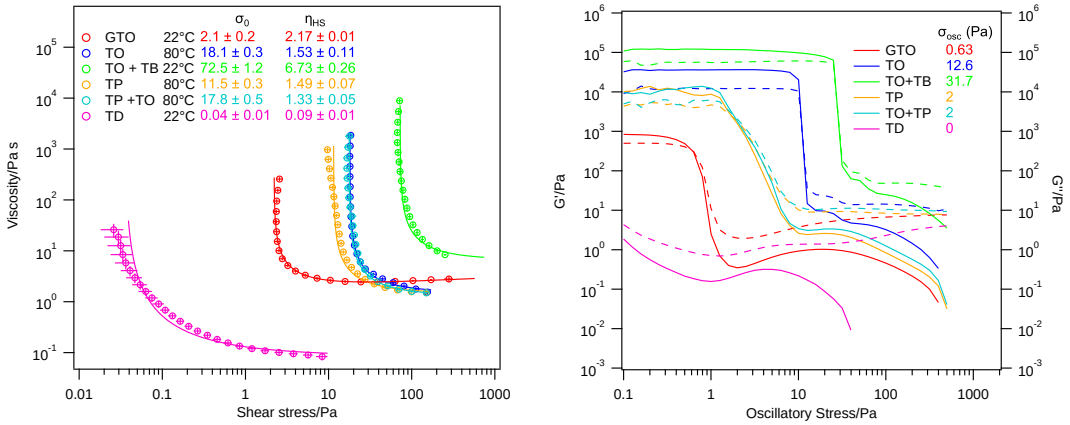

Figure 2.2 *Rheology of 65% w/w sucrose suspensions in various oils with 0.6% lecithin and 0.2% PGPR. Left panel: Steady state rheology showing viscosity vs stress stress data (hollow circles) fitted to the Bingham plastic model (solid line). Right panel: Oscillatory rheology studies showing viscoelastic response of the suspensions where G' is the elastic modulus (solid line) and G'' is the storage modulus (dashed line).*

The suspensions in all triglyceride oils exhibit an oscillatory yield stress, i.e. a cross over point at which G″ exceeds G′, of the same order of magnitude as the steady state yield stress. In contrast for the suspension in tetradecane G″ is always greater than G′, suggesting the suspension doesn't have a viscoelastic yield stress or has already yielded at oscillatory stress of 0.01 Pa. Furthermore, no real yielding behaviour is observed in the steady state rheology measurements. There is a shear thinning followed by a very low high shear viscosity, which is not representative of chocolate rheology. Additionally, the suspension sediments into a sucrose rich part with an oil rich part at the top. For these reasons, it was decided to only use triglyceride oil as a replacement for cocoa butter in model chocolate.

In further investigations in this thesis, 65% w/w sucrose in triglyceride oil suspensions were used as model chocolate suspensions. Mainly TO and GTO were used as model oils as they are liquid at room temperature; oleic acid is a majority fatty acid tail component of cocoa butter and medium chain triglycerides have been extensively used in literature to study food suspensions and emulsions. TP and TB were used only as dopants in TO when the deuteration level of the oil needed to be tuned.

2.3 Materials and Methods

Sucrose, triglyceride oil and surfactants (lecithin, PGPR and model lecithin: POPC) are used throughout this work and this section details the characterisation of these materials. There is also a description of the sample preparation method used to make sucrose in oil suspensions to be used as model chocolate suspensions

2.3.1 Sucrose

The sucrose used in this work was milled crystalline icing sugar sourced from British Sugar by Mars Chocolate, UK. The size distribution of the sucrose particles was measured using a Diffraction Particle Sizer as shown in the left panel of Figure 2.3. Five runs were measured and the graph shows the average % distribution by volume as a function of particle size with the error bars given by the standard deviation of the data sets and the average statistics for the data are shown in the annotation. The mean particle size measured was 10.9 ± 0.1 μm with a standard deviation of 5.9 ± 0.1 μm. This is a broad distribution for which the measured values for cumulative mass intercept d10, d50 and d90[4] are 5.1 ± 0.1, 9.6 ± 0.1 and 17.3 ± 0.2 μm respectively. As can be seen from the figure, a trimodal distributions is observed, with peaks at 6.1 ± 0.1, 12.4 ± 0.1 and 24.3 ± 0.1 μm fitted using a log normal distribution. This could be due to sucrose particles sticking together in clusters of 2 and 4 or the distribution itself could be trimodal. The right panel of Figure 2.3 shows an SEM image of the particles confirming the broad distribution in size.

2.3.2 Oils

For initial rheology studies the oils used were $\geq$ 99% pure Glyceryl Trioctanoate (GTO), $\geq$ 60% Glyceryl Trioleate (TO), $\geq$ 80% Glyceryl Tripalmitate (TP), $\geq$ 99% Glyceryl Tributyrate (TB) and $\geq$ 99% Tetradecane (TD). For more detailed rheology studies $\geq$ 99% pure Glyceryl Trioctanoate (GTO) and $\geq$ 99% pure Glyceryl Trioleate (TO) were used. All the oils were sourced from Sigma Aldrich,

[4]d-values can be thought of as the particle size which divides the samples mass into a specified percentage when the particles are arranged on an ascending mass basis. For example the d10 is the diameter at which 10% of the sample's mass is comprised of particles with a size less than this value.

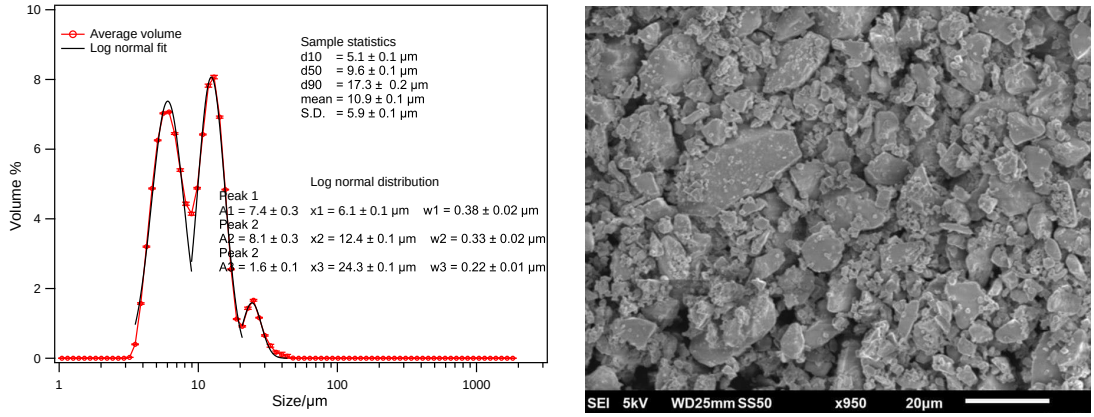

Figure 2.3 *Characterisation of the crystalline icing sucrose powder obtained from British Sugar. Left panel: Volume % distribution as a function of the particle size measured for the sucrose powder using a diffraction particle sizer. Right panel: SEM image of the sucrose powder.*

UK. The deuterated oils used for neutron scattering and reflectivity studies were obtained from ISIS deuteration facility, Oxford, UK (d-GTO and d-TB), QMX Laboratories, UK (d-GTO and d-TP) and National Deuteration Facility, ANSTO, Australia (d96-TO).

The potential impurities (<1%) present in the $\geq$ 99% pure GTO and $\geq$ 99% pure TO are di-glycerides and mono-glycerides which can be surface active. To investigate the interfacial activity of these impurities, interfacial tension of the triglyceride/water interface was measured and compared to values found in literature. TO has a surface tension of 32.5 ± 0.5 mN/m and GTO of 29.5 ± 0.5 mN/m. These are higher than the values for these triglyceride/water interface found in literature: $29 - 31$ mN/m for TO/water interface and $25 - 29$ mN/m for GTO/water interface [32–34]. The interfacial tension of the triglyceride/water interface does not change over a period of 60 mins. Additionally, surface tension of the 60% pure TO/water interface was measured and found to be 8 mN/m, significantly less than that of pure TO/water interface. These interfacial tension measurement suggest that the concentration of the surface active impurities is sufficiently small that there is no apparent driving potential for them to adsorb at the triglyceride/water interface. Once surfactants are present the impurities need to compete with the interfacially active surfactant. As can be seen by the change in contact angle measurements discussed in Chapter 5, the added surfactant show greater activity for the sucrose interface irrespective of the purity of the triglyceride. This is potentially due to the presence of polar head group in

the case of phospholipids and polar glycerol backbone in the case of PGPR.

The molar mass and density of various oils is summarised are Table 2.3, and the chemical structure is given are Appendix A.1.

2.3.3 Surfactants

Lecithin, which is mainly phospholipids, was obtained from Mars Chocolate, UK. Lipidomics investigation of the samples[5] confirmed that the main components are triglycerides, phosphatidylcholine (PC), phosphatidylethanolamine (PE) and phosphatidylinositol (PI) with alkyl chain having 14-18 carbon atoms (see Figure A.3). The phospholipid distribution is 20-28% PC, 10-15% PE, 10-15% PI, 5-10% phosphatic acid (PA). POPC and d31-POPC, which were used as a model lecithin, were obtained from Avanti polar lipids, USA.

PolyGlycerol PolyRicinoleate (PGPR), comprising a backbone of polyglycerol with polyester side chains of ricinoleic acid, was obtained from Mars Chocolate, UK. NMR studies, ^{1}H and ^{13}C, were done on the PGPR samples and compared to the paper by Orfanakis *et al.* [5] (see Figure A.6). These confirm that PGPR is polydisperse consisting of polyglycerol moieties of various lengths being esterified by ricinoleic acid and estolides and to a lesser extent by oleic and linoleic acids. DOSY NMR was also carried out on the samples (see Figure A.7) to get an idea about the diffusion coefficient of the species present in the PGPR sample. The DOSY NMR suggests we have a less polydisperse PGPR distribution as compared to the one observed by Orfanakis *et al.* and that the average radius of the diffusing moiety is $\sim$4 nm. This is possibly due to PGPR micellar aggregates and has been confirmed using scattering studies.

The sucrose crystal has hydroxyl groups which can interact with the polar head groups in the phospholipids in Lecithin and the unreacted OH in the polar glycerol backbone of the PGPR forming hydrogen bonds. PC and PE are both zwitterionic surfactants and can therefore form hydrogen bonds with sucrose, whereas PA, PI, and glycerol form hydrogen bonds due to the charge present in the surfactants or via their hydroxyl groups. The number of hydrogen bonds formed between the sucrose and the surfactant, and therefore the strength of interaction with sucrose, will depend on the head group of the surfactant [35, 36], with the strength of interaction being greatest for PI followed by PC, PE, PA and glycerol. Keeping

[5]Lipidomics performed by Phil Whitfield at University of the Highlands and Islands.

this in mind and the abundance of the PC in lecithin a long chain partially saturated PC is a good model for lecithin.

The molar mass and density of various surfactants are summarised in Table 2.3 and the lipidomics, NMR data and the structure of model phospholipids and PGPR are given in Appendix A.2.

Table 2.3 *Molar mass and density of the various oils and surfactants.*

Chemical	Formula	Molar mass g/mol	Density g/cm^3
Sucrose	$C_{12}H_{22}O_{11}$	342.3	1.59
GTO	$C_{27}H_{50}O_6$	471	0.956
d-GTO	$C_{27}D_{50}O_6$	521	1.058
TO	$C_{57}H_{104}O_6$	885	0.91
d96-TO	$C_{51}D_{96}H_8O_6$	982	1.009
TP	$C_{51}H_{98}O_6$	807	0.875
d-TP	$C_{51}D_{98}O_6$	906	0.982
TB	$C_{15}H_{26}O_6$	302	1.032
d-TB	$C_{15}D_{26}O_6$	328	1.104
POPC	$C_{42}H_{82}NO_8P$	760	1.01
d31-POPC	$C_{42}D_{31}H_{51}NO_8P$	791	1.05
Lecithin	Lipid Mixture (see Appendix A.2)	750-800	1.034
PGPR	$(C_3H_5O_2)_n(C_{18}H_{32}O_2)_m$	1150-1200	0.957

2.3.4 Sample Preparation for Model Chocolate Suspensions

Sucrose in triglyceride oil suspensions were made by mixing 65% w/w sucrose with surfactant solution in the triglyceride oil. The required amount of surfactants were first dispersed in the triglyceride oil by vortex mixing followed by sonicating for 10 mins. Sucrose (65% w/w) was added to this solution and the suspension was mixed using a vortex mixer followed by IKA T10 Basic mixer at at ∼10000 rpm for 2 mins till a smooth paste is obtained. This process mimics the conching of chocolate during industrial manufacturing.

2.3.5 Rheology Measurements on Model Chocolate Suspensions

Suspension rheology experiments were performed on a stress-controlled rheometer, TA Instruments AR 2000, using a 40 mm cross-hatched plate-plate geometry, to avoid wall slip. The working gap was 500 μm with temperature at 22°C. Steady state rheology experiments were carried out where the stress response was measured under an imposed shear rate going from 0.001-100 s^{-1}. Stress sweeps were made in the up and down direction 3 times, ensuring each point had achieved steady state, and then averaged. Oscillatory rheology experiments were done under an imposed oscillatory stress, going from 0.001-1000 Pa, and the viscoelastic response, G′ and G″, were measured.

2.4 Effect of Surfactants on the Rheology of Model Chocolate

As discussed in Section 2.2.2, the rheology of dense suspensions comprising attractive particle, such as chocolate, shows a characteristic yield stress before settling to a Newtonian flow plateau at high shear rates defined by a constant viscosity. The yield stress arises due to the Van der Waals attraction between the particles which needs to be overcome in order to make the suspension flow. It varies with the strength of the inter-particle attraction and the effective volume fraction ($\phi_j - \phi$), which is the volume fraction of the suspension (ϕ) relative to the jamming volume fraction (ϕ_j), of the particles.

The inter-particle interaction can be modified by adsorption of polymers or surfactants which can provide steric repulsion between the particles. The effective volume fraction can be decreased by either trivially reducing the volume fraction of the particles (not desirable in chocolate) or by increasing the jamming volume fraction. Recent studies on the rheology of dense suspensions show that the jamming fraction for dense suspensions depends upon the friction co-efficient between the particles [37–39]. These studies suggest that the jamming fraction increases from ϕ_{RLP} (random lose packing) to ϕ_{RCP} (random close packing) as the co-efficient of friction between particles in a suspensions is decreased from infinity to vanishingly small values. The co-efficient of friction can be reduced by creating a lubricating layer between particles. In addition to controlling the

yield stress, the effective volume fraction, $(\phi_j - \phi)$, also controls the high shear viscosity by [40]. So reducing the friction co-efficient additionally lowers the high shear viscosity as well.

Surfactants are used to alter the rheology of the molten chocolate suspensions. The two most commonly used surfactants in chocolate manufacturing are lecithin and PGPR. Other surfactants used include ammonium phosphatide, commonly called YN, and sucrose esters. The influence of addition of surfactants on rheological properties of chocolate has been of keen interest as it affects the manufacturing. There have been studies focussed on understanding the effect of surfactant adsorption on the rheology of chocolate made using bulk properties, e.g. viscosity, yield stress, adsorption and sedimentation behaviour, and interfacial tension [8, 9, 28, 41, 42]. However, these studies do not provide a mechanism as to how the surfactants influence the inter-particle interaction and thereby change the rheology of molten chocolate.

In this section we discuss the effect of lecithin and PGPR, the two main surfactants used in chocolate, on the high shear viscosity and yield stress of 65% w/w model chocolate suspensions. We have also looked at how POPC (model phospholipid) and PGPR affect the flow properties to better understand the interaction between polymers and phospholipid surfactants. These studies form the basis for further structural investigation to understand the role of lecithin and PGPR in modifying the rheology of molten chocolate.

2.4.1 Lecithin and PGPR

The main surface active components in lecithin are phospholipids, $\sim$50% by composition. Addition of lecithin in small quantities, $0.1 - 0.3\%$ (w/w), significantly reduces the viscosity and yield stress of chocolate. However, further addition of lecithin, $> 0.3\%$ (w/w), increases the yield stress of chocolate. PGPR on the other hand is a polymeric molecule which has a small effect on the viscosity but dramatically reduces the yield stress [8]. These results are consistent with the ones observed by the Poon group in Edinburgh [10, 30] for the rheology of sucrose in triglyceride oil suspensions. The effect of lecithin and PGPR on the rheology of 65% w/w sucrose suspensions in sunflower oil as observed by Daniel Hodgson are shown in the Figure 2.4.

Often in chocolate a combination of lecithin and PGPR are used such that

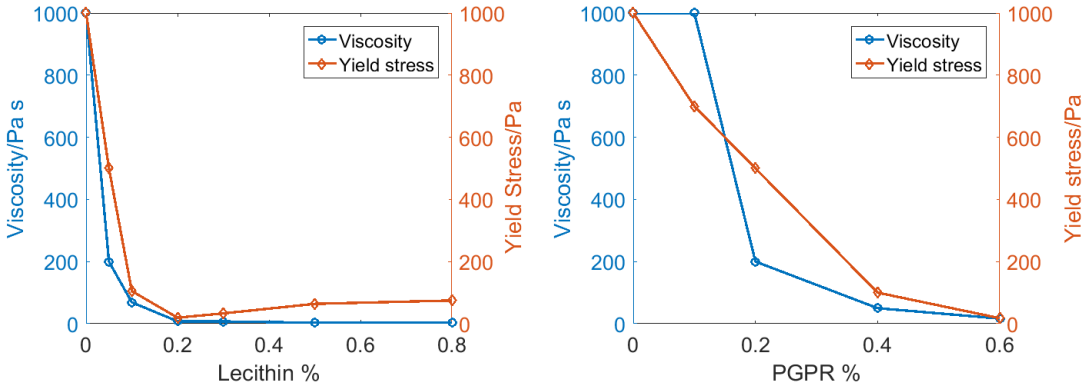

Figure 2.4 *Rheology of 65% w/w sucrose suspensions in sunflower oil measured by Daniel Hodgson showing the high shear viscosity and yield stress vs the surfactant concentration. Left panel: Effect of lecithin. Right panel: Effect of PGPR.*

both viscosity and yield stress can be reduced. It has been observed that when lecithin and PGPR are used together a lower viscosity is observed than with the same quantity of lecithin on its own, similarly the yield stress is less than the suspensions containing only PGPR. This co-operative effect has been reported in both molten dark and white chocolate [9] and in 65% w/w sucrose in sunflower oil suspensions [10]. The same effect is demonstrated for 65% w/w sucrose in pure triglyceride oil suspensions in the photographs shown in Figure 2.5. The suspension in the left panel contains 0.8% lecithin and as can be seen in the photograph does not spread (has high yield stress), whereas the suspension in the right panel containing 0.4% lecithin + 0.4% PGPR spreads readily without any applied shear (has negligible yield stress). Handling the suspensions also indicates that the suspension containing 0.4% lecithin + 0.4% PGPR has a lower viscosity than the suspension containing 0.8% lecithin only.

In order to explore this co-operative effect systematically, a series of steady state shear and oscillatory rheology experiments were performed on 65% sucrose in TO and GTO suspensions whereby the total surfactant concentration was kept constant at 0.8% while varying the lecithin to PGPR ratio. Here we completely exclude the effect of any surface active species present in the fat phase by using $\geq$99% pure TO and GTO as the fat phase. The steady state rheology is shown in Figure 2.6 and 2.7 for TO and GTO respectively. The oscillatory rheology for suspensions in both oils is shown in Figure 2.8. The data was fitted to both Bingham and Casson model, however for reasons explained in Section 2.2.2 the values quoted are from the Bingham model.

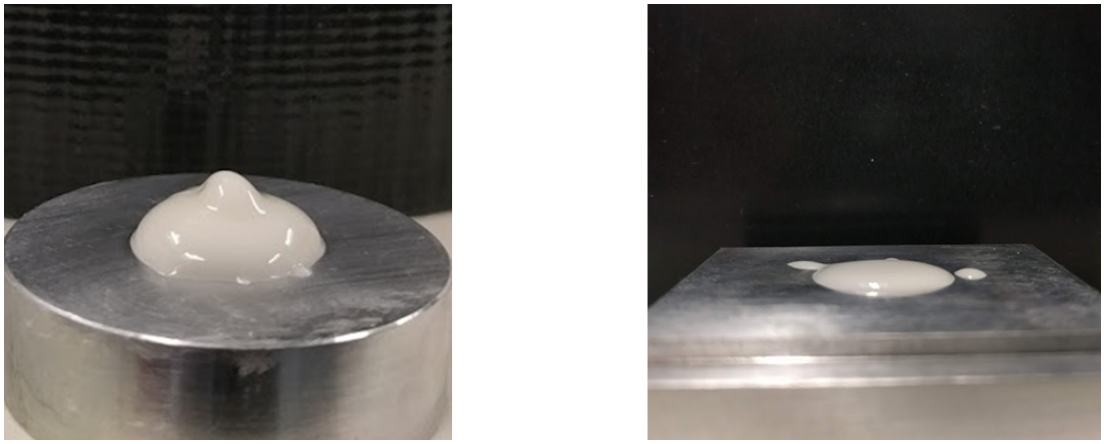

Figure 2.5 *The effect of a combination of lecithin and PGPR on the flow properties of model chocolate (65% w/w sucrose in triglyceride oil) suspensions. Left panel: Suspension with 0.8% lecithin forming a paste with a low viscosity but high yield stress (difficult to spread). Right panel: Suspension with 0.4% lecithin + 0.4% PGPR forming a paste with a low viscosity and negligible yield stress (spreads readily without any applied shear).*

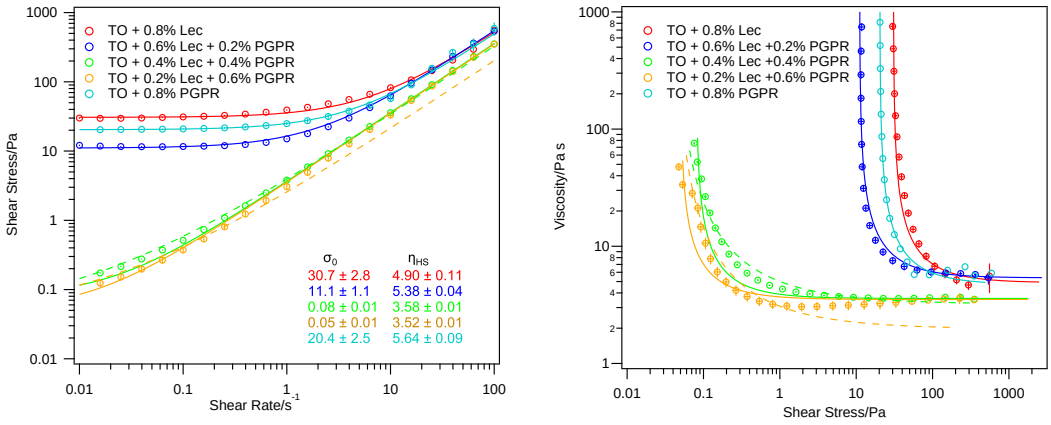

Figure 2.6 *Rheology of 65% w/w sucrose suspensions in TO with varying amounts of lecithin and PGPR at fixed total surfactant concentration of 0.8%. Left panel: Shear stress vs shear rate data (hollow circles) data. Right panel: Viscosity vs shear stress data (hollow circles). The data is fitted to Bingham model (solid line) and Casson model (dashed line).*

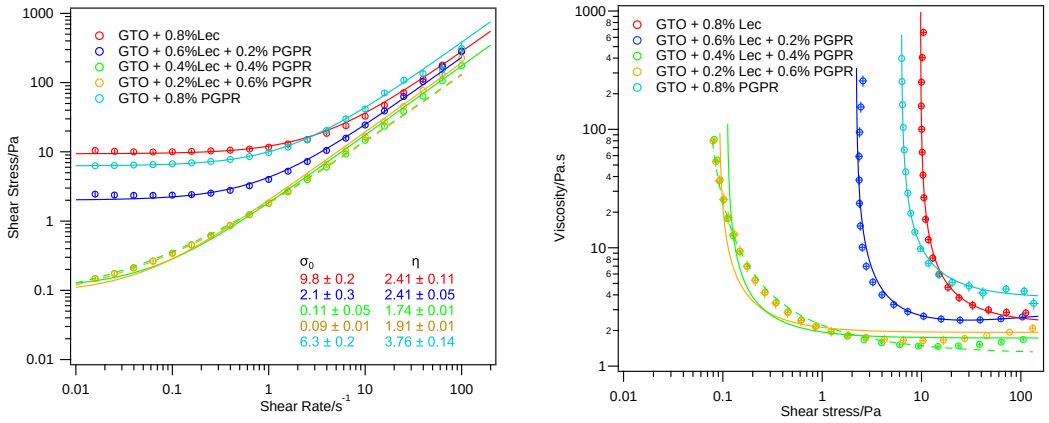

Figure 2.7 *Rheology of 65% w/w sucrose suspensions in GTO with varying amounts of lecithin and PGPR at fixed total surfactant concentration of 0.8%. Left panel: Shear stress vs shear rate data (hollow circles) data. Right panel: Viscosity vs shear stress data (hollow circles). The data is fitted to Bingham model (solid line) and Casson model (dashed line).*

As can be seen from Figure 2.6 and 2.7 it is the fraction of PGPR that is primarily responsible for controlling the yield stress of the suspensions. Samples containing lecithin only have high yield stresses of 30.7 Pa and 9.4 Pa for TO and GTO respectively. Addition of a small amount of PGPR (25% of the total surfactant amount) to replace the lecithin reduces the yield stress by a factor of 3 for TO and 9 for GTO. This drastic reduction is such that for samples in which 50-75% of the total surfactant is PGPR the yield stress vanishes ($\leq$ 0.1 Pa) for suspensions in both the oils. However, a small amount of lecithin is essential to achieve this reduction as for PGPR only samples the yield stresses of 16.6 Pa and 6.9 Pa are observed for TO and GTO respectively.

The high shear viscosity shows a less obvious dependence on the two surfactants. Adding PGPR to 25% of the total surfactants amount to replace the lecithin has little or no effect on the high shear viscosity of the suspensions, but further addition of PGPR to 50-75% of the total surfactant amount lowers the high shear viscosity. It also appears that at extremely high shear stresses, the viscosity tends to the same value for all of the suspensions with different surfactant compositions.

The oscillatory yield stress shows a similar dependence on the surfactant composition as the steady state yield stress. However the value of oscillatory yield stress is lower by a factor of 2-3 than that of the steady state yield stress. The difference is more for PGPR only sample where we observe a factor of 10-

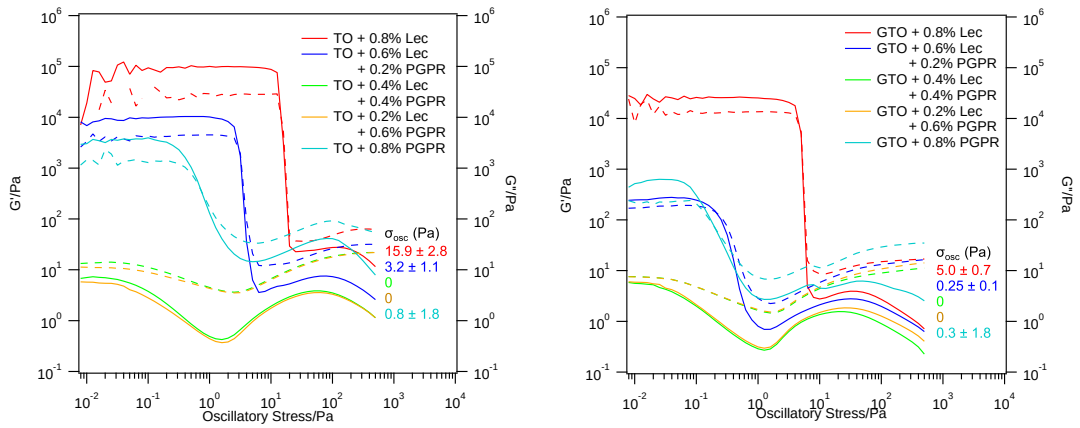

Figure 2.8 *Oscillatory rheology studies showing the viscoelastic response of 65% sucrose in oil suspensions with varying amounts of lecithin and PGPR at fixed total surfactant concentration of 0.8%, where G' is the elastic modulus (solid line) and G'' is the storage modulus (dashed line). Left panel: Suspensions in TO. Right panel: Suspensions in GTO.*

15. This suggests the surfactants forms a hierarchy of structures, one of which dominates friction (steady state yield stress) and the dominating inter-particle attraction (oscillatory yield stress) [27].

2.4.2 Minimal Model Suspensions: Model Lecithin

The principal surface active component of lecithin is phospholipids and addition of single single component PC phospholipid has a similar effect on the rheology of molten chocolate as lecithin [8]. Addition of a small amount of PC phospholipids reduces both the viscosity and yield stress. Upon further addition of the phospholipid, an increase in yield stress is observed, as is the case with suspensions with lecithin. This has been confirmed by carrying out rheology experiments on 65% sucrose in TO and GTO suspensions using POPC.

In order further unpick the phospholipid-polymer interaction, the lecithin has been replaced by a mixture of 50% POPC, chosen to be representative of the majority head group and tail distribution in the phospholipids found in lecithin, and 50% triglyceride, called Lec_{POPC}. Oscillatory and steady state rheology experiments were conducted for suspensions in TO and GTO and are shown below in Figure 2.9 and 2.10 respectively.

The rheological behaviour of suspensions containing Lec_{POPC} and PGPR mixtures

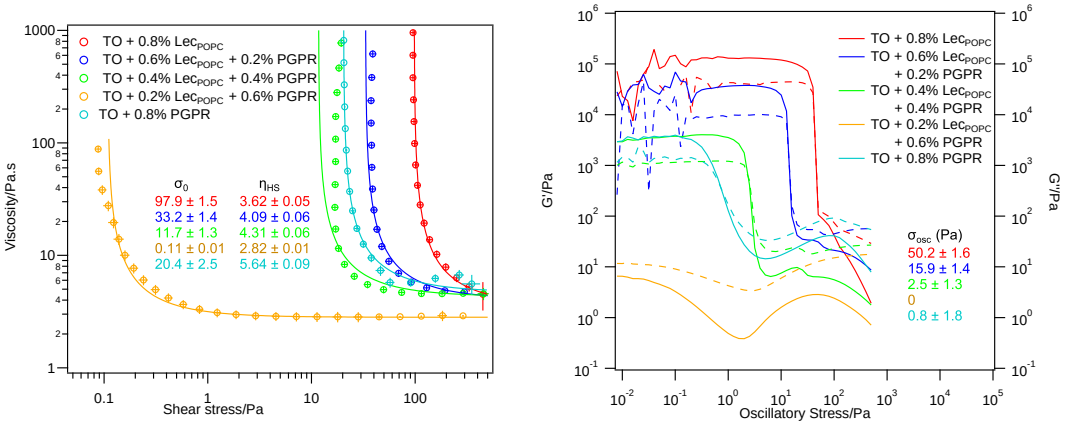

Figure 2.9 *Rheology of 65% w/w sucrose suspensions in TO with varying amounts of Lec$_{POPC}$ and PGPR and total surfactant concentration at 0.8%. Left panel: Steady state rheology showing viscosity vs shear stress data (hollow circles) fitted to the Bingham plastic model (solid line). Right panel: Oscillatory rheology studies showing viscoelastic response of the suspensions where G′ is the elastic modulus (solid line) and G″ is the storage modulus (dashed line).*

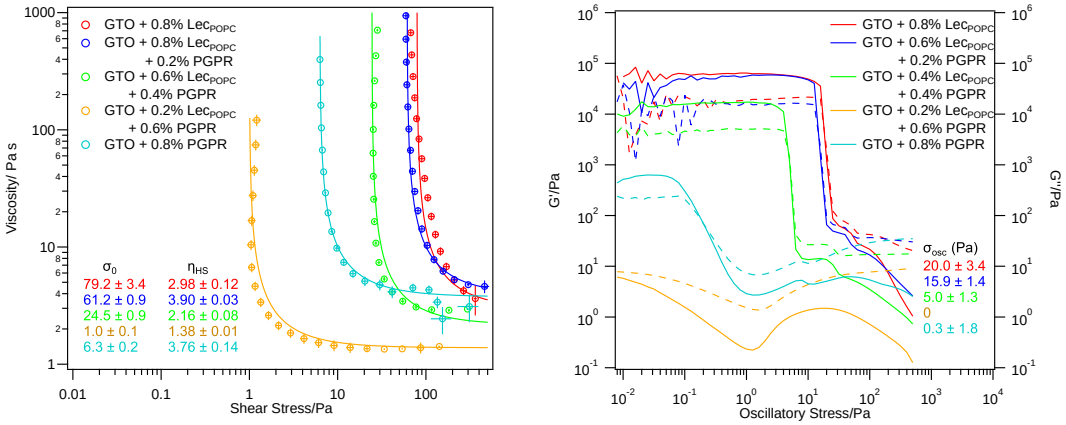

Figure 2.10 *Rheology of 65% w/w sucrose suspensions in GTO with varying amounts of Lec$_{POPC}$ and PGPR and total surfactant concentration at 0.8%. Left panel: Steady state rheology showing viscosity vs shear stress data (hollow circles) fitted to the Bingham plastic model (solid line). Right panel: Oscillatory rheology studies showing viscoelastic response of the suspensions where G′ is the elastic modulus (solid line) and G″ is the storage modulus (dashed line).*

is similar to that observed for suspensions containing lecithin and PGPR mixtures, whereby both viscosity and yield stress is reduced by having a combination of phospholipid and PGPR instead of either of the surfactants by themselves. The key difference is the lower value obtained for high shear viscosity, particularly with TO, and the higher observed yield stress. Also the amount of PGPR required to cause a drastic reduction in yield stress (σ_o<0.1 Pa and $\sigma_{osc} \approx 0$Pa) is greater than that for lecithin.

2.4.3 Phospholipid and Polymeric Surfactant: Mechanism and Summary

There are competing theories about how lecithin reduces the high shear viscosity and yield stress. On the one hand it is believed that the phospholipids in lecithin adsorbs at the sugar surface in chocolate and the lipophilic tail group aids the flow by rendering the sugar more hydrophobic [43] whereas Arnold *et al.* [29] suggest that the role of lecithin as an emulsifier is to reduce the adhesive interactions between sucrose particles by measuring vertical forces between sucrose particles in oil. Also to explain the undesirable increase in yield stress at high surfactant concentrations, it is suggested that the excess lecithin forms micellar structures in the continuous fat phase [44], which become entangled increasing adhesion between the sucrose particles [8].

Knowledge about how PGPR interacts with the sucrose interface is limited at best. It is hypothesised that the polyglycerol backbone is surface active and that it alters the nature of the sucrose surface making them more lipophilic [45]. The hydrocarbon chains in PGPR are similar to the ones found in fat implying that PGPR should be soluble in the continuous fat phase, which means that the PGPR could form a swollen polymer layer. This is turn could result in a steric repulsion between sucrose grains with adsorbed PGPR.

The combined effect of phospholipid and polymeric surfactants, summarised in Figure 2.11, is even more poorly understood. One suggestion is that there is a lecithin layer at the sucrose interface on top of which an extended PGPR layer sits. Such a structure could reduce both inter-particle interaction, due to the extended PGPR layer, and the friction co-efficient, via the lubricating lecithin layer. This doesn't explain the drastic reduction in yield stress (even compared to a pure PGPR layer) as observed in the suspensions containing lecithin and PGPR in

the ratio 50:50 and 25:75 and the reduction in viscosity for the same. Another possibility is that PGPR is responsible for breaking up rigid micellar structures in oil thereby reducing the yield stress, if the yield stress is indeed attributable to the entangled micellar structure in the oil phase. However, this still doesn't explain the systematic dependence of yield stress on the PGPR fraction of the total surfactant and the reduction in viscosity for the suspensions containing high PGPR fraction (75% of the total surfactant amount).

An alternative is that lecithin forms a lubricating layer which offers reduction in viscosity and some reduction in yield stress. A rigid lamellar layer is more effective at reducing viscosity and therefore POPC is more effective at reducing viscosity than lecithin. For lecithin and PGPR there is an interaction at play between phospholipids and PGPR which creates a swollen layer resulting in steric stabilisation and lubrication. This results in the reduction of viscosity and diminishing yield stress for certain ratio of phospholipids and polymeric surfactants as shown in the Figure 2.11.

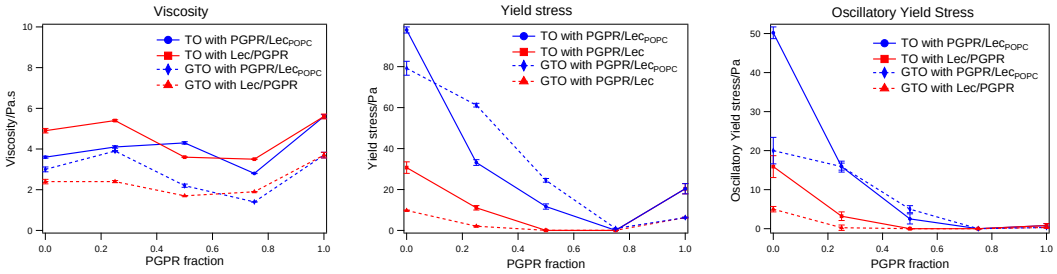

Figure 2.11 *Summary of rheology for 65% w/w sucrose in triglyceride oil (GTO and TO) suspensions containing phospholipids (lecithin and Lec_{POPC}) and PGPR with varying PGPR fraction at total surfactant concentration of 0.8% w/w. Left panel: High Shear viscosity. Middle Panel: Steady state yield stress found using the Bingham model. Right panel: Oscillatory yield stress.*

The approach taken in this thesis is to conduct detailed molecular-scale structural investigations based on scattering of neutrons and x-rays to distinguish between various hypothesis.

2.5 Conclusions

By a combination of literature review and rheological characterisation experiments, 65% sucrose in pure triglyceride oil suspensions are established as a good

model for molten chocolate. These suspensions mimic the rheology of molten chocolate exhibiting a yield stress followed by shear thinning behaviour until reaching Newtonian flow at high shear rates. A variety of triglyceride oils were studied and all of them show the characteristic chocolate behaviour. Extensive studies were carried out on suspensions in TO and GTO as these provide model molten chocolate at room temperature.

Lecithin and PGPR are added to the chocolate to stop the suspensions from coagulating and to alter the rheology of chocolate. Lecithin is effective in reducing high shear viscosity and PGPR is used to lower the yield stress. The combination of surfactants results in a co-operative effect whereby viscosity is reduced and yield stress vanishes for particular lecithin to PGPR ratios. This effect was studied in detail for both GTO and TO. Additionally a rheologically relevant minimal model chocolate suspension was established whereby lecithin was replaced with 50% POPC and 50% triglyceride (Lec_{POPC}). This shows a similar effect as lecithin on the rheology of 65% sucrose in triglyceride oil suspensions., model chocolate.

An advantage of these model suspensions is that all the components, including the oil, are well characterised and free from any unidentified surface active components allowing the effect of the added surfactants and their adsorption behaviour in molten chocolate to be studied in detail. The oil used in the suspensions can be deuterated to introduce contrast with the interfacial layer of the surfactants. In addition, the POPC can be partially deuterated which provides an additional way of distinguishing between the phospholipid and polymeric components. The aim is for the structural information to provide a molecular basis for the interaction and adsorption mechanism to explain the co-operative effect of phospholipid and polymeric surfactant on the rheology of molten chocolate.

Chapter 3

Surfactant Behaviour in Triglyceride Oil

3.1 Introduction

The surfactants used in chocolate, lecithin and PGPR, both comprise a polar and non-polar part. Lecithin is an amphiphilic surfactant with a hydrophilic head group and a hydrophobic tail and PGPR comprises a polar glycerol backbone with lipophilic ricinoleate chains. Due to the presence of a polar and non-polar group, they can be used to stabilise emulsions and suspensions, broadly called dispersions by adsorption at the polar/non-polar interface, thereby changing the particle-particle interaction. The amphiphilic nature of surfactants means that at concentrations above the critical micellar concentration they tend to form aggregate structures, called micelles, of the various types as shown in Figure 3.1. To understand the adsorption behaviour of the surfactants at the interface, we first need to learn more about the structure adopted by the surfactants in solution. This can be achieved using neutron and x-ray techniques as they probe the length scales of interest: 1 nm-100 nm [12].

In order to understand how these surfactants behave in the triglyceride fat phase, systematic rheology and structural studies using Small Angle X-ray and Neutron Scattering have been performed for the phospholipid surfactants, lecithin and POPC, and the polymeric surfactant, PGPR, and their binary combinations in GTO and TO. In Section 3.2 a detailed description is given of the preparation and

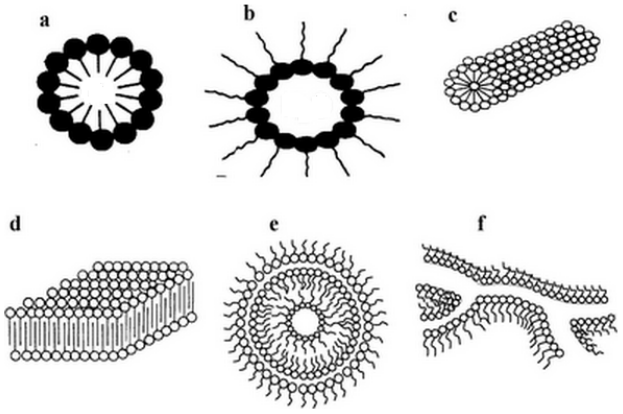

Figure 3.1 *Micellar structures formed by amphiphilic surfactant molecules. (a) spherical micelles (b) reverse micelles (c) cylindrical micelles (d) lameller structures (bilayers) (e) onion-like lamellar phases (f) interconnected cylinders. Figure courtesy of Ganguli et al. [2]*

characterisation of millimolar solutions of phospholipid, lecithin and POPC, and PGPR and their binary mixtures in triglyceride oils GTO and TO. This is followed in Section 3.3 by rheology studies on these surfactant solutions. Structural investigations performed on the surfactant solutions using Small Angle Neutrons and X-ray Scattering are then discussed in Sections 3.4, 3.5 and 3.6.

3.2 Surfactant Solutions: Preparation and Characterization

3.2.1 Materials and Sample Preparation

Triglyceride oils, GTO ($\geq$ 99% pure) and TO ($\geq$ 99% pure), were obtained from Sigma Aldrich, UK. Perdeuterated Glyceryl Trioctanoate (d-GTO) and d96-Glyceryl Trioleate (d-TO) used for d50-oil and sucrose-matched oil (sm-oil) contrast for SANS studies were obtained from the ISIS Deuteration Facility, Oxford, UK and National Deuteration Facility, ANSTO, Australia, respectively. Lecithin and PGPR were obtained from Mars Chocolate, UK. POPC (h and d-31), which is used as a model for lecithin, was obtained from Avanti Polar Lipids, USA.

The sucrose match GTO (sm-GTO) was prepared by mixing 21.6% v/v d-GTO

with 78.4% h-GTO and sucrose match TO (sm-TO) was prepared by mixing 24.4% v/v d-TO with 75.6% h-TO to obtain a mixture with the same volume averaged SLD as the SLD of sucrose, i.e. 1.72×10^{-06} Å^{-2}. The mixture was sonicated and shaken well before use to stop the d-oil from sedimenting. To reduce the amount of d-oil used, which is an expensive component, d50-GTO and d50-TO were used; to provide a high SLD solvent phase. These were prepared as a 50:50 volume fraction mixture of h and d oil. The SLD of various components used is given in Table 3.1.

Table 3.1 *X-ray and neutron scattering length density for various chemicals.*

Chemical	x-ray SLD $\times 10^{-06}$ Å^{-2}	neutron SLD $\times 10^{-06}$ Å^{-2}
Sucrose	14.4	1.7
h-GTO	9.0	0.3
h-TO	8.8	0.1
d-GTO	NA	6.6
d96-TO	NA	6.4
d50-GTO	NA	3.3
d50-TO	NA	3.1
Lecithin head[a]	14.5	1.8
Lecithin tail [a]	7.8	-0.3
PGPR head	12.4	1.4
PGPR tail	8.4	0.2

(a) POPC molecule is taken to calculate the SLD of lecithin.

The concentration of surfactants in the triglyceride oil solutions was matched to their molar concentration in chocolate suspensions, e.g. 0.8% w/w of surfactant in 65% w/w sucrose suspension in triglyceride oil corresponds to 2.4% surfactant solution in triglyceride oil. Solutions of lecithin or Lec_{POPC} (a mixture of 50% POPC and 50% triglyceride oil as used in Chapter 2), PGPR and their binary mixtures at the desired concentration were prepared by mixing the required weight of the surfactant in GTO or TO using a vortex mixer followed by sonicating the solutions for 15 minutes. While sonicating the temperature increased to 50°C, but before any measurement was made it was ensured that the solutions were at room temperature.

Lecithin in TO and GTO formed turbid yellow solutions as can be seen in the

left panel of Figure 3.2, on the other hand PGPR in TO and GTO formed clear solutions, shown in the middle panel of Figure 3.2. The turbidity suggests that lecithin forms structures which are large enough to scatter light, ∼100 nm. Upon the addition of PGPR into the lecithin solution, the solutions becomes clear as shown in the right panel of Figure 3.2, suggesting the large lecithin structures get broken up or disrupted once PGPR is present in the solution.

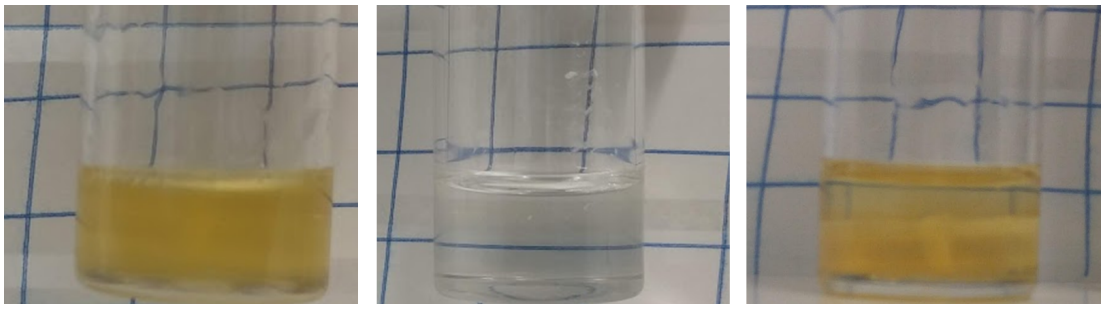

Figure 3.2 *Solutions of Lecithin and PGPR in TO. Left panel: 4.8% Lecithin in TO. Middle panel: 4.8% PGPR in TO. Right panel: 4.8% Lecithin+ 4.8% PGPR in TO.*

3.2.2 Light Scattering from Lecithin and PGPR Solutions

The surfactant solutions in GTO were pre-characterised using Dynamic Light Scattering (DLS) to to provide an indication of the size distribution of the micellar aggregates in triglyceride oil. Solutions were made with 0.5% w/w and 1% w/w lecithin or PGPR in GTO and the DLS correlation function was measured and converted into a particle size distribution as shown in Figure 3.3. The data shows the percentage distribution of the scattering particles as a function of the radius. The unweighted size distribution, depicted by the dotted line, is highly biased towards the larger particles as most of the scattering volume is taken up by the larger particles. The number linearised distribution, shown by the solid line, is biased towards the smaller particles whereas the weight linearised distribution gives the distribution of the particles normalised by weight (or volume as the density ∼1 g/cm^3).

The lecithin solutions show bimodal size distributions: one peak is centred on 4±0.5 nm for both the concentrations and the other peak is centred on 200±50 nm for 0.5% lecithin solution and 300 ± 50 nm for 1% lecithin solution shown in the left panel of Figure 3.3. The size of the smaller particles do not change with concentration and these are expected to be from single micellar arrangements in

the solutions. The size of the larger aggregates is dependant on the concentrations and probably arises due to micelles arranging into larger structures. These aggregates become bigger and also their relative weight fraction increases, from 15% to 75%, as the lecithin concentration in the solution increases from 0.5% w/w to 1% w/w, as can be seen from the peak heights in the figure.

The PGPR solutions also show a bimodal distribution with peaks centred at $\sim$ 1 nm and 150 ± 50 nm, as shown in the right panel of Figure 3.3. The small aggregate size increases with concentration of PGPR in the solutions, with the particle radius being 0.9 nm for 0.25% w/w solutions, 1.4 nm for 0.5% w/w solution and 2 nm for 1% w/w solution. The size of the larger particles is independent of the concentration. However, the relative weight fraction of the larger particle increases with concentration going from 26% for 0.25% w/w solution, 53% for 0.5% w/w solution and 60% for 1% w/w solutions.

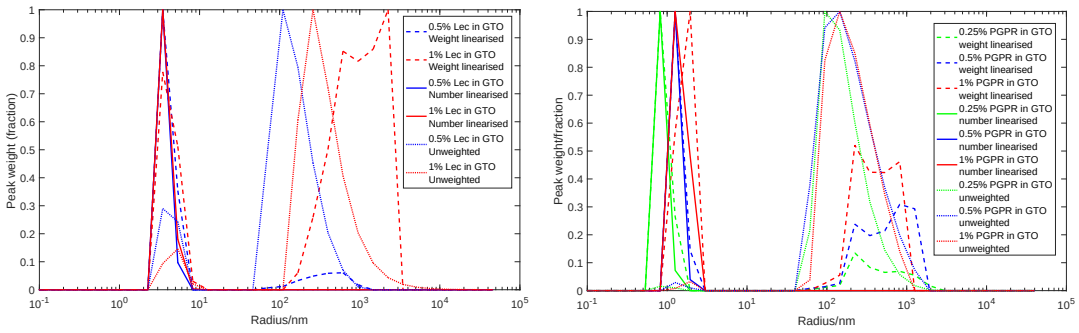

Figure 3.3 *DLS size distribution of the scattering micelles in surfactant solutions. The graph shows percentage distribution as a function of the radius with the unweighted data (dotted line), weight linearised data (dashed line) and number linearised data (solid line). Left panel: 0.5% (blue) and 1% (red) Lecithin in GTO solutions. Right panel: 0.25% (green), 0.5% (blue) and 1% (red) PGPR in GTO solutions*

For more detailed structural characterisation we turn to small angle neutron and x-ray scattering.

3.3 Rheology of Surfactant Solutions in Triglyceride Oil

The presence of large surfactant aggregates can affect the rheology of a surfactant solution, for example the worm-like micelles formed in lecithin/polyglycerol/n-decane system investigated by Hashizaki *et al.* [46]. In order to quantify the rheological effect of the structures formed by lecithin and PGPR in TO and GTO, rheology measurements were done on these surfactant solutions in triglyceride oil. The rheology measurements were done using the creep mode, in order to measure the flow properties at extremely small shear stress (0.001 Pa).

3.3.1 Creep Rheology: Method

Creep rheology facilitates the measurement of the rheological response of a sample upon the application of very small shear stress. In a creep rheology experiment the shear rate and strain response of the material is measured over a period of time upon the application of a range of shear stresses (going from low to high) as shown in Figure 3.4. Samples exhibiting viscoelastic flow behaviour give a slope of 1 on the log strain vs log time graph, i.e. strain increases linearly with time. The shear rate response of the curves (or regions of the curves) with slope of 1 ± 0.05 for log strain vs log time was then divided by the shear stress to obtain the viscosity which is plotted against the applied stress for various surfactant solutions in Figure 3.5 and 3.6. The creep measurements were made using the TA Discovery HR-2 rheometer using a 60 mm 2° cone steel plate with a working gap of 58 μm at 20°C. A constant stress was applied ranging from 10^{-3} Pa to 10 Pa and the rheological response of the sample was measured for 1000 s at each applied stress.

3.3.2 Rheology of Lecithin and PGPR Solutions in Triglyceride Oil

The viscosity vs applied stress response of solutions of lecithin and PGPR in TO and GTO are shown in the left and right panels of Figure 3.5, respectively. The triglyceride oils exhibit a viscous Newtonian fluid response, whereby they flow with a relatively high viscosity, 0.08 Pa s for TO and 0.025 Pa s for GTO, which

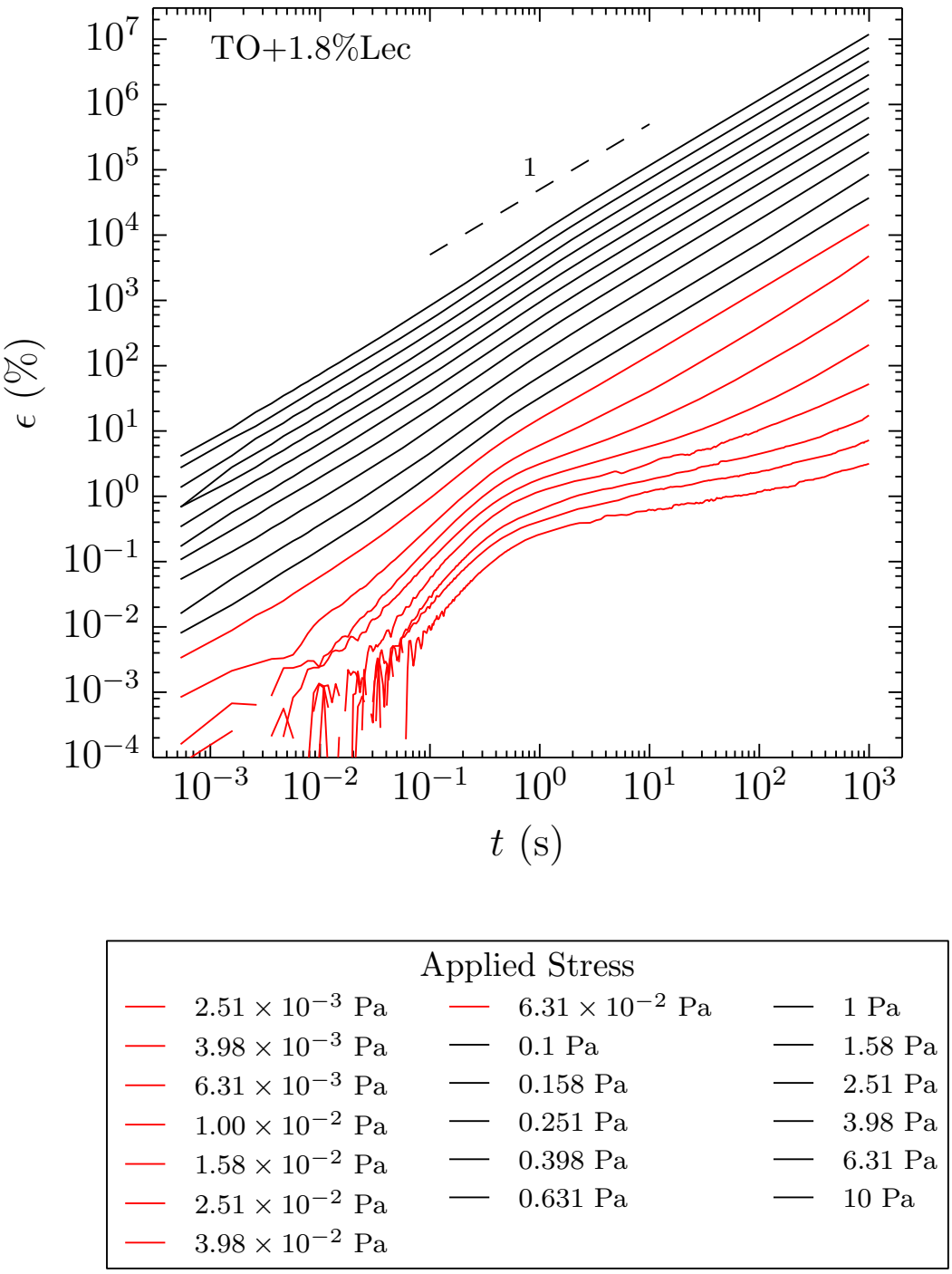

Figure 3.4 *Creep rheology response of 1.8% lecithin in TO. The graph shows strain (%) response against time for applied stress going from 0.001 Pa to 10 Pa. The black line represent the data sets for which viscoelastic flow of the solution is obtained (strain increases linearly with time), whereas the red lines represent data sets for which the sample does not flow.*

doesn't change upon the application of shear stress. The presence of PGPR in the triglyceride oil, increases the viscosity of the solutions by 10% for TO and 20% for GTO probably due to the structures formed by PGPR in the oil phase which make the solution more viscous. On the other hand the presence of lecithin gives the triglyceride oil solution a yield stress. The magnitude of the yield stress is 0.1 Pa in TO and 0.01 Pa in GTO. These values are considerably smaller than the yield stress observed for the sucrose in triglyceride oil suspensions, however this does show that the aggregate structures observed for lecithin in triglyceride oil solutions, which are also responsible for the turbidity of these solutions, can impart a yield stress. The addition of a small amount of PGPR reduces the yield stress substantially, which is possibly due to the disruption of the large lecithin structures which is also evident from the solutions going from turbid to clear as shown in Figure 3.2. The yield stress decreases from 0.1 Pa to 0.01 Pa upon the addition of 0.6% PGPR to a solution of 1.8% lecithin in TO. On further addition of PGPR the yield stress disappears. In GTO the yield stress obtained is an order of magnitude lower than in TO and disappears completely upon the addition of 0.6% PGPR to a 1.8% lecithin solution.

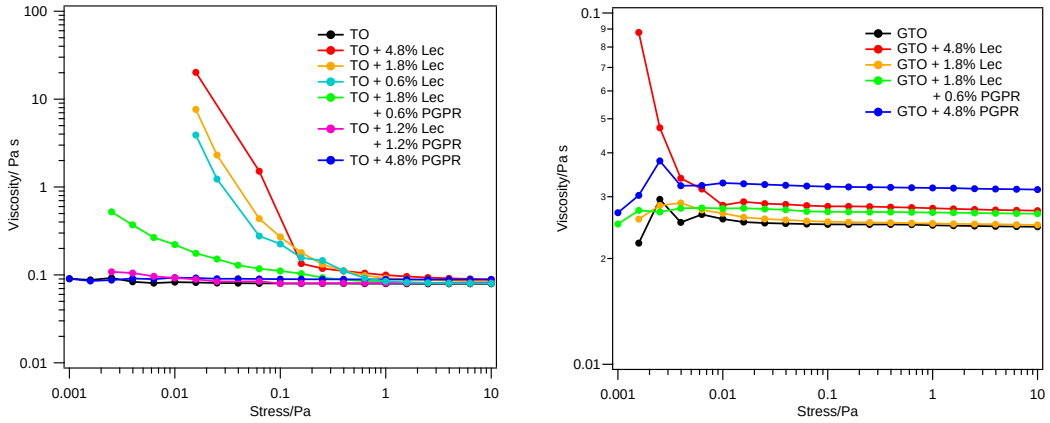

Figure 3.5 *Viscosity vs stress for solutions of lecithin, PGPR and their binary mixtures in Triglyceride oil. Left panel: Solutions in TO. Right panel: Solutions in GTO.*

3.3.3 Rheology of POPC and PGPR Solutions in Triglyceride Oil

Similar creep rheology experiments were done on Lec_{POPC}, 50% POPC + 50% triglyceride oil, so as to gain further insight into the phospholipid-PGPR

interaction, and these are shown in Figure 3.6. Lec_{POPC} also imparts a yield stress to the triglyceride oil solution. The magnitude of this yield stress is higher for both TO and GTO than the one observed for lecithin solutions. This follows the same trend as observed for model chocolate suspensions discussed in Chapter 2. As Lec_{POPC} comprises a single component it might be speculated that it will form more ordered structures as compared to the multi-component lecithin and that these more ordered structures might impart a higher yield stress. For these more ordered structures, the fraction of PGPR required to disrupt these structures appears to be higher. The Lec_{POPC} solutions in TO exhibit a yield stress of ∼1 Pa, which decreases to 0.1 Pa for a 50:50 lecithin/PGPR mixture and to 0.01 Pa for a 25:75 lecithin/PGPR mixture.

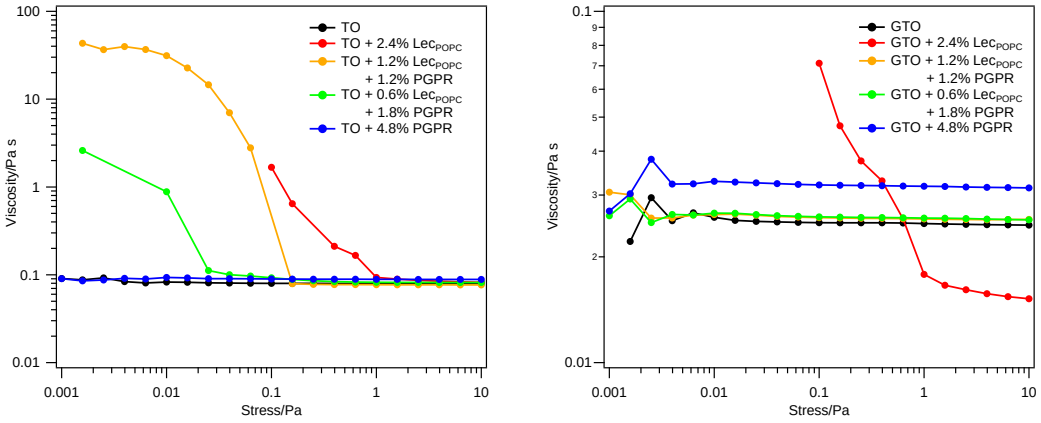

Figure 3.6 *Viscosity vs stress for solutions of Lec_{POPC}, PGPR and their binary mixtures in Triglyceride oil. Left panel: Solutions in TO. Right panel: Solutions in GTO.*

The trends in the rheology of surfactant solutions are more evident in TO than GTO as the yield stress values for solutions in GTO are smaller than TO and fall beyond the rheometer's sensitivity. However, the yield stress observed for the surfactant solutions in GTO show a similar trend as that observed for TO.

In order to substantiate the structural basis for the observed rheology of phospholipids in triglyceride oil solutions and the role of PGPR in changing these structures and therefore influencing the rheology, detailed structural investigations were done on these solutions using small angle scattering. The structures formed by the surfactants in solution also help understand the adsorption behaviour of these surfactants for sucrose in triglyceride solution, model chocolate, and the resulting interfacial structure.

3.4 Small Angle Scattering for Structural Investigations

Small-angle scattering (SAS) is a scattering technique based on the formalism described in Section 1.4 where the deflections of the radiation from its original trajectory are small (0.1-10°). It can give information about the size, shape and structure of scattering inhomogeneities in the sample.

3.4.1 Small Angle Neutron Scattering

Inhomogeneities in the SLD, $\rho(\vec{r})$, give rise to small angle scattering. For an incident beam with intensity I_0, the scattering intensity, $I(\lambda, \vec{q})$, is given as [47]:

$$I(\lambda, \vec{q}) = I_0(\lambda)\ d\Omega\ \eta(\lambda)\ T_s\ \frac{d\Sigma}{d\Omega}(\vec{q}) \tag{3.1}$$

where $\eta(\lambda)$ is the efficiency of a detector subtending a solid angle $d\Omega$ at the sample and T_s is the sample transmission. The first four terms in the equation are instrument-dependent, and not discussed here. The sample specific quantity is the macroscopic cross-section, $\frac{d\Sigma}{d\Omega}$, which is related to the differential cross-section as $\frac{N}{V}\frac{d\sigma}{d\Omega}$, and is given by the Rayleigh-Gans equation [12]:

$$\frac{d\Sigma}{d\Omega}(\vec{q}) = \frac{N}{V}\frac{d\sigma}{d\Omega}(\vec{q}) = \frac{1}{V}\left|\int_V \rho(\vec{r})e^{i\vec{q}\cdot\vec{r}}d\vec{r}\right|^2 \tag{3.2}$$

By normalising the measured differential cross-section by the sample volume, scattering from different samples can directly compared. The integral term of the RHS of Equation 3.2 is the Fourier transform of the SLD distribution and the measured intensity is proportional to the square of its amplitude. This means that all the phase information is lost and we cannot directly invert the measured scattered intensity into a SLD distribution. As is the case with the scattering cross-section, Equation 1.6, the macroscopic cross-section is also a sum of the coherent, incoherent and absorption cross-section:

$$\frac{d\Sigma}{d\Omega}(\vec{q}) = \frac{d\Sigma_{coh}}{d\Omega}(\vec{q}) + \frac{d\Sigma_{incoh}}{d\Omega}(\vec{q}) + \frac{d\Sigma_a}{d\Omega}(\vec{q}) \tag{3.3}$$

The coherent cross-section contains information about the distribution of matter in the sample. The incoherent cross-section is independent of q and just raises the background noise level. The absorption component in usually small and reduces the overall signal.

Two Phase System

In order to derive the measured macroscopic cross-section for a real system consider a two phase system as shown in the left panel of Figure 3.7. The system

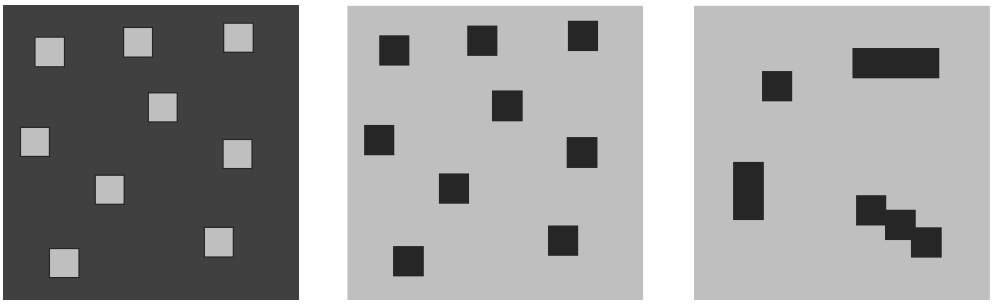

Figure 3.7 *Three systems with 1% volume fraction of scattering particles with different contrast and distribution. Left and middle panel: Same volume fraction and particle distribution of the scatterers but contrast is reversed. Middle and right panel: Same contrast and volume fraction of the scatterers but particle distribution is different. Adapted from [3]*

is comprised of two incompressible phases defined by scattering length density ρ_1 (light grey squares) occupying a volume V_1 and ρ_2 (dark grey squares) occupying volume V_2, with total volume $V = V_1 + V_2$. For this SLD distribution Equation 3.2 yields the corresponding cross-section as [3]:

$$\begin{aligned} \frac{d\Sigma}{d\Omega}(\vec{q}) &= \frac{1}{V}\left| \int_{V_1} \rho_1 e^{i\vec{q}\cdot\vec{r}} d\vec{r_1} + \int_{V_2} \rho_2 e^{i\vec{q}\cdot\vec{r}} d\vec{r_2} \right|^2 \\ &= \frac{1}{V}(\rho_1 - \rho_2)^2 \left| \int_{V_1} e^{i\vec{q}\cdot\vec{r}} d\vec{r_1} \right|^2 \end{aligned} \tag{3.4}$$

As can be seen from Equation 3.4, the final scattered intensity depends only on the difference between the SLD and the spatial arrangement of the inhomogeneities. Therefore, it is not possible to distinguish between two samples where the spatial arrangement of the phases is the same but the SLD is reversed as shown in the left and middle panel of Figure 3.7. This is the Babinet's principle and arises due

to the fact that phase information is lost when measuring scattering intensity.

Multi Phase System

For a multi-phase system with SLD of components ρ_i in a medium with SLD ρ_0, cross terms arise and the scattered intensity is given as [12]:

$$\frac{d\Sigma}{d\Omega}(\vec{q}) = \sum_{i=1}^{p}(\rho_i - \rho_0)^2 S_{ii}(\vec{q}) + \sum_{i<j}(\rho_i - \rho_0)(\rho_j - \rho_0)S_{ij}(\vec{q}) \tag{3.5}$$

where S_{ii} and S_{ij} are the partial structure factor and are defined in terms of the local number density of the constituents, n_i and n_j as:

$$S_{ij} = \int_V \int_{V\prime} \langle n_i(\vec{r}) n_j(\vec{r}\,') \rangle e^{i\vec{q}\cdot(\vec{r}-\vec{r}\,')} d\vec{r} d\vec{r}\,' \tag{3.6}$$

It becomes difficult to resolve structural details for complex multi-phase systems such as described by the Equation 3.5. In order to reduce the number of distinct scattering phases, the technique of contrast variation is applied, as depicted in Figure 3.8. Using this technique multi-phase complex structures can be resolved by conducting a series of measurements highlighting different phases in each measurement.

Contrast Variation

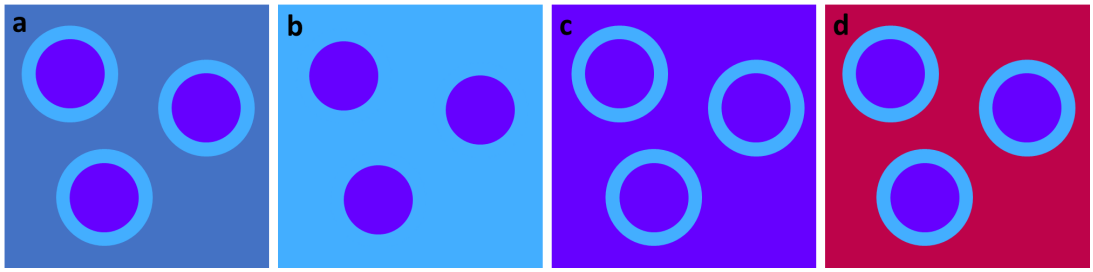

Figure 3.8 *Contrast variation for core-shell particles in SANS. (a) Hydrogenated contrast. (b) Core contrast ($SLD_{shell} = SLD_{solvent}$). (c) Shell contrast ($SLD_{core} = SLD_{solvent}$). (d) Deuterated contrast.*

Most soft matter contains hydrogen, carbon and oxygen. The coherent neutron scattering length of hydrogen (-3.74×10^{-5}Å) and deuterium (6.67×10^{-5}Å) differ significantly. By partially replacing some of the hydrogen with deuterium

in one of the phases, the scattering length density can be matched to other phases in the system and the complexity of the system can be reduced, whilst minimally perturbing the chemistry of the system.

The example depicted in Figure 3.8 shows a 3-component system of core-shell particles (core in purple and shell in light blue) in a solvent. In the natural hydrogenated contrast (solvent in dark blue), shown in Figure 3.8(a), all three phases are equally visible as is the case in the fully deuterated contrast (solvent in red), shown in Figure 3.8(d). By using a mixture of the two solvents, contrasts can be created which matches out the shell, Figure 3.8(b), or core, Figure 3.8(c). This reduces the complexity of the system to two visible phases. This technique is commonly applied to SANS from soft matter systems where by changing the hydrogen to deuterium ratio various components can be matched out to resolve complex structures.

3.4.2 Data Analysis

For soft matter systems showing isotropic scattering, the scattered intensity recorded on a 2-D detector can be averaged to get the macroscopic cross-section, $\frac{d\Sigma}{d\Omega}$, as a function of magnitude of $\vec{q}$. This can then be analysed by building a mathematical model of the SLD profile of the system, model dependent analysis, or by manipulating the scattering data to yield useful information, model independent analysis.

Model Dependent Data Analysis

The integral term on the RHS of Equation 3.4 contains information about the spatial arrangement of the scattering material. This can be represented in terms of a form factor, $P(q)$, that represents the interference of neutrons scattered from a single scatterer and the structure factor, $S(q)$, that takes into account interference between scattering caused by positional correlation of the scatterers.

For a dilute dispersion of core-shell particles, $S(q) = 1$, so the scattered intensity is [48]:

$$\frac{d\Sigma}{d\Omega}(q) = N_p P(q) + B \tag{3.7}$$

where B is the background, N_p is the number of particles and $P(q)$ is the overall

form factor given by:

$$P(q) = (\rho_p - \rho_s)^2 F_p(q)^2 + 2(\rho_p - \rho_s)(\rho_l - \rho_s) F_p(q) F_l(q) + (\rho_l - \rho_s)^2 F_l(q)^2 \quad (3.8)$$

where ρ_p is the SLD for the core-particles, ρ_l is the SLD for the shell layer, ρ_s is the SLD for the solvent, $F_p(q)$ represents the intra-particle form factor of the core-particle and $F_l(q)$ represents the form factor of the shell layer. These are discussed below.

Form Factor and Polydispersity: The form factor expresses the geometrical distribution, e.g. spherical, cylindrical, parallelepiped or core-shell modification of these, of material in a single scattering object, such as a micelle. The two form factors used for data analysis in this work are those of the sphere and cylinder [49] and their core-shell modifications [50] given below as:

$$\text{Sphere of radius } r, \qquad P(q) = \left[\frac{3\big(\sin(qr) - qr\cos(qr)\big)}{(qr)^3} \right]^2 \quad (3.9)$$

Cylinder of radius r and length $2L$

$$P(q) = \int_0^{\pi/2} f^2(q,\alpha) \sin\alpha d\alpha \quad (3.10)$$
$$\text{with} \quad f(q,\alpha) = \frac{\sin qL\cos\alpha}{qL\cos\alpha} \frac{J_1(qr\sin\alpha)}{qr\sin\alpha}$$

where J_1 is the Bessel function of the first kind and α is the angle between the cylinder axis and the scattering vector, q. These form factors give rise to a maxima/minima in the scattering intensity, arising from the constructive and destructive interference. The sharpness of the maxima/minima depends on the instrumental resolution and the polydispersity of the scattering sample. The instrument resolution is known, allowing the polydispersity to be included as an additional fit parameter.

Structure Factor: The structure factor takes into account the positional correlation in the distribution of the scattering objects in the sample. For dilute samples as there is no inter-particle correlation, $S(q) = 1$. However, in case of isotropic distribution of particles in a concentrated sample the structure factor is given by [12]:

$$S(q) = 1 + 4\pi N_p \int_0^\infty [g(r) - 1] \frac{\sin qr}{qr} r^2 dr \quad (3.11)$$

where $g(r)$ is the correlation function and is related to the potential energy function for the inter-particle interaction. By using approximate potential energy functions different structure factors can be calculated.

The fitting described in this chapter was done using the built in form factors, spherical, cylindrical and their core-shell modifications, in the NCNR small angle scattering macros [51] for Igor Pro [52] and the SASVIEW fitting program [53].

Model independent data analysis

For complex systems where it is not possible to build mathematical models, useful information can be extracted from the scattering data by using some of the constructs described below.

Guinier Analysis: The Guinier approximation considers the low q limit of the scattered intensity. For $q \ll 1/R_g$, where R_g is the radius of gyration of the scattering object, the scattering intensity is approximated as [49]:

$$I(q) = I(0)\exp\left(-\frac{(qR_g)^2}{3}\right) \qquad \text{for} \quad qR_g \ll 1 \tag{3.12}$$

The radius of gyration can be related to the size of the object by geometry. This allows as estimate of the size of the scattering object where the shape and distribution is not known precisely. This approach has been used for the analysis of SANS and SAXS from sucrose/triglyceride oil suspensions discussed in Chapter 4.

Scattering Invariant and Specific Surface: These are other useful constructs to compare scattering from complex systems, though their application is limited due to the vast q-range required, which can be experimentally challenging to realise.

Porod showed that the total small angle scattering from a sample is constant, Porod Invariant (C), irrespective of the way the sample density is distributed [54], e.g. the middle and right panel in Figure 3.7

$$\begin{aligned} C &= \int \frac{d\Sigma}{d\Omega}(\vec{q})d\vec{q} = (2\pi)^3(\rho(\vec{r}) - \overline{\rho})^2 \\ \text{For a two-phase system:} \qquad C^* &= \frac{C}{4\pi} = 2\pi^2\phi_1(1-\phi_1)(\rho_2 - \rho_1)^2 \end{aligned} \tag{3.13}$$

This can be used to calculate the volume fraction of each component in a two-phase system given the contrast or the contrast given the volume fraction.

Another important feature of small angle scattering, also given by Porod [54], is the asymptotic behaviour. This states that for $q \gg 1/D$, where D is the size of the scattering object $I(q) \propto q^{-4}$ and allows the specific surface, S/V, of the structure to be evaluated from the total scattering:

$$\frac{S}{V} = \frac{\pi}{q^*} \lim_{q \to \infty} (I(q) \cdot q^4) \qquad \text{for} \quad q \gg 1/D \tag{3.14}$$

This allows comparison between the distribution of scattering materials in different samples. e.g. in Figure 3.7 the specific surface of the scattering particles in the middle panel is greater than that in the right panel.

3.4.3 Instrument and Experimental Details

A schematic of a typical SANS instrument is shown in Figure 3.9. The neutron beam enters the instrument from the neutron guide, and passes through the velocity selector such that neutrons with certain velocity, and hence wavelength, are obtained. Before hitting the sample, the beam passes through a some collimation to get a well-directed incident beam. Thereafter, the beam is scattered from the sample and the scattered neutrons are collected using a detector. A SAXS instrument is similar but does not have a velocity selector and has slits to collimate the beam.

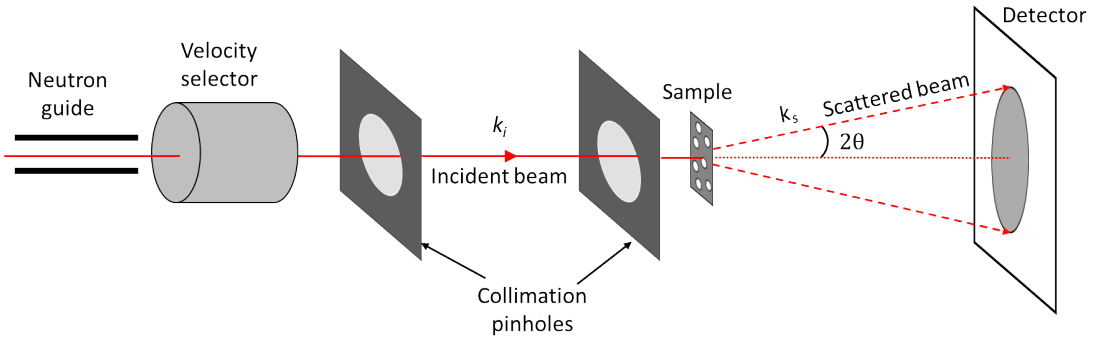

Figure 3.9 *Schematic showing the realisation of the small angle neutron scattering principle on an instrument.*

The SANS experiments detailed in this chapter were performed on SANS2D at ISIS, Oxford, UK (experiment numbers RB1510438 and RB1720334) with neutron of wavelengths $2 - 14$ Å. Using front and rear detector settings of 5 m and 12 m, a q-range of 0.001 $\text{Å}^{-1} < q < 0.4$ Å^{-1} was obtained. SAXS experiments were done on the XENOCS Nano-inXider SAXS/WAXS system which uses a Cu K-α source with wavelength 1.54 Å, giving a q-range of 0.003 $\text{Å}^{-1} < q < 0.4$ Å^{-1}. Synchrotron SAXS experiments were done on I22 at Diamond Light source, Oxford, UK (experiment number SM18397-1) with an x-ray energy of 12.4 keV, giving a wavelength of 1 Å. Using detector distance of 9.7 m, a q-range of 0.001 $\text{Å}^{-1} < q < 0.2$ Å^{-1} was obtained.

The SANS samples were put on the beamline by loading into rectangular or circular (Banjo cells) quartz cuvettes with 1 mm path length. The SAXS samples were loaded into quartz capillaries, 1 or 1.5 mm path lengths, which were then placed on the beamline.

Sample History

The SAXS measurements done on I22 were conducted as a mail-in experiment, so the samples were prepared 3-5 days before the measurements. The time gap between preparation and measurement means long time-scale micellar arrangements could have taken place. These are relevant to chocolate as the application of shear during conching can expedite the formation of the micellar structures and therefore they can exist in the fat phase in chocolate. The time scales between preparation and measurement is different from the history of the samples used for the SANS experiments, where the measurement was conducted within 24 hours of preparing the sample. This introduces a measurable effect on the size of the micelles and their arrangement into larger aggregates. Therefore, only samples with similar history are compared, i.e. SAXS measurements from different samples on I22 are compared to one another and SANS measurements from different samples are compared. In order to explore this effect of ageing SAXS measurements using the XENOCS SAXS/WAXS system were carried out on a subset of these samples before and after ageing and are discussed in Section 3.6.2.

3.5 Structural Investigation of Surfactants in Triglyceride Oil

Phospholipids form micellar structures in triglyceride oils due to their amphiphilic nature. The critical micellar concentration (cmc) of phospholipids is found to be between 0.03%-0.1% depending on the type of oil [55, 56] and the composition of phospholipid mixture [57]. The structure formed by micelles or micellar aggregates formed by surfactants depend on the following factors [58]:

1. Interaction with solvent

   Micellar structures are formed by molecules with differences in polarity between the head and the tail in order to minimize unfavourable interaction with the solvent. For example, phospholipids, with polar head groups and non-polar tails, form micelles in water with the head directed towards the solvent, whereas in non-polar solvents they form inverse micelles with the tail directed towards the solvent.

2. Shape of the molecule

   The shape of the molecule controls the packing parameter $= v/a_0 l_c$, where v is the volume of the tails, a_0 is the area of the head group and l_c is the chain length. This places geometrical constraints on the shape of the micelles that can be formed by the surfactants. A more detailed description of this is given in *Intermolecular and Surface Forces* by J. N. Israelachvili [58]. The main factors that control the shape of the molecule are:

   (a) Size of head group [59].

   Lipids with small polar head, e.g. PE, PS, PA, DPG have a molecular shape that resembles a truncated cone and favour the formation of cylindrical micelles which can further organise by packing into hcp or or cubic structures. Lipids with bulky head groups (and/or only one tail) resemble a conical structure and favour formation of tubular or spherical micelles. Lipids with similar cross-sectional area for head and tail have a molecular shape like a cylinder and favour forming to lamellar structures.

   (b) Nature of tails [60]

   In addition to the area of the head group the nature of the tails can also change the shape of the molecule and therefore the structure of

the micelles. Introducing chain branching and double bonds reduces l_c and thus increases the packing parameter. This favours inverted micellar structures. An example of this is PE lipids where saturated (or mono unsaturated) PE like POPE form a lamellar phase whereas unsaturated PE forms an inverted phase [61].

For surfactants in oil the interaction with the solvent will favour the formation of inverse micellar structures. The phospholipids found in lecithin contain a variety of head groups, PC, PE, PA and PI, as well as a range of hydrocarbon tails, mostly unsaturated. The packing parameter for PC, PI and saturated/mono-unsaturated PE lipids ≈ 1, whereas packing parameter for unsaturated PE and PA lipids is > 1. The packing parameter of a mixture of components can be treated, to the first approximation, as the mean value [58] and therefore the packing parameter for lecithin will be > 1. This will induce some curvature in the inverse micellar structures formed by lecithin. PGPR has unsaturated branched tails which and therefore will also have a packing fraction > 1. Figure 3.10 summarises the molecular shape of the surfactants studied here. The aggregate structure formed by these molecules will range from lamellar layers to spherical or cylindrical inverse micelles.

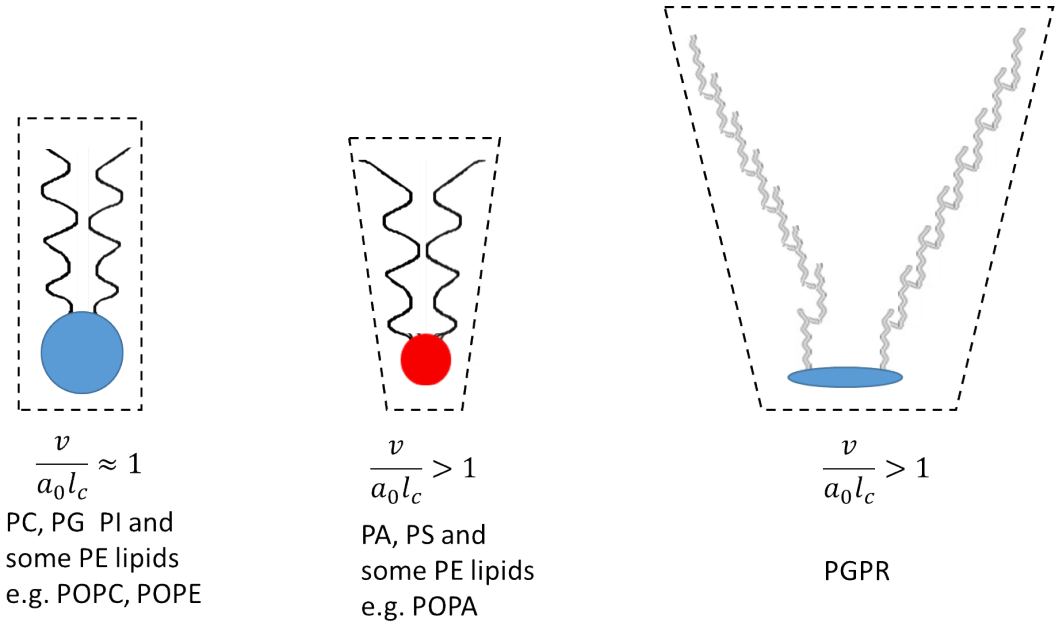

Figure 3.10 *Shape of lipids and PGPR molecules.*

It has been reported that PC phospholipids form reverse micellar structures with diameter ranging from between 3-5 nm at concentrations of 1%-10% [44].

Formation of these micelles in the oil phase could increase viscosity or yield stress of the solutions. These have also been suggested by Arnold *et al.* [29] to explain the increase in viscosity of sugar/oil suspension at high shear rates after the addition of lecithin beyond a certain point. Another possibility is the formation of more complex worm-like micellar systems. These have been reported for various additives, like lecithin, bile salts and glycerol monooleate, in a variety of non-polar solvents [62–64]. These worm-like micelles can grow due to the presence of water or other amphiphilic compounds and have a strong effect on the viscosity and other rheological properties of the system. Formation of these worm-like micelles can be investigated using SAXS/SANS as they give rise to scattering intensity proportional to q^{-1} on the length scale corresponding to the persistence length of these worm-like molecules. Worm-like reverse micelles have also been reported in lecithin/polyglycerol/n-decane systems [46] and it is also shown that these effect the rheological properties of the system.

The molar concentration of phospholipids in chocolate is $10-100$ times their cmc in triglyceride oils. At these concentrations, the surfactants will form micelles and micellar aggregates in the fat phase. The lecithin/PGPR/triglyceride oil system, present in model chocolate suspensions, has some similarity to the reported lecithin/polyglycerol/n-decane system and similar reverse worm-like micelles might very well contribute to the structure and properties of the surfactants in the model chocolate suspensions. In this work small angle scattering studies of lecithin (or POPC), PGPR and their binary mixtures in GTO and TO have been conducted to ascertain the structures formed by these surfactants in the triglyceride oils.

3.5.1 SANS from Triglyceride Oil

The solvent phase used in these structural investigation is triglyceride oil. The size of a triglyceride molecule is ~ 10 Å, which is comparable to the size of the surfactant molecules and their aggregates that we are investigating. This means that scattering is observed from the solvent phase which is a mixture of h and d triglyceride oils in the small angle region, as shown in Figure 3.11, rather than the wide angle region as would be typical for smaller solvent molecules such as H_2O/D_2O.

This scattering from the minority d-oil molecules dispersed in the h-oil phase has been fitted to a Guinier model. The radius of gyration was kept constant

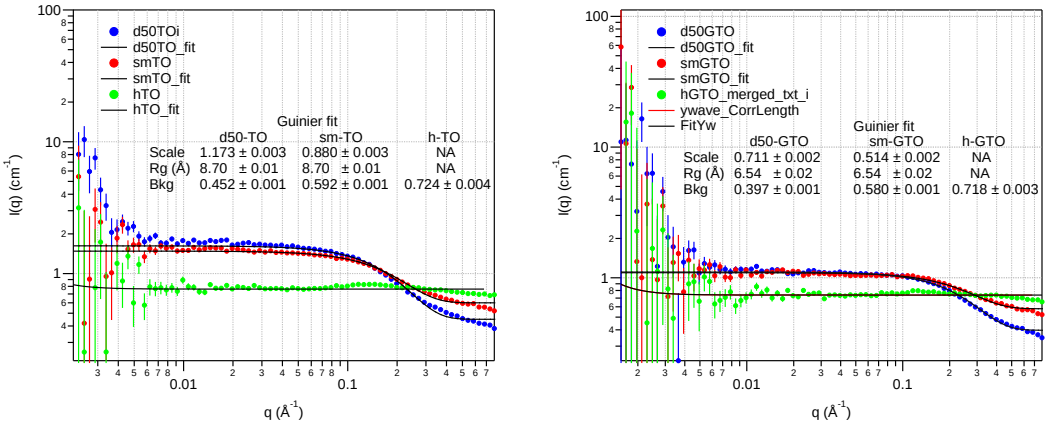

Figure 3.11 *SANS from the triglyceride oil phase at various h:d composition, h-oil, sm-oil and d50-oil. Left panel: SANS from TO. Right panel: SANS from GTO.*

between the two compositions, sm-oil and d-oil, and the scale and background were allowed to vary. As expected, the scale increase as the d-oil fraction of the mixture increases and the background decreases. The background is the highest for h-oil. The radii of gyration obtained for TO and GTO were 8.7 Å and 6.55 Å respectively. Assuming that the oil molecules form discs [65, 66], this corresponds to a radius of 12.9 Å for TO and 9.1 Å for GTO. The Tanford model [67], given by Equation 3.15, can be used to estimate the maximum size, l_{max}, for these molecules from their molecular composition.

$$l_{max} = 1.5 + 1.265 n_c \tag{3.15}$$

where n_c are the number of carbon atoms in the chain. This is applicable for saturated hydrocarbon chains and for GTO, with $n_c = 7$ gives $l_{max} = 10.3$ Å. This is in good agreement with the value for the radius obtained using SANS. The calculation for TO is more complicated as there is a double bond. It is known from the 3-D structure of Oleic acid [68], that the oleic acid chain bends at the double bond and so $n_c = 9$ was used, giving $l_{max} = 12.9$ Å again in good agreement with the value obtained for the radius of the disc.

This scattering from a combination of h-oil and d-oil solvent phase makes interpretation of high-q ($q > 0.1$ Å^{-1}) SANS from surfactant solutions difficult, as will be discussed later.

3.5.2 SANS and SAXS from Lecithin Solution

SAXS was measured from solutions of lecithin in TO, with concentrations ranging from 0.12% w/w to 4.8% w/w, and is shown in Figure 3.17. The data exhibits q^{-4} scattering at $q \leq 0.01$ Å^{-1}, which can be attributed to scattering from large aggregates, size > 100 nm. For $q \geq 0.01$ Å^{-1}, q^{-1} scattering is observed which is characteristic of cylindrical micelles. Additionally Bragg peaks are observed at $q \approx 0.11$ Å^{-1}, possibly associated with more ordered packing of the cylindrical micelles.

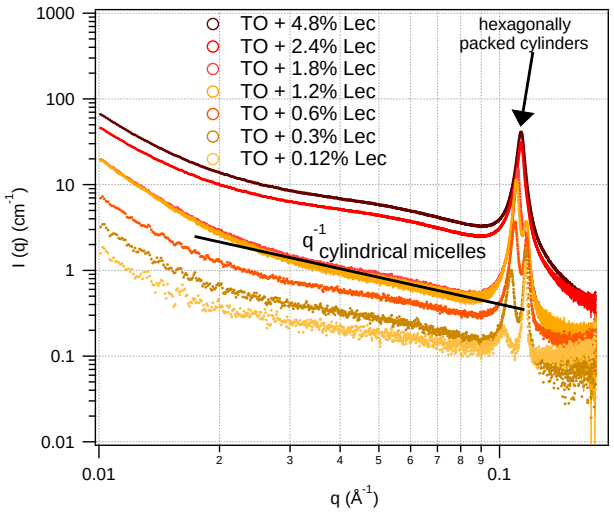

Figure 3.12 *SAXS from solution of lecithin in TO with concentration ranging from 0.12% w/w to 4.8% w/w.*

The scattering curve from TO + 2.4% w/w lecithin exhibiting a single Bragg peak was fitted using the sum of the form factors for cylindrical core-shell micelles and a Lorentz peak as shown in the left panel of Figure 3.13. The phospholipid head groups assemble into the core and the hydrocarbon tails form the shell of the cylinders. The core radius was found to be 23 Å and the shell thickness 17 Å. This gives a total micelle size of 5.7 nm, consistent with studies in literature [44]. The cylinder length was determined to be 940 Å which is towards the upper end of the SAXS range. The Bragg peak position was found to be $q = 0.113$ Å^{-1}, corresponding to a d-spacing of 55.6 Å. This is consistent with packing of cylinders with size 5.7 nm. Scattering from the 0.6% w/w lecithin solutions exhibit 2 Bragg peaks at $q_1 = 0.110$ Å^{-1} and $q_2 = 0.116$ Å^{-1}, corresponding to d-spacing of 57.2 Å and 53 Å, respectively. The two distinct d-spacings could arise from two dominant micellar sizes corresponding to phospholipids comprising alkyl chains

with $16-18$ carbon atoms and $12-14$ carbon atoms aggregating separately to form hexagonally packed cylinders. At higher concentrations the two populations merge giving a rise to a single d-spacing which is in between the two values. These large structures could explain the turbidity of the lecithin solutions and the yield stress obtained for lecithin in TO solutions.

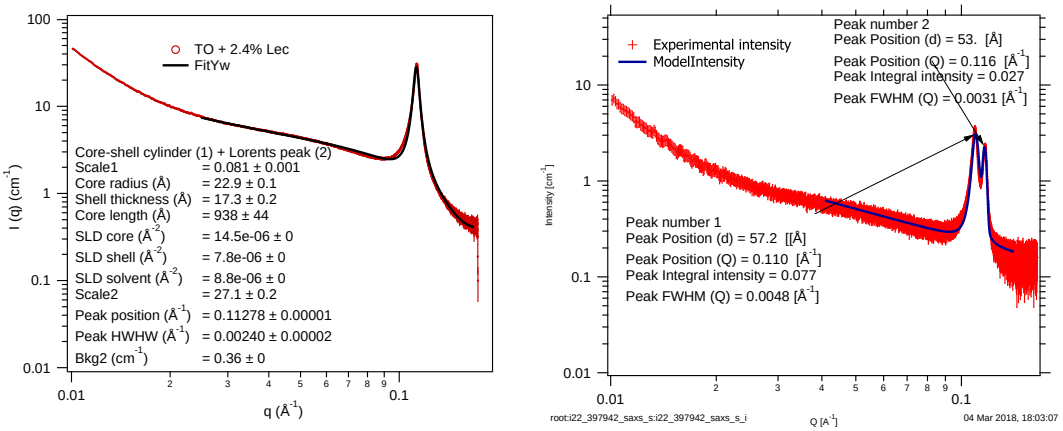

Figure 3.13 *SAXS data with fits for lecithin in TO solutions. Left panel: 2.4% w/w lecithin in TO fitted to a sum of core-shell cylidrical micelles and Lorentz peak. Right panel: 0.6% w/w lecithin in TO solution fitted to q^{-1} scattering + hexagonally packed cylinders.*

In order to confirm the structure of the cylindrical micelles, SANS was also measured for 2.4% w/w lecithin solution in TO as shown in Figure 3.14. As mentioned in Section 3.4.3, the solutions for SAXS measurements were more than 72 hours old whereas the SANS measurements were done on freshly prepared solution ($<$ 24 hours old). This may be why some of the large scale structural arrangements observed in SAXS are not observed in SANS.

The SANS data from 2.4% w/w lecithin solution can also be fitted to the sum of a power law (to fit the low q region) and the form factor for core-shell cylindrical micelles. The sm-GTO and d50-GTO contrasts were cofitted with the scale, power law exponent and scale, and the SLD of the solvent phase allowed to vary between the two contrasts. The core radius of the micelles was determined to be 19 Å and the shell thickness 9 Å, which is similar to that obtained with SAXS. The slight difference in the fitted values for the SLD of the tail region for the sm-contrast and d50-contrast can be explained by the fact that the tails are solvated. The solvent volume fraction, ϕ, in the chains can be calculated using Equation 3.16 from the SLDs obtained for the shells in the fit to the two contrasts, using the SLD of the tails, $\rho_{tails} = -0.2 \times 10^{-6}$ Å^{-2}, and the SLD of

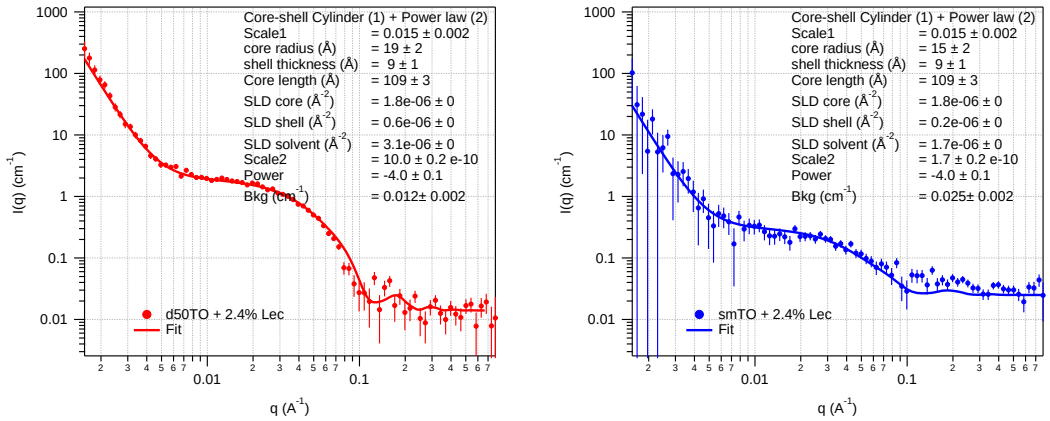

Figure 3.14 *SANS from 2.4% w/w lecithin in TO solution fitted to a sum of core-shell cylinders and power law. Left panel: d50-TO contrast. Right panel: sm-TO contrast.*

the solvent, $\rho_{solvent} = 3.1 \times 10^{-6}$ Å^{-2} as:.

$$\begin{aligned} \phi\rho_{solvent} + (1-\phi)\rho_{tails} &= \rho_{shell} \\ \implies \phi &= \frac{\rho_{shell} - \rho_{tails}}{\rho_{solvent} - \rho_{tails}} \end{aligned} \tag{3.16}$$

This gives solvent volume fraction of 23% for sm-TO and 27% for d50-TO. Although this is higher than would be expected for lipid micelles in water, as the TO fatty acid tails are similar to many components in lecithin, this is not unreasonable here.

The length of the cylindrical micelles obtained using SANS is 109 Å which is much smaller than the value obtained from SAXS of 940 Å. This could be due to the fact that the longer micelles are formed upon ageing and have not yet been formed for the SANS solutions. This is explored in more detail in Section 3.6.2.

Similar measurements were performed for lecithin solutions in GTO and are shown in Figure 3.15 and 3.16. SAXS and SANS from 2.4% w/w lecithin in GTO fitted to core-shell cylinders are shown in the right panel of Figure 3.15 and Figure 3.16, respectively.

The Bragg peak resulting from the large scale structuring is not as prominent for lecithin solutions in GTO as is the case for the solutions in TO. In 1.8% w/w lecithin solutions and 1.2% w/w lecithin solutions the small Bragg peak visible at $q \approx 0.116$ Å^{-1}, corresponds to d-spacing of 54.3 Å(left panel of Figure 3.15).

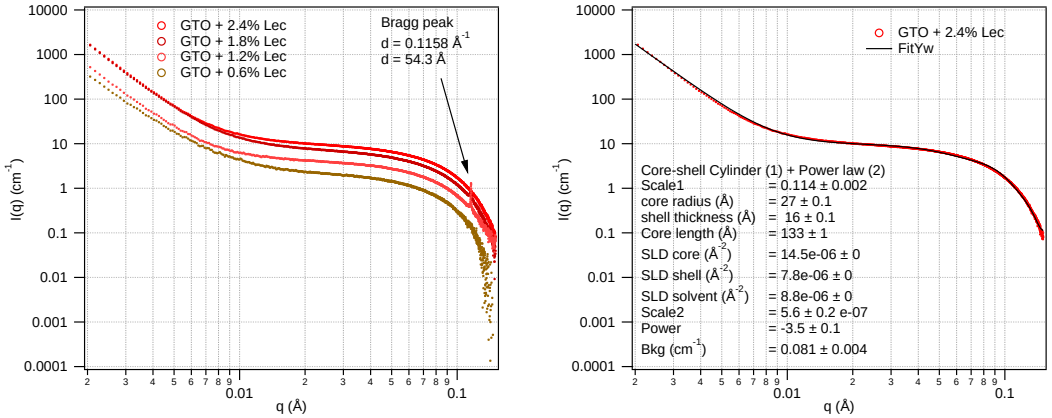

Figure 3.15 *SAXS from lecithin solutions in GTO. Left panel: SAXS data obtained for lecithin in GTO solutions with concentration ranging from 0.6% w/w to 2.4% w/w. Right panel: SAXS from 2.4% w/w lecithin in GTO solution fitted to a sum of core-shell cylinders and power law.*

The cylindrical micelles formed by lecithin in GTO have a similar cross-sectional size as the micelles in TO: radius 27 Å from SAXS and 23 Å from SANS and shell thickness 16 Å from SAXS and 8 Å from SANS. However the length of these cylindrical micelles is less even after ageing, $\sim$ 100 Å from SAXS and 70 Å from SANS from fresh solutions. This suggests that the lecithin micelles do not grow significantly in GTO upon ageing.

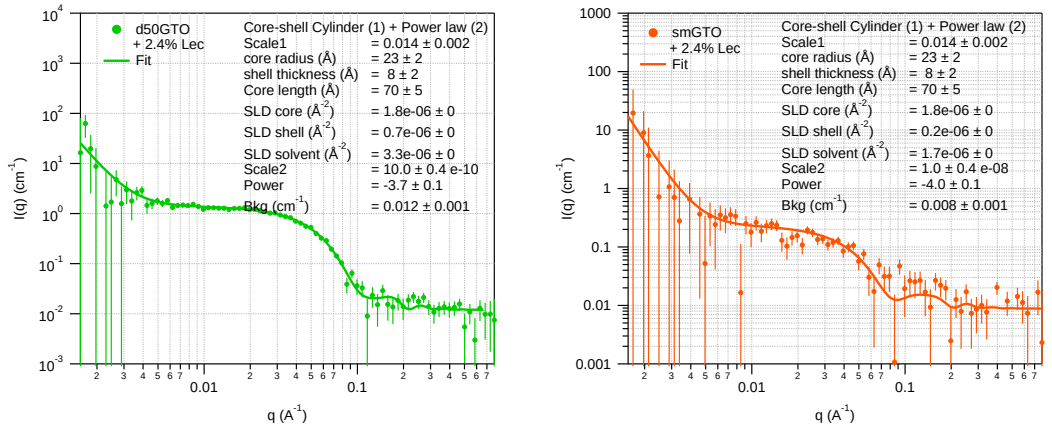

Figure 3.16 *SANS from 2.4% w/w lecithin in GTO solution fitted to a sum of core-shell cylinders and power law. Left panel: d50-GTO contrast. Right panel: sm-GTO contrast.*

Lecithin forms inverse cylindrical micelles suggesting that the packing fraction of the average lecithin molecule > 1, which introduces curvature. The structures

grow in length on ageing, possibly to avoid unfavourable interaction with the solvent at the cylinder end, especially in TO.

3.5.3 SANS and SAXS from PGPR Solution

SAXS was measured from solutions of PGPR in TO, with concentration ranging from 0.6% w/w to 4.8% w/w, and is shown in Figure 3.17. The data exhibits q^{-4} scattering at $q \leq 0.01$ Å^{-1}, which can be attributed to scattering from large aggregates, size > 100 nm. For $q \geq 0.01$ Å^{-1}, q^{-1} scattering is observed which is characteristic of cylindrical micelles. In order to further determine the structure of the cylindrical micelles SANS was also measured for 2.4% w/w PGPR solution in TO for sm and d50 oil contrast, as shown in Figure 3.18.

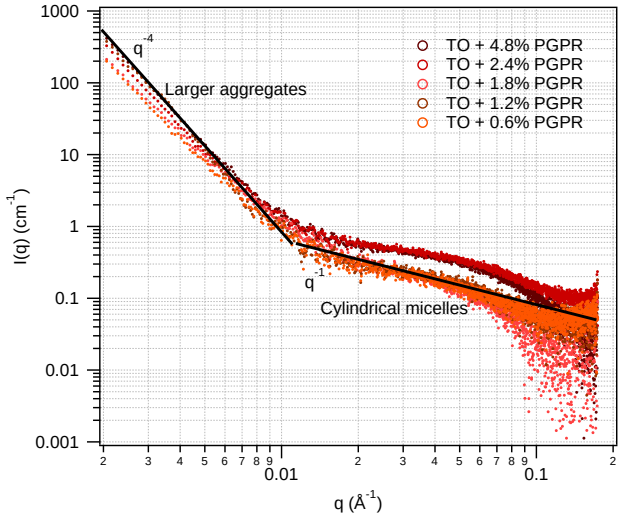

Figure 3.17 *SAXS from solution of PGPR in TO with concentration ranging from 0.6% w/w to 2.4% w/w.*

The data was fitted using a sum of power law-scattering (to fit the low q region) and core-shell cylindrical micelles. The core comprises the polyglycerol backbone (which can be considered as the PGPR head) and the shell consists of solvated polyricinoleate tails. In SAXS there is no contrast between the solvent (SLD = 8.8×10^{-06} Å^{-2}) and polyricinoleate tails (SLD = 8.4×10^{-06} Å^{-2}) and so the fitting model was reduced to a sum of a polyglycerol-rich cylindrical core and a power law. The SANS data were fitted in a self consistent fashion such that the only parameters which differed between the sm-TO and d50-TO contrasts were the background, power law scale and exponent, and the SLD of solvent and shell

(as the tails are solvated with solvent of different SLD). The fitted parameters are shown in the inset of Figure 3.18.

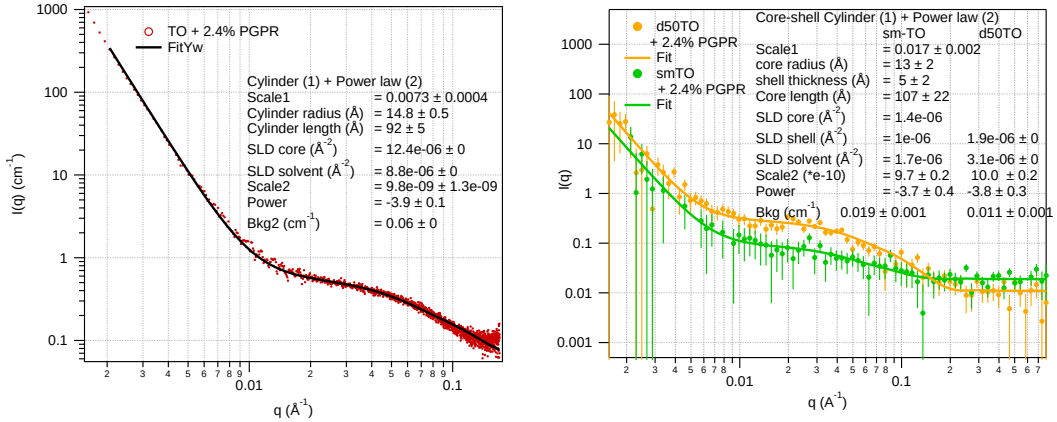

Figure 3.18 *SAXS (left panel) and SANS (right panel) from 2.4% w/w PGPR in TO fitted to a sum of core-shell cylindrical micelles and power law.*

The SAXS and SANS give consistent results. The core radius was found to be between 13-15 Å and the cylinder length between 90−110 Å. The shell thickness is determined to be 5 Å which is smaller than the expected length of the ricinoleate chains (10−15 Å). This is possibly due to high solvation of the chains which means that beyond an average distance of 5 Å from the polyglycerol core, the contrast between the chains and the solvent is lost. The solvent volume fraction, ϕ, in the shells formed by the chains can be calculated using Equation 3.16 from the fitted values for the SLD for the shells in the fit to the two contrasts, using the SLD of the tails, $\rho_{tails} = 0.2 \times 10^{-6}$ Å^{-2}, and SLD of the solvent, $\rho_{solvent} = 1.7 \times 10^{-6}$ Å^{-2} for sm-TO and 3.1×10^{-6} Å^{-2} for d50-TO. This gives an average solvent volume fraction of 53% for sm-TO contrast and 59% for d50-TO contrast, suggesting that TO is a good solvent for the ricinoleate chains of the PGPR.

Similar measurements were performed for PGPR solutions in GTO. SAXS and SANS from 2.4% w/w PGPR in GTO fitted to core-shell cylinders are shown in the left and right panel of Figure 3.19, respectively.

A similar fitting procedure as used for TO gave a core-radius of 18 − 19 Å and cylinder length of 67 − 68 Å using both SAXS and SANS. The chain length in GTO is 12 Å, higher than in TO and the solvent volume fraction in the tail region, found using Equation 3.16 with $\rho_{tails} = 0.2 \times 10^{-6}$ Å^{-2}, and SLD of the solvent, $\rho_{solvent} = 1.7 \times 10^{-6}$ Å^{-2} for sm-GTO and 3.3×10^{-6} Å^{-2} for d50-GTO, was 48% for sm-GTO and 60% for d50-GTO. This indicates that GTO even though is a

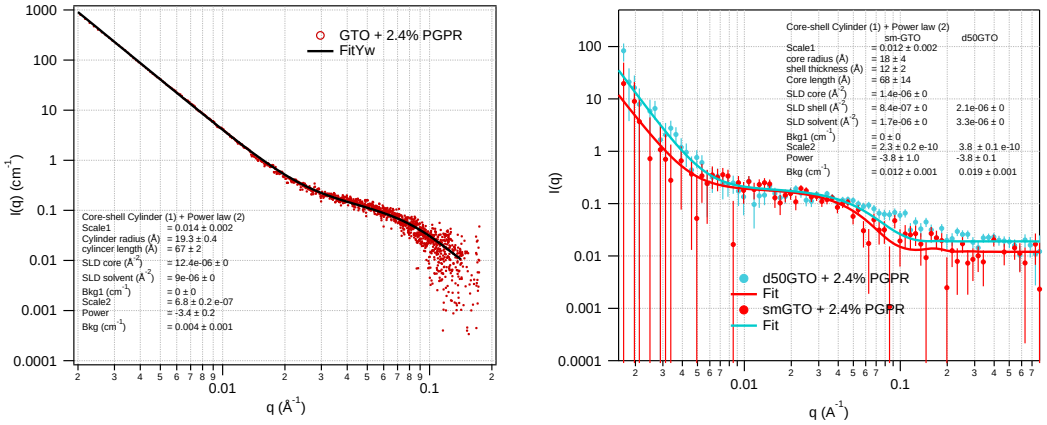

Figure 3.19 *SAXS (left panel) and SANS (right panel) from 2.4% w/w PGPR in GTO fitted to a sum of core-shell cylindrical micelles and power law.*

good solvent for PGPR, it may not be as good a solvent when compared to TO as the visible length of the tail region is greater and the volume fraction of solvent is lower, specially for sm-GTO contrast. A possible reason for this is the similarity of the oleic acid chain in TO to the ricinoleate chains found in PGPR.

PGPR has a truncated cone shape, which would give a packing parameter > 1, imposing some curvature on the micellar aggregates formed by PGPR. There is some linear character already present in the molecule due to the polyglycerol backbone and the combination of these two factors result in the formation of cylindrical micelles.

3.5.4 SANS and SAXS from POPC Solution

SAXS was measured from solutions of Lec_{POPC} (50% w/w mixture of POPC and TO) in TO, with concentration ranging from 0.6% w/w to 2.4% w/w[1], as shown in Figure 3.20. X-Ray are strongly scattered from the PC head group due to the high scattering length density of the phosphorous. The data exhibits q^{-4} scattering at $q \leq 0.01$ Å^{-1}, from the large aggregates, size > 100 nm. and a Bragg peak is observed at $q \approx 0.1$ Å^{-1}.

The Bragg peak can be fitted to lamellar structures with d-spacing of 52-59 Å depending on the concentration of Lec_{POPC}, as shown in the inset of the right hand panel in Figure 3.20. The d-spacing becomes smaller as the concentration of

[1]This corresponds to 0.3% w/w POPC and 1.2% w/w POPC in TO

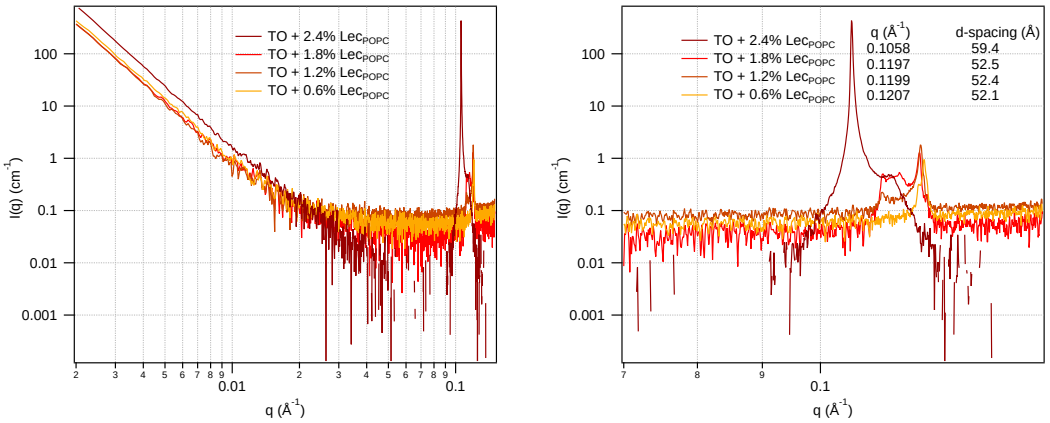

Figure 3.20 *SAXS measured from Lec$_{POPC}$ solutions in TO with concentration ranging from 0.6% w/w to 2.4% w/w. Left panel: SAXS measurements. Right panel: Bragg peaks zoomed in with their positions.*

the Lec$_{POPC}$ is reduced. POPC is single component surfactant with a cylindrical molecular shape, which will favour the formation of lamellar structures.

Similar measurements performed for Lec$_{POPC}$ in GTO show two Bragg peaks at $q_1 = 0.107$ Å^{-1} and $q_2 = 0.114$ Å^{-1}. Using the Irena diffraction tool these were shown to be consistent with a hcp structure corresponding to d-spacing of 59 Å and 55 Å respectively. An example of this fitting is shown in left panel of Figure 3.34

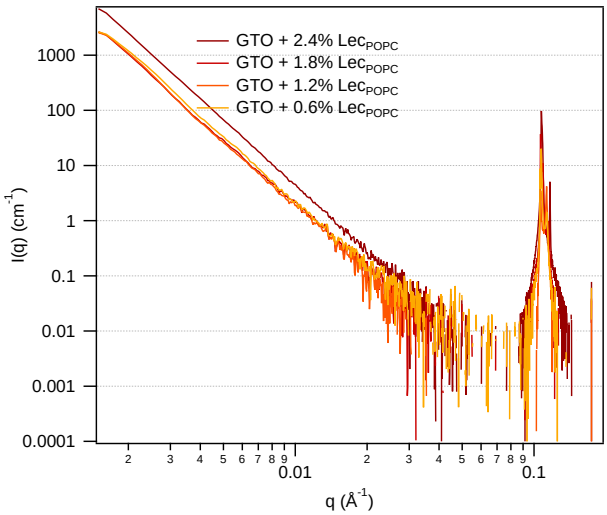

Figure 3.21 *SAXS measured from Lec$_{POPC}$ solutions in GTO with concentration ranging from 0.6% w/w to 2.4% w/w.*

This d-spacing obtained in both TO and GTO is reasonable for POPC molecule where the tail comprises C16 and C18 hydrocarbon chains. Each lamellar d-spacing corresponds to 2 head and 2 tail regions. The Tanford model, Equation 3.15, gives a chain length of $22 - 24$ Å for POPC. Using this, the size for the head group region can be calculated to be 3-6 Å a reasonable estimate for PC.

3.6 Effect of PGPR on Phospholipid Aggregates in Triglyceride Oil

The effect of PGPR on the phospholipid aggregates is important for understanding the role played by PGPR in affecting the rheology of chocolate. As discussed in Section 3.5, a mixture of two surfactants can be thought of as having an intermediate molecular packing parameter. This has the potential to exert an effect on the structure of the surfactant aggregates. In order to systematically understand this effect, binary mixtures of lecithin (or Lec_{POPC}) with PGPR at various compositions have been studied. The total surfactant concentration for these studies was kept fixed at 2.4% w/w and the weight fraction of PGPR in the binaries was set at 0.25, 0.5 and 0.75.

3.6.1 SANS and SAXS from Lecithin + PGPR Solution

SAXS was measured from solutions containing 1.8% lecithin + 0.6% PGPR, 1.2% lecithin + 1.2% PGPR and 0.6% lecithin + 1.8% PGPR in TO and is shown in Figure 3.30. The scattering from solutions containing the same lecithin concentration is also plotted for comparison.

The Bragg peak due to the hcp packing of cylindrical micelles initially shifts to lower q for 1.8% lecithin + 0.6% PGPR before completely disappearing for 1.2% lecithin + 1.2% PGPR and 0.6% lecithin + 1.8% PGPR. The cross-section of the micelles doesn't show any change when compared to that measured by SAXS from lecithin only in TO (fits shown in the insets of Figure 3.23), but the length of the cylindrical micelles shortens considerably, from 940 Å for 2.4% lecithin in TO to 145 Å for 1.8% lecithin + 0.6% PGPR and $70 - 80$ Å for 1.2% lecithin + 1.2% PGPR and 0.6% lecithin + 1.8% PGPR. This is a change in aspect ratio of

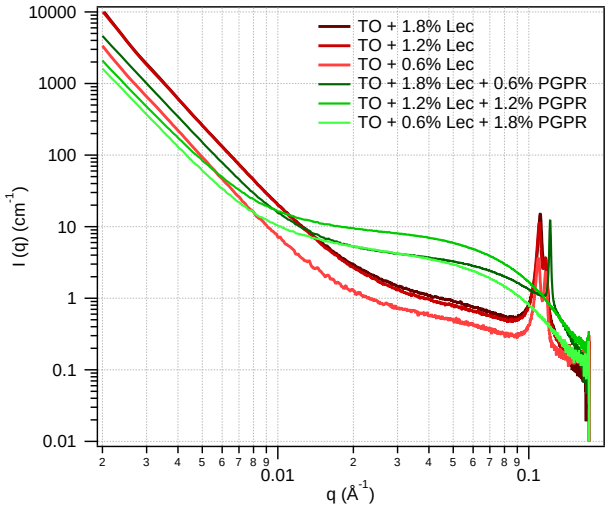

Figure 3.22 *SAXS from binary mixtures of lecithin and PGPR in TO*

the cylindrical micelles from ~ 30 to ~ 3. This suggests PGPR disrupts the hcp ordering of the phospholipid cylindrical micelles dispersing them as individual cylindrical micelles in the triglyceride oil phase as shown in Figure 3.36.

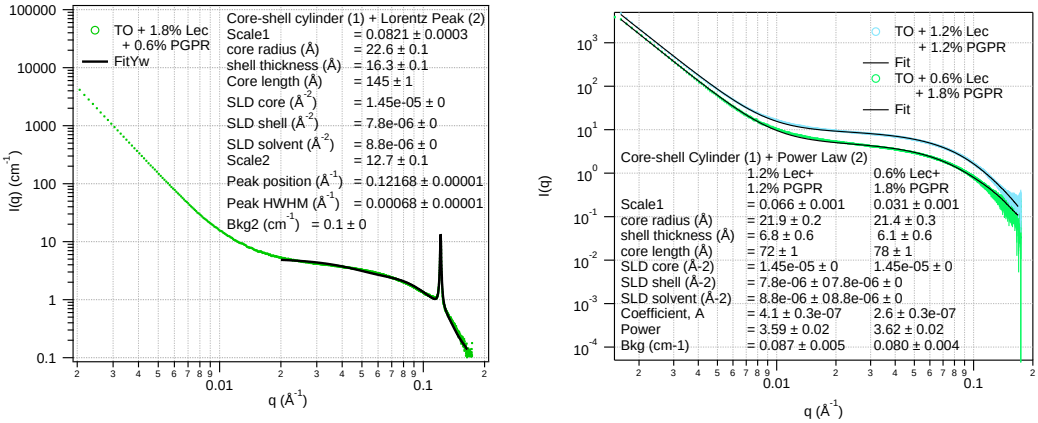

Figure 3.23 *SAXS from binary mixtures of lecithin and PGPR in TO. Left panel: 1.8% lecithin + 0.6% PGPR fitted to a sum of core-shell cylindrical model and Lorentz peak. Right panel: 1.2% lecithin + 1.2% PGPR and 0.6% lecithin + 1.8% PGPR fitted to a sum of core-shell cylindrical model and power law*

SANS measured from binary mixtures of lecithin and PGPR in TO also show a decrease in length of the cylindrical micelles, while the cross-section remains similar, as shown in Figure 3.24 and compared to Figure 3.14. The length of the cylindrical micelles decreases from 110 Å for lecithin only solutions in TO to 85 Å for 1.8% lecithin + 0.6% PGPR solution in TO to 75 Å for 1.2% lecithin + 1.2%

PGPR solution in TO. PGPR also decreases the length of the cylindrical micelles for the fresh solutions as measured by SANS, even though the effect is smaller than for the aged solutions as measured by SAXS.

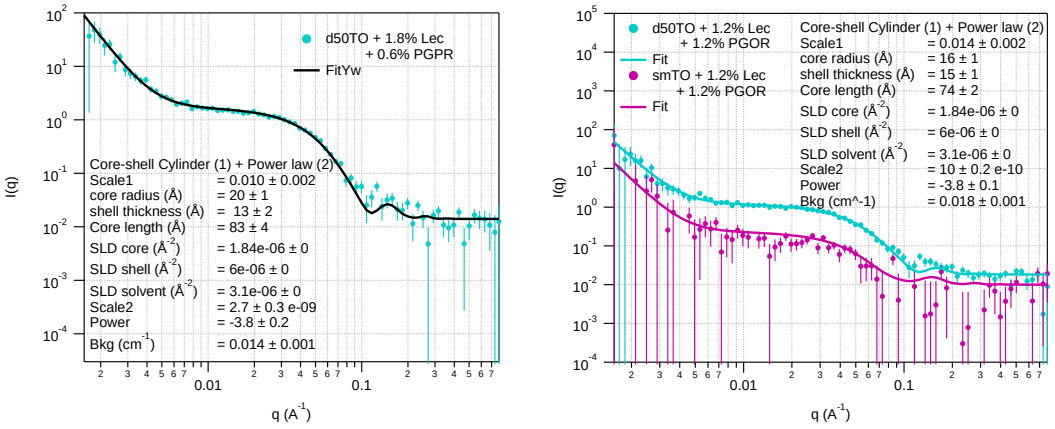

Figure 3.24 *SANS from binary mixtures of lecithin and PGPR in TO fitted to a sum of core-shell cylindrical model and power law. Left panel: 1.8% lecithin + 0.6% PGPR in d50-TO. Right panel: 1.2% lecithin + 1.2% PGPR in d50-TO and sm-TO.*

Similar SAXS studies were conducted on lecithin + PGPR solutions in GTO and are shown in Figure 3.25. PGPR has a similar effect on the cylindrical micelles formed by lecithin micelles in GTO. It reduces the aspect ratio from 5 to 2, by reducing the length of the cylinders from 140 Å to 60 Å. It does not have any effect on the cylinder cross-section.

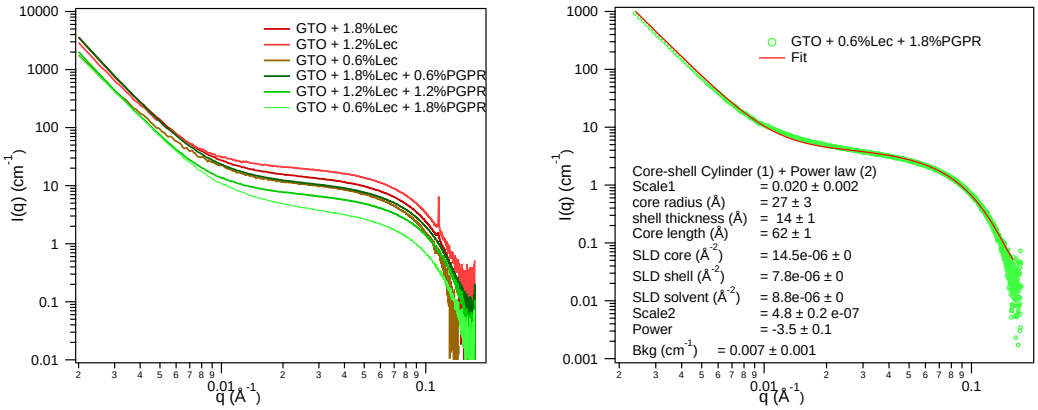

Figure 3.25 *SAXS from binary mixtures of lecithin and PGPR in GTO. Left panel: Solutions with varying binary mixtures of lecithin and PGPR in GTO. Right panel: 0.6% lecithin + 1.8% PGPR in GTO fitted to a sum of core-shell cylindrical model and power law.*

The SANS measurements on lecithin and PGPR binary mixtures in GTO also showed the effect of PGPR where the addition of PGPR decreases the length of the cylindrical micelles, as shown in Figure 3.25 when compared to Figure 3.16. However, the effect is smaller than that measured in SAXS from aged solutions. The length of the cylindrical micelles decreases from 70 Å for lecithin only solutions in GTO to 50 Å for 1.8% lecithin + 0.6% PGPR solution in GTO to 40 Å for 1.2% lecithin + 1.2% PGPR solution in GTO.

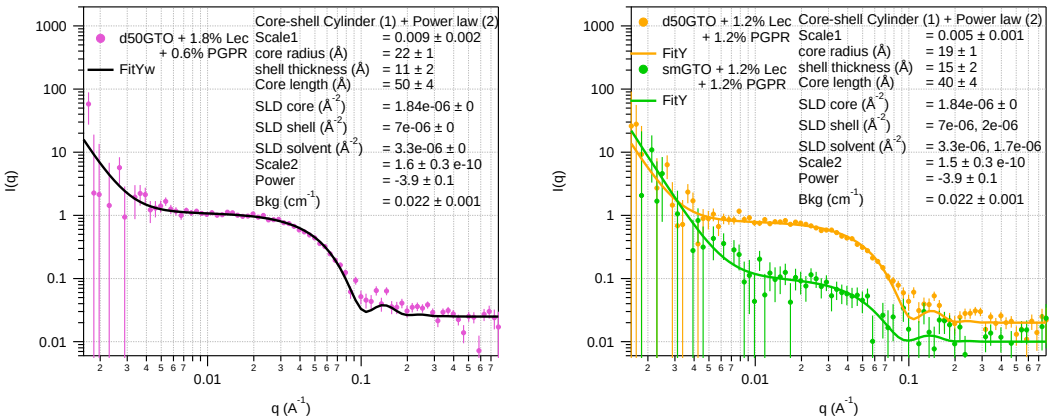

Figure 3.26 *SANS from binary mixtures of lecithin and PGPR in GTO fitted to a sum of core-shell cylindrical model and power law. Left panel: 1.8% lecithin + 0.6% PGPR in d50-GTO. Right panel: 1.2% lecithin + 1.2% PGPR in d50-GTO and sm-GTO.*

In summary, addition of PGPR decreases the aspect ratio of the cylindrical micelles by decreasing their length.

3.6.2 Effect of Ageing on Lecithin and PGPR Aggregates

The difference between SANS and SAXS measurements for lecithin-rich solutions, as discussed above, can be explained by the cylindrical micelles growing in length upon ageing to avoid unfavourable interaction with the solvent at the cylinder ends. To explore this, SAXS measurements using the XENOCS SAXS/WAXS system were carried out on fresh solutions (made $<$ 24 hours before measurement rather than $>$ 72 hours for the synchrotron x-rays) lecithin, PGPR and their binary mixtures in TO. These samples were then aged for 5 days and measured again.

SAXS from fresh and aged 2.4% lecithin in TO and 1.8% lecithin + 0.6% PGPR in TO (lecithin-rich samples) is shown in the left and right panels of Figure 3.27,

respectively. The SAXS from the fresh solutions did not display any Bragg peak and could be fit to cylindrical micelles with core-radius 25 Å, shell thickness $12-14$ Å and length $130-170$ Å, consistent with the values obtained for SANS from fresh solutions. The measurements were repeated on the same sample after ageing it for 5 days. A Bragg peak appeared at $q \approx 0.11$ Å^{-1}. This confirms that the Bragg peaks observed in the SAXS measurements for 2.4% lecithin in TO samples, discussed in Section 3.5.2, and 1.8% lecithin + 0.6% PGPR samples in TO samples, discussed in Section 3.6.1, are due to aggregation of lecithin micelles into larger structures upon ageing.

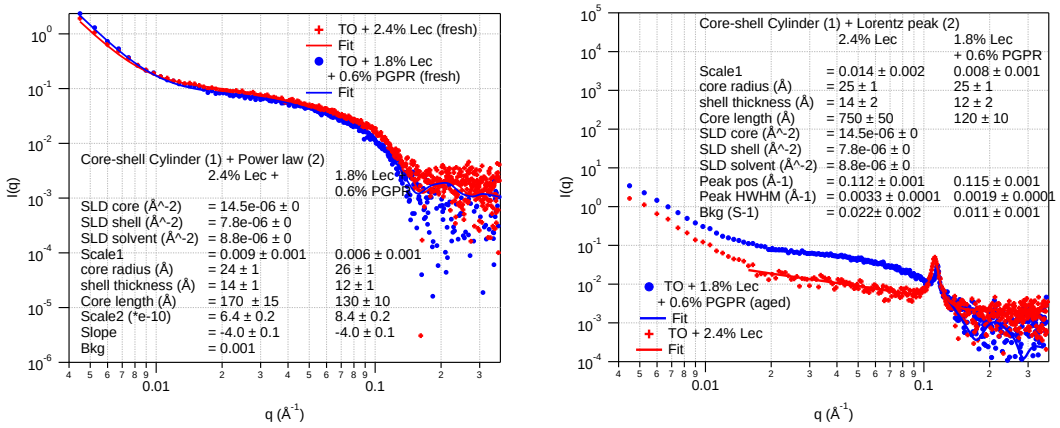

Figure 3.27 *SAXS from 2.4% lecithin in TO and 1.8% lecithin + 0.6% PGPR in TO. Left panel: SAXS from fresh samples (<24 hours old). Right panel: SAXS from aged samples (>120 hours old).*

SAXS from fresh and aged 1.2% lecithin + 1.2% PGPR in TO and 0.6% lecithin + 1.8% PGPR in TO is shown in the left and right panel of Figure 3.28, respectively. The SAXS from the fresh samples can be fitted to cylindrical core-shell micelles with radius 25 Å, shell thickness 10 Å and length 100 Å. There is no change in the size of these micelles upon ageing, consistent with the SAXS and SANS data from 1.2% lecithin + 1.2% PGPR solutions discussed in Section 3.6.1. These studies indicate that PGPR interacts with the lecithin in the cylindrical micelles and inhibits the aggregation of these micelles into large-scale structures.

SAXS from solutions of PGPR in TO solutions also shows no change upon ageing, as shown in Figure 3.29. This suggests that TO is a sufficiently good solvent for PGPR that there is no driving force for aggregation into larger structures.

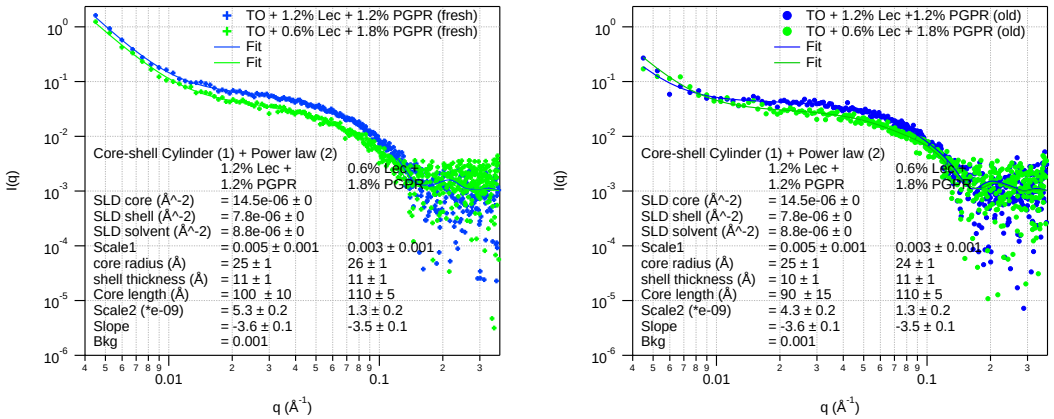

Figure 3.28 *SAXS from 1.2% lecithin + 1.2% PGPR in TO and 0.6% lecithin + 1.8% PGPR in TO fitted to a sum of core-shell cylindrical model and power law. Left panel: SAXS from fresh samples (<24 hours old). Right panel: SAXS from aged samples (>120 hours old).*

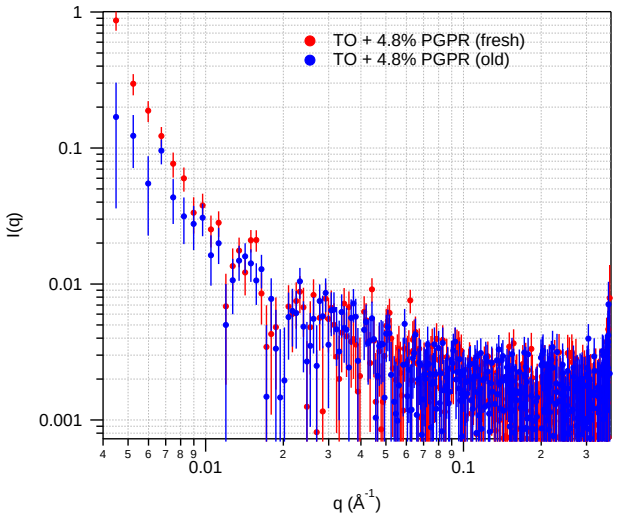

Figure 3.29 *SAXS from 2.4% PGPR in TO for fresh (<24 hours old) and aged (>120 hours old) samples.*

3.6.3 SANS and SAXS from POPC + PGPR Solution

SAXS was measured from solutions containing 1.8% Lec_{POPC}+ 0.6% PGPR, 1.2% Lec_{POPC} + 1.2% PGPR and 0.6% Lec_{POPC} + 1.8% PGPR in TO and is shown in Figure 3.30. The scattering from solutions with the same Lec_{POPC} concentration is also plotted for comparison.

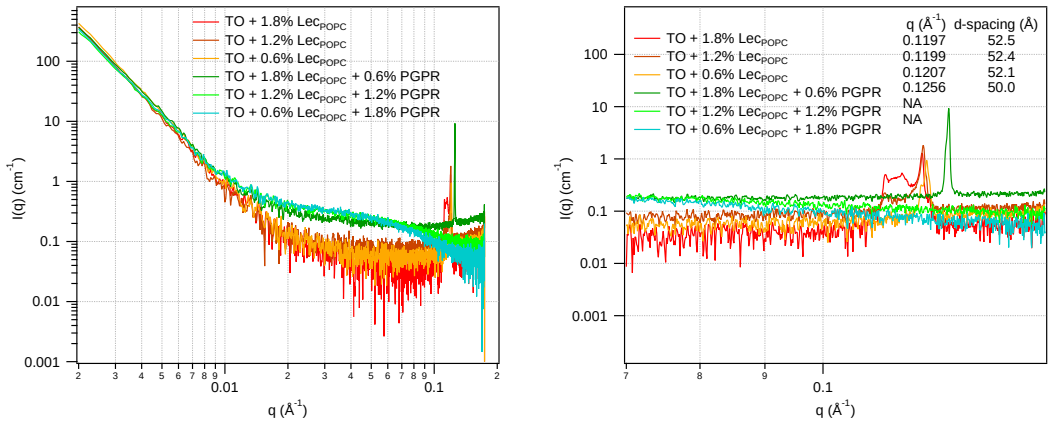

Figure 3.30 *SAXS measured from binary mixtures of Lec_{POPC} and PGPR in TO. Left panel: SAXS from Lec_{POPC} and PGPR solutions in TO. Right panel: SAXS from Lec_{POPC} and PGPR solutions in TO zommed in at the Bragg peak with positions in inset.*

The right panel in Figure 3.30, shows clearly that the Bragg peak for 1.8% Lec_{POPC} + 0.6% PGPR moves to higher q as compared to Lec_{POPC} only solutions, corresponding to a smaller d-spacing of 50 Å. At PGPR fractions above this, i.e. 1.2% Lec_{POPC} + 1.2% PGPR and 0.6% Lec_{POPC} + 1.8% PGPR, the Bragg peak disappears and instead q^{-1} scattering from cylindrical micelles is observed. The scattering can be fitted to a cylindrical core-shell model with radius between $20 - 30$ Å and length $80 - 100$ Å.

SANS studies from 2.4% Lec_{POPC}, 1.8% Lec_{POPC} + 0.6% PGPR and 1.2% Lec_{POPC} + 1.2% PGPR in h-TO display a similar trend, as shown in Figure 3.32. A Bragg peak, corresponding to lamellar structure, is observed in the scattering from 2.4% Lec_{POPC} solution in TO (green data set in the left panel of Figure 3.32) which disappears as the PGPR fraction of the surfactant mixture is increased leaving scattering from isolated cylindrical micelles as shown for 1.8% Lec_{POPC} + 0.6% PGPR (red data set in the left panel of Figure 3.32) and 1.2% Lec_{POPC} + 1.2% PGPR (right panel of Figure 3.32). Addition of PGPR introduces a curvature in the lamellar structures formed by POPC in TO turning them into

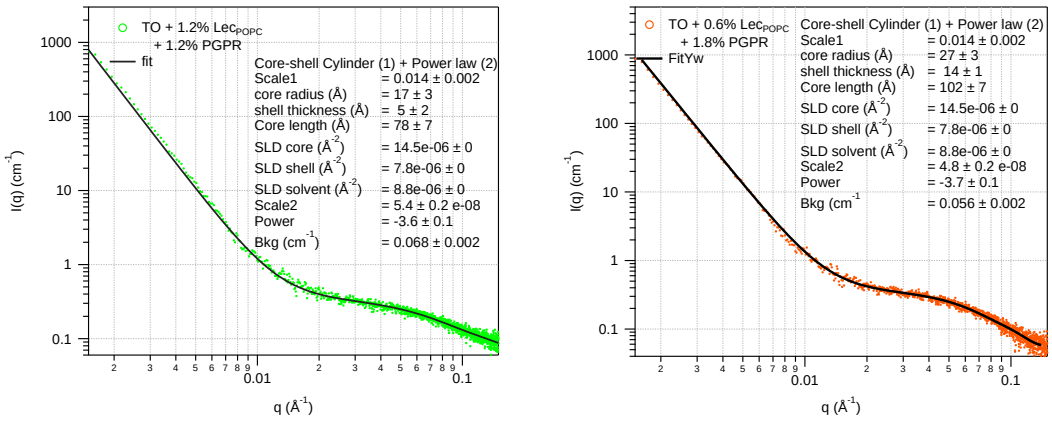

Figure 3.31 *SAXS measured from binary mixtures of Lec_{POPC} and PGPR in TO exhibiting cylindrical micelles. Left panel: 1.2% Lec_{POPC} + 1.2% PGPR. Right panel: 0.6%Lec_{POPC} + 1.8% PGPR*

cylindrical core shell micelles of radius 25-30 Å and length ∼100 Å, as depicted in Figure 3.37. This pushing apart of lamellae and formation of cylindrical micelles is similar to the effect observed in lecithin where PGPR reduces the length of the cylindrical micelles. This is strongly suggestive of the PGPR mixing into the POPC leaflets and modifying the inter-leaflet interactions, this time forcing the lamellae apart as they roll up into cylindrical micelles.

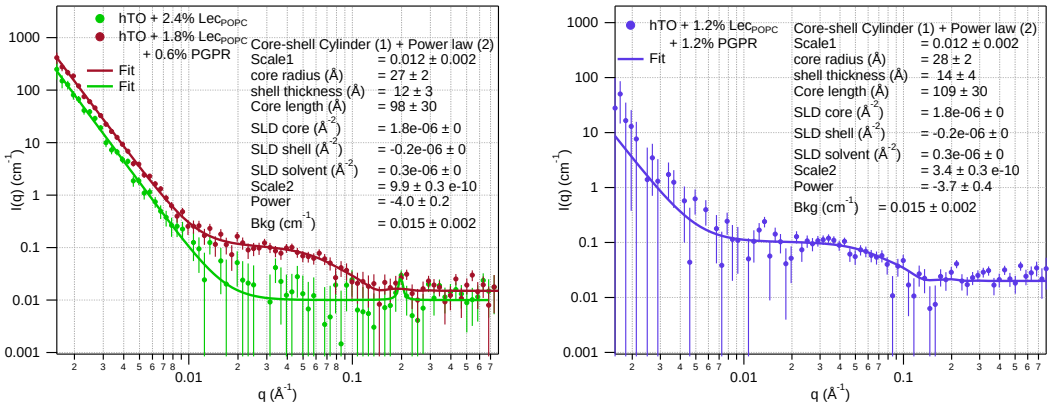

Figure 3.32 *SANS measured from binary mixtures of Lec_{POPC} and PGPR in TO exhibiting cylindrical micelles. Left panel: 2.4% Lec_{POPC} & 1.8% Lec_{POPC} + 0.6% PGPR. Right panel: 1.2% Lec_{POPC} + 1.2% PGPR.*

SAXS studies from binary mixtures of Lec_{POPC} and PGPR in GTO exhibit a trend similar to the binary mixtures in TO. As with the solutions of Lec_{POPC} only in GTO, the binary mixtures with PGPR also show a double peak for 1.8%

Lec_{POPC} + 0.6% PGPR centred at the same values of q, $q_1 = 0.107$ Å^{-1} and $q_2 = 0.113$ Å^{-1}, as shown in the left panel of Figure 3.34. The figure shows that the are peaks consistent with a hcp structure with d-spacings of 58.8 Å and 55.4 Å. Upon increasing the concentration of PGPR to 1.2% Lec_{POPC} + 1.2% PGPR, the Bragg peaks shift to higher q, $q_1 = 0.115$ Å^{-1}and $q_2 = 0.122$ Å^{-1}, corresponding to d-spacing of 54.8 Å and 51.7 Å, shown in the right panel of Figure 3.34. Upon further increasing the concentration of PGPR to 0.6% Lec_{POPC} + 1.8% PGPR, the double peaks are replaced with a single peak at still higher q, $q = 0.125$ Å^{-1}, corresponding to d-spacing of 50.4 Å, shown in the left panel of Figure 3.35. This shows that the spacing between the POPC lamellae becomes smaller upon the addition of PGPR.

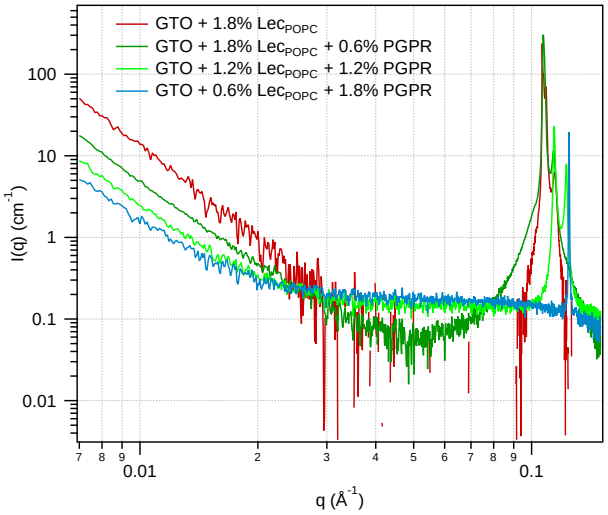

Figure 3.33 *SAXS measured from binary mixtures of Lec_{POPC} and PGPR in GTO.*

Another important feature that can be seen in the SAXS data for 1.2% Lec_{POPC} + 1.2% PGPR and 0.6% Lec_{POPC} + 1.8% PGPR, is the change in slope for $q > 0.01$ Å^{-1}. This change can be attributed to formation of micelles instead of purely lamellar structures as observed for the Lec_{POPC} only solutions and high Lec_{POPC} fraction solutions. This trend is also observed in the SANS data from these Lec_{POPC} and PGPR solutions in GTO, right panel of Figure 3.35, although detailed fitting of this micellar SANS data is not possible due to high noise resulting from the low contrast. The SAXS data was fitted using a sum of spherical micelles and Lorentz peak (shown in left panel of Figure 3.35) and a micelle radius of 17 Å was obtained. The limited q range means it is not possible to obtain further structural details about these micelles.

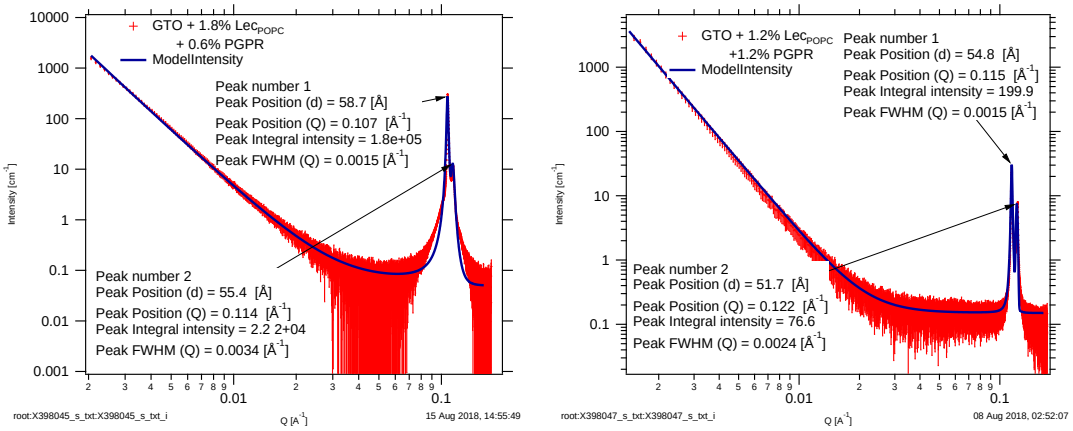

Figure 3.34 *SAXS measured from binary mixtures of Lec$_{POPC}$ and PGPR in GTO. Left panel: 1.8% Lec$_{POPC}$ + 0.6% PGPR. Right panel: 1.2% Lec$_{POPC}$ + 1.2% PGPR.*

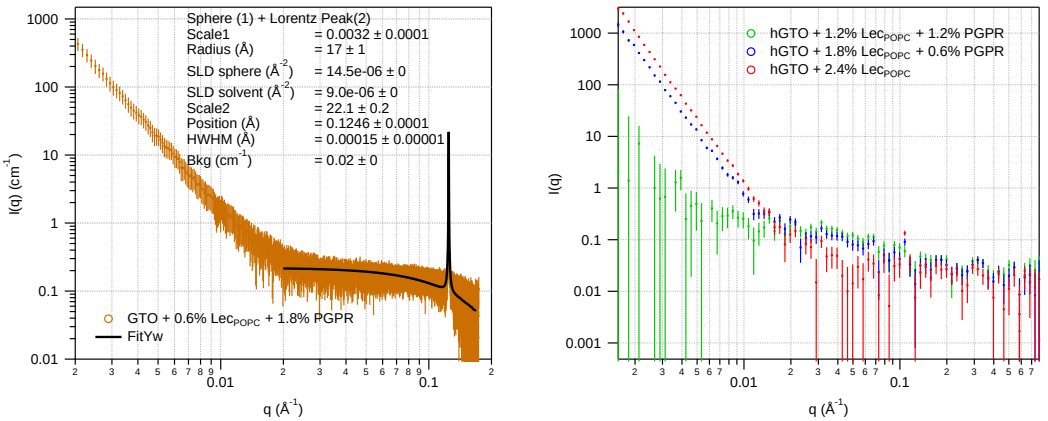

Figure 3.35 *SAXS and SANS measured from binary mixtures of Lec$_{POPC}$ and PGPR in GTO. Left panel: SAXS measured from 0.6% Lec$_{POPC}$ + 1.8% PGPR. Right panel: SANS measured from various composition of binary mixtures of Lec$_{POPC}$ and PGPR*

3.7 Conclusions

Structural and rheological studies of lecithin (and Lec_{POPC}), PGPR and their binary mixtures have provided an insight into the behaviour and interaction between these surfactants in the triglyceride oils TO and GTO.

Lecithin forms inverse core-shell cylindrical micelles in TO with the heads forming the core and the tails directed towards the triglyceride oil. The cross-section of these micelles is $\sim$50 Å and length is $100 - 150$ Å. These micelles grow in length upon ageing to $\sim$1000 Å to minimize the unfavourable interaction with the solvent at the end of the cylinders and arrange into an ordered hcp structure (manifested as the Bragg peaks in the SAXS data) depicted in the left hand side of Figure 3.36. These long structures provide a means of transmitting stress across the gaps between the plates of a rheometer explaining the observation of the yield stress exhibited by solutions of lecithin in TO. The addition of PGPR disrupts these structures and shortens the length of the micelles to $70 - 80$ Å for fresh lecithin + PGPR in TO solutions and $100 - 150$ Å for the aged lecithin + PGPR in TO solutions. The extent of the decrease in length of the cylindrical micelles depends on the PGPR fraction of the surfactant mixture, suggesting that in addition to disrupting the ordering of lecithin micelles, PGPR increases the curvature of the individual micelles as shown in the right hand side of Figure 3.36. 1.8% lecithin + 0.6% PGPR in TO solutions still show a Bragg peak upon ageing, which is lost as the PGPR fraction is further increased to 1.2% lecithin + 1.2% PGPR in TO. This shortening of the cylindrical micelles and decreasing in ordering of the micelles means that the yield stress in the system decreases until it finally disappears for high PGPR fraction solutions.

The observation of growth and ordering of the lecithin micelles upon ageing was fortuitous as it makes the effect of PGPR in disrupting these ordered lecithin structures really obvious.

For lecithin in GTO, the behaviour is similar to that in TO where lecithin forms inverse core-shell cylindrical micelles which arrange themselves into ordered structures upon ageing. The extent of ordering is less evident, as can be seen from the smaller Bragg peak. This lower extent of lecithin incorporated into these larger organised structures provides an explanation for the lower yield stress observed in rheology. It also means that the amount of PGPR required to disrupt these hcp structures is less, such that both the structuring of the cylindrical

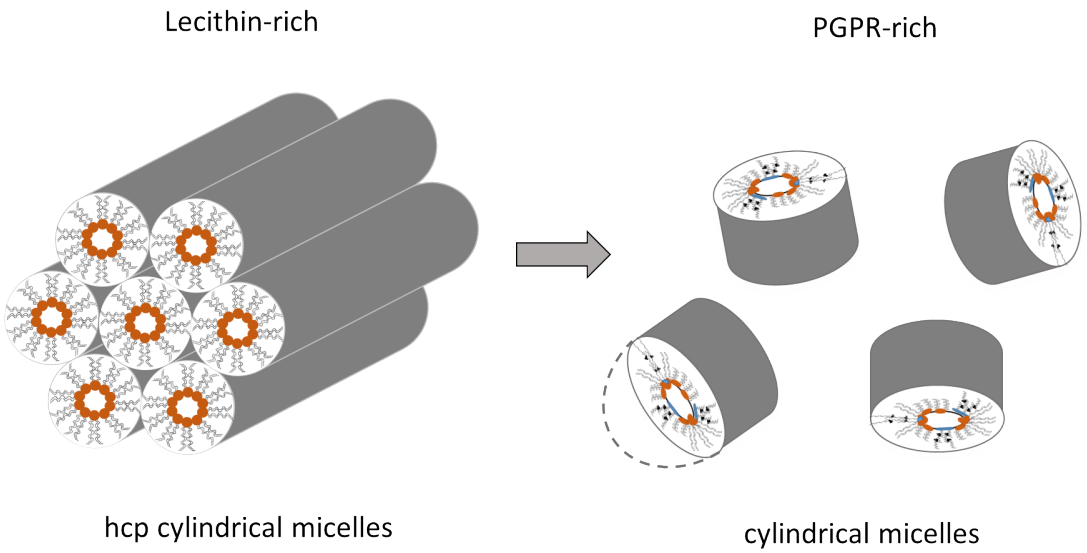

Figure 3.36 *Schematic showing micellar arrangement of lecithin and PGPR mixtures in triglyceride oil. Left: Cylindrical micelles arranging into hcp structures formed by lecithin rich solutions. Right: Micelles formed by PGPR rich solutions.*

micelles, exhibited as the Bragg peak, and the yield stress disappears for 1.8% lecithin + 0.6% PGPR in GTO.

Similar measurements were done for Lec_{POPC} (50% POPC + 50% triglyceride oil) and its binary mixture with PGPR in both TO and GTO. POPC forms lamellar structures, depicted in the left hand-side cartoon in Figure 3.37, in the triglyceride oils as is evident from the presence of the Bragg peaks. These lamellar structures impart a yield stress to the POPC solution in triglyceride oils. The addition of PGPR changes the curvature of the lamellar structures and the SAXS and SANS show presence of cylindrical micelles (or spherical in the case of GTO), as depicted in the cartoon in the middle panel and right panel of Figure 3.37 depending on the PGPR fraction of the surfactant. This provides a clear indication that PGPR mixes with the POPC leaflets, forcing them apart forming cylindrical/spherical micelles dispersed in the triglyceride oil phase, which means the solutions exhibit Newtonian flow behaviour without any yield stress.

One important observation was the shift of Bragg peak to higher q upon the addition of PGPR in the case of binary mixtures with both lecithin (Figure 3.22) and POPC (Figure 3.30 and 3.33). This suggests that counter-intuitively the d-spacing between the hcp cylinder or lamellae decreases where one might naively expect the spacing to increase in response to PGPR induced swelling the micelles.

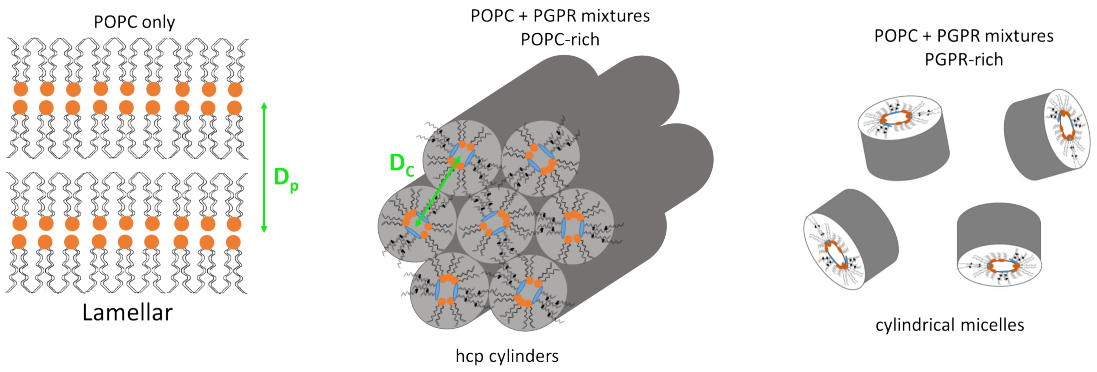

Figure 3.37 *Schematic showing micellar arrangement of Lec_{POPC} and PGPR mixtures in triglyceride oil. Left: Lamellar structures formed by Lec_{POPC} solutions. Middle: Cylindrical micelles arranging into hcp structures formed by Lec_{POPC} rich solutions.. Right: Micelles formed by PGPR rich solutions.*

This can instead be explained to be a consequence of the decrease in the tail thickness caused by an increase in the curvature (decrease in the radius of curvature) while the core-radius (measured from the SANS/SAXS data) and surfactant volume remain unchanged. If the head surface area (S) to total surfactant volume (V) remain unchanged, the change in curvature of the micelles will induce a change in the thickness of the tail region. For a planar system the ratio of volume to surface area is trivially equal to the tail length, T_p. For a cylindrical core-shell micelle of length L and core-radius r the maximum tail-thickness T_c can be calculated using the volume to surface ratio as:

$$\begin{aligned} \frac{V}{S} = T_p &= \frac{\pi(r+T_c)^2 L - \pi r^2 L}{2\pi r L} \\ \implies T_c &= (2T_p r + r^2)^{1/2} - r \end{aligned} \tag{3.17}$$

For spherical micelles of radius r, a similar calculation gives the maximum tail-thickness T_s as:

$$T_s = (3T_p r + r^3)^{1/3} - r \tag{3.18}$$

The variation in tail thickness for various geometric shapes, plotted in Figure 3.38 and shown in the cartoon in Figure 3.39, suggest that at a fixed core-radius as the curvature of the micelles increases from planar to spherical to cylindrical, the tail thickness decreases exhibited as a decrease in d-spacing between the micellar packing, which can explain the movement of the Bragg peak towards higher-q.

These results provide a mechanism for phospholipid and PGPR interaction which

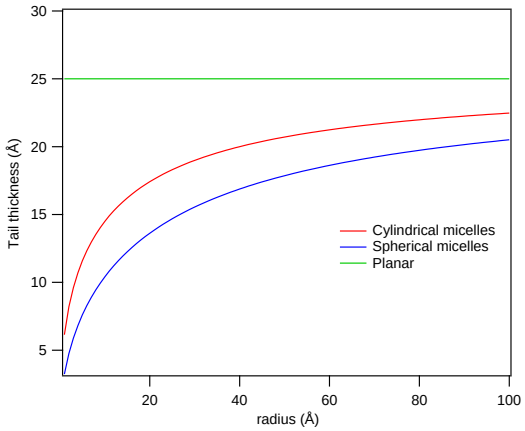

Figure 3.38 *Calculations showing the variation of the tail thickness for micelles with core-radius for micelles of varying curvatures; planar, cylindrical, spherical.*

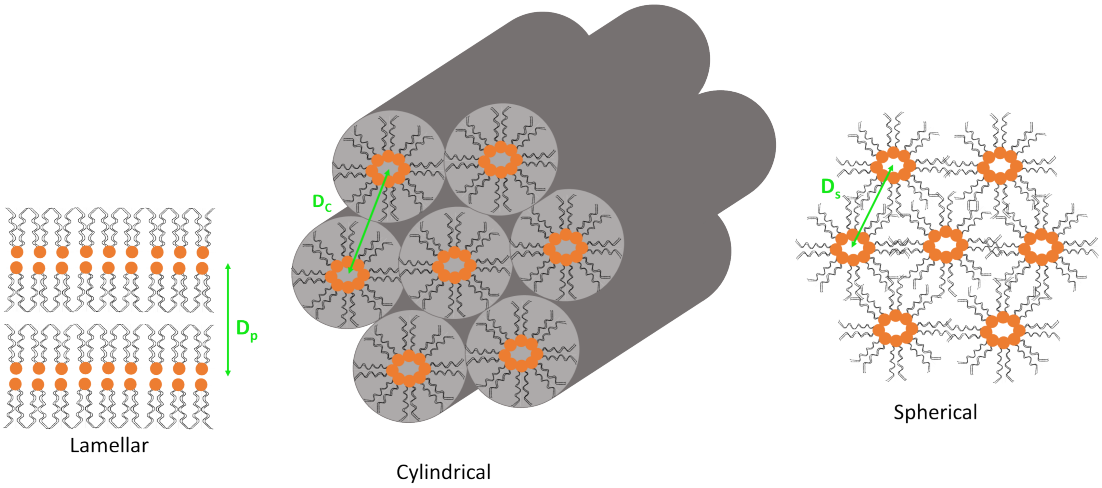

Figure 3.39 *Cartoon showing the decrease in d-spacing as the curvature of the micellar structure increases. Left to right: Lamellar structure d-spacing (D_p) > hcp cylinder (D_C) > hcp sphere ((D_s).*

results in the modification of the rheology of the solution (in the absence of sucrose interface). Phospholipids form hcp packed cylinderical micelles, in case of mixed phospholipids found in lecithin, or lamellar structures, in case of pure POPC, in triglyceride oil, which provide a means of transmitting stress. PGPR interacts with the phospholipid leaflets pushing them apart and dispersing them as individual core-shell cylindrical or spherical micelles in the oil phase. This disrupts the large scale structures in the solution that transmit stress, removing the solution yield stress. In these studies we have directly shown that PGPR interacts with lecithin and this is important in understanding the role of lecithin and PGPR as rheology modifiers when used together in model chocolate suspensions as discussed in Chapter 4.

Chapter 4

Adsorption of Surfactants in Model Chocolate Suspensions

4.1 Introduction

Lecithin and PGPR improve the dispersion of chocolate solids in the continuous cocoa butter phase and modify the rheology of molten chocolate as described in Chapter 2. It is believed that lecithin and PGPR adsorb at the solid/triglyceride interface and change the inter-particle interaction by lubricating the solid grains or by creating a steric repulsion between the solid particles, which in turn affects how the solid particles flow past each other.

Lipid lubrication has been used extensively for mechanical applications throughout history, e.g. olive oil was used on Roman roads, fatty acids are used to prevent corrosion of iron and bio-lubricants are used in engines and indeed in our own joints. In these applications, a thin lipid layer adsorbs at the solid-fluid interface reducing frictional contact [58, 69]. In the last few decades there has also been an increase in interest in the application of adsorbed polymer films to provide lubrication. The polymer chains can be tethered, either chemically or by adsorption, to the surface and in the case of a good solvent they become swollen, acting as molecular brushes that facilitate sliding [70]. This structure additionally provides steric repulsion due to the extended swollen layer. We hypothesise a combination of the two mechanisms is at play where lecithin lubricates sucrose grain by adsorption of thin phospholipid layers and PGPR

forms extended polymer brush-like layer upon adsorption at the sucrose grains which provides lubrication and steric stabilisation. Structural investigations can be carried out of the adsorbed surfactant layers at the sucrose/triglyceride interface in order to understand the mechanism behind the effect of lecithin, PGPR and their combinations on the rheological properties of molten chocolate.

In this chapter, adsorption of lecithin and PGPR in model chocolate comprising a sucrose in triglyceride oil suspension is discussed. In Section 4.2, a literature review of previous adsorption studies of lecithin and PGPR in chocolate systems is presented. In Section 4.3 structural investigations using Small Angle X-Ray and Neutron Scattering (SAXS and SANS) of the model chocolate suspensions, established in Chapter 2, are discussed. Finally in Section 4.4 the particle-particle correlation between sucrose grains is measured using Spin Echo Small Angle Neutron Scattering (SESANS) allowing a direct relationship between inter-particle interaction and rheology to be drawn.

4.2 Adsorption of Phospholipids and Polymeric Surfactants

Various studies have been conducted to investigate the adsorption of lecithin and PGPR on model systems to understand the influence of lecithin and PGPR on the rheological properties of chocolate. Using confocal microscopy studies on sucrose/Triolein suspensions containing the surfactants, Vernier found that both lecithin and PGPR separately adsorb on the sucrose surface [8]. When a mixture of lecithin and PGPR is added to the suspension, lecithin displaces the PGPR from the sucrose surface owing to the higher affinity of the PC in lecithin to the polar sugar interface. PGPR appeared to exist in the bulk phase in addition to being adsorbed at the interface. These studies are consistent with the simulations done by Kindlein *et al.* [36] which suggest that phospholipids adsorb at the sucrose/cocoa butter interface with their head group oriented towards the sucrose interface with the strength of the attachment dependant on the headgroup-sucrose interaction.

Middendorf *et al.* [71] have also investigated the adsorption of lecithin and PGPR at the sucrose interface and found that higher amount of lecithin is adsorbed onto sucrose, 2.69 mg/m^2, as compared to PGPR, 0.18 mg/m^2. Middendorf

et al. propose that PGPR combines with the fat and make weakly bound structures which can act as spacers between the sucrose grains. This reduces inter-particle interactions and allows the suspension to flow better, thereby reducing yield stress. To further study the adsorption behaviour of lecithin and PGPR, Middendorf *et al.* performed AFM experiments using a standard silicon cantilever in nitrogen atmosphere. Both lecithin and PGPR increased the adhesion forces between the sucrose surface and the silicon nitride, as the interaction between the lipophilic parts of surfactants and the silicon nitride tip are higher than those between more uncovered polar sucrose surfaces, and the effect was larger for lecithin than PGPR. Although this contrasts with the results by Arnold *et al.* [29], it still suggests that PGPR and lecithin both adsorb on the sucrose surface, with lecithin having a higher surface activity. An important point to note is that these studies were conducted in nitrogen atmosphere as opposed to the continuous triglyceride fat phase present in chocolate.

Dedinaite *et al.* measured the forces acting between polar mica surfaces interacting across solutions of triolein containing PE, PGPR and a mixture of PE and PGPR using surface force measurements [72] to understand the adsorption of these surfactants. Solutions of triolein with PE and PGPR both displayed force barriers as a result of adsorption of the surfactants onto the mica surface. Triolein solutions with PE displayed two force barriers: an outer weak force barrier at a separation of $100 - 120$ Å and an inner strong force barrier at a separation of $70 - 75$ Å. These distances are larger than a bilayer coverage of PE (one on each mica surface) and Dedinaite *et al.* suggested this can be attributed to some king of structuring of the triolein molecules in between the two PE coated hydrophobic mica surfaces. We suspect these can equally be attributed to greater than monolayer coverage of the PE at the mica surface. Solutions of triolein with PGPR on the other hand exhibited repulsive forces, which ranged upto approximately 150 Å. Dedinaite *et al.* attribute this to 75 Å long loops and tails of the polymer extending into the triolein from each mica surface. The force increases gradually as the separation between the mica surfaces decreases, and can be attributed to an outer dilute polymer region which can be compressed and an inner near-surface dense polymer region of $22 - 30$ Å (corresponding to a separation of $45 - 60$ Å for the two surfaces). For solutions of triolein with PE and PGPR long range repulsion is observed extending upto $\sim$1500 Å. The force slowly rises as the separation is decreased to about 500 Å before hitting a hard-wall. These studies show the PE and PGPR both adsorb onto the polar mica surface, with PGPR resulting in longer range repulsion as compared to PE. A mixture of

PGPR and PE in Triolein gave rise to a longer ranged and stronger repulsive force than with either just PGPR or just PE. This suggests an interaction mechanism when the two surfactants are used in combination, consistent with the rheological effect of phospholipid and polymeric surfactants, whereby a mixture of PGPR and lecithin is more effective in lowering both the yield stress and viscosity of sucrose/oil suspensions than the equivalent concentration of either of the two surfactants by themselves.

These studies have provided useful insight into the adsorption of phospholipid and polymeric surfactant PGPR at various polar interfaces and their role in modifying interaction between these interfaces. However, their relevance in explaining the role of molten chocolate suspensions is limited for the following reasons:

- The rheological relevance of the interfacial interaction between polar mica surfaces (Dedinaite) or silicon/sucrose surfaces (Middendorf) to the chocolate system cannot be established.

- Confocal studies such as the one done by Vernier introduce fluorescent dyes which are known to be surface active [73] and so could change the interfacial activity of lecithin and PGPR in the model chocolate suspensions.

- The studies described above give no structural details or an interaction mechanism for the effect of lecithin, PGPR or their binary mixture. Open questions remain about the nature of the interfacial films formed by the surfactants, for example, how is the surfactant material distributed and, in the case of binary mixtures, whether it is an intercalating layer of lecithin and PGPR or does one surfactant sits on top of the other.

To better understand the structure of interfacial surfactant films and their role in modifying rheological properties of molten chocolate, detailed structural investigations at the sucrose/triglyceride oil interface have been carried out. These were done on the rheologically relevant model chocolate suspensions described in Chapter 2 using Small Angle Scattering, discussed in Section 4.3, and on planar interfaces, discussed in Chapter 5, 6 and 7.

4.3 Small Angle Scattering from Model Chocolate Suspensions

4.3.1 Small Angle Scattering from Dense Suspensions

Small Angle Neutron and X-ray Scattering (SANS and SAXS) can be used to determine the adsorbed amount and distribution of interfacial films of thicknesses $1 - 100$ nm. The steric force barriers obtained by Dedinaite *et al.* using Surface Force Apparatus between polar mica surfaces in Triolein containing PE, PGPR and their binary mixture suggest the surfactant films range from $5 - 100$ nm in thickness, which means that they can be characterised using Small Angle Scattering. An interfacial surfactant film creates an inhomogeneity in the scattering length density of the suspensions that can be detected by SANS and SAXS. The principle of Small Angle Scattering from high volume fraction suspensions, such as chocolate, is the same as described in Chapter 3, however, there are additional complications due to multiple scattering and the structure factor between the sucrose grains has an effect on the measured intensity. The multiple scattering effect means that some of the detailed structural information can be obscured but it remains possible to extract properties such as radius of gyration, R_g, of the films and whether the scattering comes from a fractal or diffuse object using the analysis method described in Section 4.3.2.

SANS and SAXS experiments were carried out on 65% w/w sucrose in triglyceride oil suspensions with SAXS and SANS providing complementary contrasts. SAXS was measured using hydrogenated triglyceride oil (h-oil) whereas for SANS two contrasts were used, fully deuterated (d-oil) and sucrose-matched (sm-oil) triglyceride oil, obtained by mixing h-oil and d-oil in the appropriate volume fraction to obtain scattering length density matched to that of sucrose.

The adsorbed phospholipid + polymer layer can be visualised using the core-shell analogy described in Section 3.4. A pictorial representation of this is shown in Figure 4.1, where the sucrose grains, shown in purple, can be considered to be the core and the adsorbed interfacial surfactant layer as the shell with the phospholipid head-group shown in red and tail-rich or polymer region shown in blue. By changing the scattering length density of the continuous oil phase, various components of the system can be highlighted. The h-oil contrast, where the SLD of oil is similar that of the tails, from SAXS (left panel), gives information

about the sucrose/oil interface and the adsorbed phospholipid layer due to contrast from the head-group. The d-oil contrast in SANS (middle panel) provides complementary information by highlighting the tails in the interfacial layer. In the sm-oil contrast (right panel), the scattering from the sucrose/oil interface is minimised highlighting the adsorbed surfactant layer.

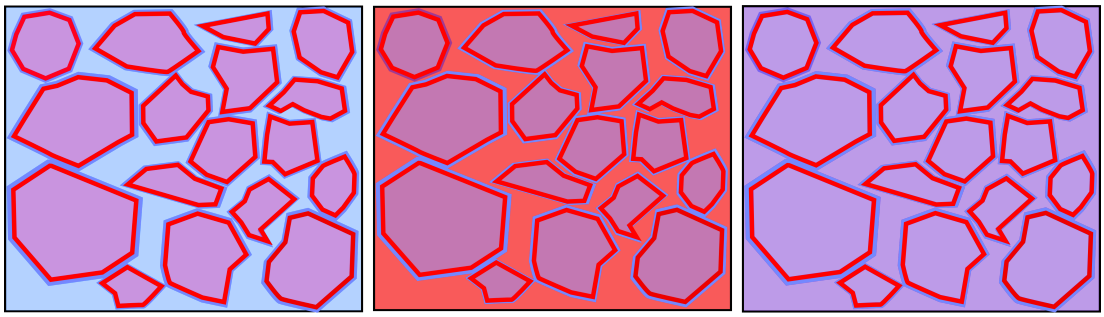

Figure 4.1 *Small Angle Scattering contrasts for adsorbed surfactant+polymer layer in sucrose/triglyceride suspensions. Left panel: h-oil contrast (SAXS). Middle panel: d-oil contrast (SANS). Right panel: sm-oil contrast (SANS).*

Equation 3.8, as discussed for core-shell particles in Chapter 3, can also be applied for the discussions presented here where $F_p(q)$ is the intra-particle form factor for sucrose and $F_l(q)$ is the form factor for the adsorbed interfacial layer. The first term in Equation 3.8 represents the contribution to the scattering arising from the sucrose particles and can be denoted as $I_{pp}(q)$, the third term gives the contribution from the interfacial layer denoted by $I_{ll}(q)$ and the second term provides the particle-interfacial layer interference term denoted by $I_{pl}(q)$. If the curvature of the surface is small ($qR_p \gg 1$), which is always the case in this situation, then the various contributions to the scattering intensity can be written as [74]:

$$I_{pp}(q) = (\rho_p - \rho_s)^2 \frac{2\pi A_p}{q^4}\left[1 + \frac{1}{q^2 R_p^2}\right] \tag{4.1}$$

$$\begin{aligned} I_{pl}(q) &= (\rho_p - \rho_s)(\rho_l - \rho_s)\frac{4\pi A_p}{q^4}\left[\int_0^t \phi(z)\cos(qz)\mathrm{d}z - qR_p\int_0^t \phi(z)\sin(qz)\mathrm{d}z\right] \\ &\approx -(\rho_p - \rho_s)(\rho_l - \rho_s)\frac{4\pi A_p}{q^3}\int_0^t \phi(z)\sin(qz)\mathrm{d}z \qquad \text{for} \quad qR_p \gg 1 \end{aligned} \tag{4.2}$$

$$I_{ll} = (\rho_l - \rho_s)^2 2\pi A_p \left[\frac{1}{q^2} \left| \int_0^t \phi(z) \exp(iqz) \mathrm{d}z \right|^2 + \tilde{I}_{ll} \right] \tag{4.3}$$

where A_p is the area per unit volume of the particles, R_p is the radius of the particle, $\phi(z)$ is the SLD profile of the interfacial layer, t is the thickness of the interfacial layer, and ρ_x is the SLD of the x phase. In the case of sm-contrast ($\rho_p = \rho_s$), I_{pp} and I_{pl} are 0 and the SANS intensity can be used to calculate the distribution of the interfacial adsorbed films. However, perfect solvent matching is difficult and therefore, even in the sm-contrast some scattering from I_{pp} and I_{pl} is present. To estimate the relative contributions of the scattering from the interfacial layers and the sucrose (because of the imperfect matching), we can take a ratio of I_{ll} to I_{pp} (r_{llpp}) and I_{ll} to I_{pl} (r_{llpl}). For the simplest case where the SLD profile is a step function and $qt \ll 1$, the integral in Equation 4.2 can be approximated to $qt^2/2$ and the mod square of the integral in Equation 4.3 can be approximated to t^2, giving r_{llpp} and r_{llpl} as.

$$r_{llpp} = \frac{I_{ll}(q)}{I_{pp}(q)} = \frac{(\rho_l - \rho_s)^2}{(\rho_p - \rho_s)^2} \times t^2 q^2 \tag{4.4}$$

$$r_{llpl} = \frac{I_{ll}(q)}{I_{pl}(q)} = \frac{(\rho_l - \rho_s)}{(\rho_p - \rho_s)} \tag{4.5}$$

For surfactants absorbed at sucrose interface in sm-oil, $(\rho_l - \rho_s) \approx 2 \times 10^{-6}$ Å^{-2} and $(\rho_p - \rho_s) < 0.1 \times 10^{-6}$ Å^{-2}, due to imperfect matching. For 10 nm thick interfacial layers, $r_{llpp} > 4$ and $r_{llpl} > 20$. The ratio r_{llpp} will be greater for thicker layers ($r_{llpp} > 36$ for 30 nm thick films at $q = 0.001$ Å^{-1}) and at higher q ($r_{llpp} > 400$ for 10 nm thick films at $q = 0.01$ Å^{-1}). These calculations give I_{ll} at q=0.00156Å^{-}1 to be 200 cm^{-1} for 5 nm thick films, which is comparable to the Lecithin data (thinnest films) as shown in Figure 4.3(4.3). The scattered intensity also changes with the surfactant composition, which affects the thickness of the films and $(\rho_l - \rho_s)$ for the interfacial layer but does not change the I_{pp} contribution. These observations suggests that while some scattering in the sm-contrast can be attributed to the scattering from the sucrose particles (I_{pp}), most of the scattering is from the adsorbed interfacial films (I_{ll}) with some contribution from the interference term (I_{pl}). Therefore qualitative information about the thickness and nature of the surfactant films can be obtained from the sm-contrast in SANS.

In the d-contrast SANS and h-contrast SAXS all three contributions to Equation 3.8 will be present, especially at low q. In order to obtain the scattering from the interfacial films, this low q scattering needs to be sytematically treated and is done using the Beaucage model, detailed in Section 4.3.2 and the implementation is explained in Section 4.3.5.

4.3.2 Data Analysis Using the Beaucage Model

The Unified fit model, also called the Beaucage model, was developed by Greg Beaucage to fit SAS data from complex systems that contain multiple levels of related structural features [75, 76]. The levels are comprised of a Guinier part, $I(q) = G\exp\left(\frac{-q^2R_g^2}{3}\right)$, and a power law tail, $I(q) = Bq^{-p}$. This model can be used to obtain a radius of gyration (from Guinier fits) and the nature of the scattering object (from the power law) for complex systems where an analytic model for the scatterer is either difficult or impossible to derive. Different q regimes contain information about the various structural levels and the function described in Equation 4.6 models both the Guinier exponential and structurally limited power-law regimes without introducing new parameters beyond those used in local fits.

$$I_i(q) = \sum_{i=1}^{n} G_i\,\mathrm{e}^{-\frac{q^2R_{g_i}^2}{3}} + B_i\,\mathrm{e}^{-\frac{q^2R_{g_{i+1}}^2}{3}}\left[\frac{\left(\mathrm{erf}\left(\frac{qR_g}{\sqrt{6}}\right)\right)^3}{q}\right]^{P_i} \tag{4.6}$$

where n is the number of structural levels, G_i is the Guinier coeffecient and incorporates the contrast, B_i is the power law coefficient, R_{g_i} is the radius of gyration and P_i is the power law exponent, each for the i^{th} level. This approach can be used to obtain Guinier regimes buried between two power-law regimes, which is the case for sucrose in triglyceride oil suspensions stabilised by surfactants. This characterises the linear dimension of the interfacial surfactant films in these complex high volume fraction suspensions. The analysis was performed using the Unified fit model described above implemented in the Irena package for analysis of small-angle scattering data [77].

4.3.3 Materials and Sample Preparation

The sucrose used for making sucrose in triglyceride oil suspensions was obtained from British Sugar having an average particle size ∼10 μm, as characterised in Chapter 2. The lecithin and PGPR were obtained from Mars Chocolate, UK. Pure triglyceride oil, GTO (≥99%) and TO (≥99%), used as the continuous phase were obtained from Sigma Aldrich, UK. Perdeuterated Glyceryl Trioctanoate (d-GTO) and Glyceryl Tripalmitate (d-TP) used for d-oil and sm-oil contrast in SANS were obtained from QMX Laboratories, UK and ISIS Deuteration Facility, Oxford, UK.

Model chocolate suspensions for SAXS and SANS were made by mixing 65% w/w sucrose in the triglyceride oil with total surfactant concentration of 0.8% w/w while varying the ratio of lecithin to PGPR. Three contrasts were obtained by using h-oil, sm-oil and d-oil. The sucrose match GTO (sm-GTO) was prepared by mixing 21.6% v/v d-GTO with 78.4% h-GTO to obtain the scattering length density of sucrose, i.e. 1.72×10^{-06} Å^{-2}. The triglyceride mixture was sonicated and shaken well before use to stop the d-oil from sedimenting. Sucrose matched TO-TP (sm-TOTP) blend was prepared by mixing 23.7% v/v d-TP with 76.3% h-TO and the mixture was heated to 80°C. To minimise the amount of d-oil used, the total weight of these suspensions was kept at 800 mg. The required amount of lecithin (or Lec_{POPC}) and PGPR were first dispersed in the triglyceride oil by vortex mixing followed by sonicating for 10 mins. Sucrose (65% w/w) was added to this solution and the suspension was mixed using a vortex mixer followed by IKA mixer at ∼10000 rpm using the IKA T10 basic mixer for 2 mins till a smooth paste is obtained. Suspensions in sm-TOTP and d-TP were prepared at 80°C by keeping the vial in a water bath at the required temperature for the entirety of the sample preparation procedure.

4.3.4 Experimental Details

The SANS experiments detailed in this chapter used SANS2D at ISIS, Oxford, UK (experiment numbers RB1610283 and RB1710424) and D33 at ILL, Grenoble, France (experiment number 9-12-402). On D33 measurements were made using a neutron wavelength of 4.5 Å with sample-detector distance of 1.2 m and 2.0 m giving a q-range of 0.006 Å$^{-1} < q <$ 0.55 Å^{-1}. On SANS2D the neutron wavelength was $2 - 14$ Å, using front and rear detector settings of 5 m and 12 m respectively,

a q-range of 0.001 $\text{Å}^{-1} < q < 0.4$ Å^{-1} was obtained. The SAXS experiments were done on the XENOCS Nano-inXider SAXS/WAXS system which uses a Cu K-α source with wavelength 1.54 Å giving q-range of 0.003 $\text{Å}^{-1} < q < 0.4$ Å^{-1}. Using this q-range interfacial structures of 1-100 nm can be investigated.

The cell used for these suspensions were the demountable Durham rack type cells, shown in Figure 4.2. These comprise quartz windows (denoted by D in the figure) between which these paste like samples can be sandwiched using a spacer usually made out of PTFE (B). These are then placed in the Aluminium cell holder (A) and sealed and locked using the Brass ring (C). The thickness of the quartz windows was 1.5 mm on SANS2D and 2 mm on D33 and the PTFE spacer was 1.1 mm thick in both cases with inner diameter 10 mm on D33 and 13 mm on SANS2D, allowing 5 mm diameter beam to be used on D33 and 8 mm diameter beam on SANS2D. These are then placed vertically onto the beam-line and held in place with a screw. The actual dimensions of the cell and spacer do not matter as these are taken into account when reducing the data, they only affect the counting time due to the beam size that can be used and hence the effective volume of the scattering sample.

The x-ray sample cell is similar except the cell body is made of steel and has an insert in which to put the sample, the quartz windows are replaced with Kapton windows and the sealing is provided using o-rings with a PEEK cell holder. Scattering from the empty cell is subtracted from both the SANS and SAXS data so as to obtain scattering from the sample only.

4.3.5 SANS and SAXS from Sucrose in GTO Suspensions with Lecithin and PGPR

Small Angle X-Ray and Neutron Scattering were carried out on sucrose suspensions containing lecithin and PGPR in h-GTO (for SAXS) and sm-GTO and d-GTO (for SANS) as shown in the left hand panel of Figures 4.3, 4.4 and 4.5.

The sm-SANS, shown in Figure 4.3, gives information about the nature of the surfactant interfacial films, even though it cannot easily give the adsorbed amount. The scattering in the sucrose matched contrast comes from the sucrose/surfactant film interface and the surfactant film/oil interface. The low q region shows a power law dependence with the exponent changing from -3 for lecithin only suspensions to -4.4 for PGPR only suspensions with the binary

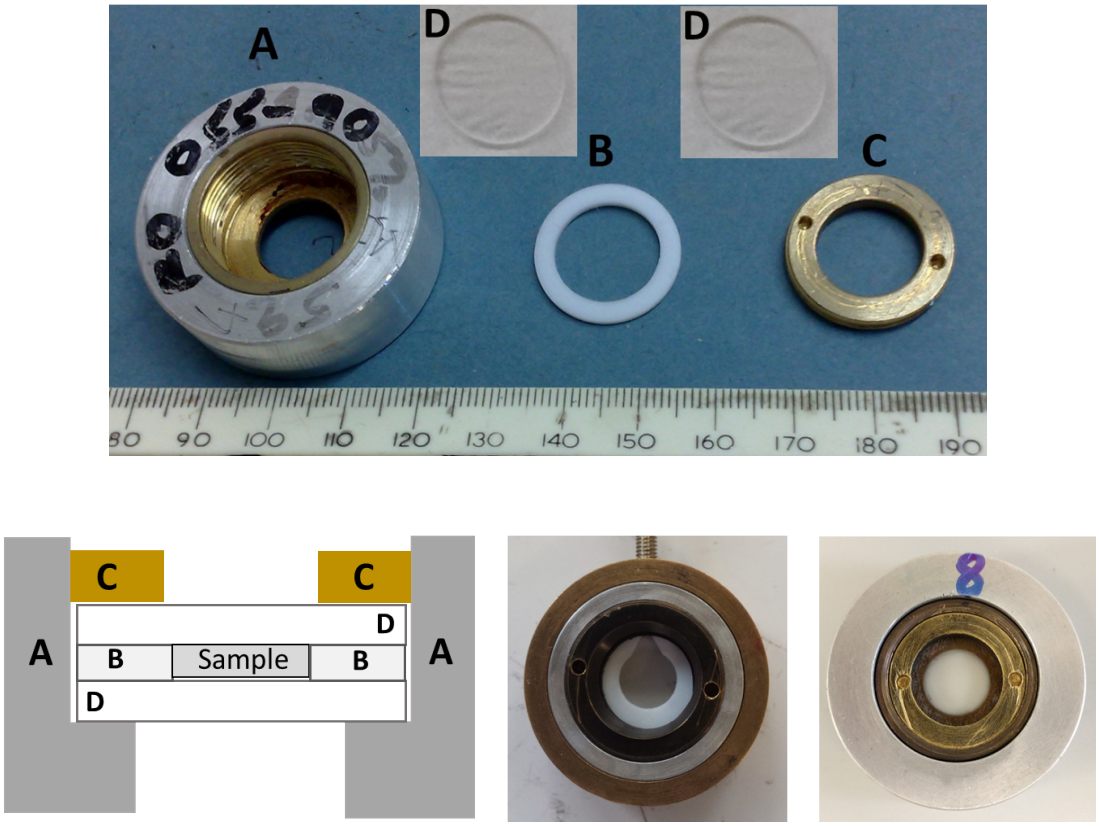

Figure 4.2 *The demountable Durham rack type cells for SANS from dense suspensions. Top panel: Picture showing various components of the ISIS Durham rack cell: A is the Aluminium cell holder, B is the PTFE spacer, C is the Brass ring for sealing the cell and D are the quartz windows. Bottom left: Schematic showing assembly of the cell. Bottom middle: Empty cell on D33. Bottom right: Cell loaded with the pastes on SANS2D.*

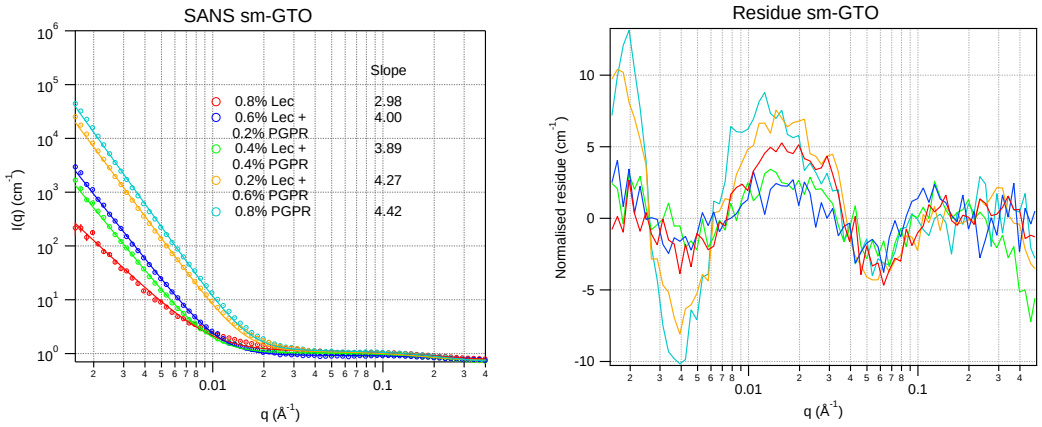

Figure 4.3 *SANS from 65% w/w sucrose in sm-GTO suspensions with varying lecithin to PGPR ratios with total surfactant concentration at 0.8% w/w. Left panel: SANS data from the suspensions. Right panel: Residue upon subtracting the low q power law scattering.*

mixtures giving intermediate values for the exponent. The error in the exponent is <1%. The value of exponent gives important information about whether the scattering interface and hence the surfactant film is disordered, fractal, diffuse or porous [78]. An exponent of -3 suggests that lecithin decorated sucrose grains form a fractal interface. The addition of PGPR makes the interface smoother as indicated by the change of exponent from -3 to -4 for suspensions with 0.6% Lec + 0.2% PGPR and 0.4% Lec + 0.4% PGPR, possibly by the incorporation of the oil solvated PGPR in the lecithin layer. Upon further increasing the PGPR fraction exponents with values < -4 are obtained for 0.2% Lec+ 0.6% PGPR and 0.8% PGPR suspensions, suggesting an extended diffuse interface, expected from a swollen polymer brush-like layer. The high q region for sm-SANS shows some characteristic scattering independent of the composition of the suspensions. When fitted this gives a radius of gyration of 8 Å, corresponding to discs of radius 11 Å, consistent with the SANS observed from sucrose matched and d50 GTO discussed in Section 3.5.1. This matches nicely to the size of the GTO molecule and this can be attributed to scattering from the minority d-GTO molecules dispersed within the h-GTO molecules which is used to create an oil that on average has a SLD that is sucrose-matched.

SAXS from sucrose suspensions in h-GTO, shown in Figure 4.5, and SANS from suspensions in d-GTO, shown in Figure 4.4, can be used to extract information about the interfacial surfactant layer. As expected from the schematic in Figure 4.1 and Babinet's principle, the SAXS and d-SANS gives complementary

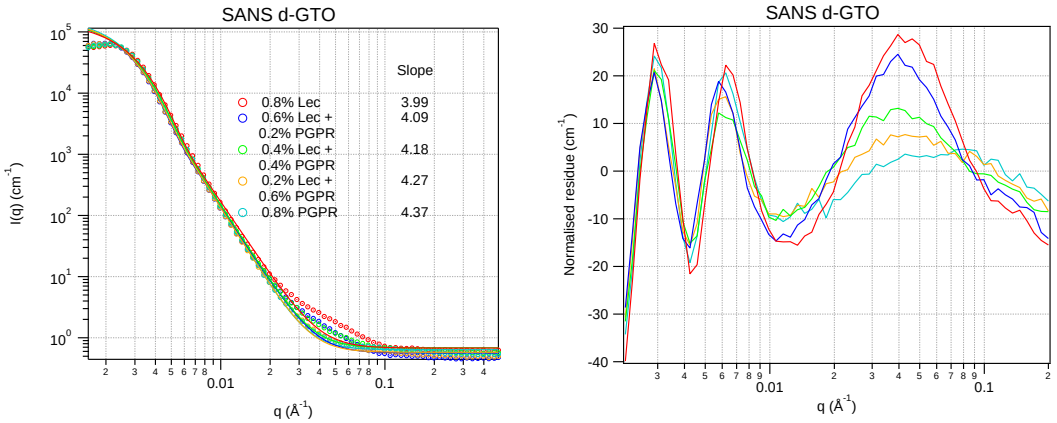

Figure 4.4 *SANS from 65% w/w sucrose in d-GTO suspensions with varying lecithin to PGPR ratios with total surfactant concentration at 0.8% w/w. Left panel: SANS data from the suspensions. Right panel: Residue upon subtracting the low q power law scattering.*

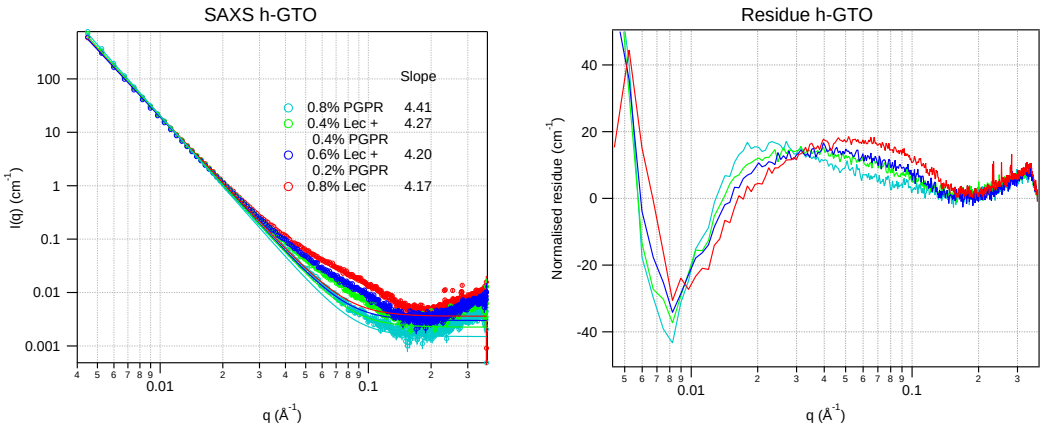

Figure 4.5 *SAXS from 65% w/w sucrose in h-GTO suspensions with varying lecithin to PGPR ratios with total surfactant concentration at 0.8% w/w. Left panel: SAXS data from the suspensions. Right panel: Residue upon subtracting the low q power law scattering.*

information. The low q region, $q < 0.02$ Å^{-1}, in both is dominated by the sucrose/oil scattering and exhibits a power law scattering with an exponent of $\sim$-4. A shoulder is observed due to the scattering from the interfacial surfactant films at $q \approx 0.1$ Å^{-1} before hitting the background at high q.

As a first step the power law scattering from the sucrose/oil interface was subtracted and the residue was plotted as shown in the right hand panel of Figures 4.4 and 4.5. This residual scattering in the low q region doesn't show any systematic trend suggesting that for a power law subtraction is a valid model for scattering for $q < 0.02$ Å^{-1}. The scattering in the region 0.02 Å$^{-1} < q < 0.2$ Å^{-1} arises from the interfacial films and as shown in the right hand panel of Figure 4.4 and 4.5 exhibits a systematic trend dependant on the surfactant mixture. The high lecithin fraction suspensions (0.8% lecithin and 0.6% lecithin +0.2% PGPR) show a distinct shoulder associated with the interfacial films. As the PGPR fraction in the total surfactant is increased, the shoulder becomes less distinct due to the extended and diffuse nature of the interfacial films for the cases when more PGPR is present. The shoulder or the peak in the residue also moves inwards as the PGPR fraction in the total surfactant in increased, suggesting that the interfacial layer is becoming thicker. This trend is clearly visible for 0.8% Lec, 0.6% Lec + 0.2% PGPR and 0.4% Lec and 0.4% PGPR in the right panel of Figure 4.4 and 4.5. Arguably this is the case for 0.2% Lec + 0.6% PGPR but this cannot be established from this analysis as the shoulder in the scattering or the peak in the residues are not clearly visible in high PGPR fraction suspensions. This qualitative analysis suggests that the scattering from these complex suspensions can be written as:

$$I(q) = Aq^{-p} + B\tilde{I}(q) + Bkg \tag{4.7}$$

The first term gives the power law scattering observed at low q from the sucrose/triglyceride oil interface. The second term represents the scattering from the interfacial surfactant films exhibited as a shoulder in the region 0.02 Å$^{-1} < q < 0.2$ Å^{-1} and can be fitted to a Guinier model with a power law tail to obtain a radius of gyration for the adsorbed surfactant films. The last term accounts for the background scattering. In order to treat the data consistently such that the radius of gyration of these interfacial films can be obtained, a two level Beaucage model was used as described in Section 4.3.2 and an exemplar fit is shown in Figure 4.6. The first level corresponds to the scattering from the

adsorbed surfactant layer, the lowest level structure in the suspensions. For this all 4 parameters, G, B, R_g and P, were allowed to vary and fitted over the q-range $0.04 - 0.15$ Å^{-1}. The second level corresponds to the scattering from the sucrose/oil interface. For d-GTO a radius of gyration along with a power law tail is observed for the low q region as well. In this case all 4 parameters were used to fit the $q < 0.02$ Å^{-1} region. In SAXS a power law decay is observed at low q. By fixing G and R_G at 0 and 10^{10}, respectively, the first term in Equation 4.6 vanishes and for the second level in the case of SAXS B and P are fitted for the $q < 0.02$ Å^{-1} region to obtain the power law scattering. The data sets and the individual fits are detailed in Appendix B. The values obtained are summarised in Table 4.1

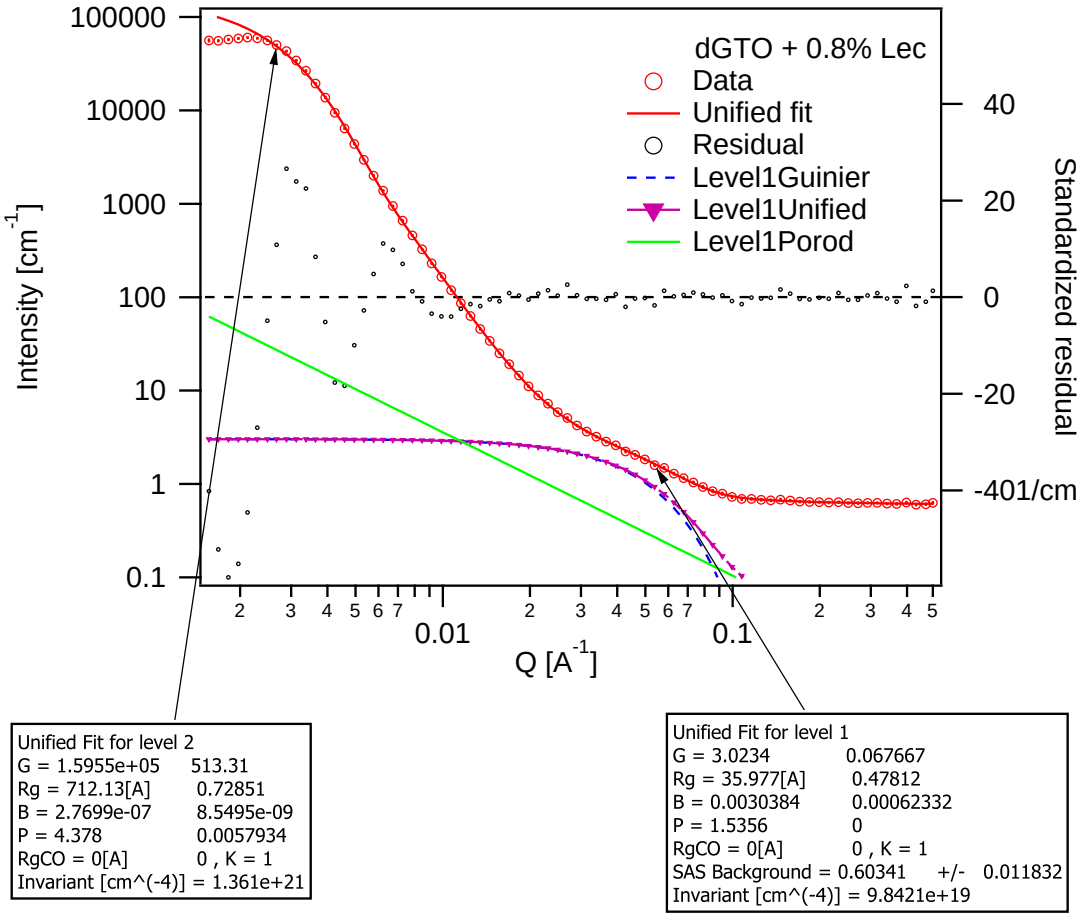

Figure 4.6 *Beaucage fit to 65% w/w sucrose suspensions in GTO with 0.8% lecithin showing a 2 level fit. Level 1 corresponds to the adsorbed surfactant layer and level 2 gives scattering from the sucrose/oil interface.*

As can be seen from the Table 4.1, the radius of gyration of the interfacial

Table 4.1 *Paramaters obtained from Beaucage Analysis for SAS from sucrose suspensions in GTO.*

Sample		d-GTO SANS				h-GTO SAXS			
Lec	PGPR	G	R_g	B	P	G	R_g	B	P
		Level1: Interfacial surfactant films							
			Å				Å	$\times 10^{-05}$	
0.8	0.0	3.0	36	0.0030	1.53	0.112	36	2.35	2.88
0.6	0.2	2.5	42	0.0026	1.60	0.095	45	5.38	2.16
0.4	0.4	2.0	51	0.0059	1.50	0.172	55	7.17	2.01
0.2	0.6	2.3	76	0.0032	1.52	-	-	-	-
0.0	0.8	-	-	-	-	-	-	-	-
		Level2: Sucrose/triglyceride oil interface							
		$\times 10^{05}$	Å	$\times 10^{-07}$			Å	$\times 10^{-08}$	
0.8	0.0	1.61	712	2.77	4.38	0	1E10	10.61	4.17
0.6	0.2	1.81	773	2.37	4.37	0	1E10	7.73	4.20
0.4	0.4	1.72	738	2.24	4.40	0	1E10	7.70	4.27
0.2	0.6	1.82	770	1.85	4.42	0	1E10	-	-
0.0	0.8	1.83	752	2.61	4.37	0	1E10	6.31	4.41

The errors don't change substantially between sample and for R_g are $\pm 1 - 5\%$, for G and P $\pm 1\%$ and for B $\pm 5 - 10\%$. The exact values are quoted along with the fits in Appendix B.

surfactant films (Level 1) increases from 36 Å to 76 Å as the PGPR fraction of the total surfactant mixture increases from 0 to 0.75. Assuming a thin film, this can be converted into thickness for dense layers with 100% surfactant volume fraction, L, using $R_g^2 = L^2/12$. This gives the thickness of adsorbed lecithin layers as 120 ± 5 Å, corresponding to 5 phospholipid monolayers. For 0.6% Lec + 0.2% PGPR the thickness is 150 ± 5 Å, for 0.4% Lec + 0.4% PGPR it is 200 ± 20 Å and for 0.2% Lec + 0.6% PGPR 260 ± 5 Å. The change of the power law exponent in the case of SAXS from -2.88 for lecithin only suspensions to -2.01 for 1:1 lecithin to PGPR suspensions suggests a change from a fractal system (power law $\sim$3) to a system comprising a swollen branched polymer statistics (power law $\sim$2).

4.3.6 SANS and SAXS from Sucrose in TO Suspensions with Lecithin and PGPR

Small Angle X-Ray and Neutron Scattering were carried out on sucrose suspensions containing lecithin and PGPR in h-TO (for SAXS) and sm-TOTP and d-TP (for SANS) as shown in the left hand panel of Figures 4.7, 4.8 and 4.9.

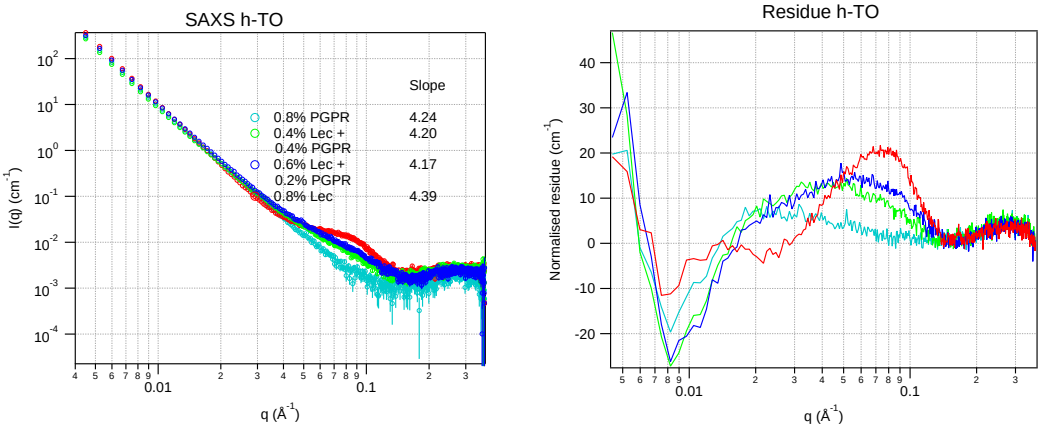

Figure 4.7 *SAXS from 65% w/w sucrose in h-TO suspensions with varying lecithin to PGPR ratios with total surfactant concentration at 0.8% w/w. Left panel: SAXS data from the suspensions. Right panel: Residue upon subtracting the low q power law scattering.*

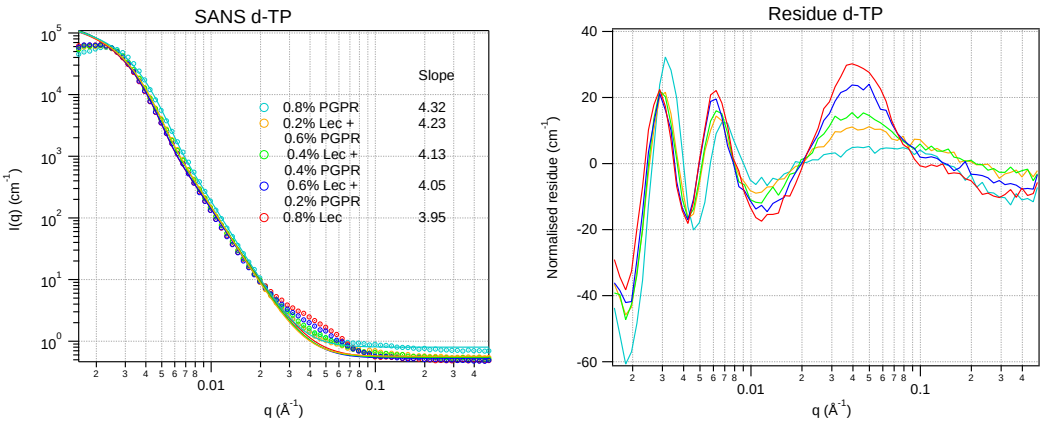

Figure 4.8 *SANS from 65% w/w sucrose in d-TP suspensions with varying lecithin to PGPR ratios with total surfactant concentration at 0.8% w/w. Left panel: SANS data from the suspensions. Right panel: Residue upon subtracting the low q power law scattering.*

The SAXS and the d-SANS for the long chain triglyceride TO and TP, Figure 4.7 and 4.8, show similar trends to those observed with the medium chain GTO.

Guinier and power law analysis was performed using the Beaucage model and the parameters are summarised in Table 4.2. The fits to the various data sets are given in Appendix B

Table 4.2 *Paramaters obtained from Beaucage Analysis for SAS from sucrose suspensions in TO.*

Sample		d-TP SANS				h-TO SAXS			
Lec	PGPR	G	R_g	B	P	G	R_g	B	P
		Level1: Interfacial surfactant films							
			Å				Å	$\times 10^{-05}$	
0.8	0.0	4.5	42	0.0033	1.54	0.071	22	1.68	3.00
0.6	0.2	3.6	44	0.0021	1.8	0.109	35	0.94	3.00
0.4	0.4	13.3	87	0.0010	2.17	0.265	52	3.20	2.29
0.2	0.6	14.2	94	0.0010	2.09	-	-	-	-
0.0	0.8	11.5	88	0.0061	1.42	-	-	-	-
		Level2: Sucrose/triglyceride oil interface							
		$\times 10^{05}$	Å	$\times 10^{-07}$			Å	$\times 10^{-08}$	
0.8	0.0	1.92	775	0.21	4.41	0	1E10	3.8	4.42
0.6	0.2	1.80	756	0.31	4.32	0	1E10	7.2	4.21
0.4	0.4	1.71	733	0.76	4.18	0	1E10	7.5	4.16
0.2	0.6	1.55	715	12.5	4.09	0	1E10	-	-
0.0	0.8	1.49	664	16.7	4.07	0	1E10	3.1	4.24

The errors don't change substantially between sample and for R_g are $\pm 1 - 5\%$, for G and P $\pm 1\%$ and for B $\pm 5 - 10\%$. The exact values are quoted along with the fits in Appendix B.

The radius of gyration of the interfacial films (Level 1) increases with the increase in the PGPR fraction of the total surfactant mixture, as is the case for suspensions in GTO. The exact values are different, which could reflect a difference in the degree of oil incorporation and/or swelling of the surfactant layers. The radius of gyration obtained from d-SANS in d-TP are larger than that obtained from SAXS in h-TO at the same lecithin:PGPR ratio. This can arise from a difference in the solvation of the layers in the two oils or from the fact that SANS measurements for d-TP were made at 80°C at which the swelling of the layers will be larger. For d-TP the thickness of the interfacial films is 145 ± 3 Å for lecithin only films, 152 ± 3 Å for 0.6% Lec + 0.2% PGPR films, 300 ± 10 Å for 0.4% Lec + 0.4% PGPR films, 325 ± 10 Å for 0.2% Lec + 0.6% PGPR films and 305 ± 10 Å for 0.8%

PGPR films. The film thicknesses obtained from SAXS for h-TO are smaller but the trend upon increasing the PGPR fraction is the same: 76 ± 3 Å for lecithin only films, 121 ± 3 Å for 0.6% Lec + 0.2% PGPR films and 186 ± 10 Å for 0.4% Lec + 0.4% PGPR films. Similar to the suspensions in GTO, as the PGPR fraction of the surfactant mixture is increased the power law exponent becomes closer to -2 indicating that the layers transition from a fractal interface to swollen branched polymer configuration.

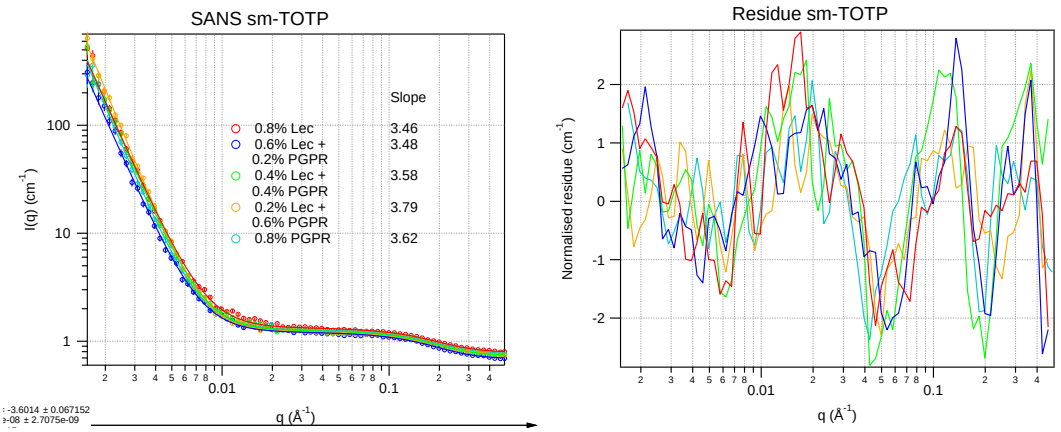

Figure 4.9 *SANS from 65% w/w sucrose in sm-TOTP suspensions with varying lecithin to PGPR ratios with total surfactant concentration at 0.8% w/w. Left panel: SANS data from the suspensions. Right panel: Residue upon subtracting the low q power law scattering.*

SANS from suspensions in sm-TOTP, Figure 4.9, gives less clear trends regarding the nature of the interfacial structures as compared to the SANS from the suspensions in sm-GTO. The exponent changes from -3.46 to -3.79 ($\pm 1\%$) as the surfactant composition in the suspensions is changed from lecithin only to 25:75 lecithin:PGPR. The exponent decreases to -3.62 for suspensions with PGPR only. This supports the hypothesis that lecithin forms fractal interfacial structures. The structures in TOTP suspensions possibly have more oil incorporated into them as compared to the structures in GTO suspensions, leading to an exponent of -3.46 instead of -3 as observed for GTO suspensions. The addition of PGPR swells these interfacial structures, albeit not to the same extent as in the GTO suspensions, reflected by the change of exponent to -3.79, which corresponds to a smoother interface. PGPR on its own shows very different behaviour in TOTP as compared to GTO. The exponent of -3.62 still corresponds to a fractal interface. A possible hypothesis to explain this is that the GTO is a better solvent for PGPR than the TO/TP mixture. We know from the SANS of PGPR in TO solutions, discussed in Section 3.5.3, that TO is a good solvent for PGPR. So this indicates

that TP is not as good a solvent for PGPR as GTO. Another possibility is the PGPR forms a near interface dense surfactant like layer with a small amount of oil incorporated giving rise to a fractal scattering with slope -3.6 followed by a highly solvated layer which has no contrast against the oil. For sm-TOTP suspensions, the high q scattering can be fit to a radius of gyration of 10 Å, which corresponds to discs of radius 13 Å. This is similar to the size of a TP molecule and as is the case for GTO this can be explained as due to scattering from the d-oil molecules.

4.3.7 SANS and SAXS from Sucrose in Triglyceride Oil Suspensions with POPC and PGPR

SAXS and SANS measurements were also made for sucrose in triglyceride oil suspensions with the lecithin replaced by Lec_{POPC}, a mixture of 50% POPC and 50% triglyceride oil. The rheology of these suspensions is discussed in Section 2.4.2. The scattering observed from these suspensions shows similar trends to those observed from the suspensions with lecithin and PGPR suspensions and is consistent with their rheology.

SANS from sucrose in sm-triglyceride oil suspensions with Lec_{POPC} and PGPR, shown in Figure 4.10, exhibits a power law scattering at low q similar to that observed for the suspensions with lecithin and PGPR and is summarised in Table 4.3 with the results for suspensions containing lecithin and PGPR for comparison.

Table 4.3 *Exponents obtained for the power law scattering observeed from 65% sucrose in sm-triglyceride oil suspensions with Lec/*Lec_{POPC} *and PGPR.*

Surfactant Composition		sm-GTO		sm-TOTP	
Lec/Lec_{POPC}	PGPR	Lec	Lec_{POPC}	Lec	Lec_{POPC}
0.8	0.0	2.98	2.91	3.46	2.97
0.6	0.2	4.00	3.29	3.48	2.96
0.4	0.4	3.89	3.40	3.58	3.31
0.2	0.6	4.27	3.97	3.79	3.67
0.0	0.8	4.42	4.42	3.62	3.62

The error in the exponents are ±1%.

For suspensions containing Lec_{POPC} only an exponent of -3.0, characteristic of

a fractal, is again observed for in both sm-GTO and sm-TOTP. The slight difference in exponent between SANS from lecithin (-3.4) and Lec_{POPC} (-3.0) interfacial films in TOTP suspensions could arise from the fact that lecithin being a multi-component system forms less ordered structures which easily incorporate oil whereas POPC forms less solvated compact fractal layers. Upon increasing the PGPR fraction in the total surfactant mixture, the exponent decreases becoming closer to -4.0 which can be attributed to a smoother interface arising from swelling of the layer by incorporating oil solvated PGPR. A greater fraction of PGPR is required to achieve this transition than in the case of lecithin. This is possibly an indication that the single component POPC layers are more ordered than the multicomponent lecithin layers, and so more PGPR is required to disrupt them. This is consistent with the rheology where more PGPR is required in case of Lec_{POPC} + PGPR stabilised suspensions as compared to lecithin + PGPR stabilised suspensions to achieve the same reduction is yield stress.

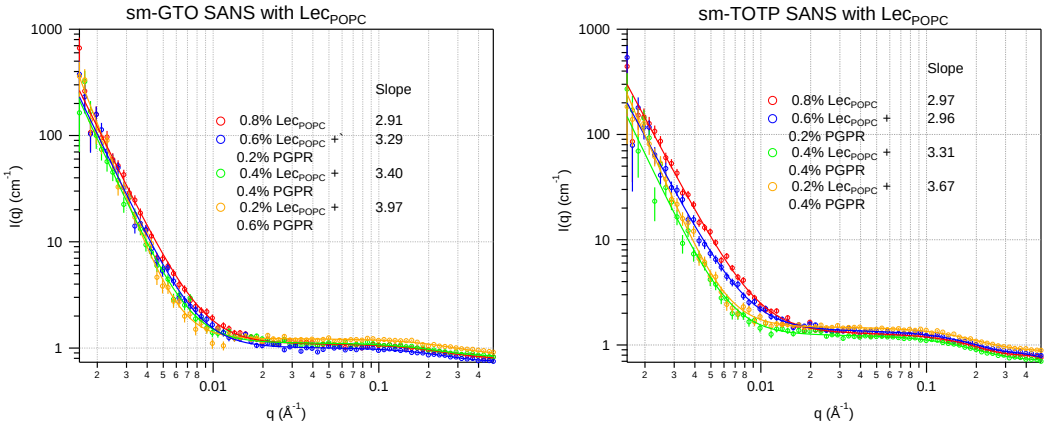

Figure 4.10 *SANS from 65% w/w sucrose suspensions in sm-triglyceride oil with varying Lec_{POPC} to PGPR ratios with total surfactant concentration at 0.8% w/w. Left panel: SANS for suspensions in sm-GTO. Right panel: SANS for suspensions in sm-TOTP.*

The radius of gyration for the Lec_{POPC}/PGPR interfacial films was found using SANS for suspensions in d-oil, Figure 4.11 and SAXS for suspensions in h-oil, Figure 4.12, using two-level Beaucage fit. The results showed similar trends as that observed for suspensions with lecithin/PGPR where addition of PGPR increases the radius of gyration of the interfacial layer. The increase in the radius of gyration can also be inferred from the peak in the residuals observed between $0.02 - 0.1\text{Å}^{-1}$ shifting to lower q upon the addition of PGPR (insets in Figure 4.11). The radius of gyration found using SANS from suspension in d-GTO increases from 38 Å to 49 Å to 68 Å to 79 Å as the PGPR fraction of the

total surfactant goes from 0 to 0.25 to 0.5 to 0.75. For suspensions in d-TP, the values for the radius of gyration at the same surfactant compositions are 46 Å, 60 Å, 69 Å and 73 Å. The values for SAXS are similar and show the same trend.

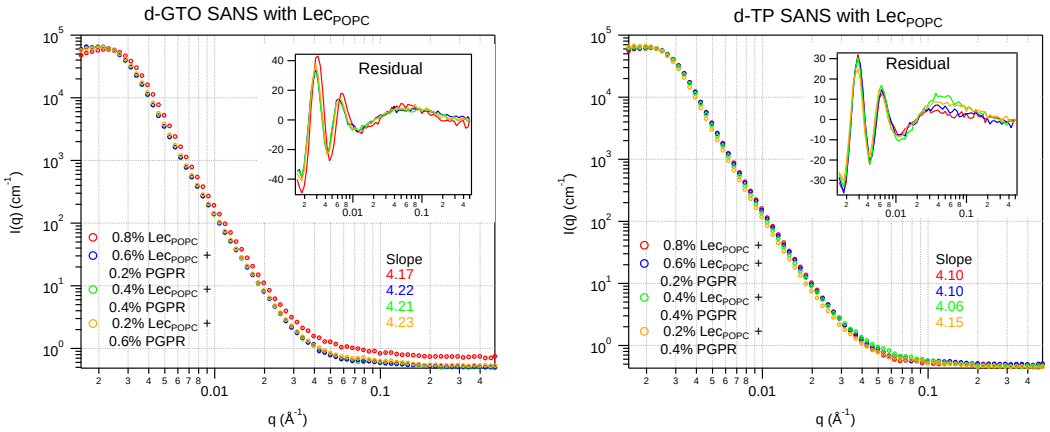

Figure 4.11 *SANS from 65% w/w sucrose suspensions in d-triglyceride oil with varying Lec$_{POPC}$ to PGPR ratios with total surfactant concentration at 0.8% w/w. Left panel: SANS for suspensions in d-GTO Right panel: SANS for suspensions in d-TP.*

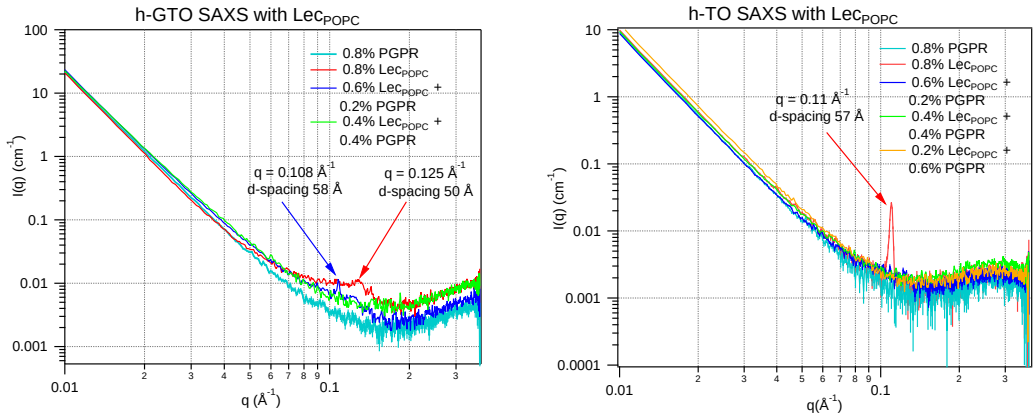

Figure 4.12 *SAXS from 65% w/w sucrose suspensions with varying Lec$_{POPC}$ to PGPR ratios with total surfactant concentration at 0.8% w/w. Left panel: SAXS for suspensions in GTO. Right panel: SAXS for suspensions in TO.*

The influence of PGPR on the ordering of the layers is more clearly visible in SAXS where a Bragg peak is observed due to the highly ordered POPC interfacial layers, as shown in Figure 4.12. Upon the addition of PGPR the Bragg peak shifts to lower q, as can be seen from the red and blue traces in the left panel of Figure 4.12. This suggests that PGPR intercalates into the POPC layers, swelling the individual layers and the entire structure becomes $2-5$ times its

original thickness depending on the PGPR fraction. At high PGPR fraction the Bragg peak vanishes, indicating that the ordered POPC layer gets disrupted by the addition of PGPR.

These studies have enabled us to determine the adsorbed layer thickness (and amount) in the rheologically relevant sucrose in triglyceride oil model chocolate suspensions. Additionally, they have allowed us to draw some inferences about the nature of the large-scale organisation of the interfacial layers from the power-law scattering and how that may affect the inter-particle interaction and thereby the rheology.

4.4 Spin Echo Small Angle Neutron Scattering from Model Chocolate Suspensions

To directly measure the effect of the interfacial surfactant films on the particle-particle correlation function we have carried out Spin Echo Small Angle Neutron Scattering (SESANS) experiments on the model chocolate suspensions with the same composition as above. Using SESANS the large scale organisation of particles can be probed on length scales that exceed the grain size in opaque samples, such as these model chocolate suspensions.

4.4.1 SESANS Technique and Data Analysis

SESANS is based on the Larmor precession of polarised neutrons in a magnetic field, which can be used to encode the transmission angle and the path length of the neutrons through the precession device. Consider a neutron beam travelling in the x-direction with the polarisation vector in the y-direction. A precession device comprises a magnetic field region of length L having magnetic field B tilted by an angle θ_0 with respect to the incoming neutron beam. Upon entering this region the two spin states of the neutrons are separated in the z-direction by the spin echo length (SEL), z, given by [79]:

$$z = \frac{c\lambda^2 LB\cot(\theta_0)}{2\pi} \tag{4.8}$$

where λ is the neutron wavelength and $c = 4.632 \times 10^{14}$ T^{-1} m^{-2} is the Larmor precession constant. Experimentally the spin echo length can be tuned by changing any of the parameters in Equation 4.8. A SESANS instrument comprises two such precession devices with opposite magnetic fields, one placed before and one after the sample, as shown in Figure 4.13.

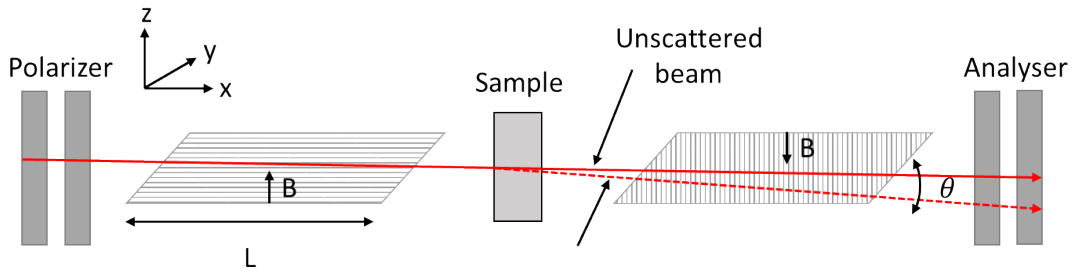

Figure 4.13 *Schematic showing the principle of Spin Echo Small Angle Neutron Scattering*

In the absence of a sample, the precession in the second device will cancel the precession of the magnetization due to the first. This results in the magnetization of the neutron beam becoming focussed again and the original polarisation vector is obtained. In the presence of a scattering sample, the scattered neutrons will have different path lengths through the second precession device and therefore the precession in the two devices will not cancel leading to depolarisation of the neutron beam. The detected polarisation of the scattered neutron, P_n, as a function of the SEL, z, is given as [80]:

$$\frac{P(z)}{P_0} = \exp[\tilde{G}(z) - \tilde{G}(0)] = \exp[\tilde{G}(0)(G_0(z) - 1)] \tag{4.9}$$

where $\tilde{G}(z)$ is the SESANS correlation function and $G_0(z) = \tilde{G}(z)/\tilde{G}(0)$ is the normalised SESANS correlation function experimentally measured in a SESANS experiment. $\tilde{G}(0)$ is the total scattering probability and is expressed in terms of the SAS total cross section (Σ_S) or the macroscopic cross section, $\Sigma = \Sigma_S/V$, as:

$$\begin{aligned} \tilde{G}(0) &= \frac{\Sigma_S}{S} = \Sigma t \\ &= \lambda^2 t(\Delta\rho)^2\phi(1-\phi)\xi \quad \text{for two phase system} \end{aligned} \tag{4.10}$$

where, S is the beam cross section, t is the thickness of the sample, ϕ is the volume fraction of one of the phases, $\Delta\rho$ is the difference in SLD for the two

phases and ξ is the correlation length.

The polarisation measures the correlation between the scattering length density integrated along the path of the neutron beam averaged over a large volume. Therefore the SESANS correlation function can be expressed in terms of the autocorrelation function of the SLD, $\gamma(r)$ as:

$$\begin{aligned}\tilde{G}(z) &= (2/\xi)\int_0^\infty \gamma(x,0,z)dx \\ &= (2/\xi)\int_0^\infty \frac{\gamma(r)r}{(r^2-z^2)^{1/2}}dr \quad \text{For an isotropic density distribution}\end{aligned} \tag{4.11}$$

The scattering intensity, $I(q)$, is related to the autocorrelation function, $\gamma(r)$, by Fourier transform and to the SESANS correlation function by the Hankel transform. This cycle is illustrated in Figure 4.14 which shows how measurements using SANS and SESANS can be related to one another.

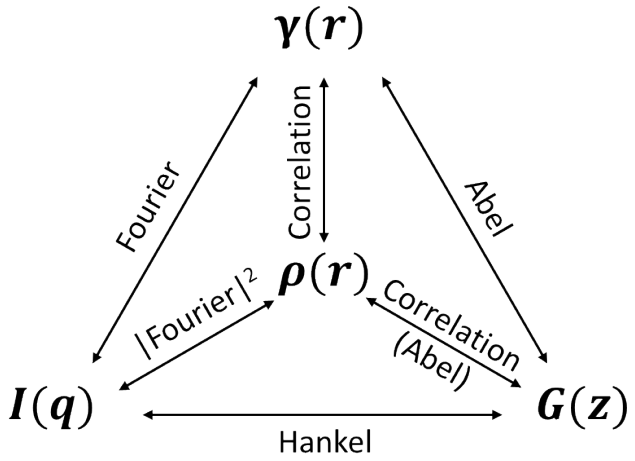

Figure 4.14 *Relationship between the autocorrelation function, $\gamma(r)$, SESANS correlation function, G(z), and the SANS intensity, I(q), for the isotropic density distribution, $\rho(r)$, reproduced from Anderson et. al. [4].*

In a SESANS experiment the polarisation decay, $P(z)/P_0$, is measured as a function of the SEL, z. Qualitative analysis of the data can be done as described in the paper by Anderson *et. al.* [4]. Dilute suspensions show exponential decaying polarisation with z. Concentrated suspensions with mono-disperse particles show a decay with a bump corresponding to the nearest neighbour distance and a fractal system shows a constantly decaying polarisation. To obtain information about

the correlation length in the system, a simple exponential model can be used to describe the SESANS correlation function as below [4, 81]:

$$G(z) = \exp\Big(-\frac{z}{\xi}\Big)^{r} \tag{4.12}$$

where r gives information about the nature of the phase boundary. Using this SESANS correlation function the log polarisation decay is gives by:

$$\log\left(\frac{P(z)}{P_0}\right) = A\left[\exp\Big(-\frac{z}{\xi}\Big)^{r} - 1\right] \tag{4.13}$$

where A is the scattering probability. By fitting this functional form to the polarisation decay measured in the SESANS experiment, the correlation length in the various samples can be compared.

4.4.2 Materials and Sample Preparation

Suspensions of sucrose, 65% w/w, in triglyceride oil with lecithin and/or PGPR were prepared at a total surfactant concentration of 0.8% w/w. The materials and sample preparation are the same as described for Small Angle Scattering experiments in Section 4.3.3. The contrasts used to formulate the suspensions for SESANS were h-GTO and h-TO, sm-GTO and 40:60 v/v mixture of h- and d-GTO, d40-GTO (instead of d-GTO used for SANS). As shown by Equation 4.10, the depolarisation in the neutron beam depends on the scattering contrast between the phases, $\Delta\rho$. For d-GTO the contrast is extremely high, $\Delta\rho = 5.0 \times 10^{-6}\text{Å}^{-2}$, so the polarisation, $P(z)/P_0$, would decay too quickly to enable structural information on the particle length scale to be extracted, as it means that the polarization remaining at the SEL of interest is too noisy. In order to decrease the rate of decay of polarisation, d40-GTO for which $\Delta\rho = 1.2\times10^{-6}\text{Å}^{-2}$ has been used.

4.4.3 Experimental Details

The SESANS experiments detailed in this chapter used LARMOR at ISIS, Oxford, UK (RB1720354). Measurements were done at two angles: 20° and 40°, allowing the full range of spin echo lengths of interest to be measured. Neutrons of wavelengths $2 - 12$ Å were used which from Equation 4.8 correspond to SELs

of $0.2 - 9.5$ μm for 40° and $0.5 - 19.5$ μm for 20°.

The sample cells used for these experiment were based on the demountable Durham rack cells detailed in Section 4.3.4 and shown in Figure 4.2. By changing the thickness of the spacers used in the cells, the decay of the polarisation could be controlled. For sm-GTO, where the polarisation decay is slow due to the low scattering volume, which arises only from the interfacial surfactant layers, spacers with thickness 2.60 ± 0.05 mm were used, made out of Brass washers stuck to the Quartz windows using double-sided sticky tape. For h-GTO ($\Delta\rho = 1.4 \times 10^{-6}$Å^{-2}), h-TO ($\Delta\rho = 1.5 \times 10^{-6}$Å^{-2}) and d40-GTO ($\Delta\rho = 1.2 \times 10^{-6}$Å^{-2}) spacers with a thickness of 0.24 ± 0.03 mm, constructed using washers made out of Kapton sheet stuck to the Quartz windows using double-sided sticky tape, were used.

4.4.4 SESANS from Sucrose in GTO Suspensions with Lecithin and PGPR

SESANS measured from sucrose suspensions in GTO for sm-GTO, h-GTO and d40-GTO are shown in Figure 4.15, 4.16 and 4.17, respectively. These measurements can provide a direct measure of the particle-particle correlation function on the length scale of upto 20 μm. The log of the depolarisation, Equation 4.13, is plotted as a function of the SEL, z and was fitted to the function given in Equation 4.12. Initially r was allowed to vary but it was found that $r = 1 \pm 0.2$ fitted all the data sets and there was no dependence of the fit on the value of r. In order to limit the number of free parameters and to be able to compare the different values of correlation lengths, r was fixed at 1.

For suspensions in sm-GTO, the scattering contrast comes from the interfacial films, and therefore the polarisation decay is extremely small. From the left panel of Figure 4.15, it is clear that the SESANS depolarisation from lecithin rich suspensions, 0.8% Lec and 0.6% Lec + 0.2% PGPR, does not reach a well-defined plateau within the instrumental window of $0 < \text{SEL} < 10$ μm. Extending the instrumental window out to SEL < 20 μm also does not result in a clear plateau. The large uncertainty associated with the fit to Equation 4.13 confirms that there is no well-defined correlation length for these lecithin rich suspensions. The continuous slow decrease of the depolarisation is instead consistent with scattering from a fractal object as would be formed by a suspensions in which the

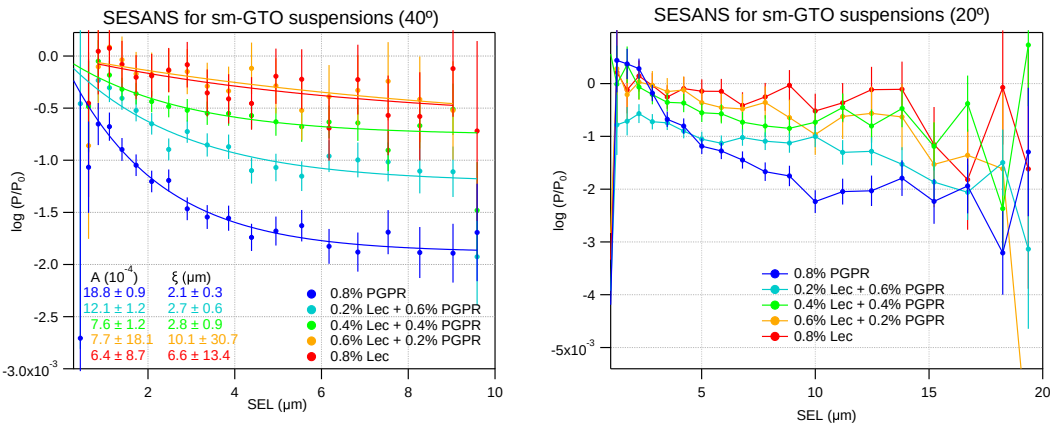

Figure 4.15 *SESANS measurements at* 40° *(left panel) and* 20° *(right panel) from 65% w/w sucrose suspensions in sm-GTO with varying lecithin to PGPR ratios with total surfactant concentration at 0.8% w/w.*

sucrose grains are in adhesive contact mediated by a lecithin film. Once the PGPR fraction is greater than 0.2%, it can be seen that the SESANS depolarisation does reach a well-defined plateau and can be fit to Equation 4.13 with a well-defined correlation length in the region $\xi = 2.1 - 2.8$ μm. As the oil is contrast-matched to the sucrose grains, to the neutrons the surfactant film will appear as a hollow shell and this correlation length is consistent with the size of the sucrose particle.

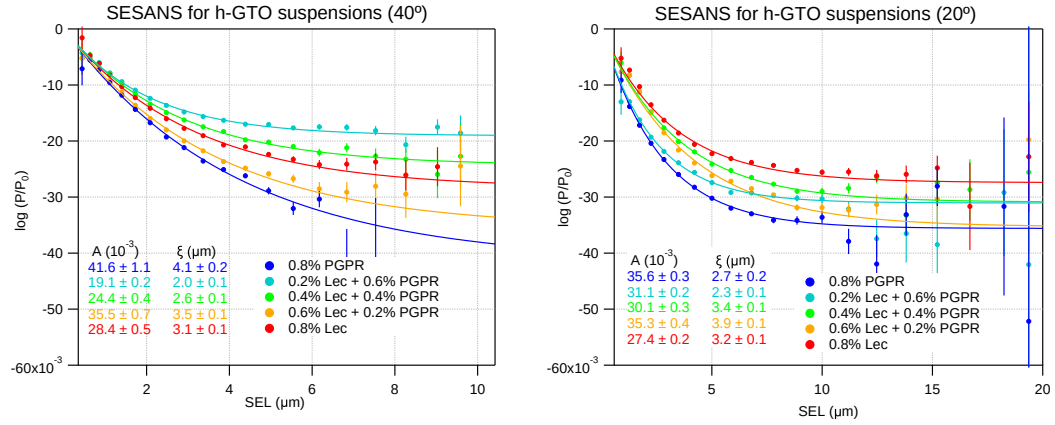

Figure 4.16 *SESANS measurements at* 40° *(left panel) and* 20° *(right panel) from 65% w/w sucrose suspensions in h-GTO with varying lecithin to PGPR ratios with total surfactant concentration at 0.8% w/w.*

By contrast in h-GTO a finite correlation length corresponding to a distinct plateau in the SESANS depolarisation is observed from all the suspensions. In this contrast the discontinuity in the SLD occurs at the surcrose interface and there is

a difference in SLD between the sucrose grains and the oil-filled spaces between the grains, which means that the correlation function for distinct particles is observed irrespective of whether or not they are in contact. The correlation length for all the suspensions was in the region $\xi = 2 - 4$ μm, consistent with the sucrose particle size. Given that the sucrose particles are irregularly shaped and polydisperse it is complex to try to read too much into the variation of correlation length determined by the fit to an expression for a simple two-phase system as described by Equation 4.13. SESANS depolarisation from suspension in d40-GTO exhibits a similar behaviour with $\xi \approx 3$ μm, as expected from Babinet's principle.

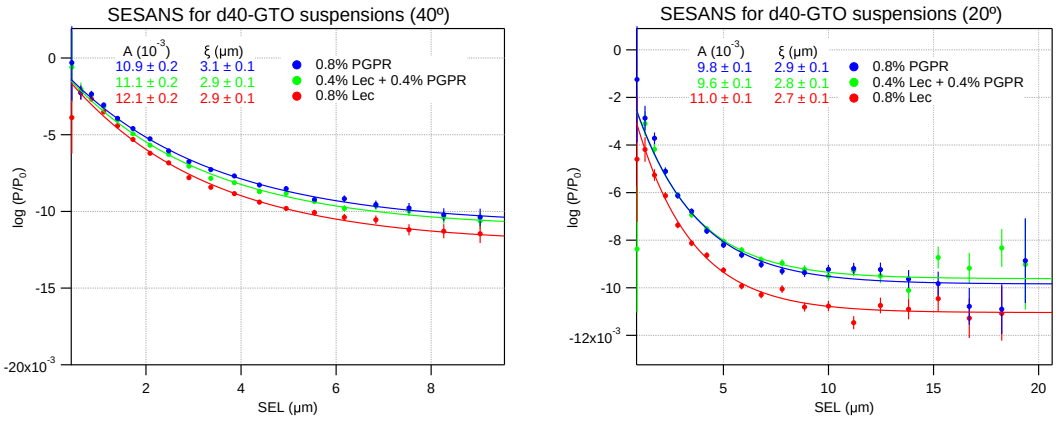

Figure 4.17 *SESANS measurements at* 40° *(left panel) and* 20° *(right panel) from 65% w/w sucrose suspensions in d40-GTO with varying lecithin to PGPR ratios with total surfactant concentration at 0.8% w/w.*

In addition to the correlation length, another feature that is observed in the SESANS depolarization is a bump due to the nearest neighbour correlation at SEL ≈ 10 μm, corresponding to the average diameter of the sucrose particles. Appearance of this second peak is a signature of a liquid-like order for a suspension as it suggests that distinct particles are observed rather than a jammed structure [4]. This bump is most clearly visible for suspension containing 0.8% PGPR in d40-GTO and h-GTO (SEL ≈ 12 μm) and 0.4% Lec + 0.4% PGPR in d40-GTO and h-GTO (SEL ≈ 11 μm), as shown in the right panels of Figures 4.16 and 4.17 This suggests that the sucrose particles in the suspensions containing high PGPR fraction are fully separated but sufficiently closely spaced resulting in liquid-like ordering.

4.4.5 SESANS from Sucrose in TO Suspensions with Lecithin and PGPR

SESANS was measured from sucrose suspensions in h-TO only and are shown in Figure 4.18. The qualitative behaviour is similar to the h-GTO suspensions, where once again well-defined plateaus are observed corresponding to a finite length of $\xi = 3 - 4$ μm. The SESANS depolarisation and correlation lengths are more tightly grouped for the suspensions in TO than in GTO and the particle-particle correlation appears to be less influenced by the surfactant composition. This behaviour is similar to the power-law decay observed in the SANS data from sm-TOTP suspensions, shown in Figure 4.9 and discussed in Section 4.3.6. This can be attributed to TO being a better solvent for lecithin and PGPR, so the lecithin films are more solvated in the first place and therefore are less affected by lecithin to PGPR ratio.

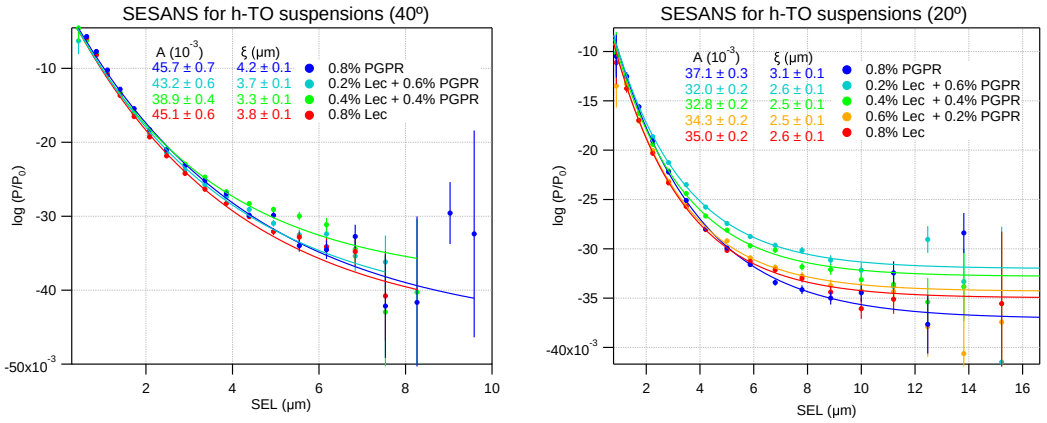

Figure 4.18 *SESANS measurements at* 40° *(left panel) and* 20° *(right panel) from 65% w/w sucrose suspensions in h-TO with varying lecithin to PGPR ratios with total surfactant concentration at 0.8% w/w.*

The suspensions with 0.4% Lec + 0.4% PGPR and 0.2% Lec + 0.6% PGPR reach a plateau the quickest, suggesting they have a smoother interface i.e. more distinct phase boundaries. Also the nearest neighbour bump is observed for suspensions containing 0.4% Lec + 0.4% PGPR and 0.2% Lec + 0.6% PGPR at SEL $\approx$ 8 μm), as shown in the right panel of Figure 4.18. This suggests that in these suspensions the sucrose grains are fully separated and all positional constraints are released. This would be consistent with the absence of a yield stress and easiest flow of the suspension.

4.5 Conclusions

Adsorption and structural investigations on the rheologically relevant model chocolate suspensions, 65% w/w sucrose in a medium chain triglyceride oil, GTO, and long chain triglyceride, TO and TP, were carried out using SAXS, SANS and SESANS. The SANS and SAXS studies establish the radius of gyration or second moment of distribution, of the interfacial films for different surfactant compositions and provide information about the nature of these films. The main results from these studies can be summarised as:

- Phospholipids form compact layers with a radius of gyration between $30 - 40$ Å, corresponding to 5 monolayers. The radius of gyration increases by a factor of $2 - 4$ as the PGPR fraction of the total surfactant mixture is increased from 0 to 0.75 for suspensions in both medium and long chain triglyceride oil. This indicates that the incorporation of the oil-solvated PGPR swells the interfacial layer.

- Replacing lecithin with a 50:50 mixture of POPC and triglyceride oil (minimal model chocolate suspensions) gives similar adsorbed amount in the interfacial films. The POPC layers are more ordered as indicated by the observation of clear Bragg peaks.The Bragg features observed shift to lower q upon the addition of PGPR, suggesting that the individual phospholipid layers swell upon adding PGPR and total thickness of the interfacial films increases.

These changes in the interfacial surfactant films structure modifies the inter-particle correlation function between sucrose grains measured directly using SESANS. This also modifies the power law scattering observed in SANS and can be used to explain the changes in the rheology of molten chocolate suspensions with surfactant composition. For the lecithin (or $\mathrm{Lec_{POPC}}$) cases, the sucrose grains are in contact due to the adhesive interaction between the lecithin layers. This results in the surfactant film tracing out a fractal structure as observed in SESANS and a power law exponent of -3 in SANS at low q. The positional constraints on the sucrose grains means that a yield stress must be reached for the suspension to flow. Once flowing, the high stress viscosity is determined by the shearing of the phospholipid layers between the sucrose grains. Increasing the PGPR fraction causes an increase in the separation of the phospholipid layers

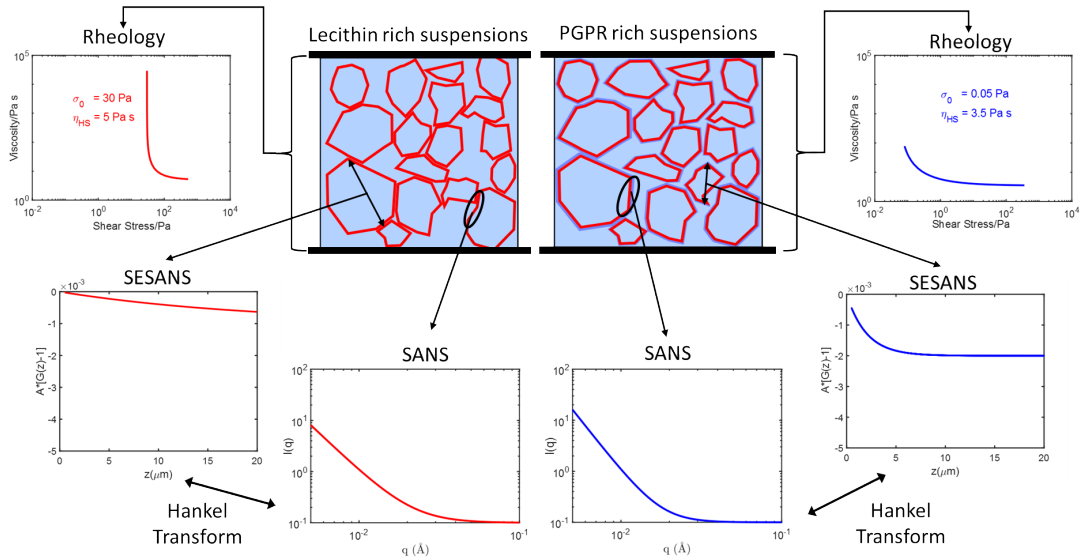

Figure 4.19 *Summary of rheology and interfacial structural measurements done for lecithin/PGPR in sucrose in triglyceride oil suspensions.*

that make up the interfacial surfactant layer due to the incorporation of the the oil-solvated PGPR. This leads to repulsion between the sucrose grains and pushes them apart. This separation of the sucrose grains has a number of effects: the interfacial films now trace out the separate particles rather than a connected fractal structure, this gives rise to a finite correlation length in SESANS, which is comparable to the particle dimension ($\xi \sim 3$ μm), a second bump is observed in the SESANS polarisation decay indicating liquid-like ordering and a change in the exponent of the power law scattering is observed in SANS from -3 (characteristic of a fractal) to -4 (typical of separate diffuse interfaces). Moving the particles out of contact removes the positional constraints, allowing the suspensions to flow without a yield stress. The behaviour described above is illustrated schematically in Figure 4.19.

Using these studies the adsorbed amount and the nature of surfactant films in these sucrose/triglyceride oil suspensions has been established. Using this a mechanism is hypothesised based on the structure of the interfacial surfactant films to explain the effect of lecithin and PGPR on rheology of molten chocolate. Multiple scattering from these high-volume fraction suspensions mean that the detailed volume fraction of these interfacial films cannot be obtained as can be achieved for dilute colloidal suspensions. To further investigate the detailed interfacial layer structure I zoom in at a single interface by developing an analogous planar model system discussed in Chapter 5-7.

Chapter 5

Planar Sucrose Substrates as Model Chocolate Interfaces

5.1 Introduction

As discussed in Chapter 4, Small Angle Scattering provides adsorbed amounts and dry thickness for the interfacial surfactant films for sucrose in triglyceride oil suspensions. The high solid volume fraction of these samples mean that due to the effects of multiple scattering and averaging of the isotropic scattering, the details of the interfacial volume fraction profiles cannot be extracted as is the case with dilute colloidal suspensions. Conceptually, this can be overcome by zooming in at a single, well-defined sucrose-triglyceride interface which can then be used to carry out adsorption studies, using contact angle tensiometry and Quartz Crystal Microbalance with Dissipation monitoring (QCM-D), and detailed structural investigations, using neutron and x-ray reflectivity. The grazing angles of incidence in these reflectivity studies requires sucrose substrates that are several square centimetres, flat and atomically smooth. For this work, these substrates were developed by spin-coating sucrose from aqueous solutions onto silicon blocks or wafers.

These spin-coated sucrose substrates are then used to carry out interfacial investigations of the phospholipid surfactant, lecithin, and polymeric surfactant, PGPR, at the sucrose/triglyceride oil interface using contact angle tensiometry and QCM-D. Contact angle tensiometry provides rapid access to the interfacial

activity of these surfactants and QCM-D studies provide information about the adsorbed amount of the surfactant and additionally some information about the distribution of this adsorbed material via the dissipation monitoring. Further these planar substrates can be used in flow cells for measuring specular reflectivity (Neutron and X-ray) to get structural details of the interfacial surfactant layer, discussed in Chapter 6 and 7.

In this chapter the preparation and characterisation of these planar spin-coated sucrose substrates is first discussed in Section 5.2. Thin films of sucrose with thicknesses ranging from 10 nm to 2 μm have been prepared by spin-coating onto silicon substrates, with the thicknesses measured using X-ray Reflectivity (thin films, thickness <250 nm) and QCM-D (thick films, thickness >250 nm). The crystallinity of these thin sucrose films is determined using Grazing Incidence X-Ray Diffraction. Having produced these well-defined sucrose films, interfacial activity of lecithin and PGPR at the sucrose/triglyceride interface is measured using contact angle tensiometry, discussed in Section 5.3, and interfacial adsorption studies of lecithin and PGPR from triglyceride oil, Glyceryl Trioctanoate (GTO) and Glyceryl Trioleate (TO), are carried out using QCM-D, discussed in Section 5.4. A comparison is then drawn between the adsorbed amount of surfactants at the sucrose interfaces in suspensions measured using small angle scattering and at the planar sucrose interfaces measured using QCM-D to present a possible model for the surfactant structures that can explain how they influence the rheology of molten chocolate in Section 5.5. In Chapter 6 and 7, the details of this model are investigated with reflectivity techniques.

5.2 Planar Sucrose Substrates

Uniform sucrose films of thickness ranging from few nm to few μm, for adsorption and structural studies, can be produced by spin-coating onto planar substrates [82]. In addition to the thickness and smoothness, the planar sucrose should ideally be crystalline with the (100) surface exposed as this is the predominant exposed habit of the sucrose grains used in formulating chocolate [36].

5.2.1 Preparation of Sucrose Thin Films

Spin-Coating

Spin-coating is a commonly applied technique to produce thin films onto flat substrates [83]. The advantage of spin-coating is its ability to quickly and easily produce very uniform films, ranging from a few nanometres to a few microns in thickness. A schematic depicting the various stages of this process is shown in Figure 5.1. A small amount of solution containing the material to be spin-coated is spread in the centre of the substrate which is stationary or spinning at a low speed, usually around $\sim$ 100 rpm (Step 1). The substrate is then rotated at a higher speed usually of the order of 1000 rpm and the material to be spin-coated is spread evenly under the effect of the centrifugal force (Step 2). Airflow dries the majority of the solvent, leaving a thin uniform film (Step 3) and finally the remainder of the solvent is evaporated by heating or under vacuum or both (Step 4). In order to obtain a thin uniform spin-coated film, the solvent should wet the substrate completely.

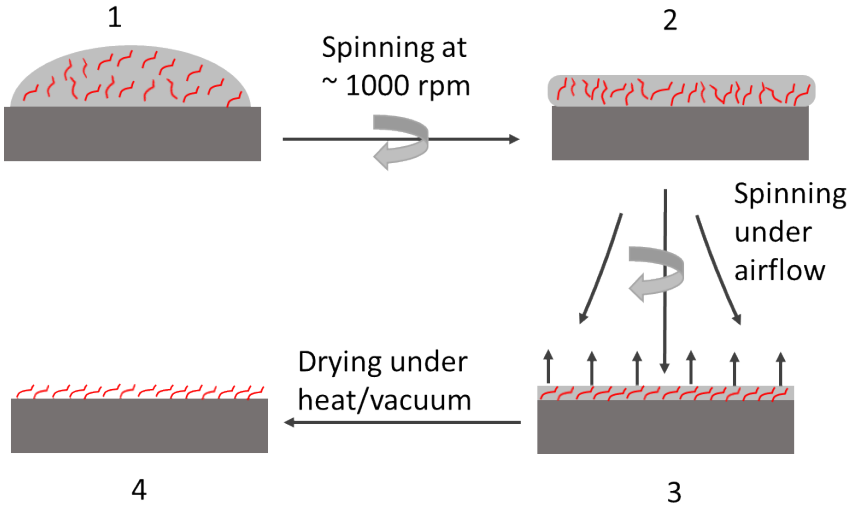

Figure 5.1 *Schematic depicting the various steps in the spin-coating process.*

The thickness of the film, t, depends on the spin speed ω ($t \propto 1/\sqrt{\omega}$), the concentration of the material in the solution, the evaporation rate and the viscosity of the solvent. These factors can change between different spin-coating runs and therefore the thickness should be measured every time before use.

Spin-Coating of Sucrose Films onto Silicon Substrates

Using the approach described in Section 5.2.1 sucrose films of thickness ranging from 10 nm to 1.8 μm were spin-coated onto silicon substrates from millimolar aqueous solutions of sucrose. The silicon substrates used for spin-coating were either 55 mm diameter blocks (thickness 5 mm) or 1" diameter wafers sourced from PI-KEM Ltd. These were cleaned first using piranha solution, a 5:4:1 mixture of water, concentrated sulphuric acid and 30% hydrogen peroxide, and then u-v ozone for $30 - 50$ mins or oxygen plasma for 1 min. The u-v ozone or oxygen plasma is necessary to create a hydrophilic, high surface energy surface onto which the sucrose is spin-coated. For spin-coating onto QCM-D sensors, silicon oxide Q-Sense E4 sensors were used, which were cleaned first with 2% SDS solution followed by u-v ozone. The sucrose used was crystalline icing sugar sourced by Mars Chocolate, UK from British Sugar, UK, with average particle size $\sim$10μm (characterisation detailed in Chapter 3) dissolved in Millipore Milli-Q water with resistivity 18.2 MΩ cm and TOC = 4 ppb. The desired concentration, 30-1800 mM, of the sucrose solution was made by dissolving sucrose in millipore water and sonicating for 10 minutes. This solution was then spin-coated onto the cleaned silicon substrates at 4000 rpm for 1 minute and dried under vacuum at 70°C overnight. Figure 5.2, shows pictures spin-coated sucrose films of varying thickness from 10 nm to 500 nm.

Using AFM[1] and SEM it was observed that the films were globally flat on a sub-micron scale as shown in Figure 5.3. The inset on the right panel of Figure 5.3 shows a typical AFM texture profile; which can be decomposed into waviness and local roughness components. The local roughness of the sample is very small with rms value of <1 nm. The waviness has an rms value of 2 nm and is on 10 μm length scale. This waviness can be a combination of surface topography and the finite size of the stylus tip [84]. The numerical evaluation of roughness using an AFM is always preceded by removal of waviness from the measured profile and rms roughness obtained for a 100×100 μm^2 area for this sample was 1.9 nm. This suggests that it should be possible to use XRR to characterise them at the atomic scale.

[1]The AFM images were taken in collaboration with Prof V. Koutsos by his Ph.D. student Jake McClements

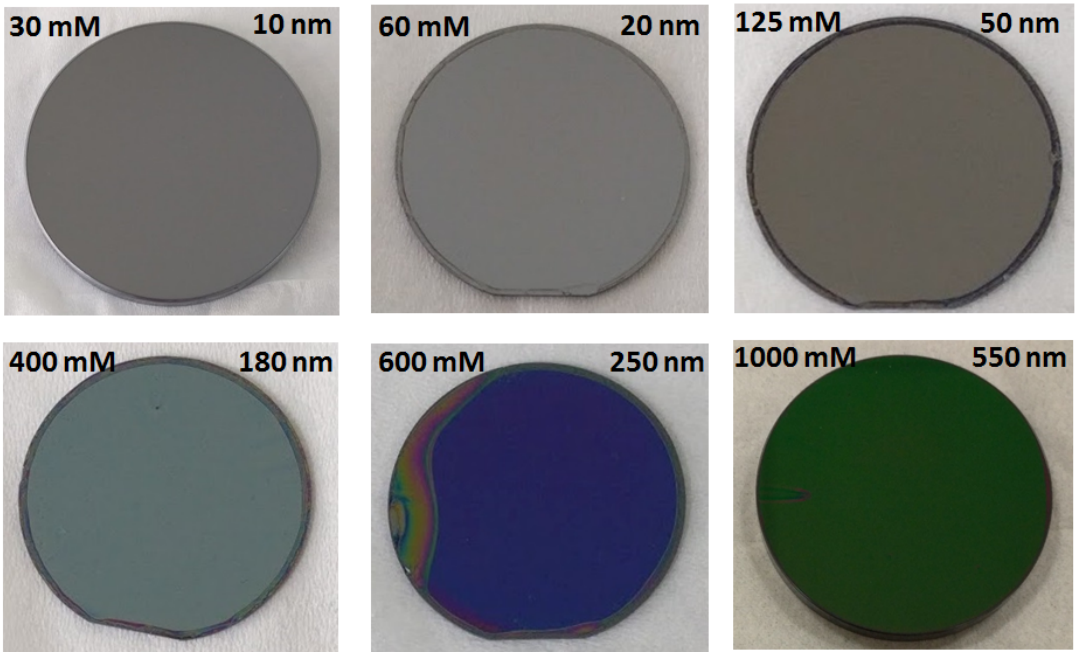

Figure 5.2 *Picture showing sucrose films spin-coated onto silicon substrates for thicknesses upto 550 nm. The annotation on the top left gives the concentration of the solution used for spin coating and on the right gives the thickness of the films. The pictures with defects are particularly chosen to help make the typically uniform films visible.*

5.2.2 Thickness Characterisation of Spin-Coated Sucrose Thin Films

The thickness of these spin-coated sucrose films was measured using X-Ray Reflectivity (XRR) for films less than 200 nm thick. For higher thickness films, there is a loss in the coherence of the x-rays reflected from either side of the sucrose film, a double critical edge appears and the Kiessig fringes become difficult to distinguish. Therefore, for thicker films QCM-D was used to measure the thickness, which provides a mass per unit area for the films. The mass per unit area can then be converted to thickness by dividing it by density of the film. The GIXRD shows these films to be crystalline so the density of the films will be the same as that of bulk sucrose (1.59 g/cm^3).

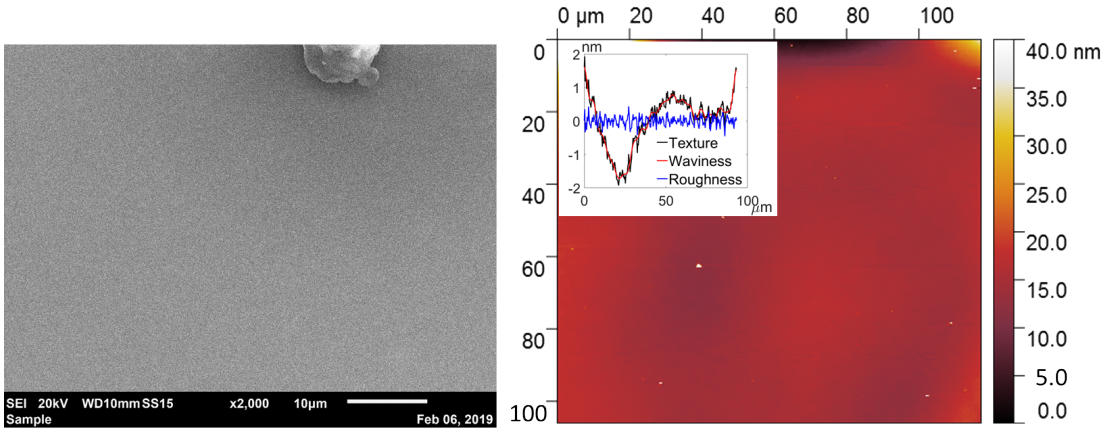

Figure 5.3 *Left panel: SEM image of a 50 nm thick sucrose film. Right panel: AFM image of a ∼1 µm thick sucrose film with the inset showing a typical line texture profile (black line) decomposed into waviness (red line) and roughness (blue line).*

X-Ray Reflectivity from Sucrose Films: Characterisation of Sub-200 nm Thick Films

X-ray reflectivity is a surface sensitive technique which can be used to probe the electron density of a sample perpendicular to the surface and can therefore provide information about the roughness of the surface, thin film thickness and density of any buried interfaces [85]. A detailed description is presented in Section 6.2, however, in principle x-ray reflectivity measures the reflected x-ray intensity as a function of incidence angle (for angle of incidence equal to angle of reflection) over a range of angles close to the critical angle for total reflection. The intensity of the reflected x-rays depends on the Fresnel reflectivity, which gives information about the density distribution of the material, and an interference pattern (Kiessig fringes) from the scattering at different interfaces, which can provide information about layer thicknesses. Therefore, it can be used to calculate thickness and material properties of layered substrates.

Specular XRR was measured from sucrose thin films with the x-rays incident from air onto the sucrose coated silicon blocks on the Rigaku lab-based diffractometer in the Material Characterisation Lab, ISIS, UK by scanning $2\theta/\Omega$ with 2θ going from $0.1 - 5^{\circ}$. The measured reflectivity is shown in the left panel in Figure 5.4, with the hollow circles representing the data points and solid lines showing the fits to the data. The silicon blocks are expected to have a thin oxide layer (from the Piranha cleaning and uv ozone) onto which the sucrose film is coated, as

shown in the cartoon layer profile in the inset of the right panel in Figure 5.4.

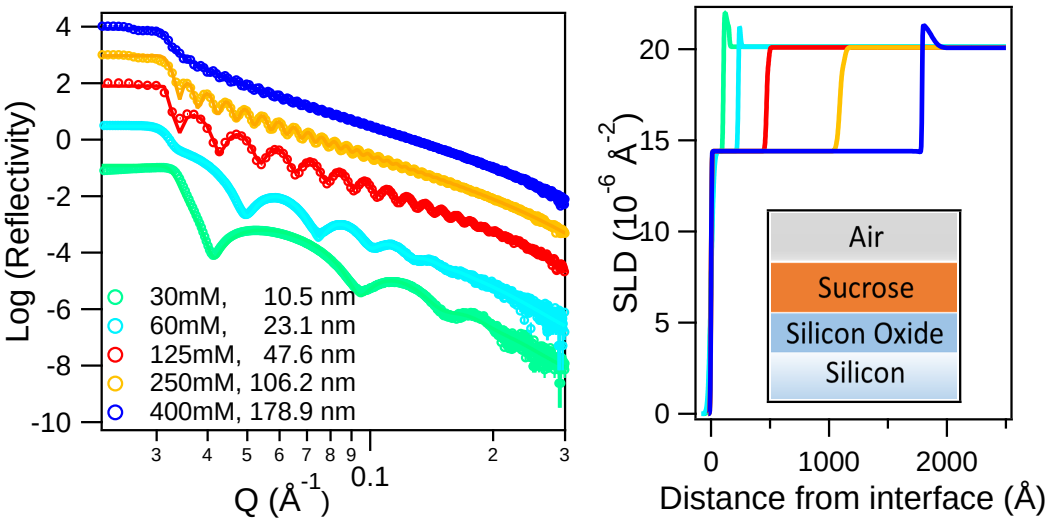

Figure 5.4 *Left panel: XRR from sucrose films spin-coated onto silicon substrate with thicknesses from 10 to 180 nm; Right panel: SLD profile for the fitted layer with the inset showing the layered profile.*

The scattering length densities (SLD) of various components are: $\text{SLD}_{\text{air}} = 0$, $\text{SLD}_{\text{sucrose}} = 14.4 \times 10^{-6}$ Å^{-2}, $\text{SLD}_{\text{SiOx}} = 22.5 \times 10^{-6}$ Å^{-2} and $\text{SLD}_{\text{Si}} = 20.7 \times 10^{-6}$ Å^{-2}. Fitting the data to the layered profile results in sucrose layer thicknesses of $10 - 250$ nm depending on the concentration of the spin-coating solution shown in Figure 5.4 and summarised in Table 5.1(left). For films of thickness greater than and equal to 150 nm a double critical edge due to reflection from air/silicon interface and sucrose/silicon interface is observed.These thicker films have been additionally characterised using QCM-D.

QCM from Sucrose Films: Characterisation of μm Thick Films

Quartz Crystal Microbalance (QCM) is a widely used technique to characterise the thickness or added mass of attached thin films on substrates [86]. In QCM, the sensor, a quartz crystal sandwiched between a pair of electrodes, is oscillated at its resonant frequency by applying an alternating voltage. The resonant frequency depends on the total mass of the sensor and any layers that are attached to the surface. The addition of a small mass decreases the resonant frequency of the sensor, as shown in Figure 5.5. By measuring the change in frequency, the added mass can be determined with ng/cm^2 accuracy, which can be converted to a thickness using the density of the film. In addition to the shift in frequency,

the dissipation (QCM-D) from the oscillating signal can be measured, which provides information about the rigidity of the film; small changes are expected for a rigid layer and higher changes for soft diffuse layers. The principle of dissipation monitoring and its application are discussed further in details in Section 5.4.1.

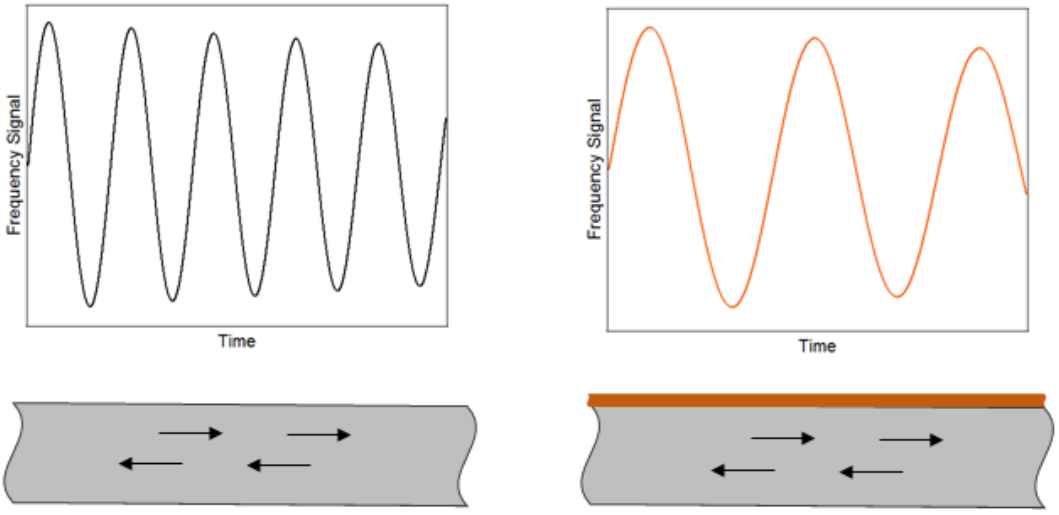

Figure 5.5 *A schematic showing the change in frequency upon the addition of mass for a QCM sensor.*

To determine the thickness of the spin-coated sucrose layers, QCM-D measurements were done on the Biolin Scientific E4 Q-Sense Instrument [87] at ISIS, Oxford, UK. A quartz crystal sensor spin-coated with sucrose was oscillated and the difference in the resonant frequency compared to that of the same sensor without the sucrose film was measured for each of the odd modes and divided by the n for that mode to give ΔF. As the relative change in frequency ($\Delta F/F$) is $< 0.05\%$ and the film is rigid exhibiting low dissipation, the Sauerbrey relation [88], Equation 5.1, can be used to convert ΔF into a mass per unit area, m_f:

$$m_f = -\frac{\Delta F}{2F^2} \times Z_q \tag{5.1}$$

where F is the original frequency of the sensor and Z_q is the acoustic impedance of the material, which are 4.95 MHz and 8.8×10^6 kg m^{-2} s^{-1} respectively for the sensor used here. Assuming a uniformly thick layer of a density ρ (1.59 g cm^{-3}

for sucrose), this m_f can be converted into a thickness:

$$t = \frac{m_f}{\rho} \tag{5.2}$$

Table 5.1 *Sucrose thickness calculated from XRR (left) and QCM-D (right)*

Conc mM	Layer thickness SiOx nm	Layer thickness sucrose nm	Roughness sucrose nm
30	1.7	10.3	0.7
60	1.0	22.7	2.0
125	1.8	47.4	1.1
250	1.1	106.6	0.5
400	1.6	179.2	0.7
600	3.8	243.3	0.5

Conc mM	Layer thickness sucrose nm
125	55
650	273
1000	542
1400	967
1800	1850

The XRR and QCM-D results are in good agreement with one another. The thickness increases as the concentration of the sucrose in the solution used for spin-coating is increased as shown in Figure 5.6. The red data set (hollow diamonds) shows sucrose films spin-coated onto Silicon blocks or wafers from sucrose solutions from 30-600 mM concentration resulting in films with thicknesses in the range 10-250 nm as determined from fits to the x-ray reflectivity measured from the films. A linear dependence of thickness on the concentration of the spin-coating sucrose solution is observed, red solid line in Figure 5.6 . The blue data set (hollow circles) shows sucrose films spin-coated onto silicon oxide QCM-D sensors from 125-2000 mM sucrose solutions resulting in films with thicknesses in the range of 55 nm to 2 μm. A quadratic dependence of thickness with concentration of the spin-coating sucrose solution is observed, solid blue line in Figure 5.6. The deviation from the linear fit at higher concentration comes from the change in viscosity of the spin-coating solution, which means less of the solution that is spread is spun off during spin-coating. This combined effect of viscosity and concentration results in an increase in the rate at which the film thickness increases with the concentration.

These results show nm to μm thick sucrose films can be obtained by spin-coating onto clean hydrophilic silicon blocks or wafers with varying thickness. The roughness of these films, as determined from fits to the XRR, was small enough (<2 nm) that they can be used as substrates for further interfacial studies.

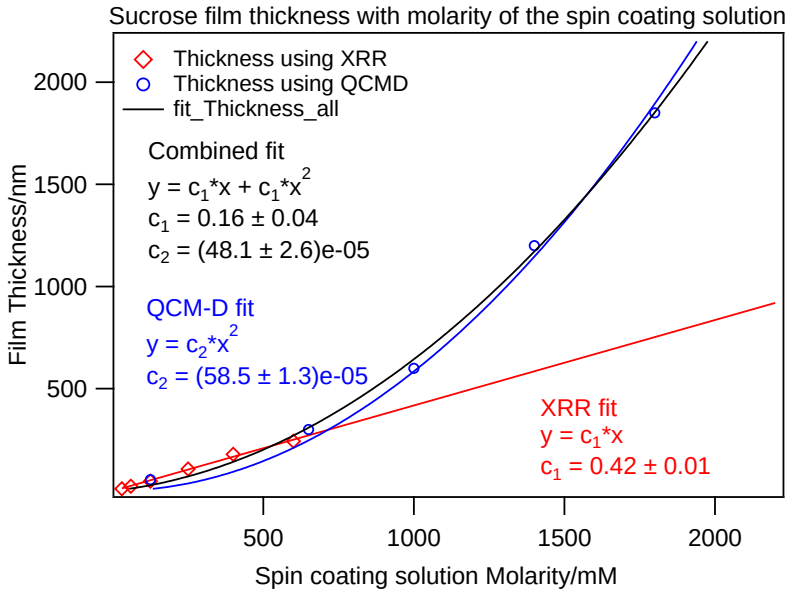

Figure 5.6 *A plot showing the dependence of spin-coated sucrose film thickness on the concentration of sucrose in the spin-coating solution with linear and quadratic fits.*

5.2.3 Crystallinity Characterisation of Spin-Coated Sucrose Thin Films

The crystallinity of these thin sucrose films is important as the physical properties of sucrose depends on its crystalline or amorphous nature [89]. In food formulations, especially in chocolate, crystalline sucrose is used with low water content. To measure the crystallinity of these films X-Ray Diffraction (XRD) was first measured in transmission using the Rigaku lab based diffractometer at the Material Characterisation Lab, ISIS, Oxford, UK with $2\theta/\theta$ scanning from 5-120° and a resolution of 0.1° at a scan rate of 1°/min.

As can be seen from Figure 5.7, no discernible peak from the sucrose film was observed with the XRD signal being dominated by the silicon substrate as a consequence of the thinness of the sucrose films compared to the silicon substrate. To overcome this, Grazing Incidence X-Ray Diffraction (GIXRD) was measured from these thin films.

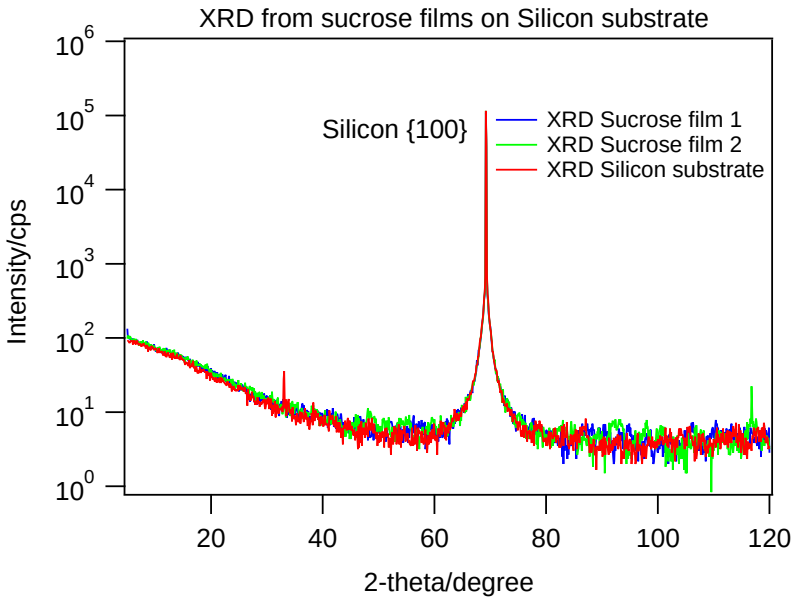

Figure 5.7 *XRD from 2 μm sucrose films coated onto silicon substrates with the silicon (100) peak*

GIXRD for Measuring Crystalline Structure of Thin Films

XRD measurements of sub-micron films using conventional $2\theta/\theta$ scanning methods produces a weak signal from the film and an intense signal from the substrate. One way to avoid the intense signal from the substrate and get a stronger signal from the film itself is to perform a 2θ scan with a fixed grazing angle of incidence, Ω, popularly known as GIXRD as shown in Figure 5.8 [90]. The fixed angle is chosen to be slightly above the critical angle for total reflection of the film material and the beam is diffracted in the plane of the surface of the sample by the angle 2θ. The penetration depth of the incident wave is limited and therefore the signal is dominated by the thin surface layer of interest.

GIXRD from Thin Sucrose Films

The crystallinity of these thin films was characterised by measuring GIXRD using the Rigaku lab based diffractometer at ISIS, Oxford, UK with the x-rays incident from air on the sucrose thin films with 2θ going from 5-60° at $\Omega = 0.7°$ as shown in Figure 5.9.

The left panel in Figure 5.9 shows GIXRD from films with thickness from 300-

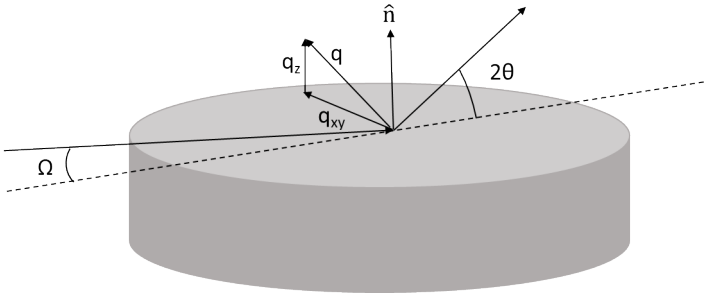

Figure 5.8 *A schematic showing the principle of GIXRD.*

1500 nm with resolution in 2θ of 0.01°. Bragg peaks are observed from the films but these peaks start to drop below the background for films of thickness below 1000 nm. To enhance the signal the resolution was reduced to 0.05° as shown in right panel Figure 5.9. This increases the signal by an order of magnitude and observe the Bragg peaks remain visible from films down to 170 nm. To further enhance the features from the thin films, the data from the top right was divided by the GIXRD signal from silicon substrates as is shown in Figure 5.10. This shows the thinner films are still crystalline and the loss of signal is because of the small amount of material present in these thin films. The observed Bragg peaks are at $q = 0.956$ Å^{-1}($2\theta = 13.46°$) and $q = 1.41$ Å^{-1}($2\theta = 19.91°$) which correspond to planes with d-spacings of 6.58 Å and 4.46 Å.

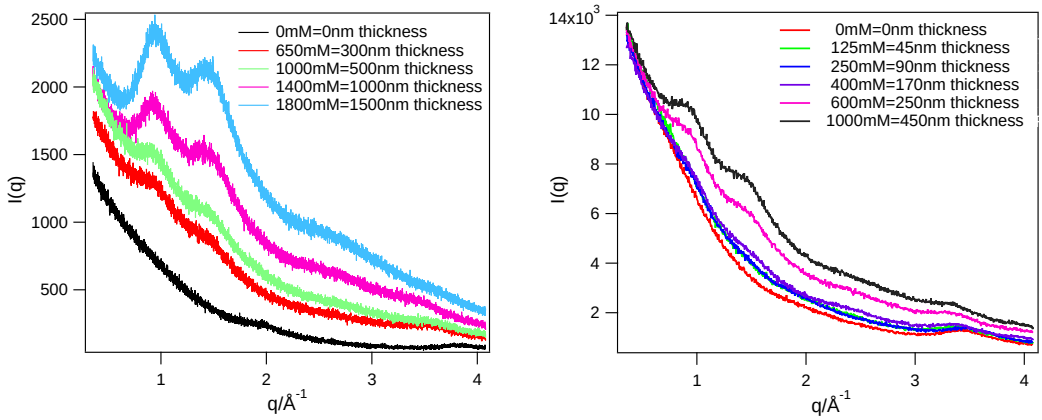

Figure 5.9 *Grazing incident XRD (GIXRD) from sucrose films of thicknesses ranging from 10 nm to 1500 nm.*

Crystalline sucrose has a monoclinic crystal habit [91]. Using $a = 10.89$ Å, $b = 8.69$ Å, $c = 7.77$ Å and the angle $\beta = 103°$, we can find d-spacing for various

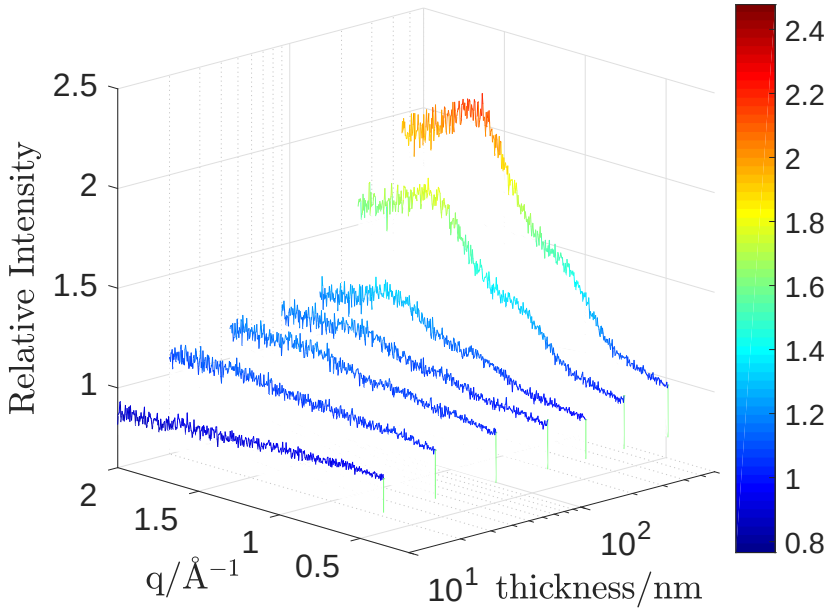

Figure 5.10 *A waterfall plot of the GIXRD relative intensity (Signal from spin-coated film divided by the bare substrate signal) for various films with thickness <500 nm.*

lattice planes using the formula:

$$\frac{1}{d^2} = \frac{h^2}{a^2 \sin^2 \beta} + \frac{k^2}{b^2} + \frac{l^2}{c^2 \sin^2 \beta} - \frac{2hl}{ac \sin^2 \beta} \tag{5.3}$$

where h, k and l are the Miller indices. Equation 5.3 predicts a d-spacing of 4.35 Å for the (020) plane, as for monoclinic crystals we expect a systematic absence of $2k + 1$ reflections, and 6.72 Å for (110) plane. This suggests we are growing the films along the (100) plane, meaning the exposed upper surface is relevant to the crystal habit of sucrose in food formulations such as chocolate.

5.3 Interfacial Activity of Surfactants at Sucrose/Triglyceride Interface

The planar crystalline sucrose substrates can now be used to study the interaction of lecithin and PGPR with the sucrose interface in a triglyceride oil medium. This understanding can give us information about the surfactant interfacial layer that

influences the rheology of sucrose/triglyceride suspensions (model chocolate).

To establish the interfacial activity of lecithin and PGPR at the sucrose/triglyceride interface tensiometry experiments have been conducted. Spin-coated sucrose substrates have been used to measure the contact angle of triglyceride oil at the sucrose interface with and without surfactants using a sessile drop and the air/triglyceride oil interface has been studied using a pendant drop.

5.3.1 Interfacial Tensiometry

Interfacial tensiometry is a widely used technique to study the activity of surfactants or particles at interface. Liquid-fluid interfaces can be studied using the pendant drop method, left (top-bottom) and middle (bottom-top) panel of Figure 5.11, and solid-liquid interfaces using the sessile drop method, right panel of Figure 5.11.

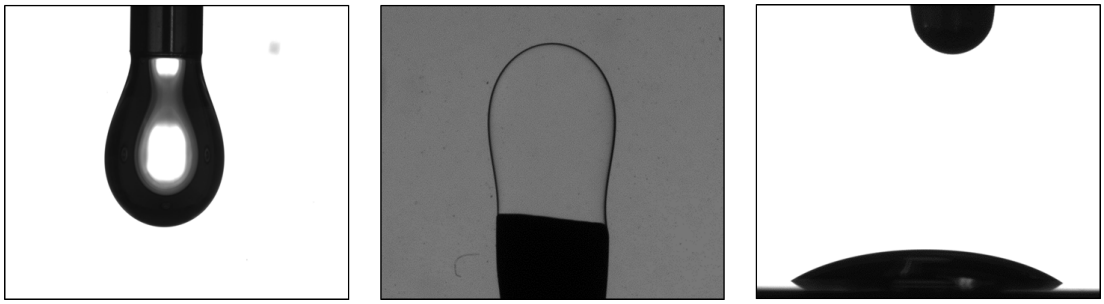

Figure 5.11 *A figure showing various ways of measuring interfacial tension. Left: Top-bottom pendant drop for TO in air. Middle: Bottom-top pendant for TO in 60% w/w sucrose solution. Right: Sessile drop for TO on spin-coated sucrose substrate.*

In a sessile drop experiment a drop of a liquid is deposited onto the solid substrate and the contact angle is measured, as shown in Figure 5.12, which determines the boundary condition for thermodynamic equilibrium between the three phases: solid, liquid and gas. The shape of the liquid/gas interface is determined by the Young Laplace equation, as is the case in the pendant drop, by balancing the Laplace pressure with the hydrostatic pressure.

If the solid/liquid interfacial energy is denoted by γ_{SL}, the solid/gas by γ_{SV} and liquid/gas (same as interfacial tension) by γ_{LV} then the equilibrium contact angle,

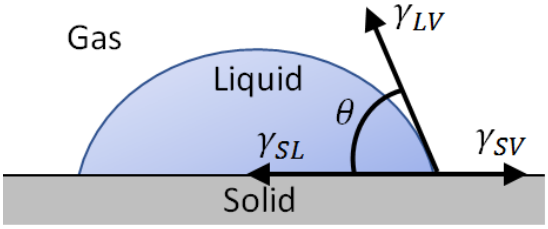

Figure 5.12 *A schematic showing a liquid droplet on a solid substrate where the contact angle of the droplet is such that it balances the interfacial energy of solid/liquid (γ_{SL}), liquid/gas (γ_{LG}) and solid/gas interface (γ_{SG}).*

θ is determined by Young's equation [58] as:

$$\gamma_{SV} = \gamma_{SL} + \gamma_{LV} \cos\theta \tag{5.4}$$

The solid/liquid interfacial energy can be calculated if the solid/gas and liquid/gas interfacial energies are known. The liquid/gas interfacial energy can be calculated using the pendant drop method. The solid/gas interfacial energy can be determined using the free energies of cohesion and adhesion for two phases as given in Girifalco and Good [92]:

$$\gamma_{SL} = \gamma_{SV} + \gamma_{LV} - 2\Phi(\gamma_{SV}\gamma_{LV})^{1/2} \tag{5.5}$$

where Φ is a constant and is given by the theory as:

$$\Phi = \frac{4(V_S V_L)^{1/3}}{\left(V_S^{1/3} + V_L^{1/3}\right)^2} \tag{5.6}$$

where V_S and V_L are the molar volumes of the liquid and solid phases, respectively. Equation 5.4 and 5.5 can be used to eliminate γ_{SV} giving:

$$\gamma_{SL} = \gamma_{LV}\left(\frac{(1+\cos\theta)^2}{4\Phi^2} - \cos\theta\right) \tag{5.7}$$

Using Equation 5.7 the sucrose/triglyceride interfacial energy and how it changes upon the addition of lecithin and PGPR can be calculated by measuring the contact angle of triglyceride oil at the sucrose interface (θ) and the triglyceride oil/air interfacial tension (γ_{LV}) in the presence and absence of surfactants.

5.3.2 Materials and Method

Sucrose was spin coated onto 1" silicon wafers from millimolar aqueous solutions using the method described in Section 5.2.1 to prepare substrates for sessile drop experiments. The triglyceride oils that were studied were $\geq$ 99% pure Glyceryl Trioleate (TO), $\geq$ 99% pure Glyceryl Trioctanoate (GTO) and $\geq$ 60% purity Glyceryl Trioleate (TO60) all sourced from Sigma Aldrich, UK. Lecithin and PGPR were obtained from Mars Chocolate, UK.

All tensiometry measurements carried out in this thesis were done using the Drop Shape Analyser from KRUSS GmbH. To measure the interfacial activity of lecithin and PGPR at the sucrose/triglyceride interface, sessile drop experiments were conducted whereby a droplet of the triglyceride oil, with and without lecithin, PGPR and their binary mixture, was deposited on a spin-coated sucrose film as shown in right panel of Figure 5.11. The contact angle of the droplet was measured for 30-60 mins. The value of the contact angle was determined using the Circle method [93] as this is the most accurate method for contact angles of $\leq 20°$[2]. Three measurements done for each of the surfactant concentration and the oil however in the figures only one is plotted for clarity. The repeatability of the data is better than 2° which is comparable to the error in contact angle estimation due to the circle method which is $2-3°$. To determine the air/triglyceride oil interfacial tension and how this changes with the addition of surfactants, pendant drop experiments were carried out whereby a droplet of triglyceride oil with and without the surfactants was suspended from a needle in air and the interfacial tension was monitored for $15-60$ mins. Again 3 measurements were collected for each of the data set but only 1 is shown in the graphs for clarity. The repeatability between the runs was within 1 mN/m which is comparable to the error in interfacial tension calculated by the instrument using the Young-Laplace method ($0.5-0.6$ mN/m).

[2]The contact angle was calculated using the Tangent methods and the height-width method in addition to the circle method. The trend shown by the contact angle upon the addition of surfactants is the same, even though the exact values depend on the method used.

5.3.3 Interfacial Tensiometry with Lecithin and PGPR in Triglyceride Oil

The contact angle measurements as a function of time made for a droplet of GTO, TO and TO60, with and without lecithin and PGPR, are shown in the left panel of Figure 5.13, 5.14 and 5.15, respectively.

The triglyceride oils wet the sucrose interface displaying relatively low contact angles, $\sim 15^\circ$ for pure TO and GTO and $\sim 25^\circ$ for TO60. This implies that the role of lecithin and PGPR is primarily as rheology modifiers rather than to assist sucrose/triglyceride interfacial wetting, as previously claimed [94]. The addition of the surfactants does decrease the contact angle of all the oils tested, suggesting that the surfactants are adsorbing to the interface. For pure TO and GTO the contact angle drops from $\sim 15^\circ$ for oil without surfactants to $\sim 5^\circ$ following the addition of lecithin, PGPR and their binary mixture. The decrease in contact angle observed on the addition of lecithin is quick (timescale $\sim$ seconds) compared to PGPR (timescale $\sim$ minutes) reflecting the smaller size of the interfacially active phospholipid molecules in lecithin. For TO60 addition of PGPR doesn't result in a decrease in contact angle, but for lecithin and lecithin + PGPR mixture the contact angle decreases from $\sim 25^\circ$ to $\sim 15^\circ$. A possible explanation for not observing a decrease in contact angle upon addition of PGPR is the presence of mono- and di glycerides in the TO60 which are interfacially active and can adsorb at the sucrose interface, and the adsorption energy is too high for them to be displaced by PGPR. The phospholipids present in lecithin have greater interfacial activity for the sucrose surface due to the polarity in the head groups and therefore can displace the mono- and di-glycerides. The contact angle obtained from a mixture of lecithin and PGPR in oil is very similar in all cases, in time-scale and value, to the contact angle obtained by lecithin only in oil which suggests that lecithin preferentially adsorbs to the sucrose interface, but needs further confirmation.

The triglyceride oil/air interfacial tension measurements as a function of time for a droplet of GTO, TO and TO60, with and without lecithin and PGPR, are shown in the right panel of Figure 5.13, 5.14 and 5.15, respectively. The triglyceride oil/air interfacial tension is $\sim$30 mN/m for all oils tested, 29 mN/m for GTO, 32 mN/m for TO and 30 mN/m for TO60, as shown in Table 5.3. PGPR has no effect on the interfacial tension of triglyceride/air interface however lecithin lowers the interfacial tension by $10-20\%$. The triglyceride oil/sucrose contact angle and

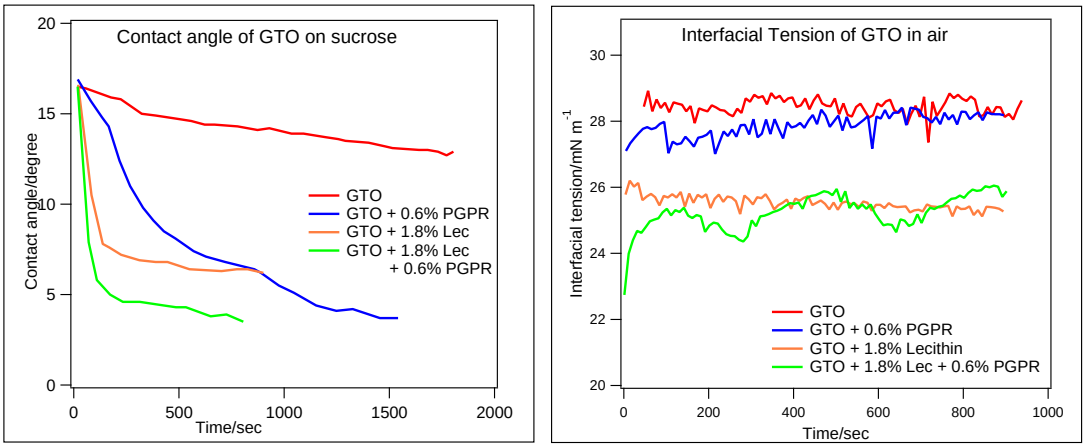

Figure 5.13 *Left panel: Graph showing the contact angle with time for a droplet of GTO on the sucrose surface with and without lecithin and PGPR. Right panel: Graph showing the GTO/air interfacial tension with and without lecithin and PGPR.*

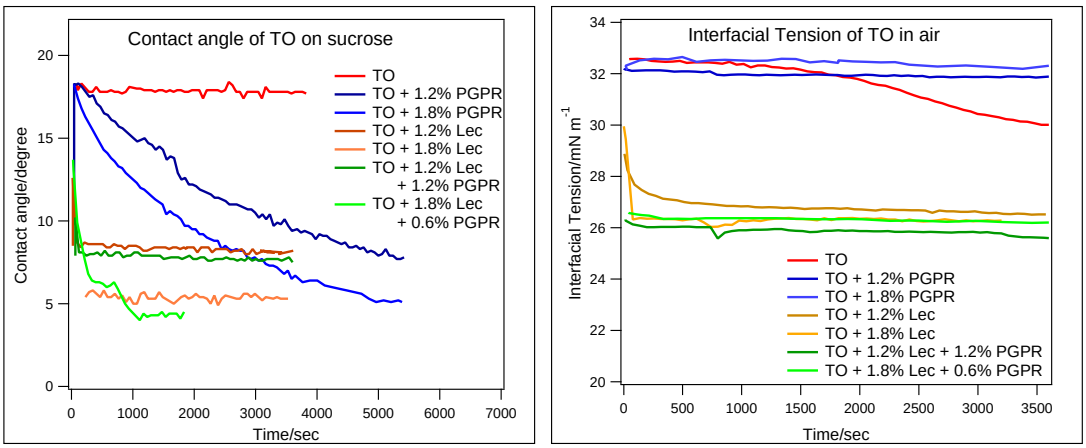

Figure 5.14 *Left panel: Graph showing the contact angle with time for a droplet of TO on the sucrose surface with and without lecithin and PGPR. Right panel: Graph showing the TO/air interfacial tension with and without lecithin and PGPR.*

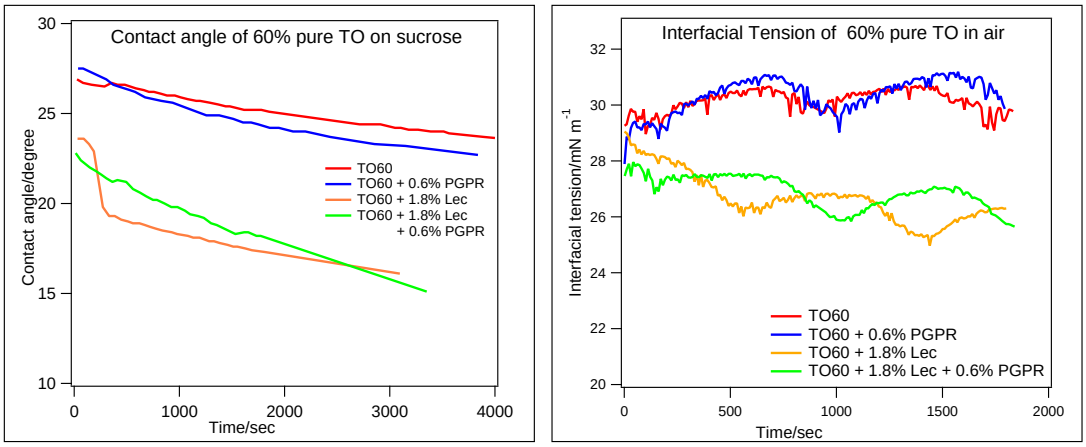

Figure 5.15 *Left panel: Graph showing the contact angle with time for a droplet of TO60 on the sucrose surface with and without lecithin and PGPR. Right panel: Graph showing the TO60/air interfacial tension with and without lecithin and PGPR.*

the triglyceride oil/air interfacial tension values can now be used to calculate the sucrose/triglyceride oil interfacial energy and how it changes upon the addition of surfactants using Equation 5.7. To calculate Φ for sucrose/TO and sucrose/GTO using Equation 5.6, the molar volumes, V_m, for sucrose, TO and GTO were used as shown in Table 5.2. The values obtained for the sucrose/triglyceride oil interfacial energy, with and without lecithin and PGPR, are summarised in Table 5.3

Table 5.2 *Calculations for the molar volume and Φ (Equation 5.6) for sucrose/GTO and sucrose/TO systems.*

	Molar weight g/mol	density (ρ) g/cm^3	Molar volume (V_m) cm^3/mol	Φ
sucrose	342.3	1.59	215.3	NA
GTO	470.7	0.956	492.4	0.981
TO	885.4	0.91	973.0	0.939

As can be seen from Table 5.3 lecithin, and its binary mixture with PGPR reduce the interfacial energy of sucrose/triglyceride interface by 8-15%. When only PGPR is present the change in the interfacial energy is negligible. This suggests that lecithin is more interfacially active than PGPR and so will preferentially adsorb at the sucrose interface.

Table 5.3 *Summary of Contact Angle and Interfacial tension for lecithin and PGPR in GTO, TO and TO60*

Surfactant %		θ[1] degree	γ_{OA}[2] mN/m	γ_{SO}[3] mN/m	$\Delta\gamma_{SO}/\gamma_{SO}$[4] % change
lecithin	PGPR	GTO			
0	0	12.9	28.6	1.081	0
0	0.6	4.1	28.6	1.100	1.8
1.8	0	6.2	26.1	1.001	-7.4
1.8	0.6	3.5	26.2	1.010	-6.6
lecithin	PGPR	TO			
0	0	17.8	32.1	4.092	0
0	1.2	10.2	32.0	4.195	2.5
0	1.8	8.8	32.4	4.273	4.4
1.2	0	8.4	26.8	3.533	-13.6
1.8	0	5.3	26.3	3.489	-14.7
1.2	1.2	7.8	25.8	3.412	-16.6
1.8	0.6	4.1	26.3	3.493	-14.6
lecithin	PGPR	TO60			
0	0	25.1	30.1	3.708	0
0	0.6	24.2	30.6	3.781	2.0
1.8	0	17.3	26.5	3.388	-8.6
1.8	0.6	18.2	26.9	3.426	-7.6

The values for contact angle and interfacial tension quoted here are the values obtained after 30 min or at the end of the experiment, whichever was later, and are averaged over 3 runs.
[1] Contact angle for the oil droplet containing surfactants on sucrose.
[2] Interfacial tension at the oil/air interface calculated using the pendant drop method.
[3] Interfacial tension at the sucrose/oil interface calculated using 5.7.
[4] The fractional change in interfacial tension upon the addition of surfactants $(\gamma_{SL}^{\text{surfactant}} - \gamma_{SL}^{\text{oil}})/\gamma_{SL}^{\text{oil}}$ expressed as a percentage.

5.4 Adsorption of Surfactants at Planar Sucrose/Triglyceride Oil Interface

Having established the interfacial activity of the surfactants at the sucrose interface, QCM-D sensors spin-coated with sucrose have been used to further investigate the adsorption of lecithin and PGPR at the planar sucrose/triglyceride interface. The adsorption at planar interfaces can then be compared to the adsorption of surfactants in sucrose/triglyceride suspensions to establish the utility of the planar interface approach for understanding the interfaces in sucrose/triglyceride suspensions.

5.4.1 Quartz Crystal Microbalance with Dissipation Monitoring

The QCM principle as discussed in Section 5.2.2 is applicable to thin ($\Delta F/F<2\%$), rigid films (small dissipation) measured in air (no dependence on the viscosity and density of the contacting fluid). However by incorporating the dissipation monitoring (QCM-D), the technique can be used to study the adsorption of soft films in liquid [95]. A soft adsorbed layer will not completely couple to the oscillation of the QCM-D sensor and hence the Sauerbrey equation will underestimate the mass at the surface and the dampening of the sensor's oscillation due to the dissipation, as shown in Figure 5.16, needs to be incorporated to calculate the adsorbed mass and thickness.

The dissipation, D, is the inverse of the quality factor Q and is defined as

$$D = \frac{1}{Q} = \frac{E_{dissipated}}{2\pi E_{stored}} \tag{5.8}$$

where $E_{dissipated}$ is the energy dissipated in one cycle and E_{stored} is the energy being stored in the oscillating system.

For oscillations in a simple Newtonian bulk liquid with viscosity, η_l, and density, ρ_l, the changes in frequency, ΔF_{liquid} and dissipation, ΔD_{liquid} are given as [96]:

$$\Delta F_{liquid} = -F_0^{3/2}\sqrt{\frac{n\rho_l\eta_l}{\pi Z_q^2}} \tag{5.9}$$

$$\Delta D_{liquid} = 2F_0^{1/2}\sqrt{\frac{\rho_l \eta_l}{n\pi Z_q^2}} \tag{5.10}$$

where n is the overtone number, F_0 is the fundamental resonant frequency for the crystal and Z_q is the acoustic impedance as described in Equation 5.1. However, for more complex fluids with viscoelastic properties, a shear modulus needs to be incorporated.

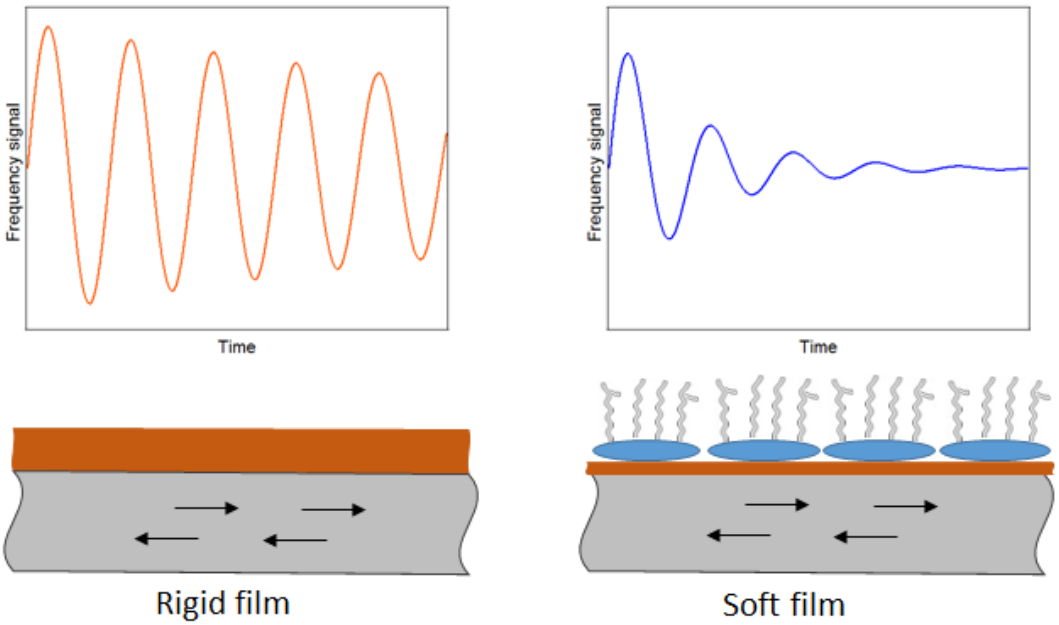

Figure 5.16 *A schematic showing the dampening of the frequency of the oscillating signal for a soft layer, as compared to the same mass of rigid film, added onto the QCM-D sensor.*

By modelling the viscoelastic properties of the fluid and/or the soft adsorbed layers, how the fluid and/or the layers couple to the oscillations of the quartz crystal and the effect of this coupling on the frequency and dissipation of the oscillations can be understood. The viscoelastic properties can be described using the viscosity, η, and shear modulus, μ and modelled using either the Maxwell or Voigt model [97]. Maxwell's model is best suited to describe systems (polymer or surfactant solutions) that flow like fluids whereas, the Voigt model is used to describe systems which do not flow such as adsorbed polymer or surfactant layers.

In the Voigt model, which is used to understand the response of adsorbed layers in this work, the viscoelastic element is described by a complex shear modulus as

given in Equation 5.11. The complex modulus consists of a frequency independent real component, $G' = \mu$, called the storage modulus and an imaginary component called loss modulus, $G'' = 2\pi F\eta$, that increases linearly with frequency.

$$G^* = G' + iG'' = \mu_{ly} + 2\pi F i\eta_{ly} \tag{5.11}$$

where μ_{ly} and η_{ly} are the shear modulus and viscosity of the adsorbed viscoelastic layer, respectively. Using a continuum mechanics approach, as described by Voinova *et al.* [98], the change in frequency, ΔF_{layer}, and dissipation, ΔD_{layer}, for the n^{th} overtone for a viscoelastic adsorbed layer of density ρ_{ly} in a viscous bulk fluid of viscosity η_l and viscous penetration depth δ_l are given as:

$$\Delta F_{layer} = -\frac{F_0}{\pi Z_q}\left[\frac{\eta_l}{\delta_l} + h_{ly}\rho_{ly}\omega - 2h_{ly}\left(\frac{\eta_l}{\delta_l}\right)^2 \frac{\eta_{ly}\omega^2}{\mu_{ly}^2 + \omega^2\eta_{ly}^2}\right] \tag{5.12}$$

$$\Delta D_{layer} = \frac{2}{\pi n Z_q}\left[\frac{\eta_l}{\delta_l} + 2h_{ly}\left(\frac{\eta_l}{\delta_l}\right)^2 \frac{\eta_{ly}\omega}{\mu_{ly}^2 + \omega^2\eta_{ly}^2}\right] \tag{5.13}$$

In this model, the adsorbed layer is represented by density (ρ_{ly}), viscosity (η_{ly}), elastic modulus (μ_{ly}), and thickness (h_{ly}). The elastic modulus provides information about the rigidity/softness of the film and the viscosity provides information about how fluid the layer is. By keeping the density of the adsorbed layer fixed at 1.02 g cm^{-3} in this case, the other parameters can be fitted to the change in frequency, ΔF, and dissipation, ΔD, of the 3^{rd} and 5^{th} overtone.

A similar analysis is possible for a Maxwell material as would be appropriate for the adsorption of liquid-like layers, where the viscoelastic response of the material is given as:

$$G^* = \frac{1}{1/\mu_{ly} - i/2\pi F\eta_{ly}} \tag{5.14}$$

The Maxwell model was used to characterise the triglyceride oil at the sucrose interface.

5.4.2 Materials and Method

QCM-D measurements were performed using the Q-Sense E4 instrument in the Biolab at ISIS, Oxford, UK. Silicon oxide quartz sensors were spin coated with sucrose layers using the method described in Section 5.2.1. The spin-coated sensors were used in a flow module through which the triglyceride oils and their solutions with lecithin and PGPR were flowed at 0.7 mL/min using a peristaltic pump. Glyceryl Trioctanoate (GTO) and Glyceryl Trioleate (TO) with $\geq$99% purity were sourced from Sigma Aldrich, UK and lecithin and PGPR were obtained from Mars Chocolate, UK. The measurements for GTO were made at room temperature, whereas the measurements for TO made at 40°C because the viscosity of TO at room temperature is sufficiently high ($\sim$ 100 mPa s) such that the damping of the oscillations is too large for the Q-sense software to be able to reproducibly detect a resonant frequency. The frequency is measured in Hz and the dissipation is recorded as a fractional change in parts per million.

A typical QCM-D experimental protocol includes measuring the oscillations in air and then under the flowing triglyceride oil, which results in a reduction in frequency. Once a stable frequency and dissipation response has been achieved for oscillations in the oil, the solution of surfactant in the oil is flowed through the cell for 5-10 mins and the frequency and dissipation response for modes upto the 9^{th} overtone are measured. A step change in the frequency and dissipation is observed due to the adsorption of the surfactants at the interface. After about 30 mins the substrate is rinsed by flowing pure triglyceride oil. The Q-tools software [99] is used to model the viscoelastic response of the adsorbed layers using the Maxwell model for the triglyceride oil and the Voigt model for the surfactant layers using at least the 3^{rd} and 5^{th} overtone, unless specified otherwise. The triglyceride oil is expected to be fluid and hence the Maxwell model is best suited to describe the viscoelastic properties of the triglyceride oil layering at the sucrose interface whereas the adsorbed surfactant layers do not reach steady flow making the Voigt model a better choice to characterise their viscoelastic response.

The data collected from the QCM-D for measurements made under oil were noisy due to a combination of the high damping and digitisation. A fast Fourier transform of the data showed no particular frequency dependence in the noise on the signal as shown in the left panel of Figure 5.17. To smooth the signal to see if small changes in frequency and dissipation can be detected, a Savitzky Golay filter was applied [100]. The Savitsky Golay filter fits successive sub-sets of

adjacent data points with a low-degree polynomial by the method of linear least squares. By optimising the order of the polynomial and the number of points in the sub-set, high noise reduction can be achieved while preserving any transitions due to real physical effects. The MATLAB function $y = \text{sgolayfilt}(x, n, len)$ was used, where x is the original signal to be filtered, n is the polynomial order, len is the length of the data sub-set fitted to the polynomial and y is the filtered output. By trial and error a polynomial of order 3 and sub-set length of 51 yielded the optimum smoothing of the data sets as shown in Figure 5.17. All fitting has been done using the filtered data sets.

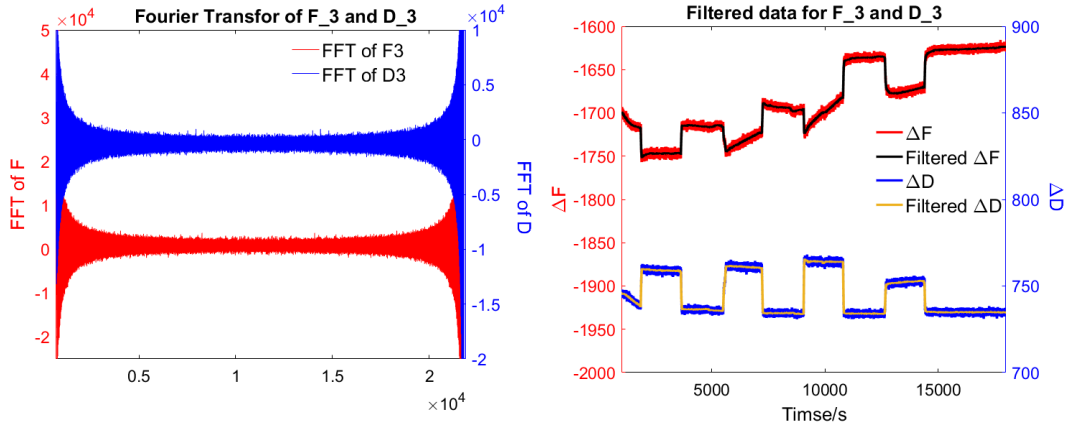

Figure 5.17 *Left panel: The fast Fourier transform of the frequency and dissipation signal for the third overtone of one of the QCM-D data sets. Right panel: The raw QCM-D frequency (red) and dissipation (blue) data for surfactants in GTO for the third overtone and the filtered frequency (black) and dissipation (orange) data using the Savitsky Golay filter*

5.4.3 QCM-D at Sucrose/Triglyceride Oil Interface

Triglyceride Oil at Sucrose Interface

When GTO or TO at 40°C is flowed through the QCM-D cell a change in frequency and dissipation is observed as shown in Figure 5.18 as compared to the oscillations in air. The ΔF and ΔD for the 3^{rd} overtone for GTO are 1700 Hz and 740 ppm, respectively, and for TO they are 1750 Hz and 895 ppm, respectively. It is known from the rheology measurements made in the absence of sucrose, discussed in Section 3.3.2, that GTO and TO are simple Newtonian fluids with viscosities of 22 mPa s and 31 mPa s, respectively. Therefore, it is reasonable to

try to fit the changes in frequency and dissipation, ΔF and ΔD, for oscillation in the triglyceride oil medium using Equations 5.9 and 5.10. As can be seen from the resulting dashed line fits in Figure 5.18, the simple Newtonian fluid model does not fully describe the system, and some additional mass loading in the form of a viscoelastic layer is required to improve the fit. A $5-10$ nm thick viscoelastic interfacial layer was included using the Maxwell fluid model followed by a bulk Newtonian viscous fluid. This model fits the data well, as can be seen by the solid black line fits to the data in Figure 5.18.

The requirement to introduce a proximal viscoelastic layer at the sucrose interface to fit the frequency and dissipation shift for the oscillation in GTO and TO suggests that the oil is structuring into a well-defined layer at the sucrose interface. In the absence of an interface the oil behaves as a purely Newtonian liquid, as discussed in Section 3.3, but once a sucrose interface is present viscoelastic layers of upto 10 nm, corresponding to 3-5 layers of the triglyceride, are observed. This indicates that the triglyceride interacts with the sucrose resulting in structuring of the near-interface layer of the triglyceride oil. This interaction can also explain the wetting of the sucrose surface by the triglyceride oil giving rise to the low contact angle observed in tensiometry.

The shear modulus and viscosity of these proximal triglyceride oil layers is 1 MPa and 10 mPa s for GTO & 2 MPa and 2 mPa s for TO, respectively. The shear modulus is consistent with the values observed for soft films in literature, $0.1-100$ MPa [101–104]. This shear modulus suggests that the interfacial film has some solid-like properties and can sustain a shear stress. The viscosity of the interfacial layer is significantly smaller than the viscosity of the bulk triglyceride oil. It must be noted that the viscosity obtained for the layered triglyceride oil is the apparent viscosity for the viscoelastic material and will be highly frequency dependant, therefore it is not meaningful to compare it to the bulk Newtonian viscosity. However, this value provides a point of comparison for the apparent viscosity obtained from viscoelastic modelling of the adsorbed surfactant layers.

Lecithin and PGPR at Sucrose/Triglyceride Oil Interface

Solutions of lecithin, PGPR and their binary mixtures in GTO were flowed through the QCM-D cell at room temperature, and a typical frequency and dissipation response measured for the third overtone is shown below in the left panel of Figure 5.19. As can be seen from the figure the addition of the surfactants

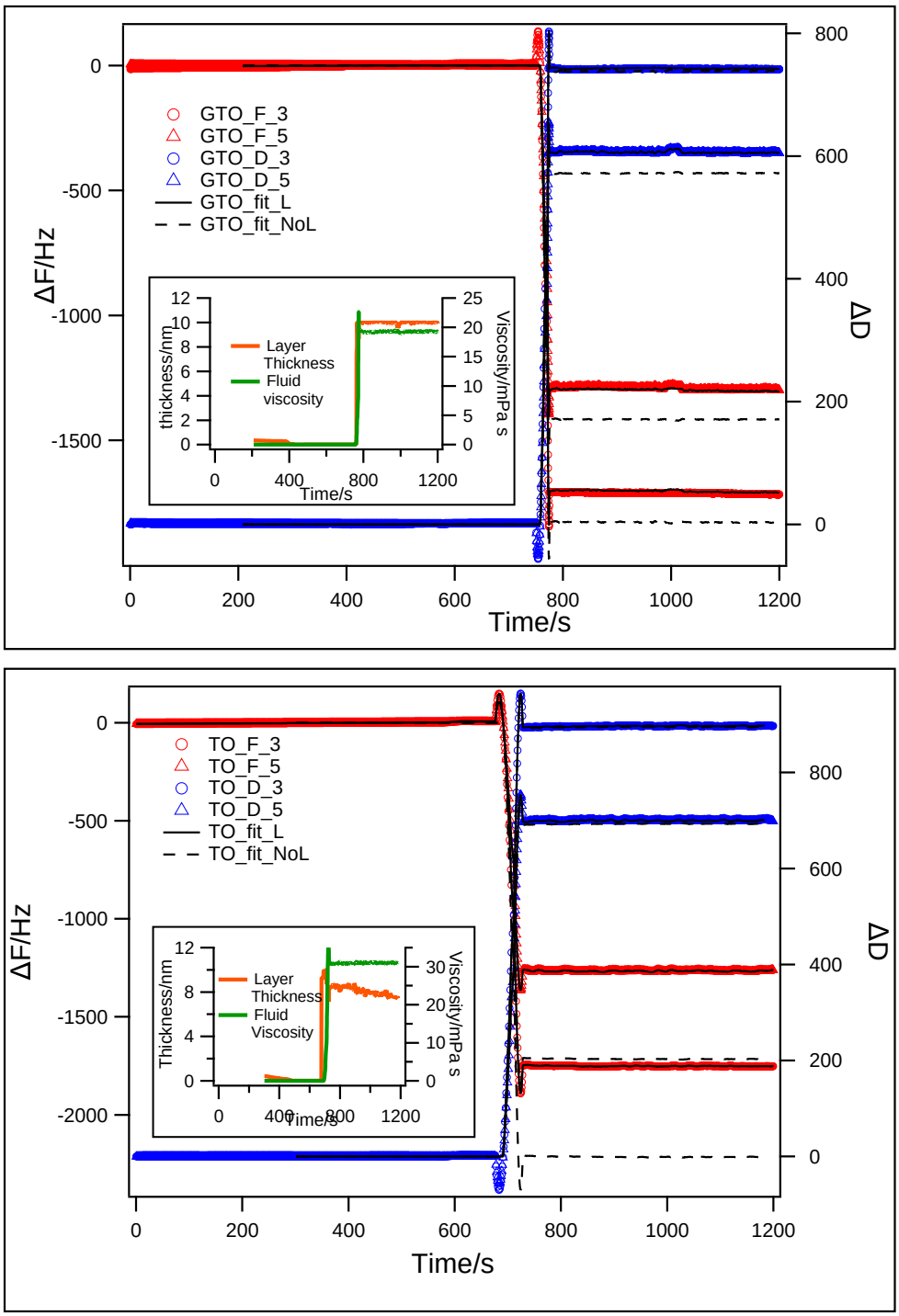

Figure 5.18 *QCM-D measured for triglyceride/sucrose interface: GTO (top) and TO (bottom). The graph shows the frequency (left axis) and dissipation (right axis) signal of* 3^{rd} *and* 5^{th} *harmonics and how they change upon addition of the triglyceride at 700 s. The black line shows the fit to the data using a Maxwell's fluid model with a thin interfacial viscoelastic layer (solid) and without any viscoelastic layer (dashed). The inset shows the viscosity of the bulk phase (change from air to triglyceride oil) on the right axis and the thickness of the interfacial viscoelastic triglyceride layer on the left axis.*

changes the frequency and dissipation. The ΔF for lecithin and PGPR are 36 Hz and 110 Hz, respectively and the ΔD are 22 ppm and 45 ppm, respectively. For the mixture of 1.8% Lec and 0.6% PGPR the ΔF and ΔD are 41 Hz and 33 ppm, respectively. Other mixtures of lecithin and PGPR give similar ΔF, between 40 and 50 Hz, but the dissipation increases as the PGPR content of the surfactant mixture is increased.

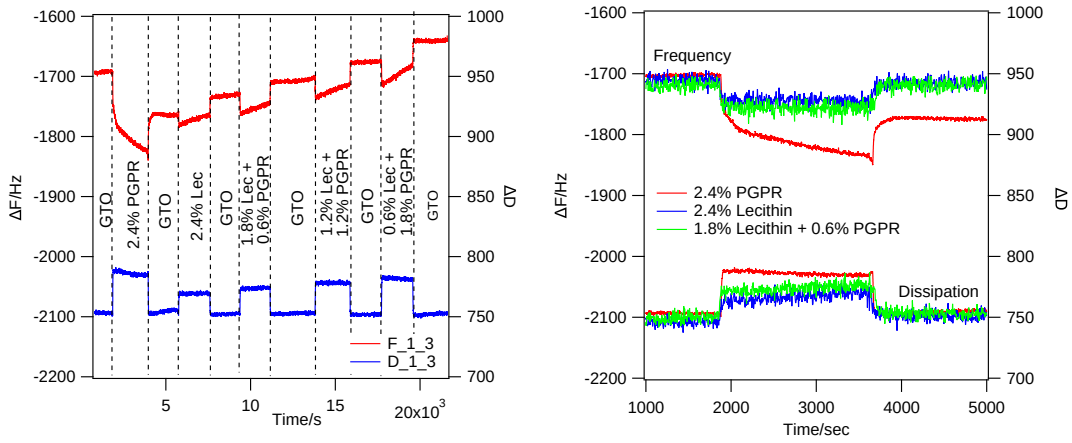

Figure 5.19 *QCM-D measured for the GTO/sucrose interface with solution containing lecithin and PGPR. Left panel: A series of injections: lecithin, PGPR and their binary mixtures with intermediate rinsing steps; showing a change in frequency and dissipation of the signal. Right panel: Graph showing a comparison between ΔF and ΔD for solutions of lecithin, PGPR and a binary combination.*

For lecithin, PGPR and their binary mixtures in TO the solutions were flowed through the QCM-D cell at 40°C, and a typical frequency and dissipation response measured for the third overtone is shown below in the left panel of Figure 5.20. The noise is higher for TO than GTO due to measurements being made at higher temperature and the considerable damping of the signal due to the higher viscosity of the oil. The noise was significantly reduced by applying the filter but the signal cannot be improved further without compromising the transitions in the frequency and dissipation due to the adsorption of the surfactants. The trend in ΔF and ΔD upon the addition of the surfactants is similar to that for GTO. For the lecithin only case ΔF is 65 Hz and ΔD is 13 ppm, for the PGPR only case they are 112 Hz and 28 ppm and for 1.8% lecithin and 0.6% PGPR they are 90 Hz and 20 ppm. In general, for both the oils it is observed that PGPR results in a higher dissipation than the lecithin only case, which is suggests that PGPR forms extended diffuse layers resulting in higher dissipation for the same adsorbed mass whereas lecithin forms compact layers with lower dissipation. Also for the

binary mixtures the addition of PGPR increases the dissipation suggesting the layers become more diffuse.

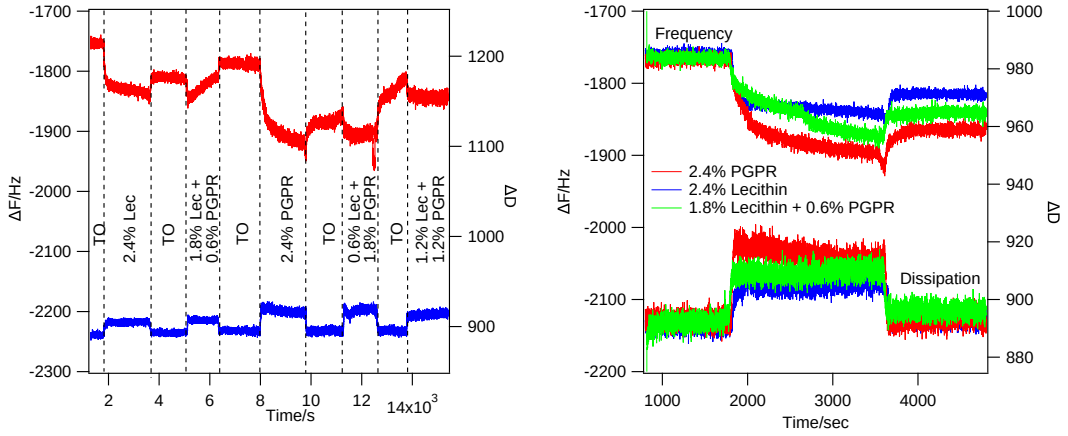

Figure 5.20 *QCM-D measured for the TO/sucrose interface with solution containing lecithin and PGPR. Left panel: A series of injections: lecithin, PGPR and their binary mixtures with intermediate rinsing steps; showing a change in frequency and dissipation of the signal. Right panel: Graph showing a comparison between ΔF and ΔD for solutions of lecithin, PGPR and a binary combination.*

The data was fitted using the Voigt model in the Q-tools software as shown in the left panels of Figures 5.21 and 5.22. The viscosity, η_{ly} doesn't change as the thickness of the layer or the concentration of the surfactant solution flowed through the QCM-D cell changes for the same surfactant solution. This is potentially due to the fact that the viscosity of the oil is already extremely large at 20-30 times that of water, and so the measurement is not able to detect small changes in the adsorbed layer viscosity. A preliminary fit for the viscosity was done for the 2.4% surfactant solution and then the viscosity of the layers at different concentrations was kept constant and the thickness and shear modulus were fitted as these parameters have a greater impact on the fit as the layer changes. The fitted values are shown in the right panels in Figure 5.21 and 5.22 and are summarised in Table 5.4 for lecithin, PGPR and their binary mixtures in GTO and TO.

In both oils, the addition of more surfactant leads to thicker layers. Lecithin in GTO forms thinner layer than the same amount of lecithin in TO, which suggests that lecithin layers in TO experience greater adhesion and tend to forms larger aggregate structures. At a given concentration, PGPR forms thicker layers than lecithin. By increasing the PGPR fraction in the surfactant mixture the layer increases in thickness by up to 50% for GTO and 200% for TO, for the

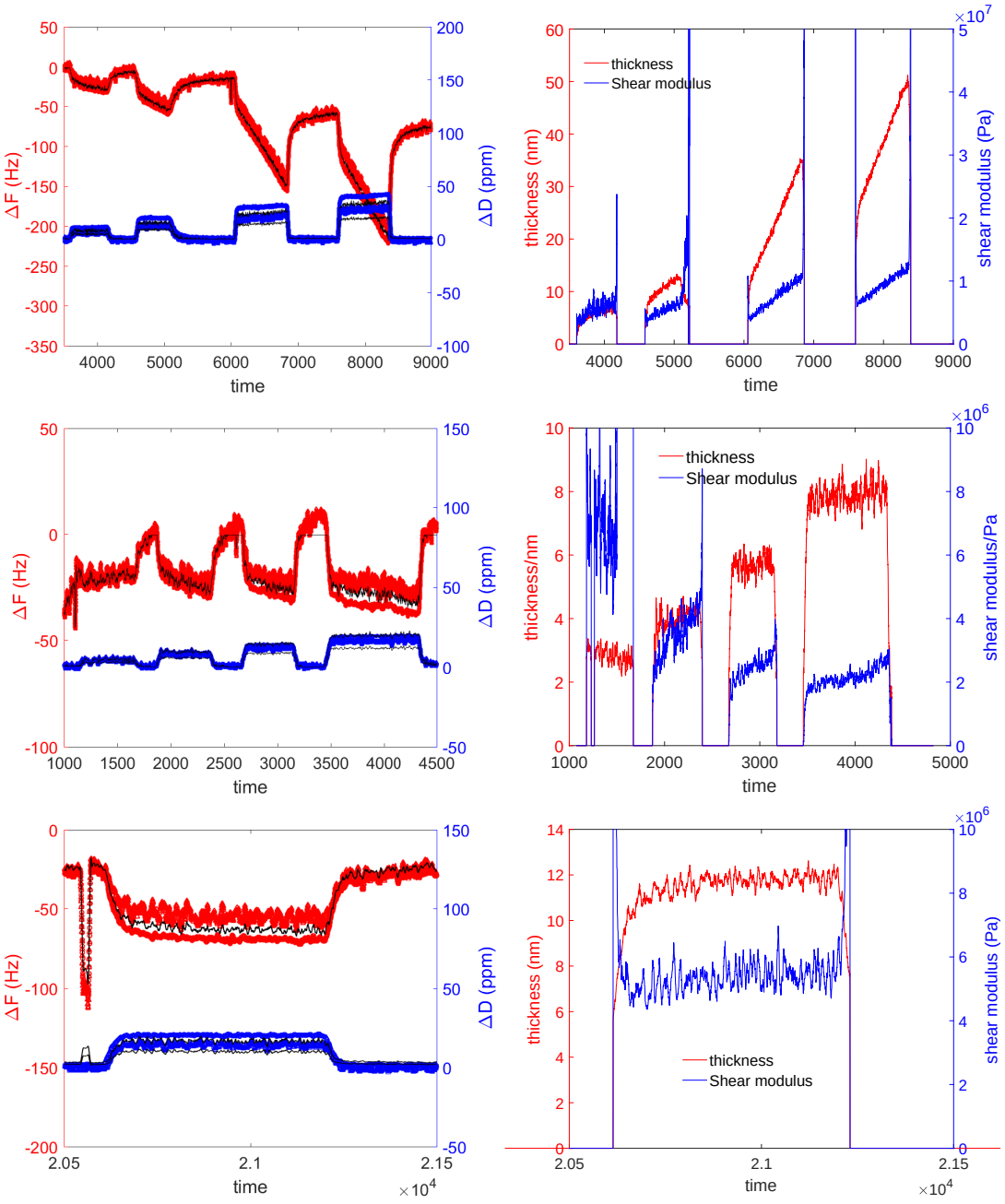

Figure 5.21 *QCM-D from solutions of surfactants in GTO with frequency (red) and dissipation (blue) data for the 3^{rd} and 5^{th} overtone and the Voigt model fit (black line) to the data using Q-tools on the left hand side. The right hand side shows the thickness (red) and the shear modulus (blue) obtained from the fits. Top panel: PGPR concentration series showing subsequent injections of 0.6%, 1.2%, 1.8% and 2.4% PGPR in GTO. Middle panel: lecithin concentration series showing subsequent injections of 0.6%, 1.2%, 1.8% and 2.4% lecithin in GTO. Bottom panel 1.2% lecithin + 1.2% PGPR in GTO.*

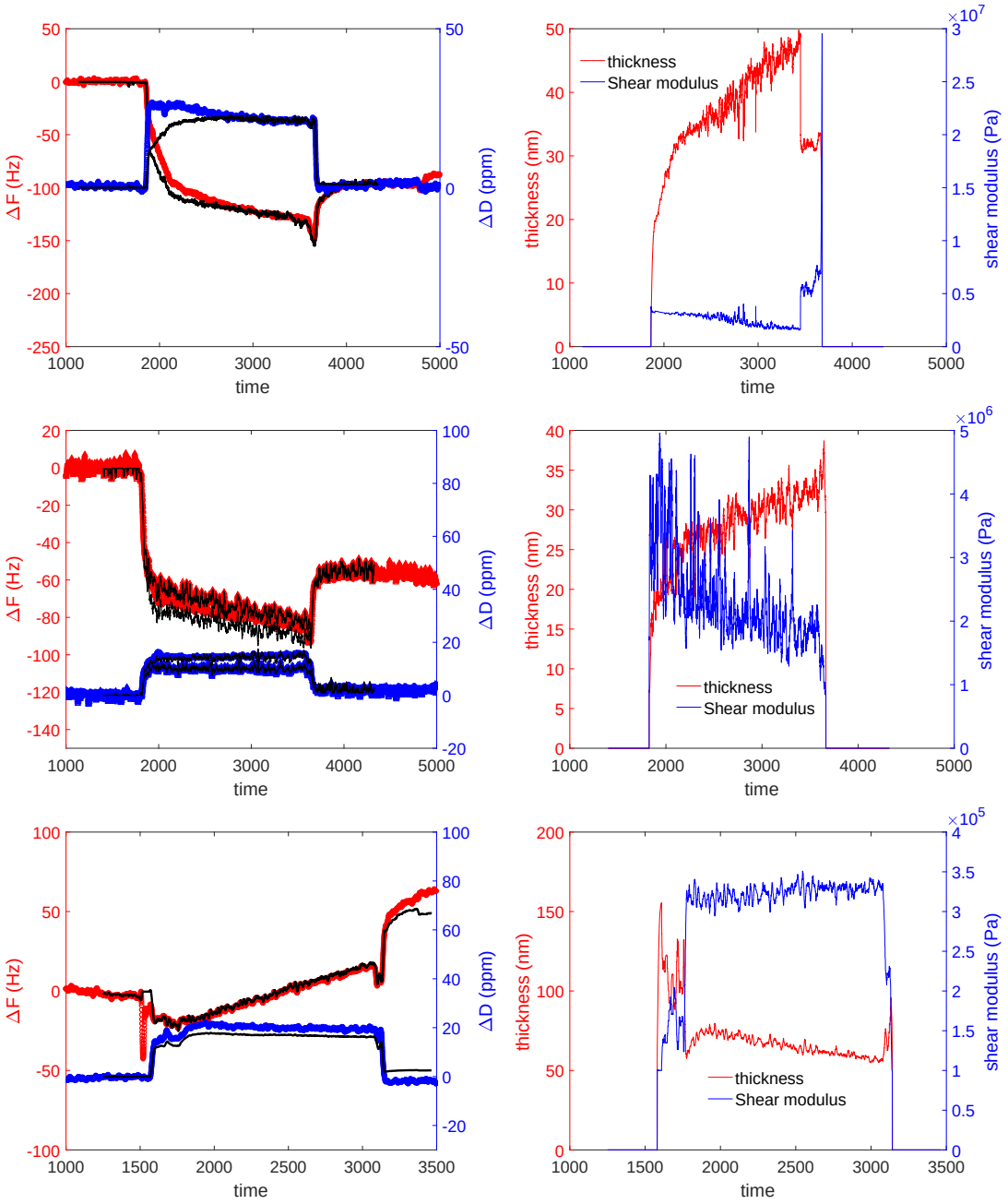

Figure 5.22 *QCM-D from solutions of surfactants in TO with frequency (red) and dissipation (blue) data for the 3^{rd} and 5^{th} overtone and the Voigt model fit (black line) to the data using Q-tools on the left hand side. The right hand side shows the thickness (red) and the shear modulus (blue) obtained from the fits. Top panel: 2.4% PGPR in TO. Middle panel: 2.4% lecithin in TO. Bottom panel: 0.6% lecithin + 1.8% PGPR in TO.*

Table 5.4 *Summary of the QCM-D data fits for the thickness and viscoelastic properties of the surfactant layers at the sucrose/triglyceride interface*

Surfactant %		η_{ly}[1] mPa s	h_{ly}[2] nm	μ_{ly}[3] MPa
lecithin	PGPR	GTO[4] at 20°C		
0	0	10 ± 1	9.8 ± 0.3	1.1 ± 0.1
0	0.6	500	5.5 ± 0.2	5.5 ± 0.3
0	1.2	500	10.1 ± 0.5	6.3 ± 0.5
0	1.8	500	23.1 ± 1.1	8.1 ± 0.9
0	2.4	500	37.6 ± 1.2	10.4 ± 1.3
0.6	0	1000	2.8 ± 0.1	42.7 ± 9.1
1.2	0	1000	3.9 ± 0.1	3.6 ± 0.2
1.8	0	1000	5.4 ± 0.2	2.4 ± 0.1
2.4	0	1000	7.3 ± 0.3	2.0 ± 0.1
1.8	0.6	1000	10.5 ± 0.1	7.1 ± 0.4
1.2	1.2	1000	11.7 ± 0.1	5.7 ± 0.3
0.6	1.8	1000	19.8 ± 0.2	4.1 ± 0.3
lecithin	PGPR	TO[4] at 40°C		
0	0	2.4 ± 0.3	8.4 ± 0.2	2.3 ± 0.3
0	0.6	50	7.7 ± 0.2	19.5 ± 0.8
0	1.2	50	27.2 ± 0.9	5.9 ± 0.6
0	2.4	50	36.5 ± 0.9	3.1 ± 0.2
1.2	0	100	11.6 ± 0.2	39.4 ± 2.7
1.8	0	100	16.7 ± 0.2	18.7 ± 2.5
2.4	0	100	23.7 ± 1.0	3.5 ± 0.2
1.8	0.6	150	27.7 ± 0.6	2.3 ± 0.1
1.2	1.2	150	36.9 ± 0.5	1.4 ± 0.1
0.6	1.8	150	70.9 ± 2.2	0.3 ± 0.1

[1] The viscosity that was used to fit the Voigt model.
[2] h_{ly} is the thickness of the layer obtained using the Voigt model fit which can then be converted into an adsorbed amount, Δm_{ly}, by multiplying it with the density of the layer (1.02 g cm^{-3}).
[3] μ_{ly} is the shear modulus of the adsorbed layers.
[4] The viscosity, η_l, for GTO and TO are taken to be their bulk values of 22 mPa s and 31 mPa s and the density, ρ_l, are taken as 0.956 g cm^{-3} and 0.91 g cm^{-3} respectively. These are the same values used to fit the oil only data.

1:3 lecithin to PGPR mixtures. This suggests that lecithin forms a relatively compact and rigid layer at the sucrose/triglyceride interface whereas addition of PGPR results in a more diffuse/extended layer evident from the higher ΔD for PGPR. The binary mixtures form structures that result in ΔF and ΔD response that are intermediate between those observed for lecithin and PGPR alone, where increasing the amount of PGPR in the surfactant mixtures makes the layer more diffuse as the PGPR helps in trapping oil in the layer and making it more swollen.

The shear modulus obtained for the surfactant layers is 10 times and the viscosity is $20 - 100$ times that for the oil layer. This suggests that the surfactant layers have more stress bearing capacity than the oil layer indicated by the larger shear modulus and also have higher resistance to deformation indicated by the larger viscosity. For PGPR in GTO the shear modulus of the layer increases as the thickness of the layer increases, consistent with the increase in concentration of PGPR in the solution. The shear modulus in general depends on two factors: the intrinsic material deformation property and the geometry of the layer. The monotonic increase in the shear modulus with thickness suggests that the PGPR layer formed in GTO has a constant deformation property as will be the case for a polymer brush layer [105]. The presence of a polymer brush-like layer, resulting in a diffuse layer, is also consistent with the exponent of < -4.2 observed for the low q power law dependence of the SANS from model chocolate suspensions in GTO with 0.8% PGPR. For lecithin in GTO and PGPR and lecithin in TO the shear modulus decreases as the thickness of the layer increases which indicates that the deformation property of the material decreases quicker than the thickness increases. This suggests we are absorbing a near interface surfactant layer that is stiff, possibly a high volume fraction monolayer, followed by layers which are loosely bound to the interface as would be the case for adsorption of micelles of lecithin and PGPR. The binary mixtures also have shear modulus which decrease as the thickness of the layer increases, which again indicates that the deformation property decreases as the thickness increases.

In addition to short time scale adsorption studies, long time scale studies were carried out for lecithin, PGPR and their 1:1 binary mixture in TO. It was observed that lecithin and PGPR stabilised at a thickness of 45 nm and 90 nm, respectively, after $4 - 5$ hours. However, the binary mixture grew to 100s of nm in a span of $10 - 18$ hours. This suggest that the binary mixture is capable of forming very

large swollen structures over long time scales by incorporating more oil[3].

5.5 Comparison with Adsorption of Lecithin and PGPR in Sucrose in Triglyceride Oil Suspensions

As is shown in Chapter 4, SAXS and SANS give the adsorbed layer thickness of lecithin in sucrose/triglyceride suspensions as 8 nm in GTO and 12 nm in the longer chain Tripalmitin. This is very similar to the values obtained by QCM-D of 7 nm for 2.4% lecithin in GTO and 23 nm for 2.4% lecithin in TO. The difference in thickness between TO and TP can be explained as a consequence of either higher adsorption in TO than in TP or due to larger amount of solvent being entrained in the phospholipid layers in the case of the long chain triglyceride due to the similarity between the oleic and palmitic acid tails with the tails of majority components in lecithin than in the case for GTO. Increasing the PGPR fraction of the surfactant mixture results in increases in the layer thickness measured using scattering for sucrose/triglyceride oil suspensions and determined here for planar sucrose/triglyceride oil interfaces by fitting the QCM-D data. A 3:1 lecithin/PGPR mixture results in a layer thickness of 10 nm for suspensions in GTO and 11 nm suspensions in TP determined from scattering and 11 nm for GTO and 28 nm for TO obtained from QCM-D whereas a 1:1 mixture results in layer thickness of 13 nm suspensions in GTO and 21 nm suspensions in TP measured by scattering and 12 nm for GTO and 37 nm for TO obtained for QCM-D and a 1:3 mixture results in layer thickness of 17 nm for suspension in GTO and 22 nm for suspensions in TP measured by scattering and 20 nm for GTO and 70 nm for TO obtained for QCM-D.

The increase in dissipation measured in QCM-D as the PGPR content increases and the less pronounced shoulders (or change in slope) in small angle scattering are consistent with the layers becoming more diffuse. The values of the adsorbed amount obtained from QCM-D are higher than those obtained from scattering as there will be some triglyceride oil entrained by the absorbed layer which adds mass (lowers frequency) and is responsible for the high dissipation of these layers. The oil entrained is higher for the longer chain TO than for the GTO as evident

[3]In chocolate making process the formation of these large structures can be expedited by applying shear during conching

from the difference between the scattering and QCM-D measurements between GTO and the longer chain oils. Another factor that may be responsible for the difference is the fact that the same molar concentration of the surfactants has been used in the suspensions measured by scattering and planar substrates QCM-D but the amount of surface area available for the adsorption of the surfactant is higher in the suspensions as compared to planar substrates. The two techniques give consistent results for lecithin only, 3:1, 1:1 and 1:3 lecithin/PGPR mixtures. However, for PGPR only samples it was not possible to obtain an adsorbed layer thickness using scattering as there is no contrast between PGPR and oil. The scattering curve does decay as $q^{-4.4}$ for suspensions in GTO, which is consistent with an extended diffuse interface. QCM-D gives the adsorbed layer thickness for PGPR at the sucrose interface, 37 nm for 2.4% PGPR in both GTO and TO. Furthermore, the higher ΔD observed for the PGPR rich mixtures is consistent with a diffuse interface that couples to the solution, increasing dissipation.

Based on the complementary scattering and QCM-D measurements, we hypothesise that lecithin forms a densely packed layer comprising either lipid layers or micelles which entrap small amount of oil. Such a layer can lubricate the sucrose grains thereby reducing friction between them and has a high load bearing capacity and hence reduces the viscosity of the suspension. However, as the layer is relatively thin it is not very effective at reducing the yield stress between the particles. On the other hand PGPR forms a solvated polymer layer which is both diffuse and extended. This extended layer provides a steric repulsion, osmotically pushing the sucrose grains apart reducing the Van der Waals interaction between the particles and therefore reducing the yield stress of the suspensions. However, the lower rigidity of these solvated polymer layers makes them less effective at providing lubrication, especially at high shear stress as the layer deforms. This makes PGPR less effective at reducing the high shear viscosity of the suspension. A binary mixture of the two surfactants can form a structure which has the lubrication and load bearing capacity of the semi-rigid lecithin layers reducing the high shear viscosity of the suspension, whilst the presence of the polymer, solvated by oil, swells that layer providing the steric repulsion required to lower the yield stress of the suspension. How the lecithin and PGPR are arranged in these layers remains an open question: whether there is a surface bound lecithin layer decorated by PGPR or the molecules are mixed within the layers. This structural detail cannot be provided by either QCM-D or scattering from suspensions. However, the agreement between the two suggests that planar sucrose substrates can be used to carry out detailed structural investigation of the surfactant layers

at the sucrose/triglyceride. In Chapter 6 and 7, neutron and x-ray reflectivity from planar sucrose/triglyceride oil interface are used to conduct more detailed structural investigation of these surfactant films.

5.6 Conclusions

A procedure for fabricating planar spin-coated sucrose films of thicknesses in the range μm−nm onto silicon substrates which can be used for detailed interfacial adsorption and structural studies has been developed. The planar spin-coated sucrose films are crystalline with the (100) crystal plane facing the surface, making it relevant for examining surfactant interactions with sucrose. These substrates have then been used for interfacial activity and adsorption studies.

Contact angle tensiometry demonstrates that the triglyceride oils wet the sucrose interface as the contact angle for both TO and GTO is $<20^\circ$ and QCM-D from the sucrose/triglyceride oil interface shows the formation of $\sim$10 nm thick viscoelastic layers capable of sustaining a shear stress. These studies indicate that the role of the added surfactants is not as a wetting agent but rather as rheology modifiers. This suggests that the interfacial structure and viscoelastic properties of the surfactants are important to understand their role as rheology modifiers.

Addition of surfactants lowers the contact angle of the oil droplet to $\sim5^\circ$ indicating that the surfactants adsorb at the sucrose interface. This is also confirmed by the QCM-D studies where a change in frequency and dissipation is observed upon the addition of surfactants. To fully explain the shifts in ΔF and ΔD obtained in the QCM-D measurements it is necessary to assume that the adsorbed layer has viscoelastic properties which can be modelled using the Voigt model. In both TO and GTO and for both lecithin and PGPR increasing the surfactant concentration in the solution leads to higher adsorbed amount and thicker layers. Lecithin at 2.4% w/w concentration (same molar concentration as chocolate) in both TO and GTO forms compact layers of $10-20$ nm with high viscosity. The shear modulus of the lecithin decreases as the layer thickness increases, which suggests that the near sucrose interface lecithin layer are compact and rigid but become more flexible as the layer grows, possibly consisting of adsorbed micelles. At the same surfactant concentration, PGPR forms thicker layers than lecithin, with 2.4% PGPR forming 35 nm thick layers. The shear behaviour of PGPR in TO is similar to lecithin layers, again suggesting adsorption of PGPR micelles/aggregates at

the sucrose interface. The shear modulus of PGPR layers in GTO increases as the thickness increases suggesting adsorption of a polymer brush type layer with constant shear properties with thickness. A binary mixture of lecithin and PGPR forms structures with shear properties similar to the lecithin layer but with much greater thickness than for lecithin only films. This indicates that an intermediate structure is formed between lecithin and PGPR but it is not possible to discern the details of this structure using QCM-D measurements.

The values obtained for the adsorbed amount of surfactant at planar sucrose interfaces and the nature of these surfactant films using QCM-D match well to the ones obtained using Small Angle Scattering from sucrose/triglyceride suspensions. The agreement between adsorption studies on sucrose/triglyceride suspensions and planar sucrose/triglyceride surfaces is encouraging and means that the planar spin-coated sucrose/triglyceride interfaces can be used to carry out detailed structural investigations using neutron and x-ray reflectivity studies of the adsorbed interfacial lecithin and PGPR layers to provide a more detailed structural basis for the role played by each of these surfactants in effectively reducing the viscosity and yield stress in chocolate.

Chapter 6

Reflectivity Studies at Planar Sucrose/Triglyceride Interface-I

6.1 Introduction

Chapter 5 described well-defined, crystalline, nm−μm thick, planar sucrose substrates that can be used in flow cells through which triglyceride oil is flowed. This provides a way to investigate the detailed structure at the sucrose/triglyceride interface by zooming in at a single sucrose/triglyceride interface found in the model chocolate suspensions, discussed in Chapters 2 and 4. Neutron Reflectivity (NR) and X-Ray Reflectivity (XRR) can be used to to conduct detailed structural investigations at this planar sucrose/triglyceride oil interface to better understand the interaction of the triglyceride oil and the surfactants with the sucrose interface. Reflectivity is a well established technique to study the structural details of layers at planar interfaces on the Ångstrom−nanometer scale [85] and it has been successfully applied to understand various solid/liquid interfaces, for example metal/oil [106], silicon/water [107], sapphire/water [108], mica/water [109].

In order to understand the changes caused by surfactants at the sucrose/triglyceride oil interface, it is first essential to understand the sucrose/triglyceride oil interface without surfactants. Contact angle measurements, discussed in Section 5.3.3, show that the triglyceride oil wets the sucrose interface. QCM-D studies, detailed in Section 5.4.3, show the presence of a ∼10 nm triglyceride oil

layer at the sucrose interface with viscoelastic properties different from the bulk. XRR and NR can be used to provide the structural details of this triglyceride layer to understand the underlying interaction mechanism.

In this chapter structural investigations at sucrose/triglyceride oil interface without surfactants using NR and XRR are discussed. In Section 6.2 a brief overview of the neutron and x-ray reflectivity technique is provided followed by the experimental and cell design for low volume (and therefore small beam footprint) laminar flow cells and sandwich cells. Thereafter, in Section 6.3 reflectivity studies of triglyceride oil at the sucrose interface are discussed which provide molecular understanding of the layering of triglyceride oil at the sucrose interface.

6.2 Neutron and X-Ray Reflectivity from Thin Interfacial Films at Solid-Liquid Interface

Neutron and X-Ray Reflectivity are powerful surface sensitive techniques often used together to characterize surfaces, thin films and interfaces [85]. They are typically used to investigate buried interfaces on the nanoscale, $1-100$ nm, which matches nicely to the dimension of the triglyceride and surfactant molecule and films observed in the model chocolate systems and so can be used to provide structural details of the adsorbed surfactant layers at the sucrose/triglyceride oil interface.

6.2.1 Theory of Reflectivity

Reflectivity is a scattering technique based the same formulation as described in Section 1.4, with the caveat that the Born approximation of weak scattering is no longer true. Specular reflectivity measures the elastic interaction of neutrons or x-rays with a sample, with the angle of reflection equal to the angle of incidence. The reflectivity measured depends on the variation in the scattering length density (x-ray or neutron) profile normal to the interface, which can be used to determine the structure and composition of systems [107].

A schematic representation of specular neutron and x-ray reflection from a solid/liquid interface is shown in Figure 6.1. Generally in reflectivity experiments,

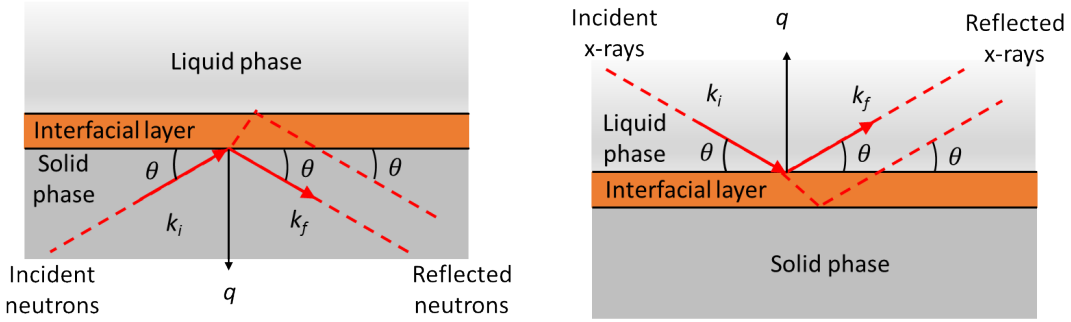

Figure 6.1 *Schematic showing the geometric optics for specular reflection from an interfacial layer at solid/liquid interface. Left panel: Neutron Reflectivity. Right panel: X-Ray Reflectivity.*

the neutrons are incident from the solid phase (typically silicon substrate) whereas x-rays are incident from the liquid phase due to the relative penetration depth of the radiation in the two bulk phases. Substrates such as silicon, alumina, etc are transparent to neutrons whereas energetic x-rays, as produced from synchrotron sources, have greater penetration depth through liquids such as water or oil. Apart from this difference in experimental design and the comparison drawn in Section 1.4.3, the theory for reflection of neutrons and x-rays is the the same. The discussion presented here is based on *Introduction to Small Angle Neutron Scattering and Neutron Reflectivity* by A. K. Jackson [3].

Due to their wave nature, neutrons and x-rays obey the same laws as electromagnetic radiation, with the electric vector perpendicular to the plane of incidence. Hence most of the constructs of classical optics are also applicable to neutron and x-ray reflection. As in classical optics to observe interference effects from the interface, there must be a change in the refractive index across it [110]. The refractive index, n, at the boundary between the two media is defined as:

$$n = \frac{k_2}{k_1} \tag{6.1}$$

where k_1 and k_2 are the wave vectors in media 1 and 2, respectively. The refractive index of of the material relative to vacuum can be written as [107]:

$$n = 1 - \frac{\lambda^2 \rho_i}{2\pi} \tag{6.2}$$

where ρ_i is the SLD of the medium and λ is the wavelength of the scattered radiation. The imaginary contribution to Equation 6.2 arising from the complex

nature of the scattering length due to the absorption cross-section has been neglected. This is negligible for all the materials considered in this thesis and is only relevant to strong absorbers such as cadmium.

The refractive index for most media is less than unity i.e. $n<1$, and so neutrons are totally externally reflected when incident from air, or other material of lower SLD, to a material of higher SLD e.g. silicon or D_2O. Snell's law gives the critical angle, θ_c, below which total internal reflection occurs as:

$$\cos\theta_c = \frac{n_2}{n_1} \tag{6.3}$$

Expanding $\cos(\theta_c)$ for small θ and substituting back in Equation 6.2 gives:

$$\theta_c = \lambda\sqrt{\frac{\Delta\rho}{\pi}} \tag{6.4}$$

where $\Delta\rho$ is the difference between the SLD of the two media. This can be redefined in terms of the critical scattering vector, q_c, as:

$$q_c = \sqrt{16\pi\Delta\rho} \tag{6.5}$$

The specular reflectivity from the interface between two media is given by Fresnel's law, where for $\theta \leq \theta_c$ the reflectivity $R = 1$ and for $\theta \geq \theta_c$:

$$R = |r|^2 = \left|\frac{n_1\sin\theta_1 - n_2\sin\theta_2}{n_1\sin\theta_1 + n_2\sin\theta_2}\right|^2 \tag{6.6}$$

where r is the Fresnel's reflection coefficient and θ_1 and θ_2 are the angles of reflection and refraction respectively. At high q the reflectivity falls off as q^{-4}, given by:

$$R(q) = \frac{16\pi^2\Delta\rho^2}{q^4} \tag{6.7}$$

This is known as Fresnel's decay and describes reflection from a planar smooth interface. The presence of an interfacial layer between the two bulk media will alter the reflectivity producing Kiessig fringes in the measured reflectivity profile. The spacing between these fringes, Δq, gives the thickness of the film, d, as:

$$d = \frac{2\pi}{\Delta q} \tag{6.8}$$

In case of more than one layer or a more complex layer, the Kiessig fringes will be modulated, analogous to the beating effect observed for interference of

waves. Another factor that modulates the reflectivity profile is variations at the interface on the length-scale of the neutron or x-rays wavelength, for example local substrate roughness will smear the reflectivity profile and is indistinguishable from a truly diffuse interfacial layer. The effect of roughness can be accounted for by multiplying the Fresnel's reflectivity, R_0 from Equation 6.6 by the Nevot-Croce factor [111]:

$$R = R_0 e^{-q_1 q_2 \sigma^2} \tag{6.9}$$

which assumes root-mean-square Gaussian distribution of roughness, $\sqrt{\sigma^2}$, comparable to the Debye-Waller factor and also takes into account the difference in the average wave-vector either side of the interface, q_1 and q_2.

6.2.2 Data Analysis

The neutron and x-ray reflectivity data presented in this thesis were analysed using the RasCAL MATLAB procedure [112]. Custom models were constructed to simulate the measured reflectivity profiles, by modelling contributions from different parts of the interface to the SLD profiles normal to the surface. The interface is divided into a series of sub-layers. The silicon, silicon oxide, sucrose and bulk triglyceride oil layers are modelled as layers constructed from their SLD, thickness and roughness (interfacial width), with the density distribution of each layer modelled as a sum of two error functions. The interfacially layered triglyceride oil or surfactant layer is either modelled using analytical functions (layer triglyceride oil and polymer) or as the error function based layers approach described above (lecithin). The complete SLD profile is then sliced into 1 Å layers. The SLD of the various components was calculated from the sum of the component's scattering lengths within the layer and the known molecular volumes of the component groups [113].

An optical matrix method is used to calculate reflectivity from these sub-layers, in which the layer "optical properties" are determined by the model fit parameters [114]. Fitting of these parameters is achieved by means of a combination of global searches using the Covariance Matrix Adaptation Evolution Strategy (CMAES) and local search using the simplex strategy with the parameters allowed to vary within applied boundaries. The simulated reflectivity profile for a set of model parameters is calculated and compared to the measured

reflectivity profile, with an error weighted least-squares minimization of χ^2 used to direct the optimization of the parameters over a population size of 1000, for $10000 - 50000$ iterations. Rather than constructing a simultaneous global optimum of the various neutron and x-ray contrasts measured for a particular system, the different data sets are instead fitting sequentially, but in a self consistent approach. The fitting was done in this way as different silicon and sucrose substrates had to be used for each contrast and to take account of the sensitivity of the x-ray and neutron measurements for different structural elements.

Confidence bands on the parameters were determined using RasCAL's in-built Bayesian analysis based on the MCMC algorithm using 100000 MCMC points and 1000 burn-in points. This approach allows the determination of the probability distribution of the posteriors, i.e. the fit parameters, based on the defined priors. In this case Gaussian or uniform priors were used (as specified). A shaded region around the calculated reflectivity and SLD profiles shows the 95% Bayesian prediction intervals calculated from the maximum and minimum ranges of the parameter posteriors. A Bayesian approach allows the incorporation of more prior knowledge into the analysis than the Bootstrap method, whist allowing a considerable amount of flexibility. This is particularly useful for multi-technique approach as adopted in this thesis as it allows us to incorporate knowledge from complimentary techniques such as QCM-D and SANS from suspensions in specifying ranges for various fir parameters. A detailed description of Bayesian methods for reflectivity analysis can be found in Sivia *et. al.* [115] and Hughes *et. al* [116].

6.2.3 Materials and Sample Preparation

Sucrose was obtained from British Sugar with average particle size $\sim$10 μm, as characterised in Chapter 2, and dissolved in Millipore Milli-Q water with resistivity 18.2 MΩ cm and TOC = 4 ppb to prepare 125 mM solution to be used for spin-coating. Pure triglyceride oil, GTO ($\geq$99%) and TO ($\geq$99%), used as bulk phase were obtained from Sigma Aldrich, UK. Perdeuterated Glyceryl Trioctanoate (d-GTO) and d-96 Glyceryl Trioleate (d-TO) used for d50-oil contrast for the bulk phase were obtained from ISIS Deuteration Facility, Oxford, UK and National Deuteration Facility, ANSTO, Australia, respectively.

Sucrose was spin-coated onto 55 mm diameter (5 mm thick) circular silicon blocks

using the procedure described in Chapter 5. These sucrose spin-coated silicon blocks were used as substrates in low volume laminar flow cells or in sandwich cells as described in Section 6.2.4. Neutron reflectivity was measured using h-GTO, d50-GTO (50:50 volume by volume mixture of h-GTO and d-GTO), h-TO and d50-TO (50:50 volume by volume mixture of h-TO and d-TO) as the triglyceride oil bulk phase. X-ray reflectivity was measured using h-GTO and h-TO as the triglyceride oil phase.

6.2.4 Low Volume Cells for Neutron and X-Ray Reflectivity

Deuterated triglyceride oils are extremely expensive, costing £1000-£20000 for 1 g of material. In order to limit the amount the deuterated oil used two measures were applied. Firstly, instead of using a fully deuterated bulk phase as one of the contrasts, d50-triglyceride oil was used which can provide contrast for h-material particularly in the case of PGPR whilst reducing the amount of d-oil required per measurement. Secondly, low volume flow cells were developed to limit the amount of triglyceride oil required per measurement.

Low Volume Solid/Liquid Laminar Flow Cell for Neutron and X-Ray Reflectivity

Low volume laminar flow cells were developed as shown in the drawing on the left panel and photograph shown in the right panel of Figure 6.2.

The cell consists of a PEEK block with two 1.5 mm channels, one for inlet and other for outlet, running through either side of the block as shown in the left panel of Figure 6.2. A square cavity of 28×28 mm with depth 0.5 mm is present on one of the face of the PEEK block into which the solution is injected or withdrawn from using the 7 holes on each side of the cavity; one set is connected to the inlet channel and other to the outlet channel. The cell is sealed using an o-ring against the sucrose spin-coated silicon block, through which the neutron beam enters, with the sucrose spin coated polished surface facing the cavity. The flow connection to this cell were made using 1/16" PTFE tubing and connectors. A syringe pump was used to inject the solution into the cell. The sealing and filling of the cell is shown in the right panel of Figure 6.2, where the silicon block has been replaced by an optical flat so that the solution in the cavity is visible. The exchange volume of these cells is $\sim$1 mL, which limits the amount of d-triglyceride

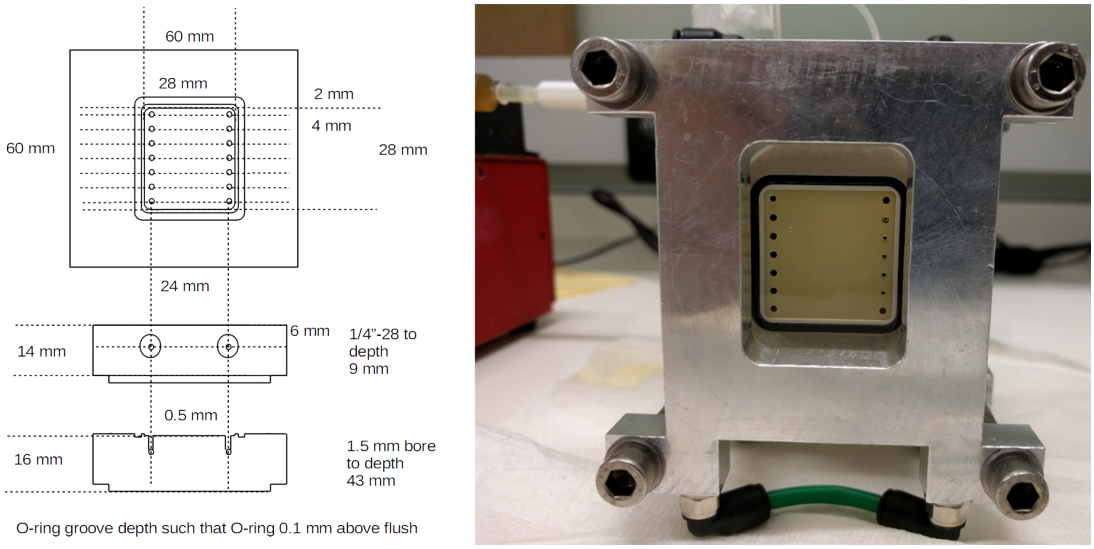

Figure 6.2 *Low volume laminar flow cell used for neutron reflectivity from sucrose/triglyceride interface. Left panel: Drawing of the cell. Right panel: A photograph showing the flow cell with an optical flat in place of the sucrose spin-coated substrate to demonstrate the filling of the cell with GTO containing lecithin.*

oil required per measurement such that 12-15 measurements could be conducted using 20 g of d50-GTO (made from 10 g of d-GTO).

An analogous cell was developed for x-ray reflectivity as shown in Figure 6.3. A thin layer of PEEK at the top of the cell cavity provides a way for the x-rays to enter without undergoing too much absorption. The silicon block with the polished sucrose spin-coated surface facing the thin PEEK side sits on a circular offset on another PEEK block. The two PEEK blocks are sealed using an o-ring and screws. The sealing is such there is a cavity of 1 mm thickness cavity between the thin PEEK side and the silicon block into which the triglyceride oil can be injected. The inlet and outlet are through the side of the cell, with injection through 1 hole and the withdrawl of solution through one hole on the other side of the cell. This set-up allows x-ray and neutron reflectivity to be measured from the same substrates.

For reflectivity measurements, the cells were assembled and filled with the triglyceride oil and reflectivity from the sucrose/triglyceride interface was measured. Thereafter, surfactant solution in the same triglyceride oil was injected and reflectivity profiles were measured until two consecutive reflectivity profiles showed no change i.e the adsorption of the surfactants had reached equilibrium.

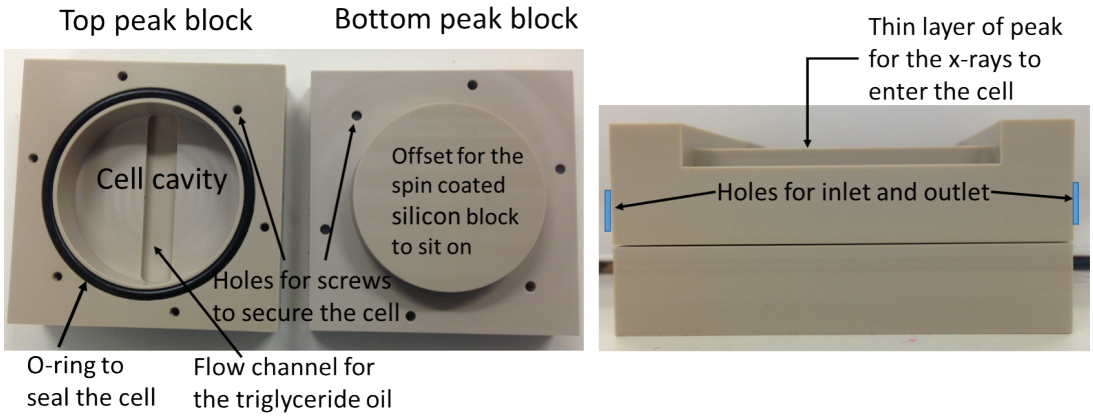

Figure 6.3 *Picture of the laminar flow cell used for x-ray reflectivity experiments.*

Low Volume Sandwich Cell for Neutron Reflectivity.

Deuterated TO is prohibitively expensive costing >£12000 for 1 g. In order to reduce the sample volume further such that 3-5 measurements could be conducted using 2 g of d50-TO (made from 1 g of d96-TO), a low volume sandwich cell was developed as shown in Figure 6.4.

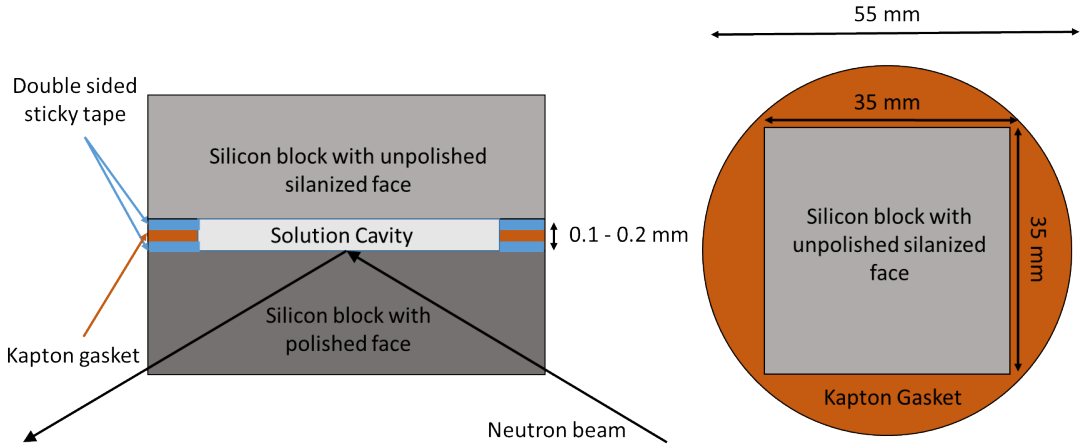

Figure 6.4 *Schematic of the sandwich cell used for neutron reflectivity experiments with d50-TO. Left panel: A cross-section showing the various vertical layers. Right panel: A layout of the unpolished silanized silicon block showing the various components.*

In this cell two silicon blocks are sandwiched together with a Kapton gasket of thickness $0.1 - 0.2$ mm held in place using double sided sticky tape as shown in the left panel of Figure 6.4. This produces a solution cavity of 200 μL into which

the d50-TO containing lecithin and PGPR can be sandwiched. A silicon block silanized with Octadecyltrichlorosilane is used on the unpolished side to provide one face of the cavity; the unpolished face means there will be no reflection from this interface. A Kapton gasket is stuck onto this with an internal cavity of 35×35 mm as shown in the right panel of Figure 6.4. A second silicon block, through which the neutron beam enters, with the polished surface spin-coated with sucrose facing the cavity, forms the other face of the cavity and completes the sandwich. It is onto this surface that a droplet of the solution is spread.

The sample solution cannot be exchanged in these cells, however they facilitate the measurement of lecithin, PGPR and their binary mixtures in d50-TO using 200 μL of solution per sample.

6.2.5 Experimental Details

The neutron reflectivity experiments detailed in this chapter were performed on OFFSPEC (RB1600043) and INTER (RB1720367) beamlines at ISIS, STFC, UK and D17 (9-13-642) beamline at ILL, Grenoble, France. The neutron wavelength at ISIS Target Station 2 is $2 - 14$ Å. On OFFSPEC using incident angles of 0.32°, 0.64°, 0.9° and 1.6°, a q-range of 0.006 $\text{Å}^{-1} \leq q \leq 0.15$ Å^{-1} was obtained and on INTER using incident angles of 0.32°, 0.9° and 2.3°, a q-range of 0.005 $\text{Å}^{-1} \leq q \leq 0.3$ Å^{-1} was obtained. On D17 the neutrons have wavelengths in the range $2 - 27$ Å. Using incident angles of 0.8° and 2.4°, a q-range of 0.006 $\text{Å}^{-1} \leq q \leq 0.25$ Å^{-1} was obtained. The x-ray reflectivity experiment detailed in this chapter was carried out on I07 (SI15202-1), Diamond, Oxford, UK. Using 24.4 keV x-rays with wavelength 0.51 Å, data was collected in a q-range spanning 0.017 $\text{Å}^{-1} \leq q \leq 0.32$ Å^{-1} by changing the incident angle and using different levels of attenuation in the incident beam.

The small sample size means that the beam foot-print also needs to be small, which is achieved using narrow slit spacings for the incident beams on the neutron reflectometers, resulting in low incident intensity of neutrons. On OFFSPEC the low incident intensity resulted in long counting times of ∼4 hours to achieve a reasonable signal to noise ratio. The reflectivity profile so obtained has smeared features because of the changes in the interfacial film due to adsorption of the surfactant over these long time-scales. These reflectivity profiles are not useful for obtaining the structure of the adsorbed interfacial surfactant films, however the experiment verified the use of the low volume-laminar flow cells with the

sucrose substrates for reflectivity studies of surfactant films at sucrose/triglyceride oil interface. They also provided qualitative information on the nature of the interfacial films and adsorption time-scales allowing the subsequent experiments on D-17 and INTER to be optimised. The counting times on INTER and D17 are $45 - 75$ min to obtain reasonable counting statistics due to higher flux and implementing a novel divergent-beam method on D17 [117, 118]. The divergent beam method allows for a wider second collimation slit, which increases the incident neutron flux. This results in a spreading of the observed specular reflectivity profile in the lateral direction. This can be taken into account by summing pixels on a 2-D detector that describe a constant q rather than a constant wavelength, called the coherent summing method [119]. Using this method, the loss of resolution caused by opening the collimating slits to increase incident flux can be recovered to a great extent such that improved signal to noise ratio can be obtained from a small foot-print sample such as ours within a reasonable counting time.

6.3 Layering of Triglyceride at Sucrose Interface - Reflectivity Study

Triglyceride based oils are used extensively as lubricants for mechanical applications. Examples include spreading of olive oil on roads by ancient Romans [120] and the currently growing use as bio-lubricant in automotive applications [121]. Studies suggest that in these applications, the triglyceride adsorb at the polar/non-polar interface reducing interfacial energy and frictional contact [122]. Dedinaite *et. al.* [123, 124] studied the interaction between mica and hydrophobised mica surfaces across triolein using surface force measurements. In each case repulsive force barriers are observed, at separations of $25 - 30$ Å and $50 - 60$Å in the case of mica, and $20 - 25$ Å and $40 - 45$Å in the case of hydrophobised mica. The presence of periodic force barriers is consistent with layering of the oil molecules [125]. The greater spacing in the hydrophilic case suggests that the molecules are oriented perpendicular to the interface possibly with the glycerol backbone adsorbed on the surface and the oleic acid tails oriented into the bulk oil. Measurement of shear forces for layered oils have indicated that the layered films can have significantly higher viscosities than the bulk, and display solid-like properties such as supporting a shear stress [126].

In many food formulations water or polar solids are present in a triglyceride fat phase, for example mayonnaise, ice cream and chocolate. Therefore, it is important to understand the interaction of triglyceride with a polar interface. Various studies have been conducted with triglyceride oil/water systems [127–132] however, studies with relevant solid interfaces are limited [8, 29]. We have developed a novel way of looking at a single sucrose/triglyceride oil interface, discussed in Chapter 5, to understand interactions relevant for food formulations, specifically chocolate. Contact angle measurements, discussed in Section 5.3.3, show that the triglyceride oil wets the sucrose interface which is consistent with an interaction of the glycerol backbone with the polar sucrose interface. QCM-D studies of triglyceride oils, GTO and TO, at the sucrose interface, discussed in Section 5.4.3, show the presence of a near interface viscoelastic triglyceride layer of 10 nm. This is a signature of the same kind of interfacially induced ordering of triglyceride molecules suggested by Dedinaite *et. al.* to explain their surface force measurements and which promotes the wetting of sucrose surface by the triglyceride oil. To investigate the structure of this triglyceride layer at the sucrose interface, x-ray and neutron reflectivity studies at the sucrose/triglyceride oil have been conducted.

6.3.1 X-Ray and Neutron Reflectivity from Sucrose/Triglyceride Oil Interface

XRR was measured from the sucrose/triglyceride oil interface for h-TO and h-GTO with the x-rays incident from the triglyceride oil phase and is shown in the left panels of Figures 6.5 and 6.6, respectively, and NR was measured for h-TO, h-GTO and d50-GTO with the neutrons incident through the silicon block as shown in the left panels of Figures 6.7 and 6.8, respectively.

The neutron and x-ray SLDs of the various components of the triglyceride oil are listed in Table 6.1. The reflectivity profile was initially fitted to a simple thin film model comprising triglyceride oil, sucrose, silicon oxide and silicon layers with thickness of each layer and the roughness of each interface as fit parameters. The fits obtained for the reflectivity profile are shown as the solid lines in the left panels and the corresponding SLD profile in the right panels of Figure 6.5, 6.6, 6.7 and 6.8.

The resultant fits for the XRR profile give an interfacial width of 35-50 Å with

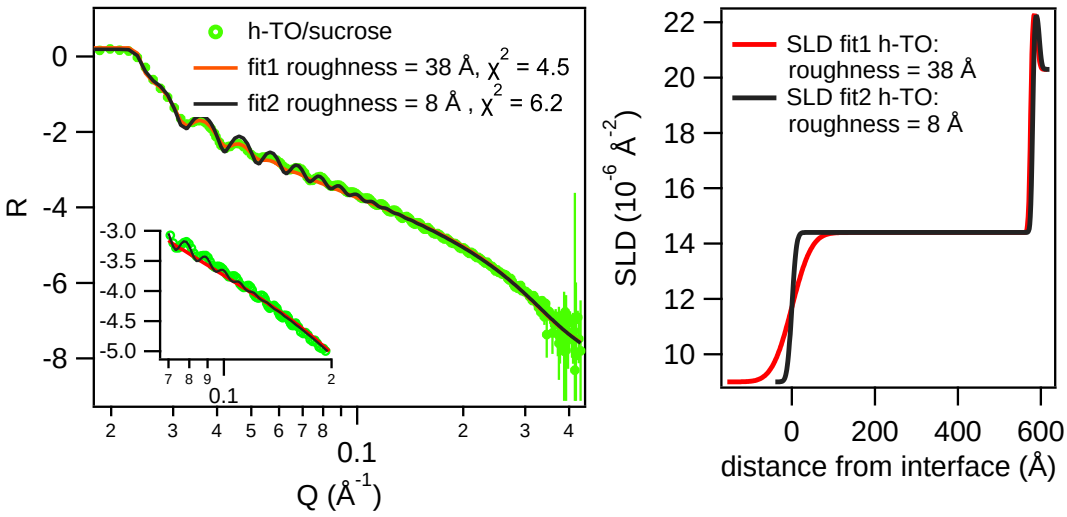

Figure 6.5 *XRR from h-TO/sucrose interface. Left panel: XRR profile (hollow circles) and the fit (solid line) using a simple layer model. The inset shows the zoomed in XRR and fits for* $0.07\ \text{Å}^{-1} \leq q \leq 0.2\ \text{Å}^{-1}$. *Right panel: SLD profile corresponding to the fit.*

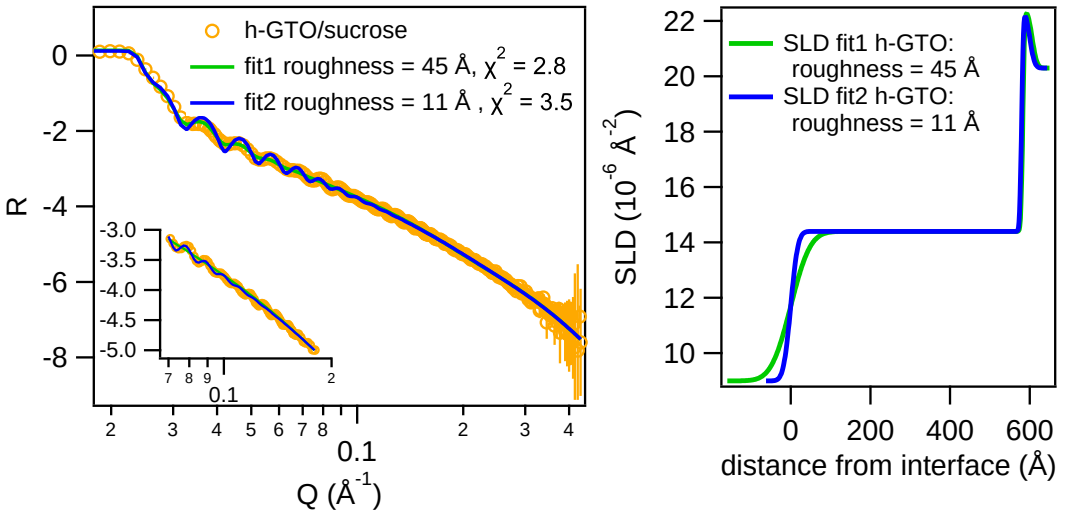

Figure 6.6 *XRR from h-GTO/sucrose interface. Left panel: XRR profile (hollow circles) and the fit (solid line) using a simple layer model. The inset shows the zoomed in XRR and fits for* $0.07\ \text{Å}^{-1} \leq q \leq 0.2\ \text{Å}^{-1}$. *Right panel: SLD profile corresponding to the fit.*

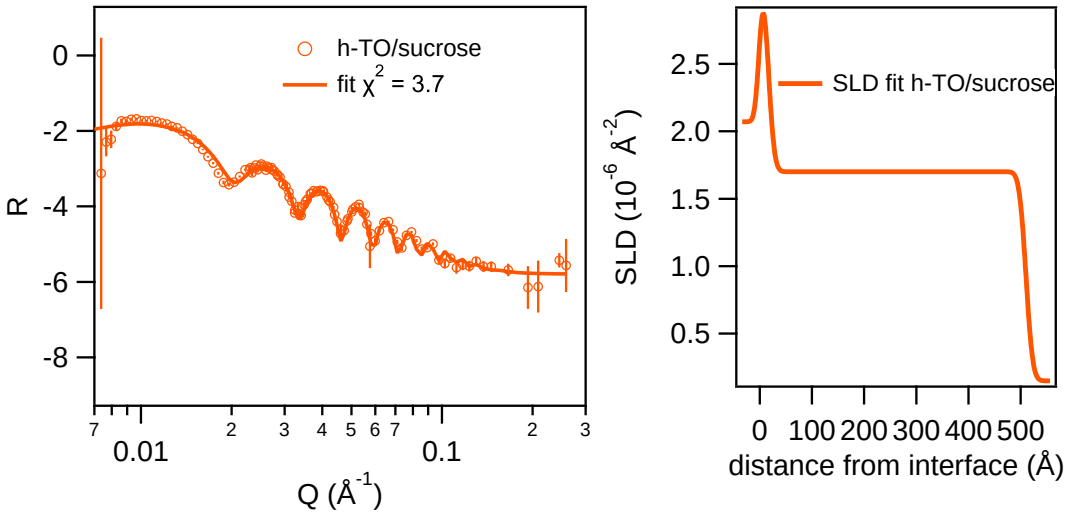

Figure 6.7 *NR from h-TO/sucrose interface. Left panel: NR profile (hollow circles) and the fit (solid line) using a simple layer model. Right panel: SLD profile corresponding to the fit.*

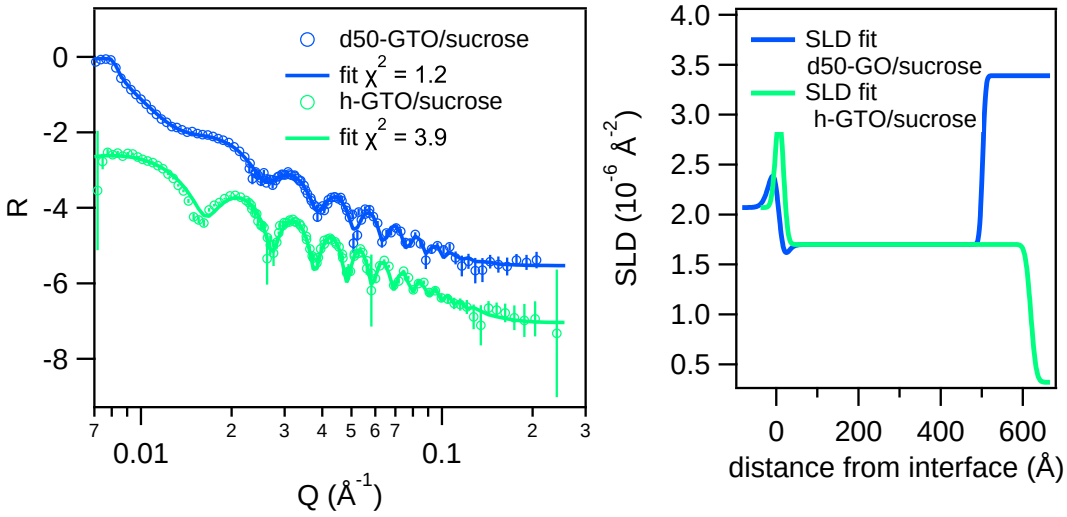

Figure 6.8 *NR from h-GTO and d50-GTO/sucrose interface. Left panel: NR profile (hollow circles) and the fit (solid line) using a simple layer model. Right panel: SLD profile corresponding to the fit.*

Table 6.1 *X-ray and neutron scattering length density for various chemicals.*

Chemical	SLD			
	x-rays $\times 10^{-6}$Å^{-2}	neutrons (h) $\times 10^{-6}$Å^{-2}	neutrons (d) $\times 10^{-6}$Å^{-2}	neutrons (d50) $\times 10^{-6}$Å^{-2}
Silicon	20.3	2.07	NA	NA
Silicon oxide	22.5	3.47	NA	NA
Sucrose	14.4	1.72	NA	NA
GTO	9.0	0.34	6.20	3.31
GTO-head	13.5	3.01	5.58	4.29
GTO-tail	7.6	-0.45	6.38	3.11
TO	8.8	0.15	NA	NA
TO-head	13.5	3.01	NA	NA
TO-tail	8.0	-0.22	NA	NA

$\chi^2 = 4.5$ for h-TO and $\chi^2 = 2.8$ for h-GTO as shown in Figures 6.5 and 6.6, respectively. Due to the large interfacial width the Kiessig fringe visibility in the fits is lost beyond $q > 0.08$ Å^{-1} as can be seen from the zoomed in XRR and fits shown in the insets of Figures 6.5 and 6.6. The sucrose substrates when characterised against air in Section 5.2.2 consistently provide a roughness of ∼10 Å for the sucrose/air interface. Upon restricting the interfacial width to 20 Å, a more realistic value for the roughness of the sucrose films, it was observed that the Kiessig fringes in the fits go out of phase with those observed in the measured reflectivity profile for $q > 0.1$ Å^{-1} and the χ^2 of the fit increased to 6.2 for h-TO and 3.5 for h-GTO. The large interfacial width required to fit the data or the large value of χ^2 obtained for the fits with more realistic value of interfacial roughness indicate that a simple layer model doesn't contain all the details of the sucrose/triglyceride oil interface that give rise to the reflectivity profile.

The NR data fits better to a simple layer model with the $\chi^2 = 3.7$ for h-TO, $\chi^2 = 3.9$ for h-GTO and $\chi^2 = 1.2$ for d50-GTO as shown in Figure 6.7 and 6.8, respectively. However, the first minima in the measured reflectivity profile from sucrose/h-TO or h-GTO interface is lower than the first minima in the calculated reflectivity profile using the simple layer model which is an indication of a deviation of the SLD near the interface from that of the bulk oil SLD.

These initial observations suggested that a more sophisticated model of the interfacial structure incorporating an orientational layering of the triglyceride

molecule with a head-rich region followed by a tail-rich region and so on is required. The physical driving force for such orientational layering being the preference for the glycerol backbone to adsorb at the sucrose interface [36]. Any such layering effect will be most evident in the x-ray reflectivity followed by the neutron reflectivity from h-TO or h-GTO as these provide the greatest contrast in the SLD between the glycerol backbone (triglyceride head) and the fatty acid chains (triglyceride tail) as can be seen from the SLD of various components of triglyceride oil in Table 6.1. For this reason the XRR and NR from h-TO or h-GTO are used to fit to a model for layering of triglyceride oil.

6.3.2 Analytical Model for Layering of Triglyceride Oil

In order to incorporate the layering of triglyceride oil analytically, a mathematical model based on an oscillatory function modulated by a decay has been used which is similar to the function used by Lau *et al.* to study the smectic ordering of liquid crystals [133]. Assuming that the triglyceride backbone adsorbs at the sucrose interface, giving rise to a region rich in triglyceride head characterised by length L_h, followed by a tail rich region characterised by a length L_t, and so on, such that the periodicity of the oscillations is $L = L_h + L_t$, and the strength of the orientational order decays with distance from the sucrose interface, the triglyceride head volume fraction, $\phi_{tgh}(z)$, can be modelled as:

$$\phi_{tgh}(z) = A\left[\left(\frac{\cos\left(z'(z)\right)+1}{2}\right)^{p} - B\right]\exp\left(\frac{-z'(z)^2}{2\sigma^2}\right) + B \tag{6.10}$$

The constant B is the volume fraction of heads in the bulk and A is the amplitude of the deviation of the head volume fraction from the bulk, which is distributed as a Gaussian function. The Gaussian decay term is straight forward and is characterised by a decay constant σ which gives the width of the distribution. Instead of using a simple cos term, we use $(\cos z + 1)^p$ as this allows two length-scales to be incorporated in the triglyceride layering; the length of the head rich region (L_h) and length of the total triglyceride layer (L). The period of the $(\cos z + 1)^p$ needs to be $2L$ which gives $z' = \pi z/L$. The volume fraction of heads in the bulk can be calculated as:

$$B = \frac{V_h}{V_h + V_t} = \frac{SLD_{TG} - SLD_{TGT}}{SLD_{TGH} - SLD_{TGT}} \tag{6.11}$$

where V_h and V_t are the molar volume of the head and tail, respectively and SLD_{TG}, SLD_{TGH} and SLD_{TGT} are the SLD of the triglyceride oil, triglyceride head and triglyceride tail, respectively, and are known parameters.

This formulation can be used to describe the correlation between molecules/layers whereby the correlation strength decays with distance from the interacting interface. Triglyceride layering is one such case as we expect the head rich and tail rich regions to have different length scales due to the difference in their volume. In this case, as the ordering of the triglyceride layers decrease with increasing distance, we expect a broadening of the head rich regions in addition to the lowering of the ϕ_{tgh} peak. To incorporate this smearing z', given by Equation 6.12, is used instead of $\pi z/L$.

$$z' = \frac{\pi z}{L(1+kz)} \tag{6.12}$$

Using the model described above, XRR and NR profiles obtained from the sucrose/h-TO or h-GTO interface were fitted using the code given in Appendix C.

6.3.3 Self-Consistent Fitting of X-ray and Neutron Reflectivity Profiles

As discussed in Section 6.3.1 any triglyceride layering at the sucrose interface will be most evident in the XRR profile due to the difference between the SLD for the glycerol backbone and the tails being the largest for x-rays. Therefore, the XRR profile was fitted first to the model described in Section 6.3.2 with the ranges of the fit parameters given in Table 6.2 using the CMAES search strategy.

The reflectivity profiles were fitted as R vs q first, followed by Rq^4 vs q fitting to fit the high q Kiessig fringes better. The final fits were obtained using the downhill simplex search strategy using narrower ranges for the fit parameters with starting values of search taken from the output of the CMAES global search. The silicon oxide and sucrose layer thickness were allowed to vary 5% on each side of the starting value and the triglyceride layer parameters were allowed to vary $\sim$50% around the starting values.

The final fits obtained for the XRR profiles for the sucrose/h-TO interface and the sucrose/h-GTO interface are shown in Figures 6.9 and 6.10, respectively. The left hand panel shows the measured XRR profile (hollow circles) and the fit (solid line) obtained using the layering model with the inset showing the zoomed in XRR

Table 6.2 *Fit parameters and their relevant limits for fitting the triglyceride layering using the model described in Equation 6.10 for the CMAES search.*

Parameter		Lower Bound	Starting Value	Upper Bound
$\text{sigma}_{\text{si/siox}}$	(Å)	1	4	10
$\text{thickness}_{\text{siox}}$	(Å)	4	10[a]	40
$\text{sigma}_{\text{siox/suc}}$	(Å)	1	4	10
$\text{thickness}_{\text{suc}}$	(Å)	400	550[a]	700
$\text{sigma}_{\text{suc/tg}}$	(Å)	1	10	20
A		0	0	1
L	(Å)	10	15	100
p		1	1	20
k	(Å^{-1})	0	0	0.15
$r(=2\sigma^2)$		1	1	20

The subscript si, siox, suc and tg, denote the silicon, silicon oxide, sucrose and triglyceride layers respectively. Thickness is defined for the layers and sigma is the interfacial width and is related to the typical roughness of layers by sigma/$\sqrt{2}$.

[a] The starting values for silicon oxide and sucrose layer thickness were taken as the values obtained from the non-layered fit and allowed to vary 20% on each side.

and the fits for 0.07 $\text{Å}^{-1} \leq q \leq 0.2$ Å^{-1}, and the right hand panel shows the SLD profile used to fit the data. The values obtained for the various fit parameters are detailed in Table 6.3. The incorporation of an interfacial triglyceride layering in the model to fit the XRR profiles from the sucrose triglyceride interface reduces the χ^2 from 4.5 for fits without layering to 2.2 for fits including layering in h-TO and from 2.8 for fits without layering to 2.1 for fits including layering in h-GTO. The visual quality of the fits improves substantially in the q-range 0.05 $\text{Å}^{-1} < q <$ 0.2 Å^{-1} when compared to Figures 6.5 and 6.6. As can be seen from the insets in the left hand panel of Figures 6.9 and 6.10, the Kiessig fringes in the fit match those observed in the measured XRR profile and the value of interfacial width (20 Å) obtained for the sucrose/triglyceride interface is reasonable when compared to the roughness obtained for the sucrose/air interface.

The volume fraction profile for the various components, silicon, silicon oxide, sucrose, triglyceride head and triglyceride tail, corresponding to the SLD profile obtained from the fit to the reflectivity data is shown in Figure 6.11. From the right on the x-axis there is a silicon layer (cyan), followed by a thin (10 Å) silicon oxide layer (magenta) and thereafter a sucrose layer (red) of ∼560 Å. After

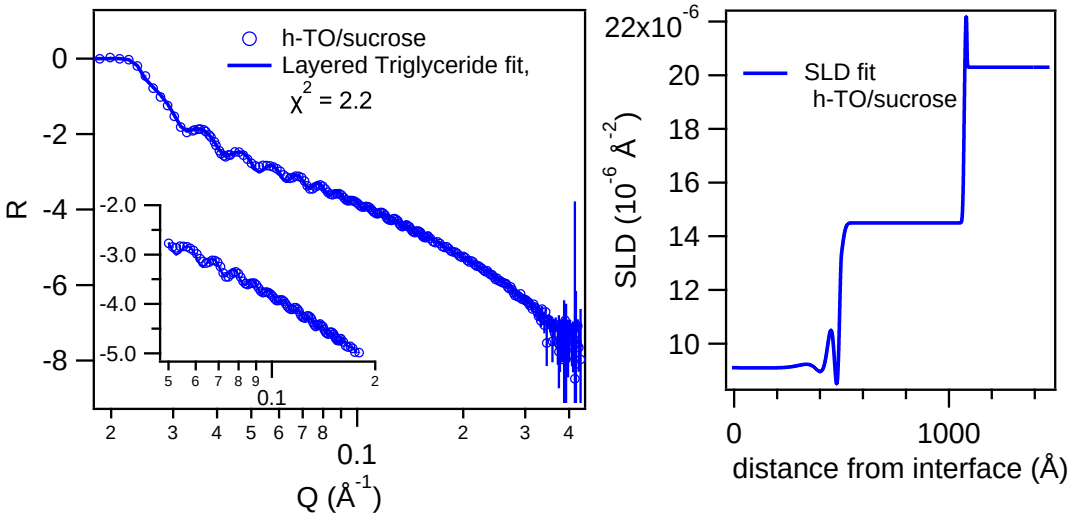

Figure 6.9 *Left panel: XRR profile measured from the sucrose/h-TO interface (hollow circles) and the fit (solid line) to the profile using the layering model described in Section 6.3.2. The inset shows the zoomed in XRR and fits for* $0.07\ \text{Å}^{-1} \leq q \leq 0.2\ \text{Å}^{-1}$. *Right panel: SLD profile corresponding to the fit.*

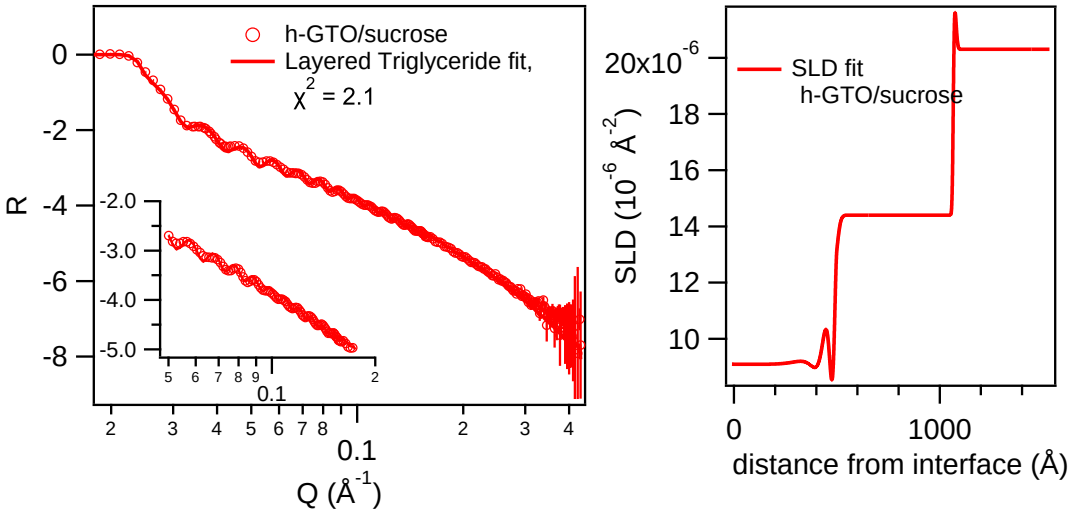

Figure 6.10 *Left panel: XRR profile measured from the sucrose/h-GTO interface (hollow circles) and the fit (solid line) to the profile using the layering model described in Section 6.3.2. The inset shows the zoomed in XRR and fits for* $0.07\ \text{Å}^{-1} \leq q \leq 0.2\ \text{Å}^{-1}$. *Right panel: SLD profile corresponding to the fit.*

Table 6.3 *Values obtained for the fit parameters using the triglyceride layering model described by Equation 6.10 for XRR from sucrose/h-TO and sucrose/h-GTO interface.*

Parameter		TO	GTO
$\text{sigma}_{\text{si/siox}}$	(Å)	2.5	10
$\text{thickness}_{\text{siox}}$	(Å)	12.6	12.2
$\text{sigma}_{\text{siox/suc}}$	(Å)	7.1	6.3
$\text{thickness}_{\text{suc}}$	(Å)	571	565
$\text{sigma}_{\text{suc/tg}}$	(Å)	20	20
A		0.7	0.65
L	(Å)	18.8	20.5
p		1	1
k	(Å^{-1})	0.15	0.15
r		4.8	4.5

The thickness and roughness of the silicon oxide and sucrose layers are dependent on the substrates.

the sucrose interface an oscillatory profile is observed for the volume fraction of triglyceride heads (green) and the tails (blue), which are out of phase with one another. At the interface a head rich region is observed with the total volume fraction of head $A + B \approx 0.9$, where B is calculated to be 0.2 for h-TO and 0.21 for h-GTO. This is followed by a tail-rich region with the total volume fraction of heads<0.1. The volume fraction for the head in the next head rich region drops to ~ 0.5 before the oscillations die out and the bulk volume fraction of head (B) and tails ($1 - B$) is obtained. The length-scale over which these oscillations are observed is $70 - 100$ Å, which is consistent with the QCM-D results that suggest and adsorbed layer of ∼10 nm.

The volume fraction profile obtained for the head and tail rich regions are consistent with the sucrose substrate inducing an orientation of the triglyceride molecule in which the polar glycerol backbone adsorbs at the sucrose interface and the oleic acid or octanoic acid chains are directed towards the bulk.

Confidence bands for the XRR fit, the SLD profile and the fit parameters for the sucrose/h-TO interface and the sucrose/h-GTO interface were obtained using Rascal's Bayesian analysis procedure as described in Section 6.2.2 and are shown in Figure 6.12 and 6.13, respectively. The top panels shows the measured XRR profile and the fit (left panels) and the corresponding SLD profile (right panels). The solid line shows the fit to the data and the shaded region around

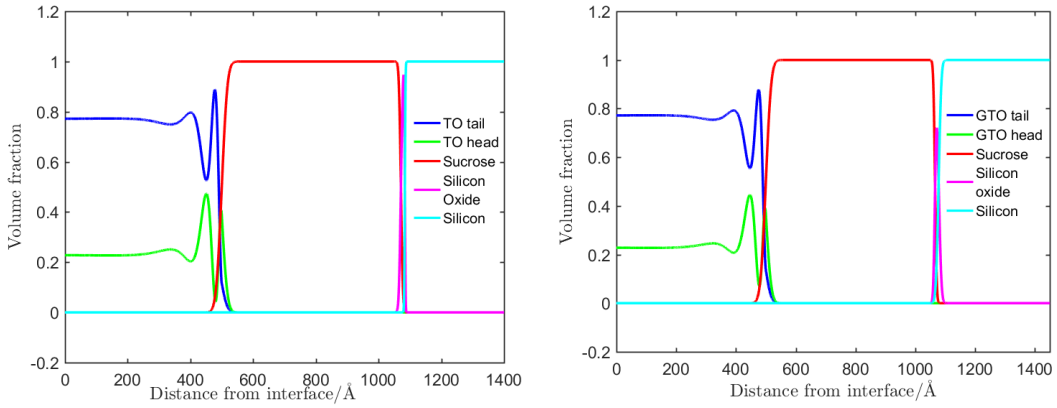

Figure 6.11 *Volume fraction profile for silicon (cyan), silicon oxide (magenta), sucrose (red) and triglyceride heads (green) and tails (blue) calculated from the SLD profile obtained from the XRR fits for sucrose/triglyceride interface. Left panel: Sucrose/h-TO system. Right panel: Sucrose/h-GTO system.*

the calculated reflectivity and SLD profiles shows the 95% Bayesian prediction intervals calculated from the maximum and minimum ranges of the parameter posteriors based on the Bayesian analysis. The posteriors obtained using the Bayesian analysis assuming uniform priors are shown in the bottom panels of Figures 6.12 and 6.13. The results obtained using the Bayesian analysis for the best fit parameters and their 95% intervals are summarised shown in Table 6.4.

From the shaded region depicting the 95% Bayesian prediction interval for the SLD profile and the XRR fit, it is evident that the cosine function with a Gaussian envelop, which produces one prominent oscillation in the SLD profile, is a good model to describe the XRR from the sucrose/triglyceride interface implying that there is some orientational layering of the triglyceride at the sucrose interface. The posteriors (bottom panel of Figure 6.12 and 6.13) show a peak in most of the parameters ($\text{sigma}_{\text{siox}}$, $\text{thickness}_{\text{siox}}$, $\text{sigma}_{\text{suc}}$, $\text{thickness}_{\text{suc}}$, L, r and A) corresponding to the best fit values; for sigma_{tg}, p and k no peak is observed. The best fit parameter estimates from the Bayesian analysis (Table 6.4) and the fit parameters found using the CMAES and simplex searches (Table 6.3) are in good agreement with one another. The value for the roughness of the sucrose/triglyceride ($\text{sigma}_{\text{siox}}$) has been restricted to 20 Å as this is a reasonable estimate for the spin-coated sucrose layer roughness as discussed in Section 5.2.2 and therefore larger values were not permitted. This roughness gets coupled with the oscillatory profile parameters as the oscillatory profile also generates a width to the interfacial region and therefore a maximum in the corresponding posterior

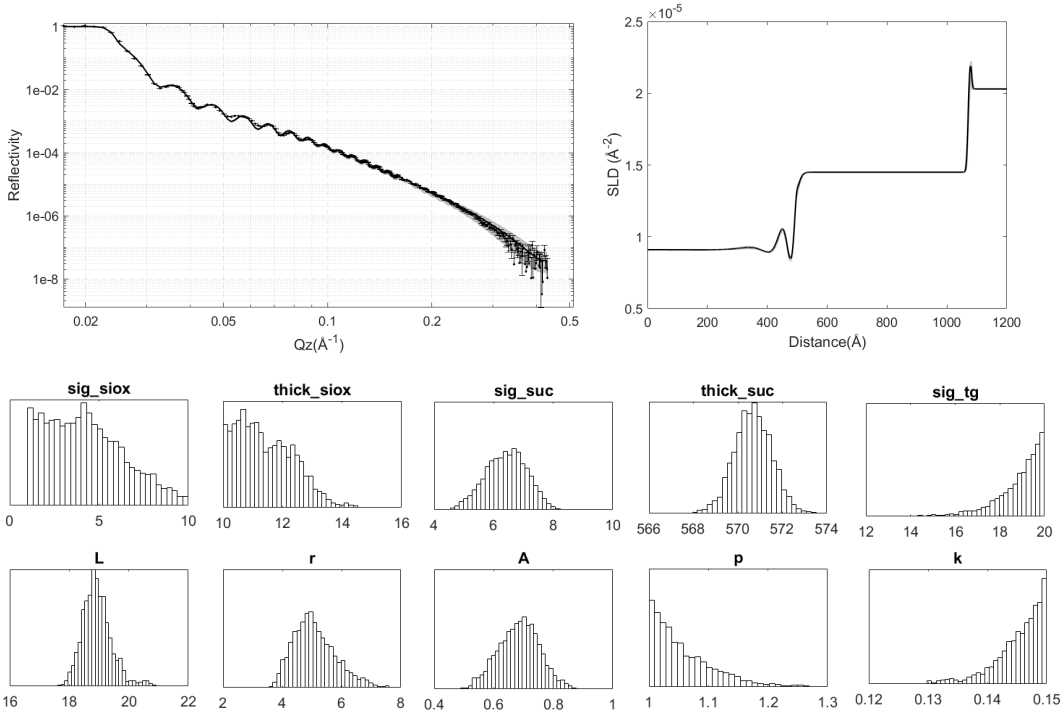

Figure 6.12 *XRR profiles from sucrose/h-TO interface fitted to the triglyceride layering model described in Section 6.3.2. Top panel: Measured XRR profile along with the fit (left panel) and the corresponding SLD profile (right) with the shaded region depicting the 95% Bayesian prediction interval. Bottom panel: The posteriors for the fit parameters assuming uniform priors using Bayesian analysis.*

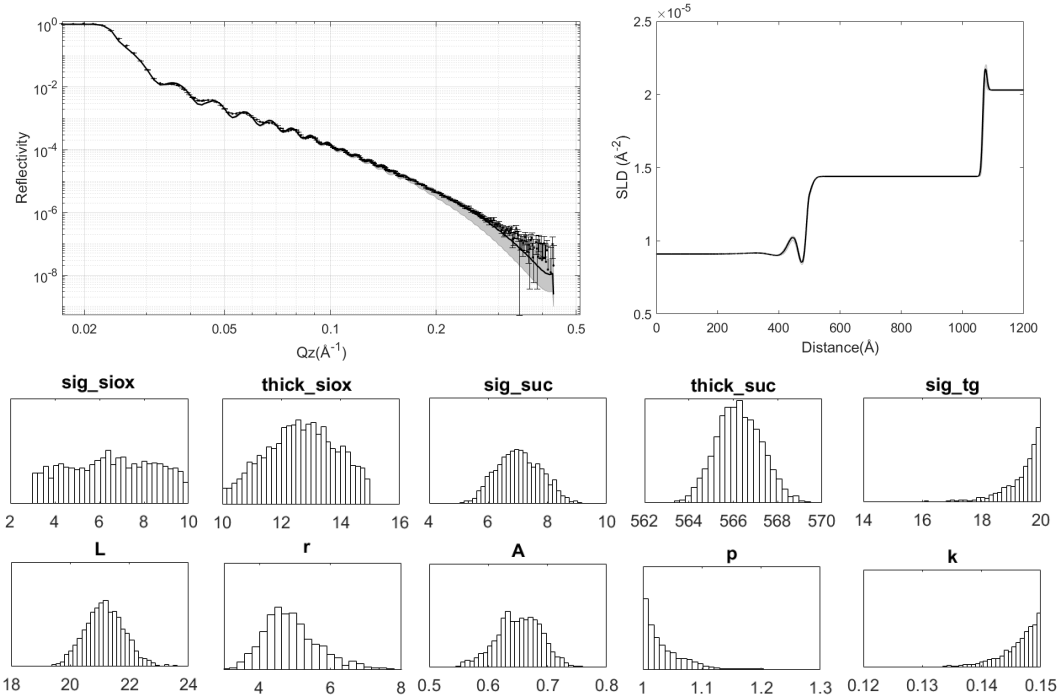

Figure 6.13 *XRR profiles from sucrose/h-GTO interface fitted to the triglyceride layering model described in Section 6.3.2. Top panel: Measured XRR profile along with the fit (left panel) and the corresponding SLD profile (right) with the shaded region depicting the 95% Bayesian prediction interval. Bottom panel: The posteriors for the fit parameters assuming uniform priors using Bayesian analysis.*

Table 6.4 *Values obtained for the fit parameters and their 95% confidence ranges (quoted in brackets) using the triglyceride layering model described by Equation 6.10 for XRR from sucrose/h-TO and sucrose/h-GTO interface.*

Parameter		TO		GTO	
		Value	(min, max)	Value	(min, max)
$\text{sigma}_{\text{si/siox}}$	(Å)	4.3	(1.13, 8.94)	6.5	(3.22, 9.71)
$\text{thickness}_{\text{siox}}$	(Å)	11.42	(10.07, 13.40)	12.7	(10.39, 14.76)
$\text{sigma}_{\text{siox/suc}}$	(Å)	6.4	(5.04, 7.69)	7.1	(5.66, 8.51)
$\text{thickness}_{\text{suc}}$	(Å)	571	(569.0, 572.3)	566	(564.3, 568.3)
$\text{sigma}_{\text{suc/tg}}$	(Å)	18.9	(16.22, 10.97)	19.3	(17.30, 19.98)
A		0.68	(0.550, 0.817)	0.65	(0.570, 0.722)
L	(Å)	18.9	(18.11, 20.15)	21.1	(19.92, 22.53)
p		1.06	(1.010, 1.198)	1.04	(1.007, 1.162)
k	(Å^{-1})	0.14	(0.134, 0.150)	0.14	(0.136, 0.150)
r		5.1	(3.96, 6.72)	4.9	(3.12, 6.89)

is not observed. The value of p has a hard lower bound of 1 as for $p < 1$, the cos function used in fitting $(1 + \cos z)^p$ is not differentiable at $z = \pm n\pi$. The best fit value of $p = 1$ indicates that a simple $(1 + \cos z)$ is a good model to describe the triglyceride layering.

Neutron reflectivity from the sucrose/h-triglyceride oil interface was fitted to the layering model with the parameter search restricted to ∼50% around the values obtained from the XRR fits. The fits so obtained for the NR profile from the sucrose/h-TO interface and the sucrose/h-GTO interface are shown in Figures 6.14 and 6.15, respectively. The left panels show the measured NR profile and the fit, and the right panels show the corresponding SLD profile with an inset showing the layered triglyceride at the sucrose interface. A shaded region around the fit and the SLD profile depicts the 95% Bayesian prediction interval. The results obtained using the Bayesian analysis for the best fit parameters and their 95% intervals are summarised shown in Table 6.5.

The fits to the NR profile from the sucrose/triglyceride interface and the corresponding SLD profile obtained again provide clear evidence of layering; a dip is required in the SLD profile below the average SLD of the oil followed by a bump before attaining the value of average SLD of the triglyceride oil to fit the data. The incorporation of this triglyceride layering decreases the χ^2 of the

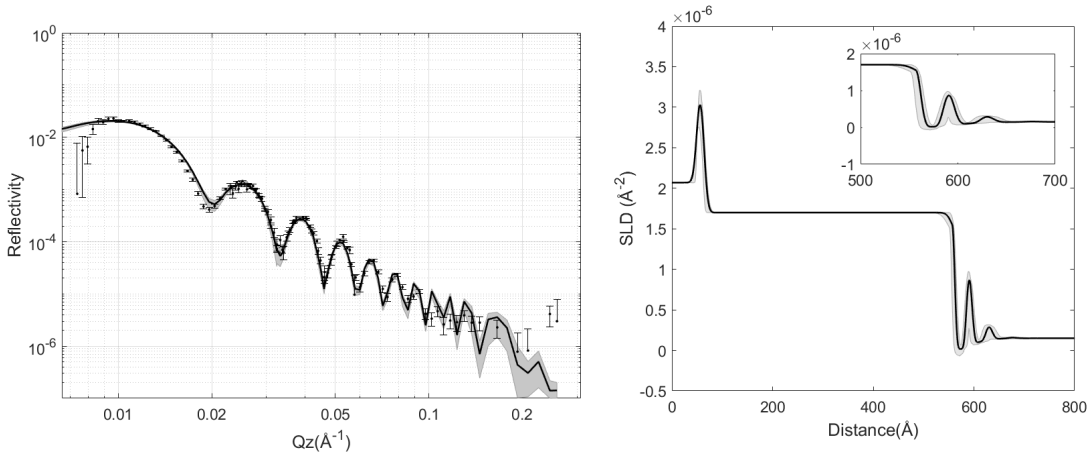

Figure 6.14 *NR profiles from sucrose/h-TO fitted to the triglyceride layering model described in Section 6.3.2. Measured NR profile along with the fit (left panel) and the corresponding SLD profile (right) with the shaded region depicting the 95% Bayesian prediction interval. The inset in the right panel shows the layered triglyceride at the sucrose interface.*

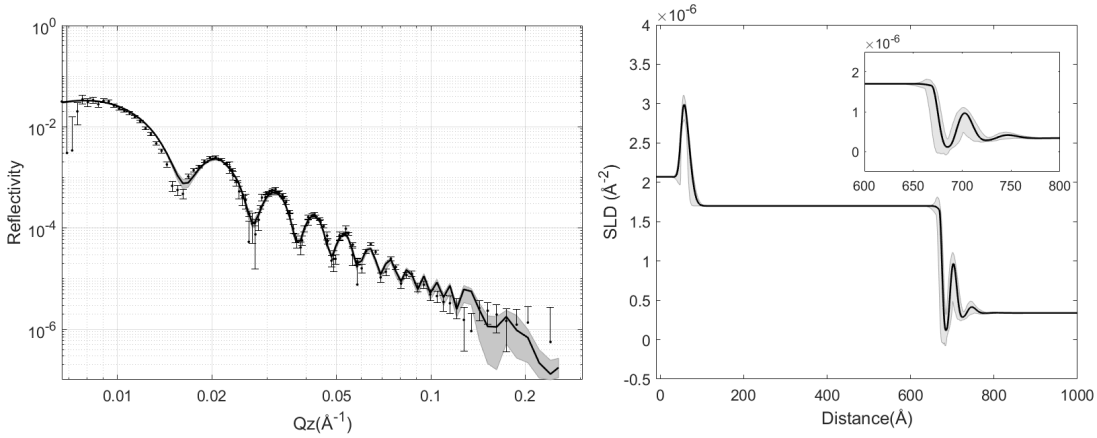

Figure 6.15 *NR profiles from sucrose/h-GTO fitted to the triglyceride layering model described in Section 6.3.2. Measured NR profile along with the fit (left panel) and the corresponding SLD profile (right) with the shaded region depicting the 95% Bayesian prediction interval. The inset in the right panel shows the layered triglyceride at the sucrose interface.*

Table 6.5 *Values obtained for the fit parameters and their 95% confidence ranges (quoted in brackets) using the triglyceride layering model described by Equation 6.10 for NR from sucrose/h-TO and sucrose/h-GTO interface.*

Parameter		TO		GTO	
		Value	(min, max)	Value	(min, max)
$\text{sigma}_{\text{si/siox}}$	(Å)	8.4	(4.82, 9.96)	8.1	(3.75, 9.93)
$\text{thickness}_{\text{siox}}$	(Å)	13.2	(11.09,15.39)	12.7	(15.06, 19.6)
$\text{sigma}_{\text{siox/suc}}$	(Å)	8.9	(6.05, 9.96)	16.8	(10.63, 19.83)
$\text{thickness}_{\text{suc}}$	(Å)	494	(491.0, 496.8)	601	(596.31, 604.75)
$\text{sigma}_{\text{suc/tg}}$	(Å)	12.2	(2.18, 19.56)	9.6	(1.53, 19.44)
A		0.44	(0.401, 0.530)	0.48	(0.402, 0.729)
L	(Å)	16.1	(15.03, 18.57)	15.7	(15.02, 17.91)
p		2.2	(1.05, 4.11)	1.27	(1.008, 1.960)
k	(Å^{-1})	0.04	(0.010, 0.069)	0.06	(0.050, 0.087)
r		7.1	(4.94, 7.96)	5.4	(3.18, 7.83)

fits from 3.7 to 3.2 for h-TO and from 3.9 to 3.1 for h-GTO. The NR fits show that at the sucrose interface the SLD profile shows increases to values greater than that of sucrose ($1.7 \times 10^{-6}\text{Å}^{-2}$) before dropping ≈ 0 (∼SLD of tails), a clear indication that there is a layer rich in glycerol backbone (SLD $= 3 \times 10^{-6}\text{Å}^{-2}$) at the sucrose interface. The distance from the interface at which the oscillation is fully damped out is again $70 - 100$ Å. This SLD profile was converted into a volume fraction profile as shown in Figure 6.16.

The volume fraction profile from the NR fits (Figure 6.16) show similar results to the volume fraction obtained from the XRR fits (Figure 6.11). There are small differences in the values obtained for A, L and r but these are within the 95% Bayesian confidence bands for the best fit estimates of these values. This is also reflected in the fact that the number of oscillations observed in the SLD or volume fraction profiles, the distance over which the oscillations are damped out and the amplitude of the second oscillation (first visible bump), which is the most significant contributor the reflectivity profile, is the same for both x-rays and neutrons. This corresponds to a self consistent fitting of the XRR and NR, where the XRR results fed into the NR to obtain the best fits. The small differences can arise from the the fact that the visibility of various components can be different for neutrons and x-rays.

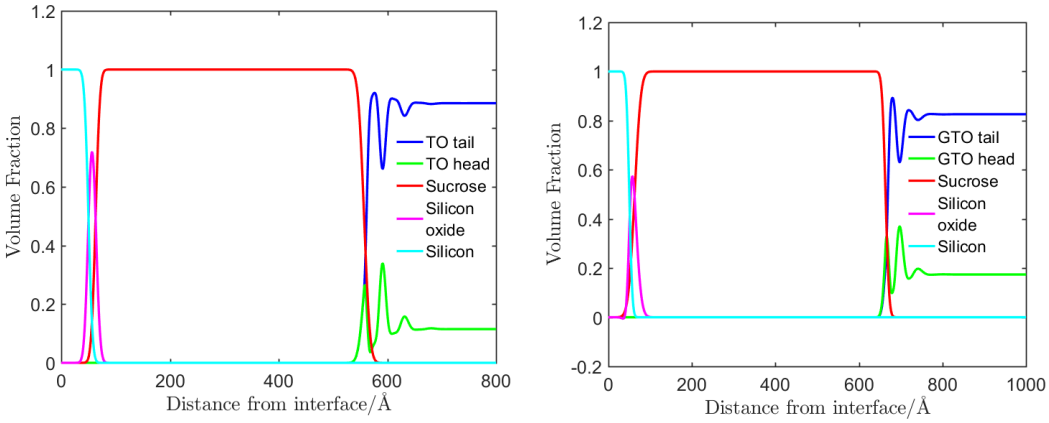

Figure 6.16 *Volume fraction profile for silicon (cyan), silicon oxide (magenta), sucrose (red) and triglyceride heads (green) and tails (blue) calculated from the SLD profile obtained from the NR fits for sucrose/triglyceride interface. Left panel: Sucrose/h-TO system. Right panel: Sucrose/h-GTO system.*

6.4 Conclusions

In this chapter x-ray and neutron reflectivity from the sucrose/triglyceride oil interface without added surfactants is discussed. The reflectivity profiles so obtained shows evidence for layering of the triglyceride oil at the sucrose interface. The layering has been fitted to an analytical model describing oscillations in the volume fraction of the glycerol back-bone (or triglyceride head) that decay with distance from the sucrose interface. The fitting indicates that the glycerol back-bone interacts with the polar sucrose interface giving rise to a head-rich region followed by a tail-rich region and so on. The dimension for the triglyceride molecule obtained from this layering is 19 Å for TO and 21 Å for GTO. The oleic acid tails have a double bond at C9 where the molecule can bend and so the length of the layered molecule for TO and GTO can be similar. The Gaussian envelop suggests that the extent of the ordering decays rapidly as the distance from the sucrose interface increases such that 2 oscillations of head-rich region followed by tail-rich regions comprising 3 monolayers of oriented triglyceride molecule as head-tail-tail-head are observed. This would be consistent with a harmonic potential observed by the triglyceride molecules due to the Van der Waals interaction from the sucrose substrate.

These studies provide the first direct measure that the triglyceride molecule is oriented with the glycerol backbone at the polar sucrose interface. This

orientational layering rationalises the wetting of the polar sucrose interface by triglyceride oil as measured using the contact angle studies in Section 5.3.3 and the presence of a triglyceride oil layer at the sucrose interface with viscoelastic properties different from the bulk determined using QCM-D as discussed in Section 5.4.3. This viscoelastic layer has some solid-like characteristics, for example a shear modulus of $1-2$ MPa, and therefore can support a finite shear stress. Klein *et al.* [125, 126] have also reported layering in oil molecules like toluene, cyclohexane and OMCTS using surface force measurements. These layers can support a finite shear stress and when compressed they become rigid with their effective viscosity increasing by $6-7$ orders of magnitude. In model chocolate suspensions, with solid weight fractions of 65% ($\phi = 0.52$), the oil needs to get into the spaces between the sucrose grains, which will be inhibited by this solid-like layering and the suspension so formed will not flow even upon the application of high shear as is experienced during the conching process. Therefore, it can be argued that the role of surfactants used in chocolates is to modify the interactional forces between the sucrose particles such that the oil can squeeze into the gaps between sucrose particles and the suspension formed can flow.

To facilitate the measurement of neutron reflectivity at multiple contrast which requires the use of expensive deuterated triglyceride oils, two types of low volume solid/liquid cells were developed: a laminar flow cell with an exchange volume of $\sim$1 mL and its XRR analogue to measure XRR from the same substrates; and a sandwich cell with a sample volume of $\sim$200 μL. These low volume flow cells enabled the measurement of NR from the sucrose/triglyceride interface following the addition of surfactants in two separate contrast, a h-oil contrast and d-rich oil (d50-oil), along with XRR from the same substrates as discussed in Chapter 7.

Chapter 7

Reflectivity Studies at Planar Sucrose/Triglyceride Interface-II: Addition of surfactants

7.1 Introduction

Crystalline spin-coated sucrose substrates in contact with triglyceride oil has been established as a model for one of the single sucrose/triglyceride oil interfaces found in model chocolate suspensions as discussed in Chapter 5. In chapter 6 it has been demonstrated that these interfaces can be used for neutron and x-ray reflectivity experiments to obtain molecular scale information about how the material is distributed at the sucrose/triglyceride oil interface. QCM-D studies for lecithin and PGPR at the planar sucrose/triglyceride interface, discussed in Section 5.4.3, show adsorption of the surfactants at the interface, resulting in layers with thicknesses of $10 - 100$ nm. Neutron and x-ray reflectivity can also be used to investigate the molecular scale details of the structure of these films.

In this chapter neutron and x-ray reflectivity measurements from adsorbed surfactant films at the sucrose/triglyceride oil interface are discussed. In Section 7.3 reflectivity from lecithin films at the sucrose interface in both TO and GTO is discussed and a comparison is drawn between interfacial lecithin films in the two triglyceride oils. Similar studies were also conducted for PGPR films at the sucrose/TO and GTO interface and are detailed in Section 7.4. Reflectivity

studies from films comprising binary mixtures of lecithin and PGPR are then discussed in Section 7.5. In addition to the multi-component lecithin, reflectivity studies were also carried out for the single component phospholipid, POPC, and its binary mixture with PGPR. These are discussed in Section 7.6. Based on these studies, the distribution of phospholipids and PGPR in the interfacial surfactant films can be derived which provides the structural details required to understand their effect on the rheology of model molten chocolate suspensions.

7.2 Materials and Methods

Sucrose was obtained from British Sugar with average particle size $\sim$10 μm (characterisation detailed in Chapter 2) and dissolved in Millipore Milli-Q water with resistivity 18.2 MΩ cm and TOC = 4 ppb to prepare a 125 mM solution to be used for spin-coating. The lecithin and PGPR were obtained from Mars Chocolate, UK and the h-POPC and d31-POPC used as a replacement for lecithin were sourced from Avanti Polar Lipids, USA. Pure triglyceride oil, GTO ($\geq$99%) and TO ($\geq$99%) to be used as bulk sub-phases were obtained from Sigma Aldrich, UK. Perdeuterated Glyceryl Trioctanoate (d-GTO) and d-96 Glyceryl Trioleate (d-TO) used to produce d50-oil contrast for the bulk phase were obtained from ISIS Deuteration Facility, Oxford, UK and National Deuteration Facility, ANSTO, Australia, respectively.

Sucrose was spin-coated onto 55 mm diameter (5 mm thick) circular silicon blocks using the procedure described in Chapter 5. These sucrose spin-coated silicon blocks were used as substrates in low volume laminar flow cells or in sandwich cells as described in Section 6.2.4. Neutron reflectivity was measured using h-GTO, d50-GTO (50:50 volume by volume mixture of h-GTO and d-GTO), h-TO and d50-TO (50:50 volume by volume mixture of h-TO and d-TO) as the triglyceride oil bulk phase. X-ray reflectivity was measured using h-GTO and h-TO as the triglyceride oil phase.

The neutron reflectivity experiments detailed in this chapter were performed on OFFSPEC (RB1600043) and INTER (RB1720367) beamlines at ISIS, STFC, UK, and D17 (9-13-642, 9-13-745) beamline at ILL, Grenoble, France. The x-ray reflectivity experiments were carried out on I07 (SI15202-1) at Diamond, Oxford, UK. The experimental details for these experiments is the same as specified in Section 6.2.5. Preliminary fits for the reflectivity profiles were obtained using

a parametrised slab model where a layered profile is constructed using thin films characterised using the SLD, thickness and a Gaussian roughness for each constituent layer. For a complicated system, such as ours, this can give rise to layer roughnesses that are greater than the corresponding thickness, which can result in negative volume fraction for the constituent components. Therefore, while this approach is useful for providing initial fits, the detailed data analysis was done using custom models within the MATLAB RasCal procedure described in Section 6.2.2.

7.3 Lecithin at Sucrose/Triglyceride Interface - Reflectivity Study

7.3.1 Neutron and X-Ray Reflectivity from Lecithin Films at Sucrose/Triglyceride Interface

To measure the arrangement of lecithin layers at the sucrose/triglyceride oil interface, neutron reflectivity was measured with the neutrons incident from the silicon interface for 2.4% solutions of lecithin in h-TO, d50-TO, and h-GTO and d50-GTO and are shown in Figures 7.1 and 7.2, respectively. In addition to the neutron reflectivity, x-ray reflectivity was also measured for the same solution with the x-rays incident through the triglyceride bulk phase and is shown in Figure 7.3.

Figure 7.2 shows NR profiles obtained at the sucrose/GTO interface, carried out using the low volume laminar flow cells described in Section 6.2.4, showing adsorption of lecithin over the time-scales of $1.5 - 4.5$ hours after injection. The left panel in Figure 7.1, shows the same for sucrose/h-TO interface over $2 - 6$ hours after injection. The black curves in all these figures show the sucrose/triglyceride interface without any added surfactants. The sucrose layer thickness was calculated from these NR profiles and used as the starting values when fitting the reflectivity profile for lecithin films. A solution containing 2.4% lecithin in the triglyceride oil is then flowed through the cell and as can be seen from the change in the position of the first minimum in the reflectivity fringes that adsorption of lecithin occurs at the sucrose interface. The adsorption appears to stabilise after 3-4 hours and the reflectivity profile measured after 3 hours was used

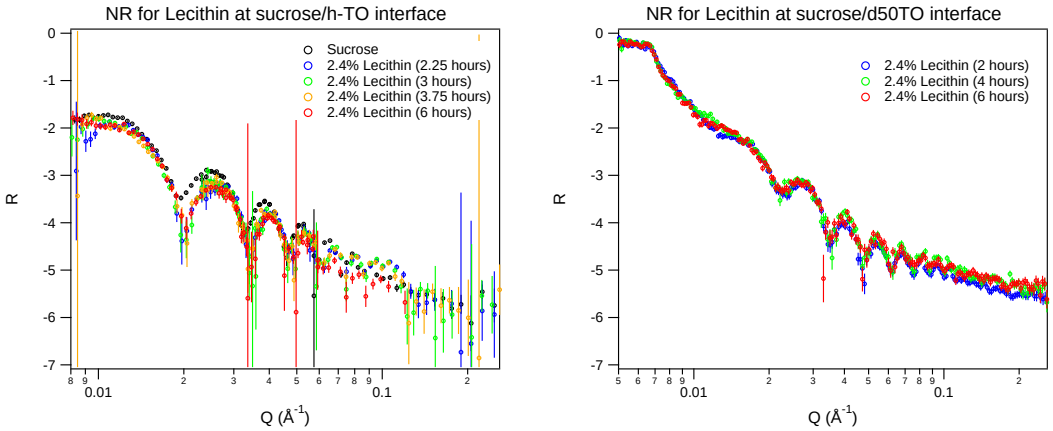

Figure 7.1 *NR from lecithin film at sucrose/TO interface. Time series showing adsorption of lecithin over a period of 2-6 hours after injecting. Left panel: Lecithin at sucrose/h-TO interface. Right panel: Lecithin at sucrose/d50-TO interface.*

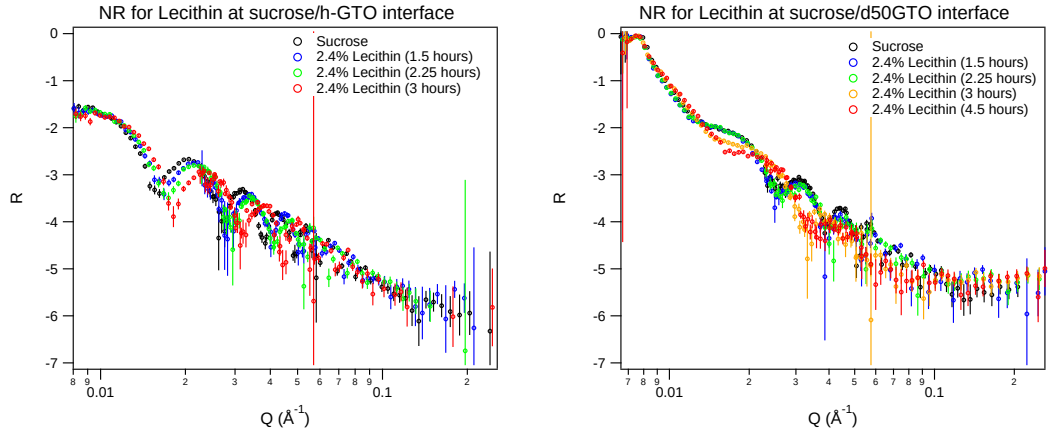

Figure 7.2 *NR from lecithin film at sucrose/GTO interface. Time series showing adsorption of lecithin over a period of 1-4 hours after injecting. Left panel: Lecithin at sucrose/h-GTO interface. Right panel: Lecithin at sucrose/d50-GTO interface.*

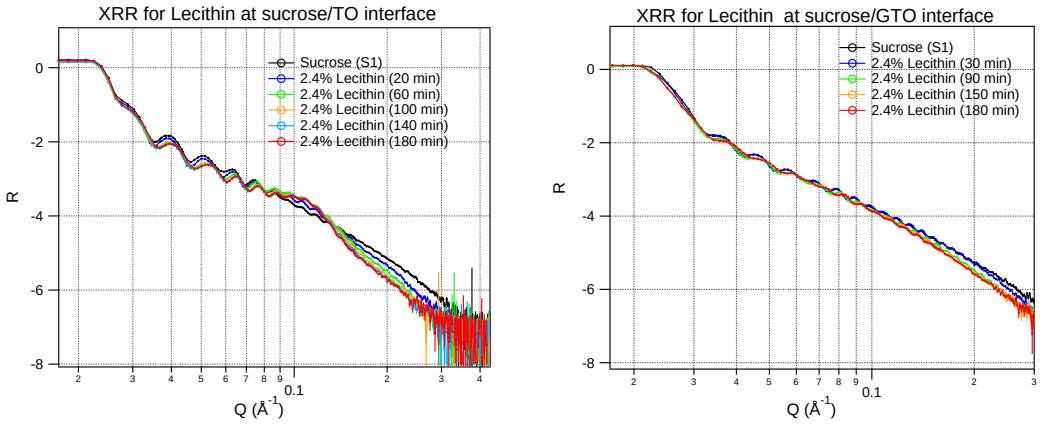

Figure 7.3 *XRR from lecithin film at sucrose/triglyceride interface. Time series showing adsorption of lecithin over a period of 20 mins to 3 hours after injecting. Left panel: Lecithin at sucrose/TO interface. Right panel: Lecithin at sucrose/GTO interface.*

for data fitting. The right panel of Figure 7.1 shows NR measured for lecithin films at sucrose/d50-TO interface using the sandwich cells described in Section 6.2.4. The sandwich cell was created using 200 μL of d50-TO solution containing 2.4% lecithin. The sucrose layer for this substrate was pre-characterised using lab-based XRR and the thickness obtained was used as the starting value when fitting the reflectivity profile for lecithin films. The left and right panel of Figure 7.3 show XRR measured from lecithin thin films at the sucrose/TO and sucrose/GTO interfaces, respectively, using the x-ray low volume laminar flow cells described in Section 6.2.4. The black curve shows the sucrose/triglyceride and was used to characterise the thickness of the sucrose films. Adsorption of lecithin results in a shoulder like feature at $q \approx 0.1$ Å^{-1}. The shoulder is more evident for TO than GTO, possibly because of the adsorbed amount of lecithin is lower in GTO than in TO. This is consistent with the adsorbed amounts obtained from the QCM-D measurements discussed in Section 5.4.

7.3.2 Data Analysis

The neutrons are incident through the silicon block, so the layer profile for the neutrons is silicon bulk phase with a thin layer of silicon oxide on top of it, followed by the sucrose layer, followed by the adsorbed lecithin layers and finally the bulk triglyceride oil. The model used for fitting the reflectivity profile for lecithin layers at the sucrose/triglyceride oil interface consists of silicon, silicon oxide,

sucrose and bulk triglyceride layers, each constructed using a sum of two error functions and characterised by their SLD, thickness and roughness as described in Section 6.2.2. On the basis of the observed surface excesses (equivalent to $5-7$ monolayers depending on the oil) derived from QCM-D and suspension SANS, coupled with the observation from the previous chapter that even the triglyceride oil layers at the sucrose interface and the observation in XRR of a well-defined feature at 0.1 $Å^{-1}$, models were constructed comprising repeating layers of phospholipid.[1]. This structure comprises repeating phospholipid layers of head-tail-tail-head regions. Each of these head/tail layers is constructed using two error functions using the area per molecule (A_{pm}) as a constraint, whereby $thick_h = V_h/A_{pm}$ and $thick_t = V_t/A_{pm}$, and the subscripts h/t denote the head or tail layer. This approach allows the heads and tails in the two layers to remain conserved. The lecithin layers might be expected to incorporate some oil and this is taken into account by including a number fraction, f, of triglyceride oil molecules per lipid molecule in the head and the tail layer. The number fraction in each of the head and tail layers can be different and is denoted as f_{h_n} and f_{t_n} where the subscripts n denotes the number of the layer. In this formalism $f = \frac{x}{1-x}$, where x is the volume fraction of the triglyceride oil in the corresponding layer.

Using this approach, the thickness of the n^{th} head ($thick_{h_n}$) and tail ($thick_{h_n}$) layers incorporating x_{h_n} and x_{t_n} volume fraction of the triglyceride oil, respectively, is given as:

$$thick_{h_n} = \frac{V_{PC_h} + V_{TG}\left(\frac{x_{h_n}}{1-x_{h_n}}\right)}{A_{pm_n}} \tag{7.1}$$

$$thick_{t_n} = \frac{V_{PC_t} + V_{TG}\left(\frac{x_{t_n}}{1-x_{t_n}}\right)}{A_{pm_n}} \tag{7.2}$$

where V_{PC_h}, V_{PC_h} and V_{TG} are the molecular volumes of the POPC head, POPC tail and triglyceride molecule, respectively. The SLD of each corresponding layer head and tail layer is given as:

$$SLD_{h_n} = (1 - x_{h_n}) * SLD_{PC_h} + x_{h_n} * SLD_{TG} \tag{7.3}$$

[1]In this work the the average lecithin phospholipid molecules is taken to be a POPC molecule. Therefore, wherever required the SLD and volumes of the lecithin layer is substituted with the SLD and volume of POPC

$$SLD_{t_n} = (1 - x_{t_n}) * SLD_{PC_t} + x_{h_n} * SLD_{TG} \tag{7.4}$$

where SLD_{PC_h}, SLD_{PC_h} and SLD_{TG} are the SLDs of the POPC head group, POPC tail and triglyceride molecule, respectively. Using this formalism, the scattering length density profile for each lipid head ($\rho_{h_n}(z)$) and tail layer (($\rho_{t_n}(z)$) can be constructed using a sum of two error functions defined by their SLD, thickness and the interfacial width:

$$\rho_{h_n}(z) = \frac{SLD_{h_n}}{2}\left[\mathrm{erf}\Big(\frac{z - I_{h_{ni}}}{\sigma_{h_{ni}}}\Big) - \mathrm{erf}\Big(\frac{z - I_{h_{nf}}}{\sigma_{h_{nf}}}\Big)\right] \tag{7.5}$$

$$\rho_{t_n}(z) = \frac{SLD_{t_n}}{2}\left[\mathrm{erf}\Big(\frac{z - I_{t_{ni}}}{\sigma_{t_{ni}}}\Big) - \mathrm{erf}\Big(\frac{z - I_{t_{nf}}}{\sigma_{t_{nf}}}\Big)\right] \tag{7.6}$$

where $I_{h/t_{ni}}$ and $I_{h/t_{nf}}$ denotes the initial and final interface of the head/tail layer with the preceding and succeeding layer, respectively, and $\sigma_{h/t_{ni}}$ and $\sigma_{h/t_{ni}}$ denotes the corresponding interfacial widths. By definition, $I_{h/t_{ni}} - I_{h/t_{nf}} = thick_{h/t_n}$, and can therefore be calculated using Equation 7.1 and 7.2. If the width at each interface is matched to the preceding and succeeding layer, this approach inherently constraints the volume fraction at each point to be 1. The multiple contrasts can be co-fitted by using the correct SLD of the triglyceride bulk-phase.

The approach for x-rays is exactly the same, apart from the fact the x-ray are incident through the triglyceride bulk phase to the layered profile is bulk triglyceride oil, followed by lecithin layers, followed by sucrose, silicon oxide and finally silicon.

Preliminary fits obtained using a parametrised slab model indicated that the lecithin layers in TO comprised of 7 monolayers and in GTO comprised on 5 monolayers of phospholipids oriented as head-tail-tail-head and so on. This is consistent with the values obtained for the adsorbed interfacial amount using QCM-D (Section 5.4). Therefore, a 7 layer model comprising phospholipid layers oriented as head-tail-tail-head and so on was implemented in MATLAB to calculate the neutron and x-ray SLD profile for lecithin layers in TO to fit the measured reflectivity profile and is given in Appendix D. The code for lecithin in GTO is a 5 layer version of the same model. The neutron codes accepts contrast flags and can simultaneously fit the h-triglyceride oil and d50-triglyceride

oil contrast. The reflectivity profiles for h-oil and d-50-oil contrasts were fitted simultaneously for both TO and GTO. The substrate parameters (silicon oxide and sucrose layer thickness and roughness) were allowed to vary independently between the two contrasts as the reflectivity profiles were measured from separate substrates, but the lecithin layer parameters described in the model above were fitted simultaneously with the fit parameters allowed to vary over ranges given in Table 7.1, first using the CMAES search, followed by the downhill simplex.

Table 7.1 *Fit parameters and their relevant limits for fitting the lecithin films at sucrose/triglyceride interface using the layered model based on the area per molecule approach.*

Parameter		Lower Bound	Starting Value	Upper Bound
$\text{sigma}_{\text{si/siox}}$	(Å)	1	4	10
$\text{thickness}_{\text{siox}}$	(Å)	4	10[a]	40
$\text{sigma}_{\text{siox/suc}}$	(Å)	1	4	10
$\text{thickness}_{\text{suc}}$	(Å)	400	550[a]	700
$\text{thickness}_{\text{layer}}$	(Å)	200	350	1000
A_{pm1-7}	($Å^2$)	40	50	130
x_{h1-2}		0	0.1	0.5
x_{h1-2}		0	0.1	0.7
x_{h3-4}		0	0.3	0.7
x_{h3-4}		0	0.3	0.9
x_{h5-7}		0	0.5	1[c]
x_{h5-7}		0	0.5	1[c]
σ_{h1-7}[b]	(Å)	3	3	5
σ_{t1-7}[b]	(Å)	4	6	8

The subscript si, siox, suc and tg, denote the silicon, silicon oxide, sucrose and triglyceride layers, respectively. Sigma is the interfacial width and is related to the typical roughness of layers by sigma/$\sqrt{2}$.

[a] The starting values for silicon oxide and sucrose layer thickness were taken as the values obtained from fits for oil only data and were allowed to vary 5% on either side.

[b] Each head/tail interface requires a finite interfacial width, but these were not fitted initially as they do not affect the SLD profiles much, whereas they significantly increase the number of fit parameters. A quick fit was done at the end to find the best-fit values for these parameters.

[c] Allowing the volume fraction of triglyceride oil in the last 2 lecithin layers to go up to 1 lets the number of layers in this formulation to be variable.

The fits so obtained for the NR profile upon simultaneous fitting of the h-oil and d50-oil contrast for lecithin at the sucrose/TO interface and the sucrose/GTO interface are shown in Figure 7.4 and 7.5, respectively. The left panels show the measured NR profile and the fit, and the right panels show the corresponding

SLD profile. A shaded region around the fit and the SLD profile depicts the 95% Bayesian prediction interval. The results obtained using the Bayesian analysis for the best fit parameters and their 95% intervals are summarised in Table 7.2.

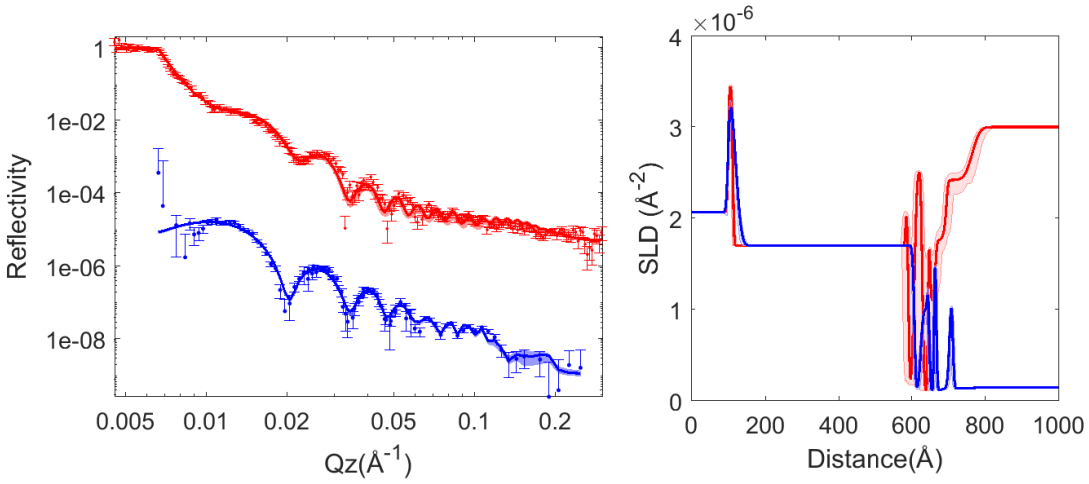

Figure 7.4 *NR profiles for lecithin at sucrose/TO interface in h-oil (blue) and d50-oil (red) contrast. The reflectivity profiles were simultaneously fitted using the error function based layer model described in Section 7.3.2. Measured NR profile along with the fit (left panel) and the corresponding SLD profile (right panel) with the shaded region depicting the 95% Bayesian prediction interval.*

The 7 layer model required to fit the NR data needs 21 fit parameters giving a χ^2 of 3.12 for the h-TO contrast. The number of parameters in this model is substantially larger than bilayer models which typically require $8-12$ parameters. In order to test the goodness and uniqueness of the fit, the fit model was changed to a 5 layer model (15 fit parameters) which gave a χ^2 of 4.17 and a model with 7 layers but A_{pm} constrained to be the same between various layers (15 parameters) which gave χ^2 of 3.67. In order to compare these results, the reduced χ^2 from the various models was compared: 3.91 for the 7 layer model with 21 parameters; 4.88 for the 5 layer model with 15 parameters; and 4.33 for the 7 layer model with 15 parameters. The reduced χ^2 values for various models in d50-TO contrast are: 2.31 for 7 layers with 21 parameters; 2.69 for 5 layers with 15 parameters; and 2.48 for 7 layers with 15 parameters. The reduced χ^2 values increase the confidence in the 7 layer fit model. However there remain concerns about how best this model can be parametrised, which can be explored by applying a Bayesian spectral analysis approach with the number of layers/parameters to be variable as used in Sivia *et. al.* [115]. A Bayesian analysis approach was also used to verify the 7 layer model where confidence intervals for various fit parameters were obtained.

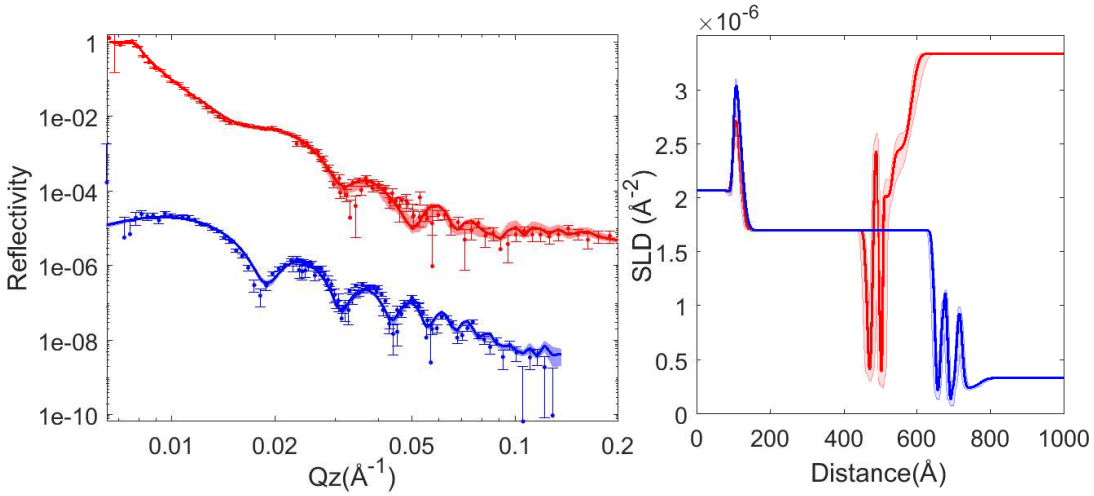

Figure 7.5 *NR profiles for lecithin at sucrose/GTO interface in h-oil (blue) and d50-oil (red) contrast. The reflectivity profiles were simultaneously fitted using the error function based layer model described in Section 7.3.2. Measured NR profile along with the fit (left panel) and the corresponding SLD profile (right panel) with the shaded region depicting the 95% Bayesian prediction interval.*

In the case that fewer layers would fit the data better, the values for variables x_{hn} and x_{tn} for the outer layers would come out $\sim$1, signifying that the layer comprises completely of triglyceride oil. This is not the case for any of the outer layers in case of TO (layers $5-7$) or GTO (layers $3-5$) in Table 7.2, which again suggests the 7 layers accurately fits the data.

The SLD profile so obtained can be converted into the total volume fraction profile of head ($\phi_{h_{total}}(z)$), tail ($\phi_{h_{total}}(z)$) and oil ($\phi_{TG_{total}}(z)$) for the entire lecithin layer by summing over the volume fraction profile of head ($\phi_{h_n}(z)$), tail ($\phi_{h_{total}}(z)$) and oil ($\phi_{TG}(z)$) in each layer, giving:

$$\phi_{h_{total}}(z) = \sum_n \phi_{h_n}(z) = \sum_n \frac{(1 - x_{h_n}) * \rho_{h_n}(z)}{SLD_{h_n}} \tag{7.7}$$

$$\phi_{t_{total}}(z) = \sum_n \phi_{t_n}(z) = \sum_n \frac{(1 - x_{t_n}) * \rho_{t_n}(z)}{SLD_{t_n}} \tag{7.8}$$

$$\phi_{TG_{total}}(z) = 1 - \left(\sum_n \phi_{h_n}(z) + \sum_n \phi_{t_n}(z) \right) \tag{7.9}$$

Using Equations 7.7, 7.8 and 7.9, the volume fraction of PC heads (red curve),

Table 7.2 *Values obtained for the fit parameters and their 95% confidence ranges (quoted in brackets) using the error function based layer model described in Section 7.3.2 for simultaneous fitting of h-oil and d-50 oil contrast for lecithin layers at the sucrose/triglyceride interface.*

Parameter		Value	(min, max)	Value	(min, max)
		d50-TO		d50-GTO	
$\text{sigma}_{\text{si/siox}}$	(Å)	3.5	(1.3, 5.8)	9.1	(7.8, 10.0)
$\text{thickness}_{\text{siox}}$	(Å)	12.8	(9.8, 15.6)	17.5	(13.1, 19.9)
$\text{sigma}_{\text{siox/suc}}$	(Å)	3.6	(1.3, 6.7)	12.8	(10.5, 14.8)
$\text{thickness}_{\text{suc}}$	(Å)	473	(463, 481)	348	(342, 355)
		h-TO		h-GTO	
$\text{sigma}_{\text{si/siox}}$	(Å)	6.1	(3.1, 7.9)	6.7	(4.8, 7.9)
$\text{thickness}_{\text{siox}}$	(Å)	21.3	(19.9, 23.0)	18.8	(15.9, 20.7)
$\text{sigma}_{\text{siox/suc}}$	(Å)	16.2	(12.2, 19.6)	16.5	(14.2, 17.9)
$\text{thickness}_{\text{suc}}$	(Å)	481	(478, 484)	528	(525, 531)
Common parameters		TO		GTO	
A_{pm1}	(Å^2)	112.7	(95.4, 129.0)	120.9	(107.3, 129.7)
A_{pm2}	(Å^2)	122.1	(106.7, 129.7)	118.4	(102.3, 129.4)
A_{pm3}	(Å^2)	127.3	(121.5, 129.9)	93.2	(81.5, 106.8)
A_{pm4}	(Å^2)	126.5	(119.3, 129.9)	124.0	(114.3, 129.8)
A_{pm5}	(Å^2)	123.5	(113.1, 129.7)	61.9	(51.5, 70.8)
A_{pm6}	(Å^2)	126.3	(118.3, 129.9)		NA
A_{pm7}	(Å^2)	108.2	(95.1 120.7)		NA
x_{h1}		0.228	0.138, 0.299)	0.000	(0.000, 0.000)
x_{t1}		0.000	(0.000, 0.000)	0.006	(0.003, 0.009)
x_{h2}		0.534	(0.491, 0.570)	0.547	(0.271, 0.640)
x_{t2}		0.074	(0.004, 0.179)	0.040	(0.009, 0.068)
x_{h3}		0.073	(0.005, 0.161)	0.335	(0.172, 0.539)
x_{t3}		0.000	(0.000, 0.000)	0.000	(0.000, 0.000)
x_{h4}		0.000	(0.000, 0.000)	0.000	(0.000, 0.000)
x_{t4}		0.000	(0.000, 0.000)	0.606	(0.499, 0.666)
x_{h5}		0.000	(0.000, 0.000)	0.000	(0.000, 0.000)
x_{t5}		0.340	(0.246, 0.431)	0.731	(0.673, 0.787)
x_{h6}		0.000	(0.000, 0.000)		NA
x_{t6}		0.573	(0.511, 0.625)		NA
x_{h7}		0.000	(0.000, 0.000)		NA
x_{t7}		0.800	(0.758, 0.830)		NA
$\text{sigma}_{\text{suc/h1}}$	(Å)	4.4	(3.1, 5.1)	3.1	(2.3, 4.3)
$\text{sigma}_{\text{t7/tg}}/\text{sigma}_{\text{t5/tg}}$	(Å)	27.8	(23.6, 29.9)	22.1	(8.0, 29.8)

All parameter values are quoted to relevant significant figures.

PC tails (blue curve) and triglyceride oil (green curve) were calculated and are shown in Figure 7.6 for TO (left panel) and GTO (right panel).

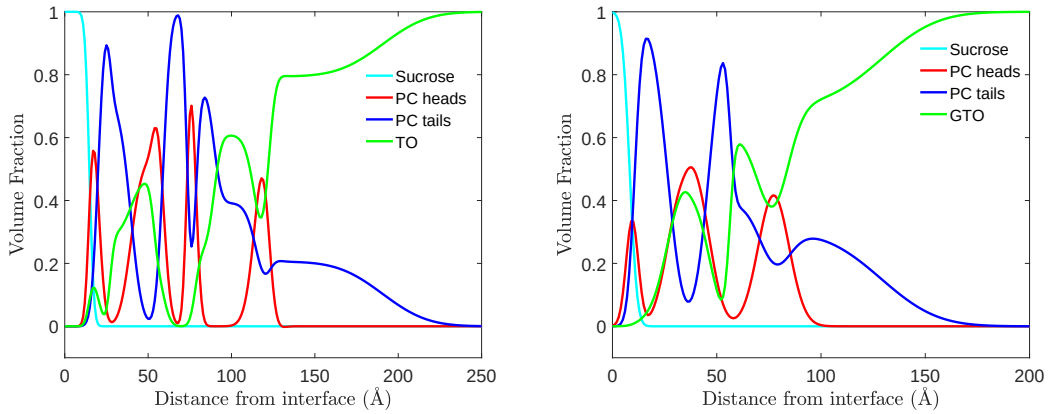

Figure 7.6 *Volume fraction profiles for PC heads (red), PC tails (blue) and the triglyceride oil (green) at the sucrose interface calculated from the SLD profile obtained from fits to the neutron reflectivity profile for lecithin at sucrose/triglyceride interface. Left panel: Lecithin at sucrose/TO interface. Right panel: Lecithin at sucrose/GTO interface.*

XRR measured from lecithin films at sucrose/TO and sucrose/GTO interface was also fitted to the 7 and 5 layer model, and are shown in Figure 7.7 and 7.8, respectively. The left panels show the measured NR profile and the fit, and the right panels show the corresponding SLD profile. A shaded region around the fit and the SLD profile depicts the 95% Bayesian prediction interval.

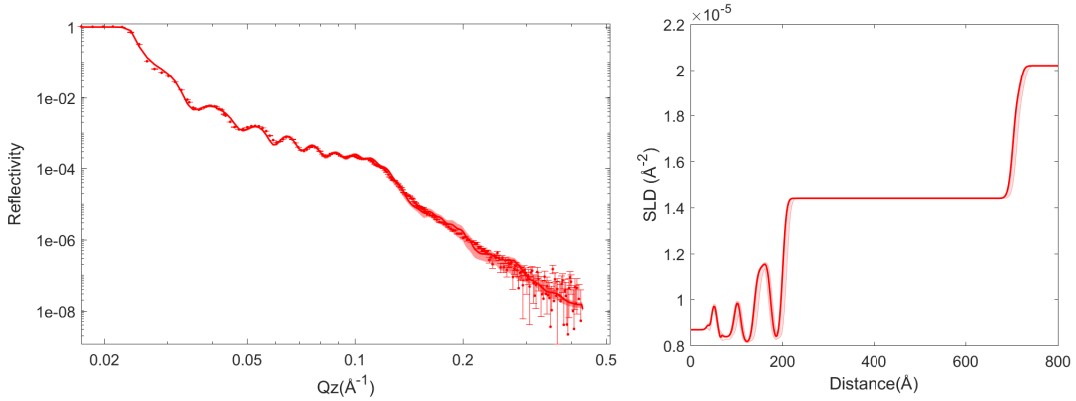

Figure 7.7 *XRR profiles for lecithin at sucrose/TO interface. Measured XRR profile along with the fit (left panel) and the corresponding SLD profile (right panel) with the shaded region depicting the 95% Bayesian prediction interval.*

The SLD profile obtained from the fits to the XRR were converted to volume fraction profiles using Equations 7.7, 7.8 and 7.9 as shown in Figure 7.9. The figure shows the volume fraction of PC heads (red curve), PC tails (blue curve)

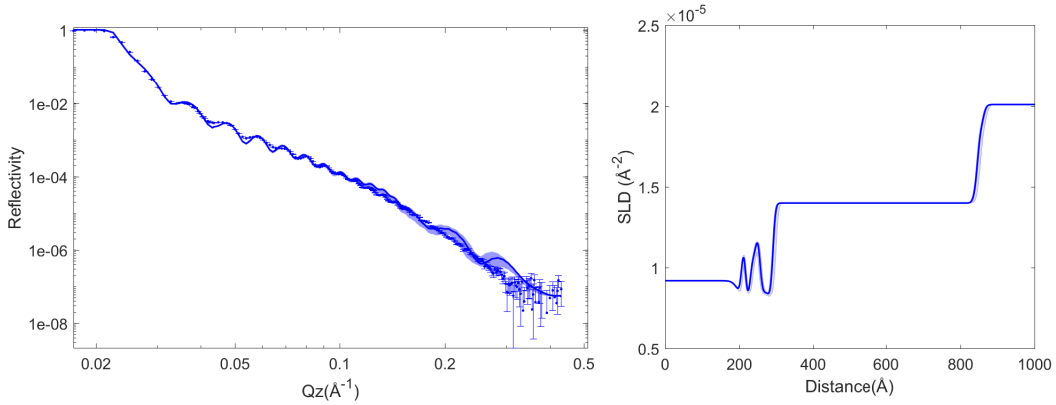

Figure 7.8 *XRR profiles for lecithin at sucrose/GTO interface. Measured XRR profile along with the fit (left panel) and the corresponding SLD profile (right panel) with the shaded region depicting the 95% Bayesian prediction interval.*

and triglyceride oil (green curve) for lecithin at the sucrose interface for TO (left panel) and GTO (right panel).

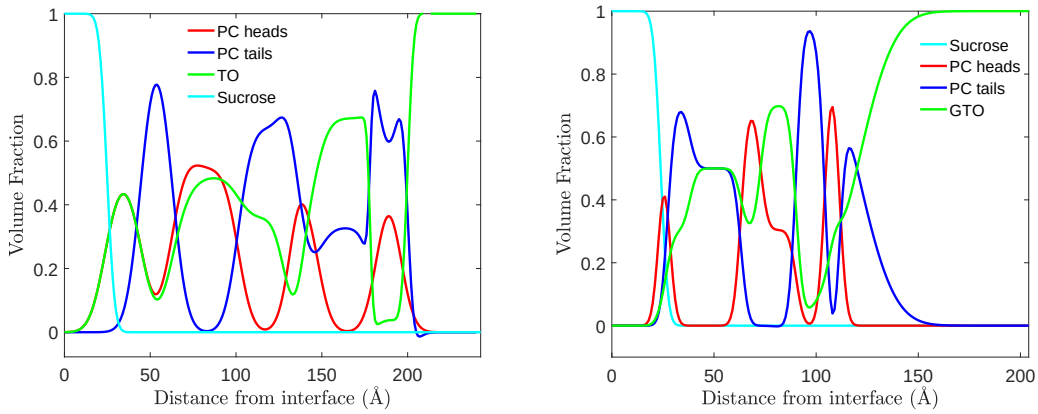

Figure 7.9 *Volume fraction profiles for PC heads (red), PC tails (blue) and the triglyceride oil (green) at the sucrose interface calculated from the SLD profile obtained from fits to the x-ray reflectivity profile for lecithin at sucrose/triglyceride interface. Left panel: Lecithin at sucrose/TO interface. Right panel: Lecithin at sucrose/GTO interface.*

The overall extent of the lecithin layers and the volume fraction profile obtained using XRR are consistent with the volume fraction obtained using NR where 7 layers are obtained for TO and 5 for GTO. The volume fraction profiles show a monolayer followed by 3-distinct peaks corresponding to bilayer/micellar region of head groups present for TO and 2 for GTO in both XRR and NR. The amount of oil incorporated in the phospholipid layers differ between XRR and NR. However

it should be noted that the solvation of lecithin layers by triglyceride oil cannot be resolved using XRR as there is no contrast between PC tails and the oil and therefore, NR fits using the two contrasts provides a better measure for solvent penetration of the lecithin layer.

7.3.3 Lecithin Interactions in TO and GTO

The volume fraction profiles for lecithin at sucrose/TO and sucrose/GTO interfaces, shown in Figure 7.6, shows that lecithin at the sucrose/triglyceride interface comprises an odd number of phospholipid layers. This can be rationalised as the polar phospholipid head group adsorbing at the sucrose interface and the alkyl tails oriented towards the triglyceride oil giving the layered structure as head-tail-tail-head and so on. Lecithin interfacial films in TO comprise 7 oriented layers extending out to 20 nm from the interface, whereas in GTO the interfacial films consist of 5 oriented layers extending upto 15 nm. The interfacial film thicknesses are consistent with the QCM-D measurements which give thicknesses of 7 nm and 23 nm for 2.4% lecithin in GTO and TO respectively.

The detailed structure shows a dense first phospholipid layer which would be consistent with inverse cylindrical micelles unrolling and adsorbing at the interface such that the head-group is oriented towards the sucrose interface and the tails towards the bulk oil. The next layer comprises a lipid bilayer with little oil, made up of cylindrical micelles fused to eliminate the curved spaces of intact cylinders that would be filled by oil. There is some overlap between the head-group and tails in the volume fraction profile suggesting the fused bilayer retains some curvature. The area per molecule of the lecithin layers is ~ 100 Å^2, which suggests that the phospholipids molecules are tilted, which is another indication that the structure has some curvature as it has been built up from lecithin cylindrical micelles adsorbed from the solution. In the case of TO there is another such fused bilayer. The amount of oil incorporated in the lecithin layers increases gradually as the distance from the sucrose interface increases, suggesting that the PC head group has a stronger affinity for the polar sucrose interface than the glycerol backbone. In both oils, the outer layer structure contains a high volume fraction of oil and overlapping head and tail regions, which would be consistent with adsorption of intact cylindrical micelles.

These well-defined lecithin layers at the sucrose/triglyceride oil interface change the inter-particle interactions of the sucrose in triglyceride oil suspensions. In

the absence of surfactants, the van der Waals attraction between grains will be determined by the Hamaker constant for sucrose/triglyceride/sucrose. The presence of a lecithin film, means that the smaller Hamaker constant for the lecithin film/triglyceride/lecithin film determines the van der Waals attraction between sucrose grains [58]. This change in inter-particle interaction upon adsorption of lecithin modifies the rheology of sucrose triglyceride oil suspensions.

The larger number of layers for lecithin in TO as compared to GTO suggests there is a greater attraction between lecithin layers in TO than in GTO, which is also apparent from the greater tendency of lecithin to aggregate into hcp structures upon ageing in TO (solution SAXS data discussed in Section 3.5.2). Additionally, it is observed that sucrose suspensions in TO exhibit a greater yield stress as compared to the suspensions in GTO. These observations together suggest that the van der Waals attraction between lecithin layers is responsible for the yield stress exhibited by sucrose suspension in triglyceride consisting lecithin only. In order to reduce the yield stress, the van der Waals attraction between these lecithin layers needs to be reduced. We argue that this is the role of PGPR in the binary mixtures.

7.4 PGPR at Sucrose/Triglyceride Interface - Reflectivity Study

7.4.1 Neutron Reflectivity from PGPR Films at Sucrose/Triglyceride Interface

To measure the distribution for PGPR at the sucrose/triglyceride oil interface, neutron reflectivity was measured from the interface between 2.4% solutions of PGPR in d50-TO and d50-GTO and spin-coated sucrose films, and is shown in Figure 7.10. The d50-triglycerides enhance the contrast of the PGPR ($\mathrm{SLD} = 0.2 \times 10^{-6}$ Å^{-2}) against the triglyceride oil bulk phase ($\mathrm{SLD_{d50TO}} = 3.0 \times 10^{-6}$ Å^{-2} and $\mathrm{SLD_{d50GTO}} = 3.3 \times 10^{-6}$ Å^{-2}).

The right panel shows NR profiles obtained at the sucrose/d50-GTO interface, carried out using the low volume laminar flow cells described in Section 6.2.4, showing adsorption of PGPR over the time-scales of $1.5-4.5$ hours after injection. The black curve shows sucrose/d50-GTO interface without any added surfactants.

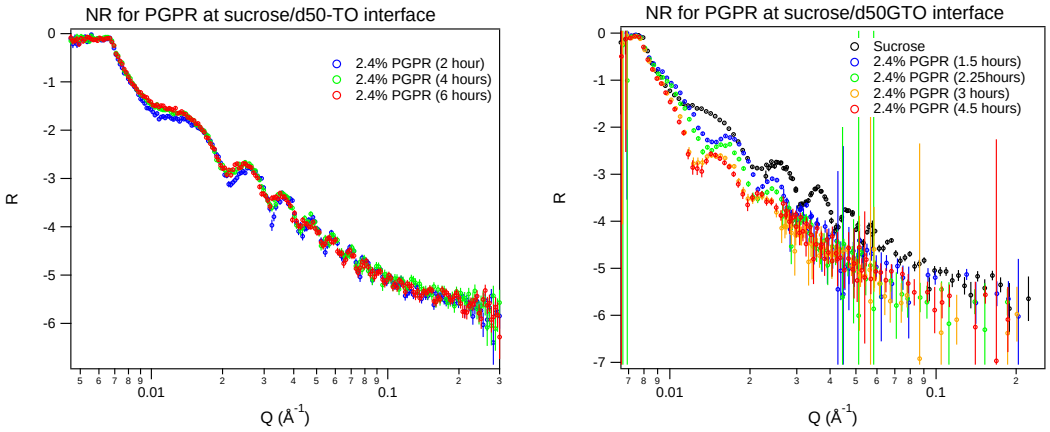

Figure 7.10 *NR from PGPR film at sucrose/triglyceride interface. Time series showing adsorption of PGPR over a period of 1-6 hours after injecting. Left panel: PGPR at sucrose/d50-TO interface. Right panel: PGPR at sucrose/d50-GTO interface.*

The thickness of the sucrose layer was calculated using this reflectivity profile to be 604 Å. A solution containing 2.4% PGPR in d50-GTO was then flowed through the cell and reflectivity was measured starting at 1.5 hours after injection. As can be seen from the figure, a clear dip is observed in the first minima upon the adsorption of PGPR (black cure to blue curve). This is indicative of h-material adsorbing at the interface. Adsorption continues upto 3 hours (orange curve) and stabilises thereafter (orange curve to red curve). The reflectivity profile obtained after 4.5 hours was used for fitting to obtain the distribution of PGPR at the sucrose interface. The left panel shows NR for PGPR at sucrose/d50-TO interface which was carried out using sandwich cells described in Section 6.2.4. The sandwich cell was created using 200 μL of d50-TO solution containing 2.4% PGPR. The sucrose layer for this substrate was pre-characterised using lab-based XRR, which gave a thickness of 463 Å, as the solution cannot be exchanged in these cells. The first measurement shows the reflectivity profile 2 hours after creating the cell (blue curve). There is small change in the reflectivity profile between 2 and 4 hours (green curve), before it stabilises (green curve to red curve). The reflectivity profile obtained after 6 hours was used for fitting.

7.4.2 Data Analysis

The layered profile for the sucrose spin-coated silicon substrates used for neutron reflectivity data fitting is the same as the one described in Section 7.3.2, where

the silicon, silicon oxide and sucrose layers are constructed using sum of two error functions and characterised by their SLD, thickness and roughness as described in Section 6.2.2. At the sucrose interface there is a PGPR layer followed by the bulk triglyceride oil. There was little prior knowledge about the distribution of PGPR[2], and therefore a spline model was used to construct the PGPR layer. The spline was parametrised using the total thickness of the polymer layer ($\text{thick}_{\text{polymer}}$), which is then divided into 9 equal regions starting with the SLD of the sucrose and ending at the SLD of the bulk triglyceride oil. The starting value for the total polymer layer thickness was taken from the values obtained for the QCM-D fits described in Section 5.4. The MATLAB code used to create the SLD profile, which was used to fit the reflectivity profile for PGPR films is given in Appendix E.1. The reflectivity profiles were fitted to the model with ranges of the fit parameters given in Table 7.3 first using the CMAES search, followed by the downhill simplex.

Table 7.3 *Fit parameters and their relevant limits for fitting the PGPR films at sucrose/triglyceride interface using the spline model.*

Parameter		Lower Bound	Starting Value	Upper Bound
$\text{sigma}_{\text{si/siox}}$	(Å)	1	4	10
$\text{thickness}_{\text{siox}}$	(Å)	4	10[a]	40
$\text{sigma}_{\text{siox/suc}}$	(Å)	1	4	10
$\text{thickness}_{\text{suc}}$	(Å)	400	550[a]	700
$\text{thickness}_{\text{polymer}}$	(Å)	100	350	700
Ppolymer1-8	(Å^{-2})	SLD_{PGPR}	1.5×10^{-6}	SLD_{TG}

The subscript si, siox, suc and tg, denote the silicon, silicon oxide, sucrose and triglyceride layers, respectively. Sigma is the interfacial width and is related to the typical roughness of layers by sigma/$\sqrt{2}$.

Ppolymer refers to the SLD values defined at each of the spline points. $\text{SLD}_{\text{PGPR}} = 0.2 \times 10^{-6}$ Å^{-2} and $\text{SLD}_{\text{TG}} = 3.0 \times 10^{-6}$ Å^{-2} for d50-TO and 3.3×10^{-6} Å^{-2} for d50-GTO

[a] Starting values for silicon oxide and sucrose layer thicknesses were taken as the values obtained from fits for oil only data and were allowed to vary 5% on either side.

In addition to the above parameters, finite interfacial widths are required for the sucrose/polymer interface and polymer/triglyceride oil interface. These do not affect the fits, as the spline itself adds an interfacial width to each of these interfaces. These parameters were kept constant at 20 Å (reasonable estimates for both the interfaces).

[2]Preliminary fit obtained using a parametrised slab model comprising 5 layers resulted in and SLD profile with polymer region consisting of thick solvated layer which some ripples in the SLD profile

The fits obtained using the spline model for PGPR at sucrose/d50-TO and sucrose/d50-GTO interface are shown in Figure 7.11 and 7.12, respectively. The top panel shows the measured NR profile and the fit (left panel) and the corresponding SLD profile(right panel). The solid line shows the fit to the data and the shaded region around the calculated reflectivity and SLD profiles shows the 95% Bayesian prediction intervals calculated from the maximum and minimum ranges of the parameter posteriors based on the Bayesian analysis. The posteriors obtained using the Bayesian analysis assuming uniform priors are shown in the bottom panel of Figures 7.11 and 7.12. The results obtained using the Bayesian analysis for the best fit parameters and their 95% intervals are summarised shown in Table 7.4.

Table 7.4 *Values obtained for the fit parameters and their 95% confidence ranges (quoted in brackets) using the spline model to fit the PGPR distribution at the sucrose/triglyceride interface.*

Parameter		TO		GTO	
		Value	(min, max)	Value	(min, max)
$\text{sigma}_{\text{si/siox}}$	(Å)	4.2	(1.3, 9.34)	6.4	(3.12, 10.71)
$\text{thickness}_{\text{siox}}$	(Å)	17.7	(15.39, 19.76)	14.4	(13.3, 15.3)
$\text{sigma}_{\text{siox/suc}}$	(Å)	5.4	(4.04, 6.69)	6.1	(5.66, 7.51)
$\text{thickness}_{\text{suc}}$	(Å)	464	(451, 483)	604	(592, 608)
$\text{thickness}_{\text{polymer}}$	(Å)	320	(269, 371)	573	(550, 649)
Ppolymer1	$(\times 10^{-6}\text{Å}^{-2})$	1.51	(1.41, 1.61)	1.75	(1.67, 1.81)
Ppolymer2	$(\times 10^{-6}\text{Å}^{-2})$	1.28	(0.99, 1.42)	1.79	(1.72, 1.85)
Ppolymer3	$(\times 10^{-6}\text{Å}^{-2})$	0.74	(0.65, 0.85)	1.94	(1.81, 2.03)
Ppolymer4	$(\times 10^{-6}\text{Å}^{-2})$	1.48	(1.16, 1.84)	2.00	(1.91, 2.10)
Ppolymer5	$(\times 10^{-6}\text{Å}^{-2})$	2.22	(1.97, 2.51)	2.28	(2.13, 2.40)
Ppolymer6	$(\times 10^{-6}\text{Å}^{-2})$	2.65	(2.47, 2.85)	2.58	(2.45, 2.76)
Ppolymer7	$(\times 10^{-6}\text{Å}^{-2})$	2.80	(2.71, 2.89)	2.98	(2.86, 3.05)
Ppolymer8	$(\times 10^{-6}\text{Å}^{-2})$	2.85	(2.72, 2.98)	3.11	(3.04, 3.23)

The SLD profile obtained from the NR fits can be deconstructed into its various components as shown in the left panel of Figure 7.13 and 7.14 for PGPR in d50-TO and d50-GTO, respectively. The silicon is depicted in cyan, the silicon oxide in blue, the sucrose in red, the bulk triglyceride oil in pink and the polymer layer in green. The green curve can be converted into the volume fraction of PGPR

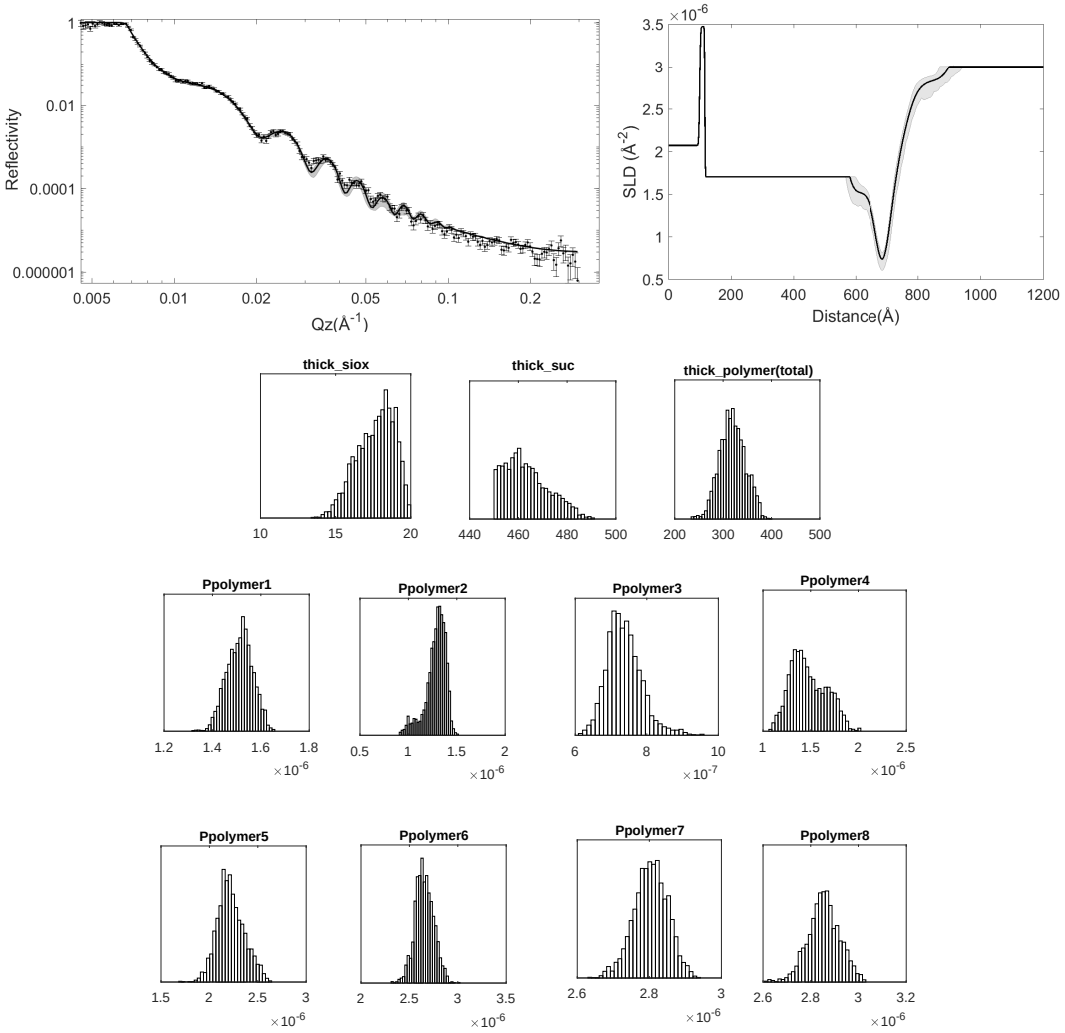

Figure 7.11 *NR profiles from PGPR at sucrose/d50-TO interface fitted to the spline model discussed in Section 7.4.2. Top panel: Measured NR profile along with the fit (left panel) and the corresponding SLD profile (right panel) with the shaded region depicting the 95% Bayesian prediction interval. Bottom panel: The posteriors for the fit parameters obtained by assuming uniform priors using Bayesian analysis.*

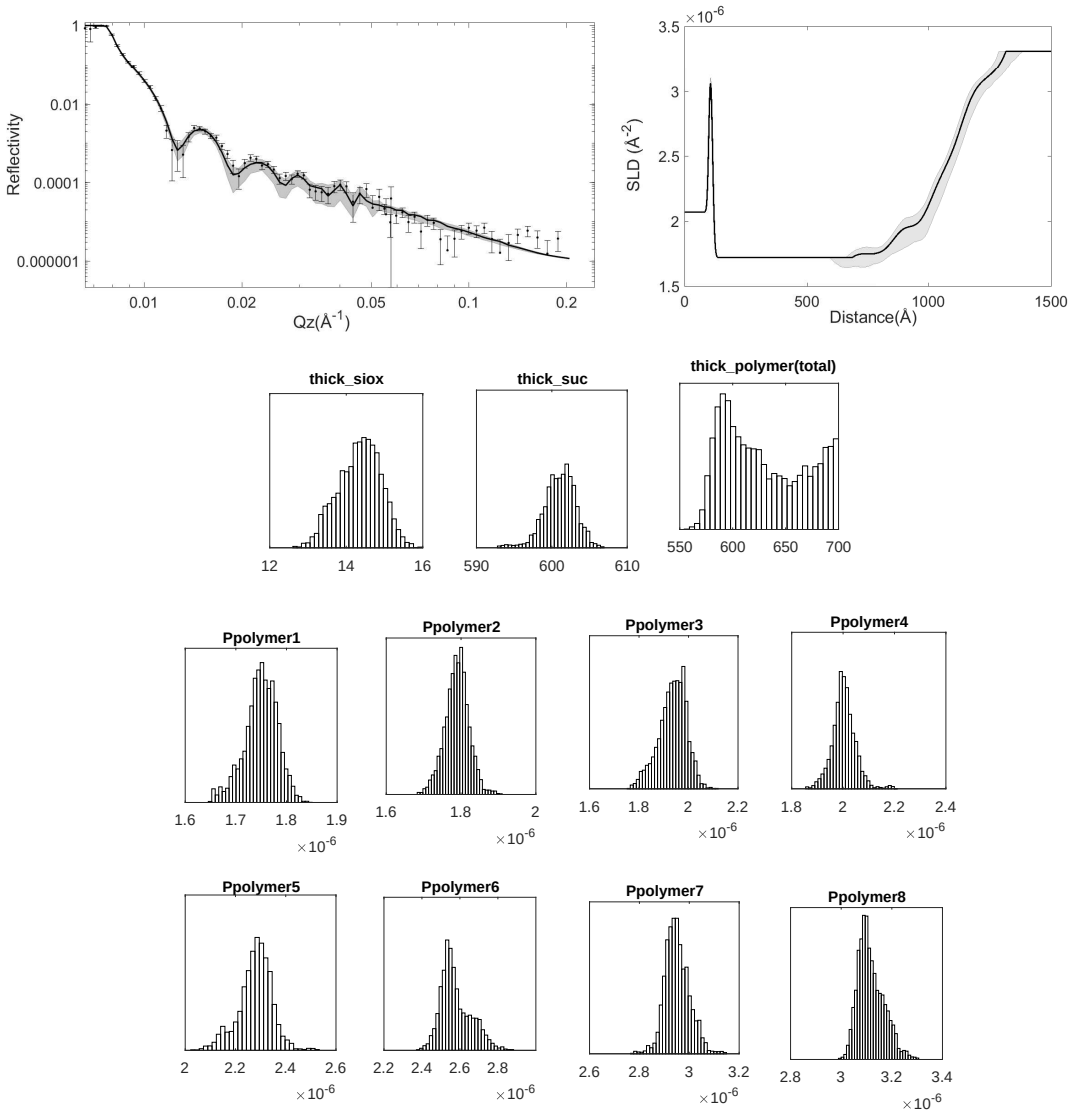

Figure 7.12 *NR profiles from PGPR at sucrose/d50-GTO interface fitted to the spline model discussed in Section 7.4.2. Top panel: Measured NR profile along with the fit (left panel) and the corresponding SLD profile (right panel) with the shaded region depicting the 95% Bayesian prediction interval. Bottom panel: The posteriors for the fit parameters obtained by assuming uniform priors using Bayesian analysis.*

$(\phi_p(z))$ and triglyceride oil $(1 - \phi_p(z))$ in the polymer layers using:

$$\begin{aligned} \phi_p(z) * SLD_{PGPR} + (1 - \phi_p(z)) * SLD_{TG} &= SLD_{layer}(z) \\ \implies \phi_p(z) &= \frac{SLD_{layer}(z) - SLD_{TG}}{SLD_{PGPR} - SLD_{TG}} \end{aligned} \tag{7.10}$$

where, SLD_{PGPR} and SLD_{TG} are the SLD of the PGPR molecule and triglyceride oil, respectively, which are known parameters, and $SLD_{layer}(z)$ is the SLD profile for the polymer layer obtained using the fits (green curve). This equation treats the polymer at a mean-field level, so the plots obtained from its application provide the distribution of the polymer segments in the layer. Using Equation 7.10, the volume fraction of PGPR segments (blue curve), and hence the volume fraction of the triglyceride oil (red curve), in the polymer layer at the sucrose/triglyceride interface were obtained as shown in the right panel of Figure 7.13 and 7.14 for d50-TO and d50-GTO, respectively.

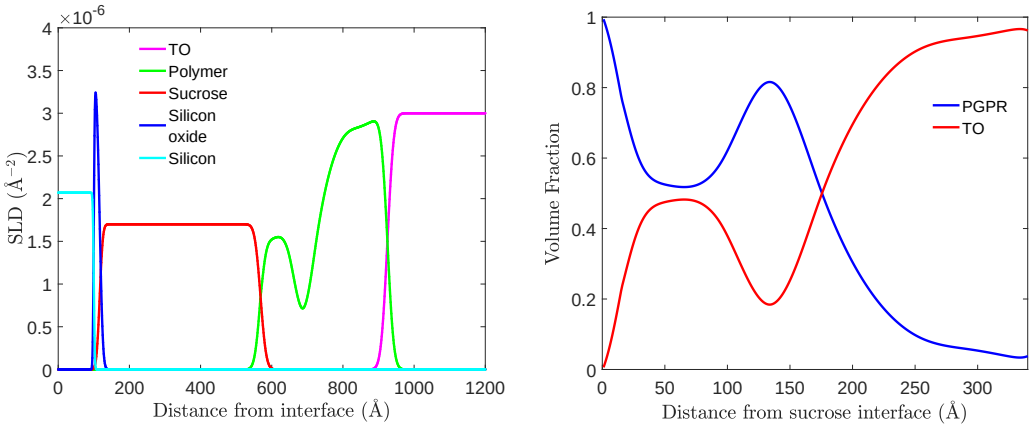

Figure 7.13 *Left panel: SLD profile obtained for the NR fits for PGPR at sucrose/d50-TO interface deconstructed into the various layers: Silicon (cyan), Silicon oxide (blue), Sucrose (red), Polymer layer (green) and the bulk d50-TO (pink). Right panel: Volume fraction profile obtained for PGPR (blue) and d50-TO (red) obtained from the polymer layer SLD (green curve in the left panel).*

7.4.3 PGPR Films at Sucrose interface in TO and GTO

PGPR adsorbs at the sucrose/triglyceride oil interface forming extended layers of thicknesses 500 Å in GTO and 300 Å in TO and in both the oils the layer entrains significant amounts of oil (>40% after the first 50 Å). The adsorption of these extended solvated layers at the sucrose/triglyceride oil interface changes inter-particle interaction by providing steric repulsion and thereby modifies the rheology of sucrose in triglyceride oil suspensions. The thickness of the layer is greater than any single dimension in the PGPR molecule and therefore, this suggests that the layer comprises PGPR aggregates. This points towards an association between PGPR molecules in the triglyceride oil, which is also evident

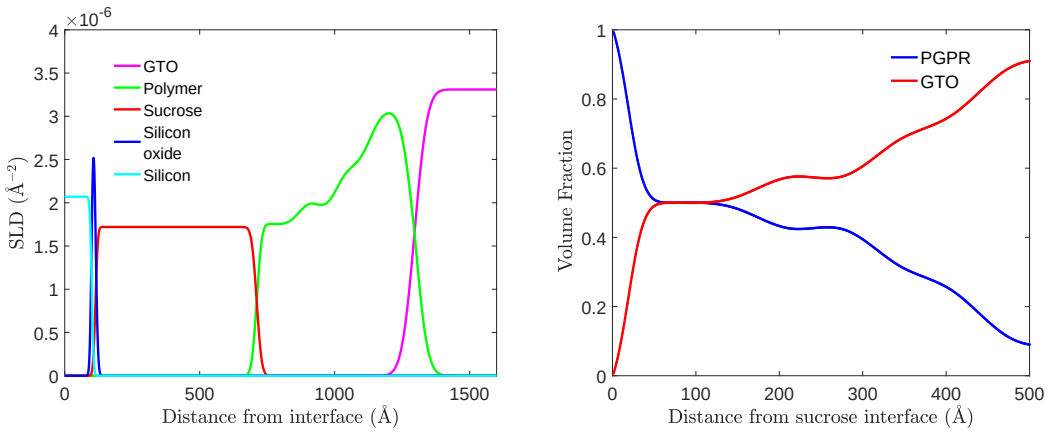

Figure 7.14 *Left panel: SLD profile obtained for the NR fits for PGPR at sucrose/d50-GTO interface deconstructed into the various layers: Silicon (cyan), Silicon oxide (blue), Sucrose (red), Polymer layer (green) and the bulk d50-GTO (pink). Right panel: Volume fraction profile obtained for PGPR (blue) and d50-GTO (red) obtained from the polymer layer SLD (green curve in the left panel).*

in the SAXS and SANS from PGPR solutions in triglyceride oil where cylindrical micelles are observed (Section 3.5.3).

The volume fraction profiles for PGPR at sucrose/TO and sucrose/GTO interface, shown in the right panel of Figure 7.13 and 7.14 respectively, are similar over the region $0-100$ Å, which is presumably due to adsorption of a first layer of PGPR micelles. The PGPR volume fraction profiles are also similar in the region far from sucrose interface where the PGPR volume fraction gradually decays to <0.1 over the last 100 Å. The regions near and far from sucrose interface govern the structure of the interfacial PGPR film and thereby the shearing of sucrose grains bearing these PGPR films at high and low shear stresses, respectively. This and thereby the shearing of two sucrose grains bearing these PGPR films. The structural similarity between PGPR films in GTO and TO in these regions means that the effect of PGPR on the rheology of sucrose suspensions at high and low shear stresses will be similar in GTO and TO.

The main difference in the PGPR volume fraction profiles arise in the intermediate region, where a distinct second layer of aggregates is observed for PGPR at the sucrose/TO interface, whereas at the sucrose/GTO interface a monotonically decreasing volume fraction profile is observed that resembles the volume fraction profile of a polymer brush which in this case would be comprised of PGPR micelles. This again indicates that there is a stronger attraction between

surfactant layers or aggregates in TO than in GTO. This difference in the PGPR volume fraction profile can also explain the difference observed in the thickness dependence of shear modulus obtained from the fits to the QCM-D data for PGPR films in GTO and TO. The material properties of the brush-like layer formed from PGPR micelles in GTO might be expected to remain constant as the thickness of the layer increases, as the volume fraction is a monotonic function that could be approximated by a step function. This volume profile will also be consistent with the power law scattering with exponent of -4.4 observed in the low q SANS from PGPR stabilised sucrose in GTO suspensions indicating an extended diffuse interface, as discussed in Section 4.3.5. On the other hand, the non-monotonic volume fraction profile obtained for PGPR at the sucrose/TO interface means that the shear modulus (determined from the fits to the QCM-D) will change when the second layer is added, i.e. the concentration is increased. The second distinct layer of PGPR aggregates will lead to a defined PGPR/oil interface which can have some fractal component due to the polydispersity in PGPR micelles and variation in surfactant coverage at the sucrose interface. This can also explain the power law scattering with exponent of -3.6 observed in the low q SANS from PGPR stabilised sucrose in TO suspensions, discussed in Section 4.3.6.

7.5 Lecithin and PGPR at Sucrose/Triglyceride Interface - Reflectivity Study

7.5.1 Neutron and X-ray Reflectivity from Lecithin and PGPR Films at Sucrose/Triglyceride Interface

To measure the structure formed by the binary mixture of lecithin and PGPR at the sucrose sucrose/triglyceride oil interface, neutron reflectivity was measured for solutions of 1.2% lecithin + 1.2% PGPR in h-TO, d50-TO and d50-GTO, and solutions of 1.8% lecithin + 0.6% PGPR in h-TO and d50-TO with the neutrons incident from the silicon interface. In addition to the neutron reflectivity, x-ray reflectivity was also measured for 1.2% lecithin + 1.2% PGPR in TO and GTO with the x-rays incident through the triglyceride bulk phase. The neutron and x-ray reflectivity profiles obtained are shown in Figures 7.15 and 7.16.

As is evident from the shift in the first minima observed in the neutron reflectivity

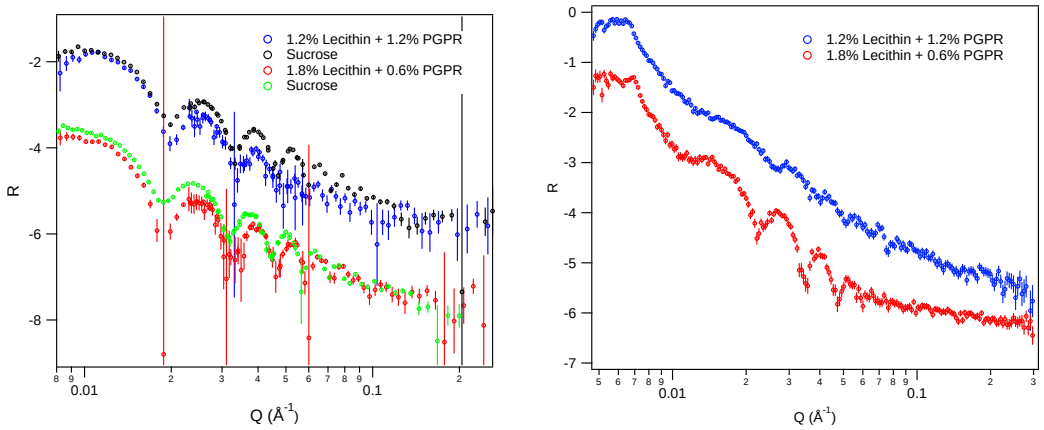

Figure 7.15 *NR from 1.8% lecithin + 0.6% PGPR (red offset by -2 on the y-axis for clarity) and 1.2% lecithin + 1.2% PGPR (blue) at the sucrose/TO. Left panel: h-TO contrast. Right panel: d50-TO contrast.*

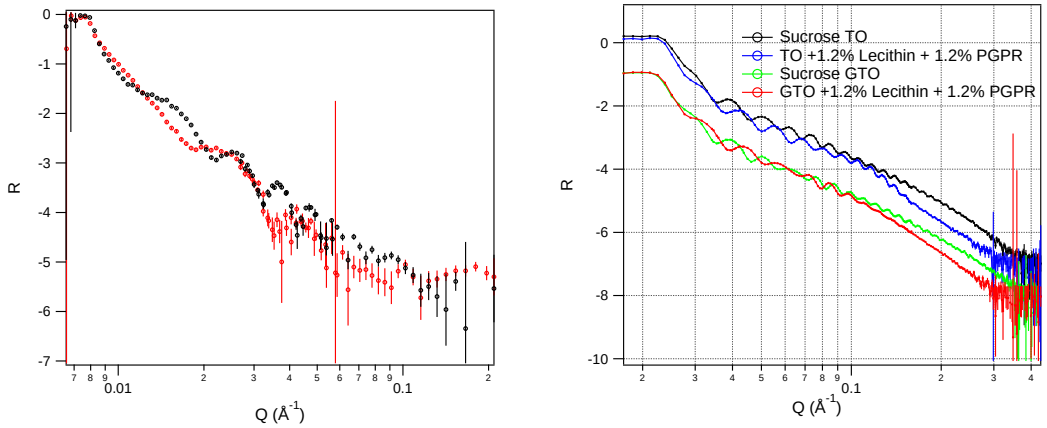

Figure 7.16 *Left panel: NR from 1.2% lecithin + 1.2% PGPR at the sucrose/d50-GTO. Right panel: XRR from 1.2% lecithin + 1.2% PGPR at the sucrose/TO (blue) and sucrose/GTO (red) interface.*

profile in the left hand panel of Figures 7.15 and 7.16, both the binary mixtures are adsorbed at the sucrose/triglyceride interface. The shift in the first minima is greater when compared to reflectivity from lecithin only films, Figure 7.1 and 7.2, suggesting that the adsorbed amount is greater. Also as the PGPR fraction of the surfactant mixture increases, the Kiessig fringes in the neutron reflectivity profile get more smeared suggesting that the interface is becoming extended and diffuse. The XRR profile for films of lecithin and PGPR binary mixtures shows features very similar to that of lecithin films (Figure 7.3), where a shoulder is observed at $q \approx 0.1$ Å^{-1}. The shoulder in GTO is more pronounced in the case of the binary mixture as compared to lecithin only films. In TO, arguably the shoulder moves slightly to lower q when compared to the lecithin only XRR profile. These observations suggest that, lecithin + PGPR mixtures result in interfacial films which have some features in common with lecithin films but are diffuse and extended like PGPR films.

7.5.2 Data Analysis

Limited information is available about the distribution of lecithin and PGPR in the binary mixtures at the sucrose/triglyceride interface. In order to provide maximum flexibility to the SLD profile for the lecithin + PGPR films, the spline model was used to construct the interfacial surfactant layer in the same way as detailed for PGPR films in Section 7.4.2. The SLD profile consists of sucrose spin-coated silicon substrates which comprises the silicon, silicon oxide, sucrose and triglyceride layers constructed using sum of two error functions and characterised by their SLD, thickness and roughness as described in Section 6.2.2, and the interfacial surfactant layer. This layer is constructed using a spline model parametrised using the total thickness of the layer ($\text{thick}_{\text{layer}}$), which is then divided into up to 13 equal regions starting with the SLD of the sucrose and ending at the SLD of the bulk triglyceride oil. The MATLAB code used to create the SLD profile is the same as that used for PGPR films and is given in Appendix E.1. The starting value for the total surfactant layer thickness was taken from the values obtained for the QCM-D fits described in Section 5.4 and is kept constrained between h-oil and d50-oil contrast, while the other parameters are allowed to vary independently with ranges given in Table 7.5. The data was first fitted using the CMAES search, followed by the downhill simplex.

The fits obtained for the NR profile using the h-oil and d50-oil contrast for 1.8%

Table 7.5 *Fit parameters and their relevant limits for fitting the lecithin + PGPR films at sucrose/triglyceride interface using the spline model.*

Parameter		Lower Bound	Starting Value	Upper Bound
$\text{sigma}_{\text{si/siox}}$	(Å)	1	4	10
$\text{thickness}_{\text{siox}}$	(Å)	4	10[a]	40
$\text{sigma}_{\text{siox/suc}}$	(Å)	1	4	10
$\text{thickness}_{\text{suc}}$	(Å)	400	550[a]	700
$\text{thickness}_{\text{layer}}$	(Å)	200	350	1000
Ppolymer1-13 (h-oil)[b]	(Å^{-2})	SLD_{TG}	1.5×10^{-6}	1.84×10^{-6}
Ppolymer1-13 (d50-oil)[b]	(Å^{-2})	0.2×10^{-6}	1.5×10^{-6}	$\text{SLD}_{\text{d50-TG}}$

The subscript si, siox, suc and tg, denote the silicon, silicon oxide, sucrose and triglyceride layers, respectively. Sigma is the interfacial width and is related to the typical roughness of layers by sigma/$\sqrt{2}$.

[b] Ppolymer refers to the SLD values defined at each of the spline points. The upper bound for Ppolymer in the h-contrast is the SLD of the POPC head group and the lower bound in the d50-contrast is the SLD of the PGPR.

[a] The starting values for silicon oxide and sucrose layer thickness were taken as the values obtained from fits for oil only data and were allowed to vary 5% on either side.

In addition to the above parameters, finite interfacial widths are required for the sucrose/polymer interface and polymer/triglyceride oil interface. These do not affect the fits, as the spline itself adds an interfacial with to both of these interfaces. These parameters were kept constant at 20 Å (reasonable estimates for both the interfaces).

lecithin + 0.6% PGPR and 1.2% lecithin + 1.2% PGPR at the sucrose/TO interface are shown in Figures 7.17 and 7.18, respectively. The top panel in both these figures shows the d50-oil contrast and the bottom panel shows the h-oil contrast. The measured reflectivity profile along with the fit are shown in the left panel and the corresponding SLD profile is shown in the right panel. A shaded region around the fit and the SLD profile depicts the 95% Bayesian prediction interval. The results obtained using Bayesian analysis for the best fit parameters and their 95% intervals are summarised shown in Tables 7.6 and 7.7.

The SLD profile obtained from the NR fits can be deconstructed into its various components as shown in Figure 7.19, where the left panel shows the deconstructed SLD profile for 1.8% lecithin + 0.6% PGPR and the right panel for 1.2% lecithin + 1.2% PGPR. The the solid line depicts the d50-contrast and the dashed line depicts the h-contrast (offset to the same sucrose interface as d50-contrast). The silicon layer is shown in cyan, the silicon oxide in blue, the sucrose in red, the bulk triglyceride oil in pink and the surfactant layer in green.

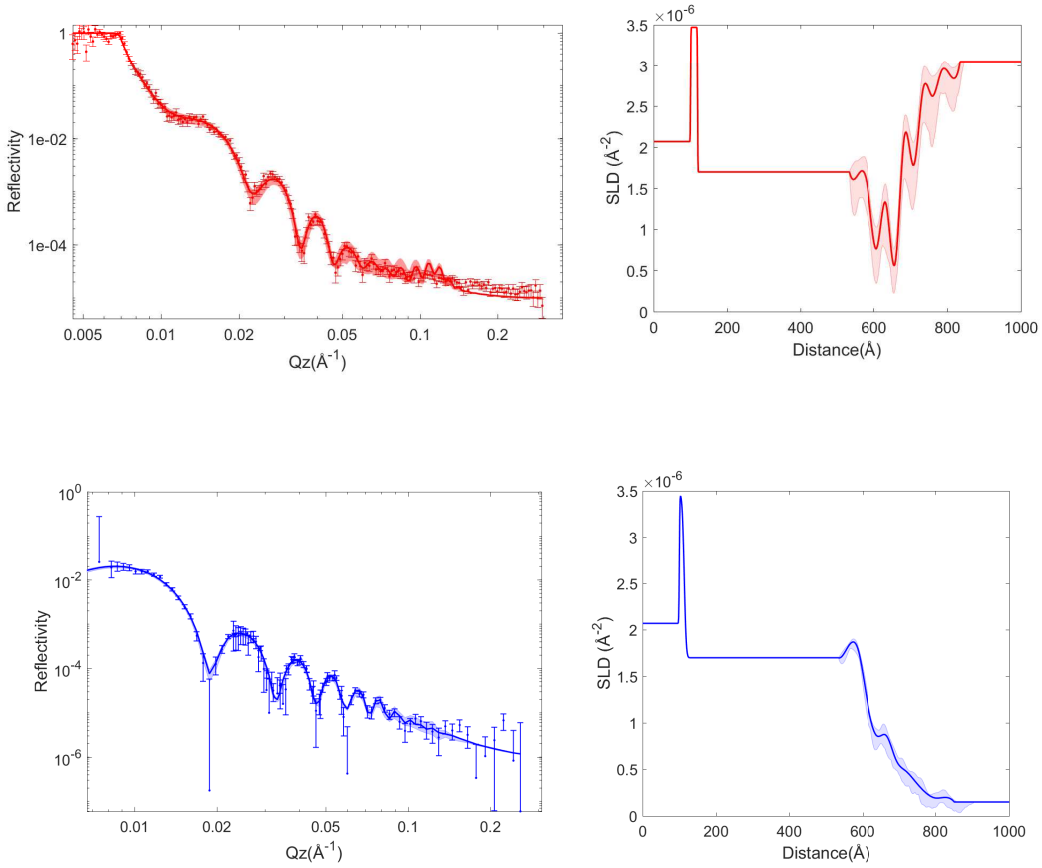

Figure 7.17 *NR profiles for 1.8% lecithin + 0.6% PGPR at sucrose/TO interface in d50-oil (top panel) and h-oil (bottom) contrast. The reflectivity profiles were fitted using the splines model discussed in Section 7.5.2 with the thickness of the surfactant layer constrained to be the same in the two contrasts. Measured NR profile along with the fit (left panel) and the corresponding SLD profile (right panel) with the shaded region depicting the 95% Bayesian prediction interval.*

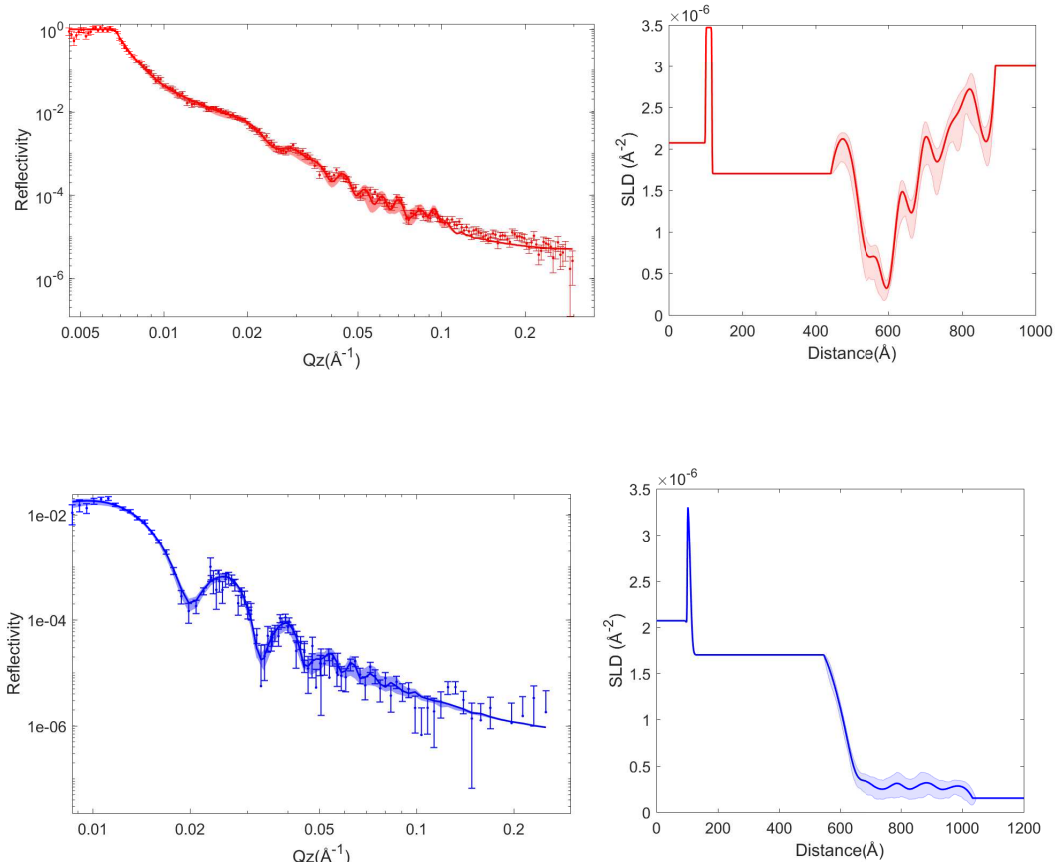

Figure 7.18 *NR profiles for 1.2% lecithin + 1.2% PGPR at sucrose/TO interface in d50-oil (top panel) and h-oil (bottom panel) contrast. The reflectivity profiles were fitted using the splines model discussed in Section 7.5.2 with the thickness of the surfactant layer constrained to be the same in the two contrasts. Measured NR profile along with the fit (left panel panel) and the corresponding SLD profile (right) with the shaded region depicting the 95% Bayesian prediction interval.*

Table 7.6 *Values obtained for the fit parameters and their 95% confidence ranges (quoted in brackets) using the spline model to fit the SLD profile for 1.8% lecithin + 0.6% PGPR at the sucrose/TO interface.*

Parameter		d50-TO		h-TO	
		Value	(min, max)	Value	(min, max)
$\text{thickness}_{\text{polymer}}$	(Å)		NA	317.4	(300.3, 352.1)
Ppolymer1	($\times 10^{-6}$Å^{-2})	1.68	(1.47, 1.89)	1.82	(1.78, 1.84)
Ppolymer2	($\times 10^{-6}$Å^{-2})	1.51	(1.27, 1.77)	1.80	(1.70, 1.84)
Ppolymer3	($\times 10^{-6}$Å^{-2})	0.77	(0.49, 1.06)	1.24	(1.01, 1.42)
Ppolymer4	($\times 10^{-6}$Å^{-2})	1.32	(0.95, 1.58)	0.86	(0.77, 0.95)
Ppolymer5	($\times 10^{-6}$Å^{-2})	0.58	(0.36, 0.83)	0.86	(0.71, 1.00)
Ppolymer6	($\times 10^{-6}$Å^{-2})	2.12	(1.80, 2.39)	0.60	(0.45, 0.73)
Ppolymer7	($\times 10^{-6}$Å^{-2})	1.78	(1.45, 2.11)	0.48	(0.36, 0.63)
Ppolymer8	($\times 10^{-6}$Å^{-2})	2.70	(2.42, 2.97)	0.37	(0.22, 0.49)
Ppolymer9	($\times 10^{-6}$Å^{-2})	2.62	(2.27, 2.91)	0.26	(0.12, 0.42)
Ppolymer10	($\times 10^{-6}$Å^{-2})	2.93	(2.80, 3.00)	0.19	(0.12, 0.26)
Ppolymer11	($\times 10^{-6}$Å^{-2})	2.87	(2.66, 2.99)	0.20	(0.12, 0.26)

The green curve can be converted into the volume fraction of phospholipid head ($\phi_h(z)$), PGPR ($\phi_p(z)$) and triglyceride oil ($\phi_o(z)$) in the polymer layers using the two contrasts with SLD profiles $\rho_1(z)$ and $\rho_2(z)$:

$$\begin{bmatrix} SLD_{PCh1} & SLD_{PGPR1} & SLD_{oil1} \\ SLD_{PCh2} & SLD_{PGPR2} & SLD_{oil2} \\ 1 & 1 & 1 \end{bmatrix} \times \begin{bmatrix} \phi_h(z) \\ \phi_p(z) \\ \phi_o(z) \end{bmatrix} = \begin{bmatrix} \rho_1(z) \\ \rho_2(z) \\ 1 \end{bmatrix} \tag{7.11}$$

where, SLD_{PChx}, SLD_{PGPRx} and SLD_{oilx} are the SLD of the PC head, PGPR and oil in the relevant contrast x. In these equations it has been assumed that the PGPR and the phospholipid tails are indistinguishable. This is not a bad assumption as the difference between the SLD of PGPR and phospholipids tails $\approx 0.2 \times 10^{-6}$ Å^{-2}, which is much smaller than the SLD difference between other components in the system. The Matrix Equation 7.11 can be solved to obtained $\phi_o(z)$, $\phi_h(z)$ and $\phi_p(z)$.

For h-oil and d50-oil contrast in NR where only the SLD of the oil changes between the two contrast, $SLD_{oil1} = SLD_{h-TO} = 0.15 \times 10^{-6}$ Å^{-2} and $SLD_{oil2} = SLD_{d50TO} = 3.0 \times 10^{-6}$ Å^{-2}, whereas the SLD of PC head and PGPR remain

Table 7.7 *Values obtained for the fit parameters and their 95% confidence ranges (quoted in brackets) using the spline model to fit the SLD profile for 1.2% lecithin + 1.2% PGPR at the sucrose/TO interface.*

Parameter		d50-TO		h-TO	
		Value	(min, max)	Value	(min, max)
$\text{thickness}_{\text{polymer}}$	(Å)		NA	488.0	(464.4, 499.7)
Ppolymer1	($\times 10^{-6}$Å^{-2})	2.12	(1.97, 2.20)	1.37	(1.30, 1.45)
Ppolymer2	($\times 10^{-6}$Å^{-2})	1.68	(1.48, 1.86)	0.90	(0.83, 0.97)
Ppolymer3	($\times 10^{-6}$Å^{-2})	0.77	(0.55, 1.00)	0.43	(0.34, 0.53)
Ppolymer4	($\times 10^{-6}$Å^{-2})	0.66	(0.45, 0.85)	0.33	(0.25, 0.42)
Ppolymer5	($\times 10^{-6}$Å^{-2})	0.37	(0.30, 0.50)	0.27	(0.17, 0.38)
Ppolymer6	($\times 10^{-6}$Å^{-2})	1.45	(1.27, 1.63)	0.26	(0.16, 0.39)
Ppolymer7	($\times 10^{-6}$Å^{-2})	1.24	(1.06, 1.43)	0.31	(0.20, 0.45)
Ppolymer8	($\times 10^{-6}$Å^{-2})	2.11	(1.90, 2.35)	0.25	(0.16, 0.38)
Ppolymer9	($\times 10^{-6}$Å^{-2})	1.85	(1.63, 2.03)	0.29	(0.16, 0.44)
Ppolymer10	($\times 10^{-6}$Å^{-2})	2.21	(2.08, 2.40)	0.31	(0.22, 0.43)
Ppolymer11	($\times 10^{-6}$Å^{-2})	2.48	(2.21, 2.70)	0.25	(0.16, 0.36)
Ppolymer12	($\times 10^{-6}$Å^{-2})	2.70	(2.43, 2.92)	0.27	(0.19, 0.35)
Ppolymer13	($\times 10^{-6}$Å^{-2})	2.13	(1.98, 2.29)	0.27	(0.21, 0.35)

same $SLD_{PCh1} = SLD_{PCh2} = SLD_h = 1.84 \times 10^{-6}$ Å^{-2} and $SLD_{PGPR1} = SLD_{PGPR2} = SLD_p = 0.2 \times 10^{-6}$ Å^{-2}, Equation 7.11 can be solved to give:

$$\phi_o(z) = \frac{\rho_1(z) - \rho_2(z)}{SLD_{hTO} - SLD_{d50TO}} \tag{7.12}$$

$$\phi_h(z) = \frac{\big(\rho_1(z) - SLD_p\big) - \big(\phi_o(z) * (SLD_{hTO} - SLD_p)\big)}{SLD_h - SLD_p} \tag{7.13}$$

$$\phi_p(z) = 1 - (\phi_o(z) + \phi_h(z)) \tag{7.14}$$

Using this formalism, the volume fraction of PC-head, PGPR (+tails) and the triglyceride oil are found and shown in Figure 7.20. The left panel shows the volume fraction profile for 1.8% lecithin + 0.6% PGPR and the right panel for 1.2% lecithin + 1.2% PGPR at the sucrose/TO interface. In the left panel, the volume fraction profile between 110 Å and 160 Å contains nothing but heads and sucrose. There is little contrast between these two and therefore the interface between them is not well defined. Furthermore, the spline model cannot be

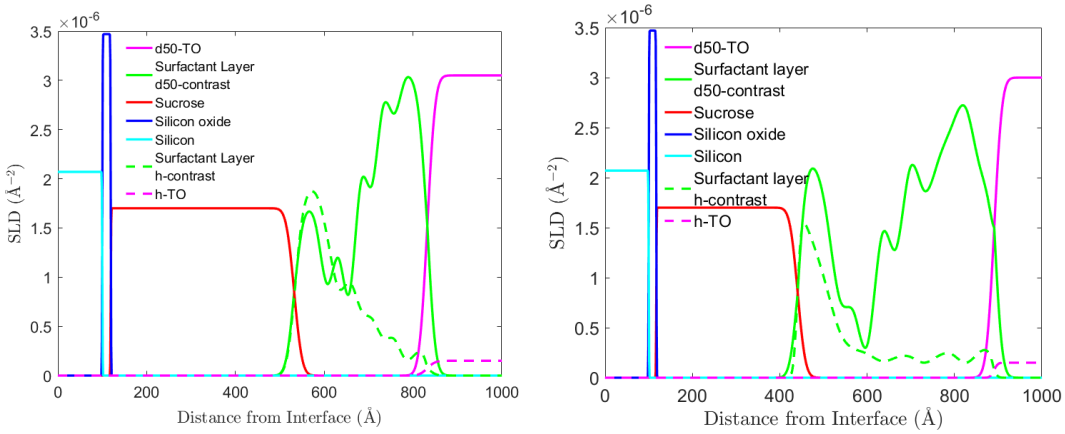

Figure 7.19 *SLD profile obtained for the NR fits for lecithin and PGPR binary mixtures at sucrose/TO interface deconstructed into the various layers: Silicon (cyan), Silicon oxide (blue), Sucrose (red), Polymer layer (green) and the bulk d50-TO (pink). The solid line represents the d50-contrast and the dashed line depicts the h-contrast (offset to the same sucrose interface as d50-contrast). Left panel: 1.8% lecithin + 0.6% PGPR. Right panel: 1.2% lecithin + 1.2% PGPR.*

constrained to limit the layer thickness. The sucrose interfacial width is probably not as high as apparent in the profile and the fit compensates for it by filling with heads, increasing the thickness of the head only region to an unrealistic value of 25 Å. I suggest that the actual sucrose layer is $\sim$ 15 Å thicker, making the head region 10 Å thick. A similar effect is observed in the right panel where the thickness of the head-rich region is potentially inflated by 10-15 Å. However, the common feature remains that there is a head-rich region followed by intermixing of PC heads and PGPR.

For 1.2% lecithin + 1.2% PGPR in GTO, NR from sucrose/d50-GTO interface and XRR from sucrose/h-GTO interface were used as the two contrasts. For the XRR, the layered profile is bulk triglyceride oil, followed by the interfacial surfactant layer, followed by sucrose, silicon oxide and finally silicon. Here splines were implemented to start at with the SLD of the bulk triglyceride oil and end at the SLD of sucrose and are given in the MATLAB code in Appendix E.2. The reflectivity profile and the obtained fits are shown in Figure 7.21. The top panel shows the NR from d50-oil contrast and the bottom panel shows the XRR from h-oil contrast. The measured reflectivity profile along with the fit are shown in the left panel and the corresponding SLD profile is shown in the right panel. A shaded region around the fit and the SLD profile depicts the 95% Bayesian prediction interval. The results obtained using the Bayesian analysis for the best

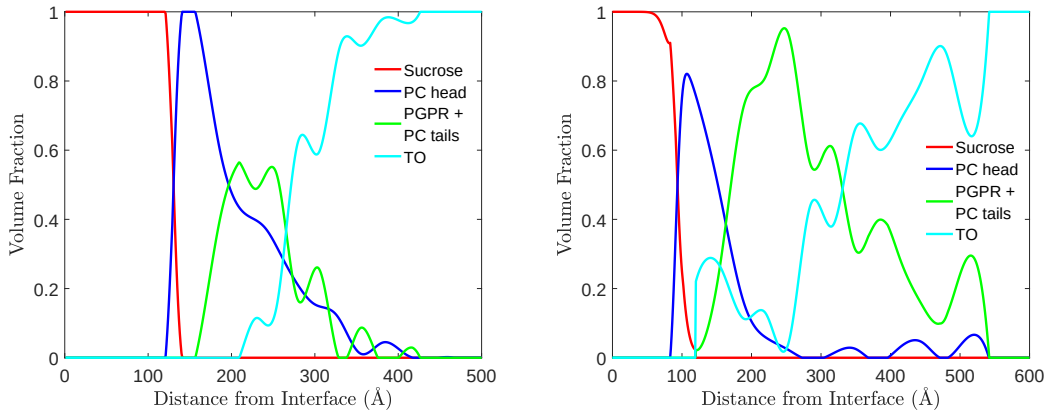

Figure 7.20 *Volume fraction profiles obtained for various components in the interfacial surfactant layer using Equation 7.11. Sucrose is depicted in red, PC-head in blue, PGPR + PC tails in green and TO in cyan. Left panel: 1.8% lecithin + 0.6% PGPR. Right panel: 1.2% lecithin + 1.2% PGPR.*

fit parameters and their 95% intervals are summarised shown in Table 7.8.

Table 7.8 *Values obtained for the fit parameters and their 95% confidence ranges (quoted in brackets) using the spline model to fit the SLD profile for 1.2% lecithin + 1.2% PGPR at the sucrose/GTO interface.*

Parameter		d50-GTO		h-GTO (XRR)	
		Value	(min, max)	Value	(min, max) [a]
$\text{thickness}_{\text{polymer}}$	(Å)	206.5	(199.6, 221.4)	NA	
Ppolymer1	($\times 10^{-6}$Å^{-2})	1.37	(1.19, 1.58)	9.69	(9.42, 9,94)
Ppolymer2	($\times 10^{-6}$Å^{-2})	1.39	(0.95, 1.79)	9.80	(9.58, 10.03)
Ppolymer3	($\times 10^{-6}$Å^{-2})	1.95	(1.30, 2.56)	10.30	(9.98, 10.59)
Ppolymer4	($\times 10^{-6}$Å^{-2})	0.70	(0.28, 1.32)	10.77	(10.47, 11.09)
Ppolymer5	($\times 10^{-6}$Å^{-2})	2.65	(2.07, 3.08)	10.67	(10.33 11.00)
Ppolymer6	($\times 10^{-6}$Å^{-2})	1.30	(0.92, 1.78)	10.69	(10.37, 11.03)
Ppolymer7	($\times 10^{-6}$Å^{-2})	2.86	(2.18, 3.28)	10.87	(10.56, 11.21)
Ppolymer8	($\times 10^{-6}$Å^{-2})	2.37	(1.92, 2.83)	11.32	(11.04, 11.63)
Ppolymer9	($\times 10^{-6}$Å^{-2})	2.96	(2.56, 3.27)	11.58	(11.31, 11.87)
Ppolymer10	($\times 10^{-6}$Å^{-2})	3.13	(2.87, 3.29)	11.69	(11.51, 11.88)
Ppolymer11	($\times 10^{-6}$Å^{-2})	3.08	(2.88, 3.25)	12.37	(12.17, 12.60)

[a] The values quoted for x-rays go from SLD of oil to SLD of sucrose as the x-ray are incident through the triglyceride oil and so the SLD profile of the sample is reversed.

The SLD profile was de-constructed in the various components as shown in the

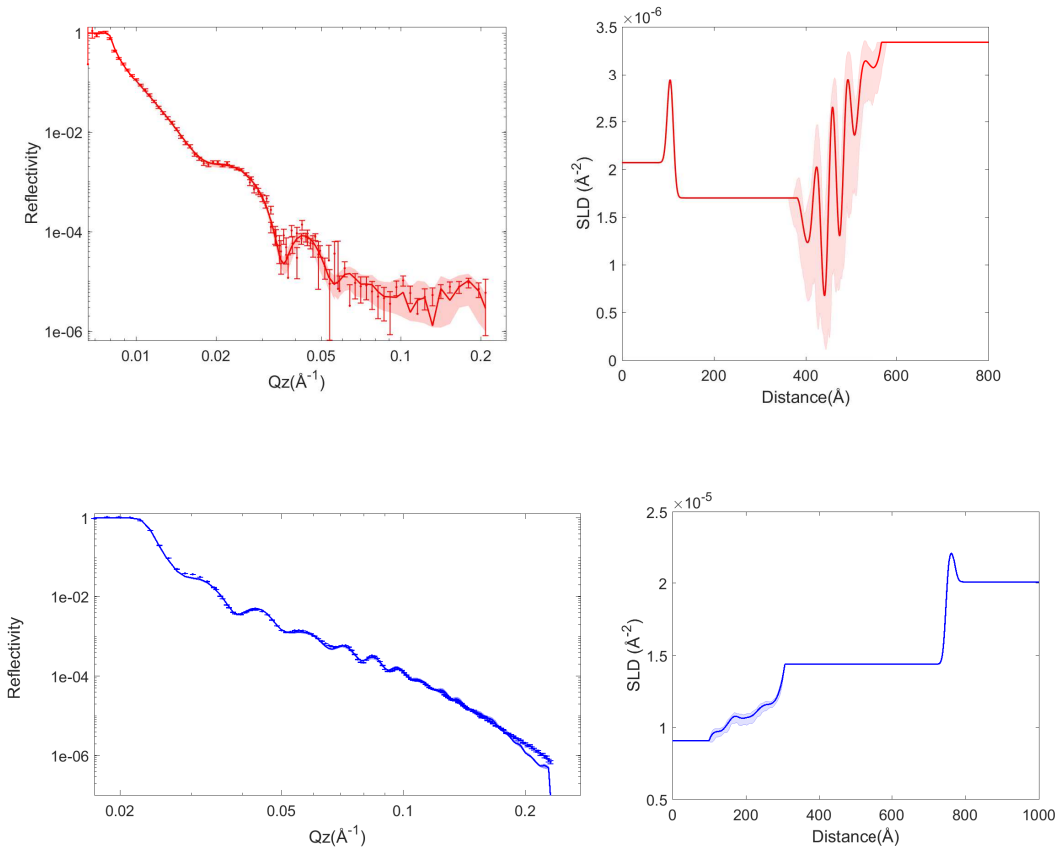

Figure 7.21 *Reflectivity profiles for 1.2% lecithin + 1.2% PGPR at sucrose/GTO interface in NR for d50-oil (top panel) and XRR for h-oil (bottom panel). The reflectivity profiles were fitted using the splines model discussed in Section 7.5.2 with the thickness of the surfactant layer constrained to be the same in the two contrasts. Measured reflectivity profile along with the fit (left panel) and the corresponding SLD profile (right panel) with the shaded region depicting the 95% Bayesian prediction interval.*

left hand panel of Figure 7.22. The NR SLD profile for d50-GTO is shown by the solid line, and the XRR SLD profile is reverse and offset to the sucrose interface for easy comparison and is depicted by the dashed line. The SLD profile obtained are converted to volume fractions using the Matrix Equation 7.11 implemented in MATLAB. In this case $SLD_{oil1} = SLD_{h-oil_x} = 9.0 \times 10^{-6}$ Å^{-2}, $SLD_{oil2} = SLD_{d50oil_n} = 3.3 \times 10^{-6}$ Å^{-2}, $SLD_{PCh1} = SLD_{PCh_x} = 14.4 \times 10^{-6}$ Å^{-2}, $SLD_{PCh2} = SLD_{PCh_n} = 1.84 \times 10^{-6}$ Å^{-2}, $SLD_{PGPR1} = SLD_{PGPR_x}, = 8.6 \times 10^{-6}$ Å^{-2} and $SLD_{PGPR2} = SLD_{PGPR_n}, = 0.2 \times 10^{-6}$ Å^{-2}, where the subscripts x and n denote x-ray and neutron SLD respectively. The volume profiles so obtained are shown in the right hand panel of Figure 7.22.

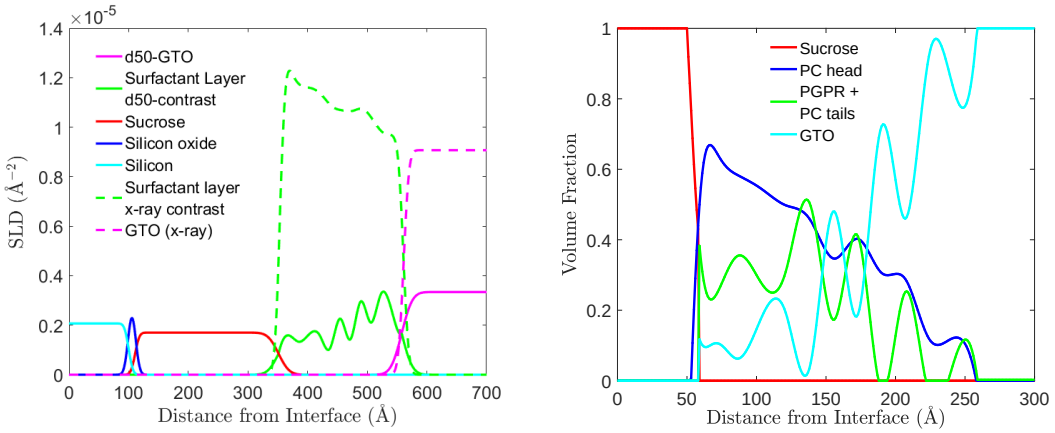

Figure 7.22 *Left panel: SLD profile obtained for the NR and XRR fits for 1.2% lecithin + 1.2% PGPR at sucrose/GTO interface deconstructed into the various layers: Silicon (cyan), Silicon oxide (blue), Sucrose (red), Polymer layer (green) and the bulk d50-TO (pink). The solid line represents the NR d50-contrast and the dashed line depicts the XRR h-contrast (reversed and offset to the same sucrose interface as d50-contrast). Right panel: Volume fraction profiles obtained for various components in the interfacial surfactant layer using Equation 7.11. Sucrose is depicted in red, PC-head in blue, PGPR + PC tails in green and GTO in cyan.*

7.5.3 Lecithin and PGPR Interaction in TO and GTO

The SLD profiles obtained for the fits to the reflectivity from lecithin and PGPR films at sucrose/triglyceride interface are shown in Figures 7.17, 7.18 and 7.21. These contain some features in common with the lecithin SLD profiles where oscillations are observed due to alternating head-rich and tail-rich regions, and others associated with the PGPR SLD profiles which show an extended interface

exhibiting a gradual change from the SLD of the polymer to the SLD of the oil.

The overall extent of this interfacial layer at the sucrose/TO interface is 32 nm for 1.8% lecithin + 0.6% PGPR mixture and 49 nm for 1.2% lecithin + 1.2% PGPR mixture. This is $3-5$ times the thickness obtained for films containing lecithin only and comparable to that for films containing PGPR only. This suggests that by replacing 25% lecithin with PGPR, the same interfacial surfactant thickness can be obtained as is the case for PGPR only films. Upon further increasing the PGPR ratio of the total surfactant mixture the thickness of the layer increases to values greater than the thickness of the PGPR only films. In the case of GTO, the thickness of the interfacial film for 1.2% lecithin + 1.2% PGPR binary mixture is 21 nm, which is smaller than the PGPR only films but $\sim$3 times that of lecithin only films.

The volume fraction profile calculated using Equation 7.11 from the fitted SLD profiles, show intermixing between lecithin and PGPR in the interfacial surfactant film, as shown in Figure 7.20 and right panel of Figure 7.22. There exists a near sucrose interface region rich in phospholipid heads. Beyond this head-rich region is an intercalated structure of PGPR and lecithin. Some bumps are present in the volume fraction profile of the PC-heads that are too broad to be associated with lipid bilayers, but can be attributed to the cores of inverse core-shell micelles. The continuous distribution of the PC heads, tails (+PGPR) and the triglyceride oil, furthermore, suggests that the layers comprise adsorbed solvated polydisperse cylindrical micelles of lecithin + PGPR. This is consistent with the solution SAXS and SANS data that suggests that incorporation of PGPR increases the curvature of lecithin micelles as discussed in Section 3.6.1. So, even if the lecithin micelles underwent some fusion in the lecithin only layers, they exhibit more curvature in the lecithin + PGPR case allowing greater oil incorporation. The two key features of the structure shown by the volume fraction profiles are: firstly, the spacing between the head oscillations (cores of the micelles) is $70-100$ Å, which is greater than the case for lecithin only structures (spacing $\sim$50 Å); and secondly the amount of oil incorporated in the structure beyond the first 100 Å is $>$ 40%, suggesting that the incorporation of PGPR into these structures leads to significant swelling of these layers. This leads to a weaker attraction between the layers than in the case of compact lecithin layers, and the thickness of the film between the sucrose grains increases by a factor of ~ 3. The solvated layers comprising lecithin + PGPR inverse core-shell cylindrical micelles provide the steric repulsion required to reduce van der Waals interaction between sucrose

grains, thereby reducing the yield stress compared to the lecithin only case.

7.6 POPC and PGPR at Sucrose/Triglyceride Interface - Reflectivity Study

The reflectivity studies with lecithin and PGPR, discussed in Section 7.5, provide adsorbed amounts and some insight into how PGPR changes interaction between lecithin structures at the sucrose/triglyceride interface. However, due to the multi-component nature of lecithin and PGPR and the and the limited contrast available, especially in the h-oil contrast, structural details and the mechanism causing the disruption can only be qualitatively hypothesised. In order to provide further insight into this understanding neutron and x-ray reflectivity studies similar to the ones conducted for Lecithin + PGPR mixtures were carried out where the the multi-component lecithin was replaced with single component Lec_{POPC} (50:50 mixture of POPC and the triglyceride oil) and are shown in Figure 7.23.

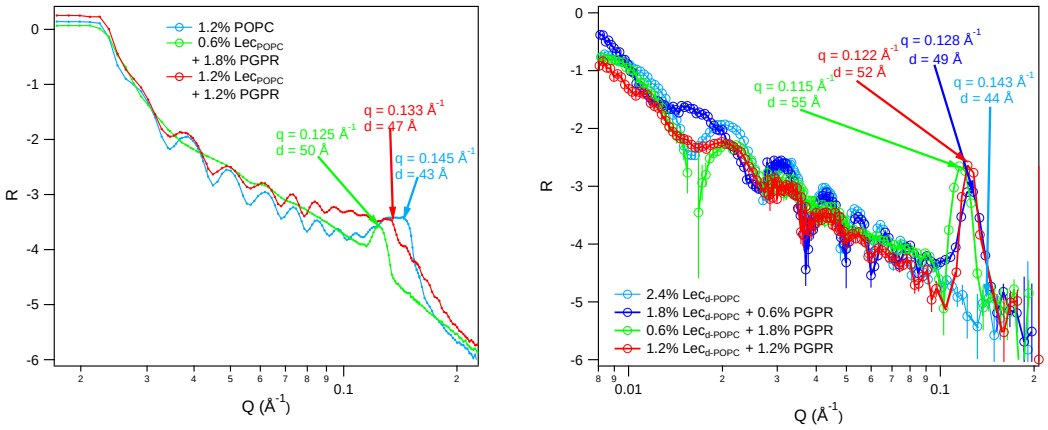

Figure 7.23 *XRR (left panel) and NR (right panel) from Lec_{POPC} and Lec_{POPC} + PGPR films at the sucrose/TO interface at various compositions of the binary mixtures. In case of NR d31-POPC was used to enhance contrast against the PGPR and oil.*

The left hand side panel of Figure 7.23 shows the XRR profiles for 2.4% Lec_{POPC} (cyan curve), 1.2% Lec_{POPC} + 1.2% PGPR (red curve) and 0.6% Lec_{POPC} + 1.8% PGPR (green curve). As can be seen in figure, on replacing the lecithin with Lec_{POPC} the shoulder like feature observed for lecithin (Figure 7.3) turns into a clearer Bragg peak like feature for Lec_{POPC} showing the presence of well defined

lamellae. The Bragg feature for Lec_{POPC} is at $q = 0.145$ Å^{-1} corresponding to a d-spacing of 43 Å. Upon increasing the PGPR content of the surfactant mixture the Bragg feature shifts inwards to $q = 0.133$ Å^{-1}, d-spacing of 44 Å, for 1.2% Lec_{POPC} + 1.2% PGPR and $q = 0.125$ Å^{-1}, d-spacing of 50 Å, for 0.6% Lec_{POPC} + 1.8% PGPR. In addition to the movement of the Bragg feature, increasing the PGPR content of the surfactant mixture also results in the smearing of the Kiessig fringes observed in the XRR profiles. This suggests that overall there is adsorption of a thicker layer resulting in an extended diffuse interface as the PGPR concentration of the surfactant mixture is increased.

The right hand side panel of Figure 7.23 shows the NR profiles for 2.4% Lec_{POPC} (cyan curve), 1.8% Lec_{POPC} + 0.6% PGPR (blue curve), 1.2%Lec_{POPC} + 1.2% PGPR (red curve) and 0.6% Lec_{POPC} + 1.8% PGPR (green curve). For NR d31-POPC was used to enhance contrast against the PGPR and triglyceride oil. The trends observed in the Bragg peak shift is similar to that observed in XRR. For 2.4% Lec_{POPC} a Bragg peak is observed at $q = 0.145$ Å^{-1} (d-spacing 44 Å) which shifts inwards to $q = 0.128$ Å^{-1} (d-spacing 49 Å) for 1.2% Lec_{POPC} + 1.2% PGPR, $q = 0.122$ Å^{-1} (d-spacing 52 Å) for 1.2% Lec_{POPC} + 1.2% PGPR, and $q = 0.115$ Å^{-1} (d-spacing 55 Å) for 0.6% Lec_{POPC} + 1.8% PGPR. Also a similar smearing of fringes is observed as the PGPR fraction of the surfactant mixture is increased.

The Bragg peak like feature confirms the presence of phospholipid lamellae for POPC which are similar to compact phospholipid layers formed by lecithin at the sucrose/triglyceride oil interface. The layers are more well-defined in the case of POPC because POPC is defined by a single packing parameter which favours bilayer formation, whereas the multi-component lecithin contains lipids with a variety of packing parameters, which will have an effect of disrupting the pure bilayer formation. Addition of PGPR leads to a swelling of the lamellae, evident from the movement of Bragg beak to lower q resulting in a larger d-spacing between layers. This supports the suggestion that PGPR intercalates into the phospholipid layers, introducing a significant fraction of oil, resulting in steric repulsion between the layers which pushes them apart. The overall increase in thickness decreases the van der Waals interaction between the sucrose grains.

The data collection for these experiments was only completed at the end of September 2018 due to several unplanned shut-downs at ILL, Grenoble, France in 2017 and 2018. Therefore, only a qualitative discussion is presented in this section. Detailed fitting of this data is currently ongoing and some preliminary

fits obtained using a simple parametrised slab model with repeating phospholipid layers are discussed in the future work section of Chapter 8.

7.7 Conclusions

Neutron and x-ray reflectivity studies were carried out for lecithin, PGPR and their binary mixtures at sucrose/triglyceride oil interface. These studies have provided structural details for lecithin, PGPR and their binary mixtures at a single planar sucrose/triglyceride oil interface, which can then be used to explain how these surfactants change inter-particle interactions and thereby modify the rheology of sucrose/triglyceride oil suspensions.

Reflectivity studies from lecithin films at sucrose/triglyceride oil interface shows formation of compact phospholipid layers of $10 - 20$ nm comprising the phospholipid head adsorbed at the sucrose interface and the alkyl tails oriented towards the triglyceride oil. The structure consists of a dense inner layer followed by lipid bilayers (two in case of TO and one in case of GTO) formed by adsorption of inverse cylindrical micelles from the solution which fuse into bilayers with little oil incorporated in the layers. The outer layer in both oils comprises solvated intact cylindrical micelles. A cartoon showing these lecithin layers at sucrose/TO interface is shown in Figure 7.24 with the red circles depicting the phospholipid head, the black lines depicting the phospholipid tails and the green ellipses depicting the TO molecule. In the case of GTO, there is only a single bilayer of the tilted phospholipids. The adsorption of these compact layers at the interface means that the van der Waals interaction between sucrose grains is determined by the lecithin film/triglyceride/lecithin film Hamaker constant as opposed to the higher sucrose/triglyceride/sucrose Hamaker constant, reducing the inter-particle interaction between sucrose grains in the suspensions, which in turn alters the rheology. However, there is a net van der Waals attraction between these compact lecithin layers, greater for TO than GTO, which means that the suspensions containing lecithin only will exhibit a yield stress.

PGPR on the other hand changes inter-particle interaction by adsorption of highly solvated extended layers of PGPR aggregates extending $30 - 50$ nm from the interface. The structure of PGPR in both GTO and TO can be divided into 3 regions: near sucrose interface ($0 - 100$ Å from the sucrose interface), the far from interface region (last 100 Å) and the intermediate region. The near interface

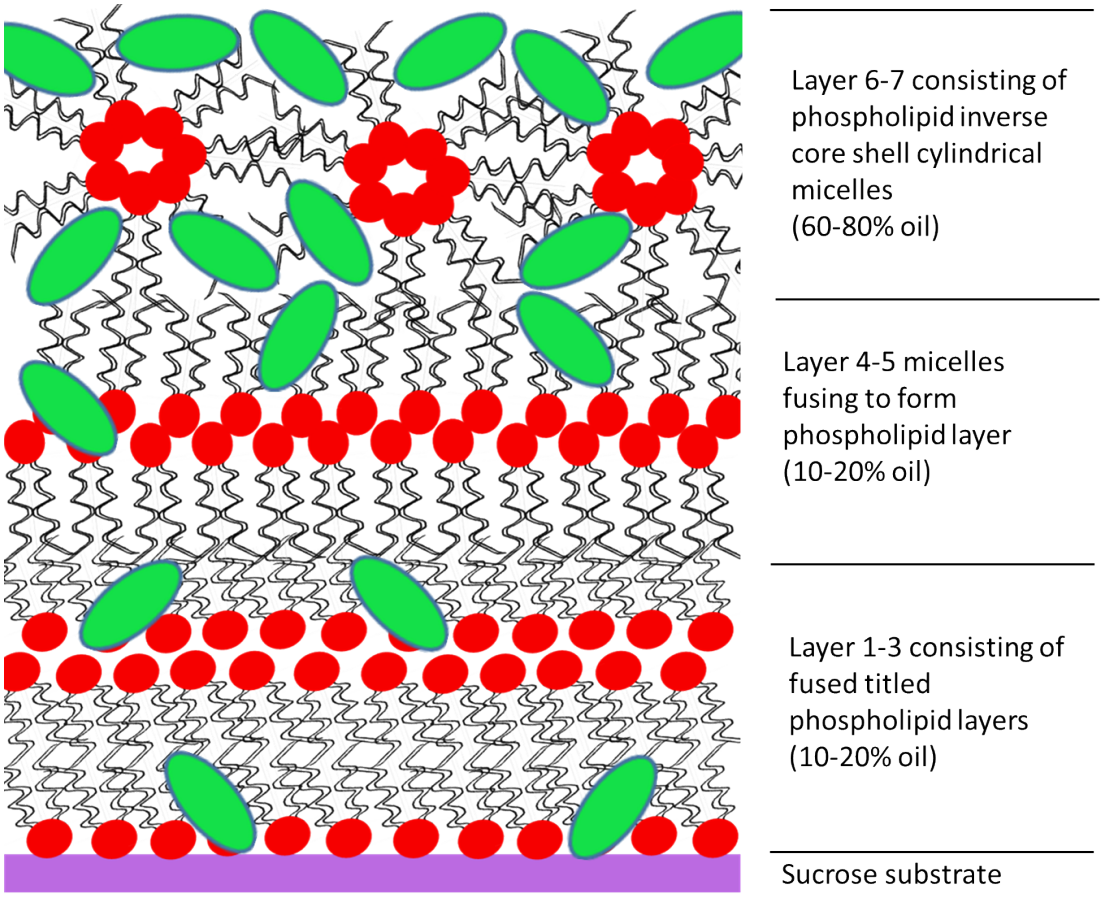

Figure 7.24 *A cartoon showing the lecithin layers at sucrose/TO interface. The red circles depict the phospholipid head, with the lines depicting the tails and the green ellipses depict the TO molecule.*

region consists of adsorbed PGPR micelles and is similar in both GTO and TO. The far from interface region is also similar in both TO and GTO where the volume fraction of PGPR gradually decays to <0.1. The near interface region is responsible for the high shear stress regime and the distal region for the low stress regime in rheology studies and therefore, the rheology of PGPR in both oils is very similar. The intermediate region shows some structural differences, where a second distinct peak of PGPR aggregates is observed for TO which is absent in GTO where the volume fraction gradually decays to 0 (following an almost parabolic trend). This indicates that PGPR layers also experience some van der Waals attraction, especially in the case of TO. These attractions can explain the yield stress exhibited by sucrose/suspensions comprising PGPR only.

The interfacial structures formed by the binary mixture at the sucrose/triglyceride interface can be visualised as solvated intermixed layers of lecithin and PGPR. The volume fraction profile shows a continuous distribution of heads with broad bumps at separation of $70 - 100$ Å, suggesting the structure comprises adsorbed solvated polydisperse cylindrical micelles of lecithin + PGPR. These solvated micellar structures are more separated than the fused lecithin bilayers and the overall thickness of the interfacial layer is $3 - 5$ times the thickness obtained for lecithin only films. A cartoon visualising these mixed lecithin + PGPR layers at the sucrose/triglyceride interface is shown in Figure 7.25. The red circles depict the phospholipid head, the blue ellipses depict the PGPR head, the black lines depict the tails for both lecithin and PGPR, and the green ellipses depict the triglyceride oil molecule.

In addition to the multi-component lecithin, x-ray and neutron reflectivity studies were carried out with single component Lec_{POPC}. These studies give a clearer signature of PGPR swelling phospholipid layers. The single well-defined packing fraction of POPC means it forms well-defined bilayer lamaellae which gives rise to Bragg peak like features. The Bragg peak like feature shifts to lower q upon increasing the PGPR component of the surfactant mixture which strongly supports the hypothesis that PGPR intercalates into the phospholipid layers leading to swelling of the lamellae. There is also evidence of thicker layers upon increasing the PGPR concentration from smearing of the Kiessig fringes.

These structural investigations suggest that PGPR incorporates into the phospholipid layers/micelles and these mixed micelles adsorb at the sucrose/triglyceride oil interface. The polyglycerol backbone is buried in the lecithin aggregate and the polyricinoleate tails extend out from the mixed micelles which allows for incorpo-

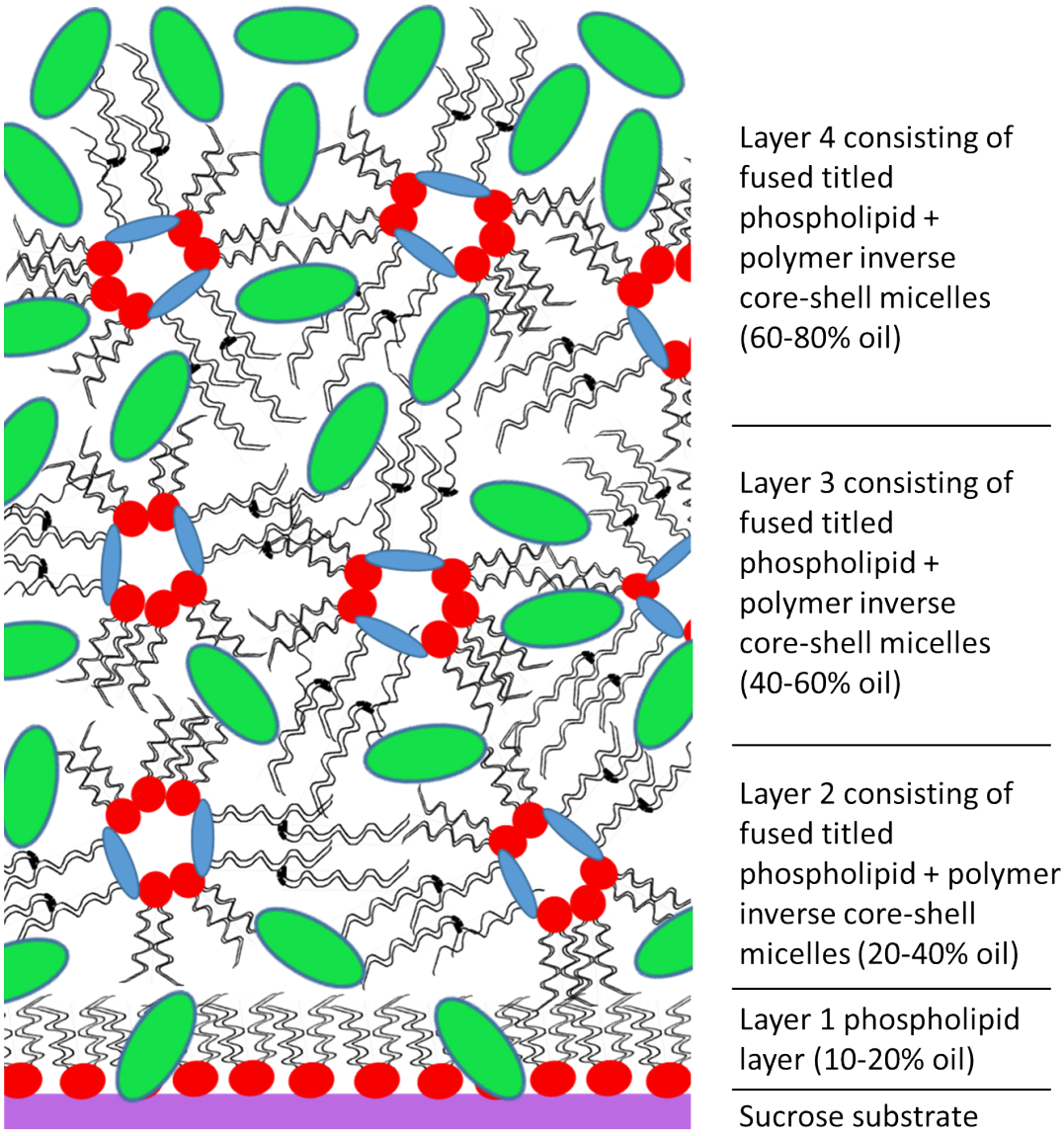

Figure 7.25 *A cartoon visualising lecithin + PGPR layers at sucrose/triglyceride oil interface. The red circles depict the phospholipid head, the blue ellipses depict the PGPR head, with the lines depicting the tails for both lecithin and PGPR and the green ellipses depict the TO molecule.*

rating oil within the layers. This results in a steric (excluded volume) repulsion between the layers and reduces the van der Waals interaction between sucrose grains as the Hamaker constant of the lecithin+PGPR/oil/lecithin+PGPR layer is more similar to that of the oil. These changes in the inter-particle interaction lead to the yield stress of the suspension being dramatically lowered. The multilayer phospholipid structure means that PGPR intermixes between several layers amplifying the steric repulsion that would result from a single PGPR layer, and that leads to the dramatic reduction in yield stress when compared to the PGPR only suspensions.

Reflectivity has provided an insight into the detailed structure of the surfactants at a single planar sucrose/triglyceride oil interface. These studies can be combined with small angle scattering studies of these surfactant in solutions (Chapter 3) and sucrose/triglyceride oil suspensions (Chapter 4) to infer the interfacial structure of the surfactants in sucrose/triglyceride suspensions. Chapter 8 brings together these approaches to present a structural model explaining the rheology of chocolate.

Chapter 8

Summary, Conclusions and Future Outlook

8.1 Summary

The rheology of molten chocolate is important for manufacturing different types of chocolate, and it also determines the energy cost required to produce them. In order to obtain flowing chocolate from a dense suspension ($> 70\%$ w/w) of sucrose, cocoa and milk solids in a continuous fat phase of cocoa butter, surfactants are added whilst shearing. Commonly used surfactants in chocolate products are natural molecules like lecithin, obtained from soy and primarily consisting of lipids, and in some cases polymeric surfactants like polyglycerol polyricinoleate (PGPR). When added in small quantities ($< 1\%$ w/w) they significantly alter the flow properties, specifically the yield stress and high shear viscosity of chocolate, while maintaining the high solid fraction of the suspensions. This reduces the amount of cocoa butter required for making chocolate, which is the most calorific and expensive constituent of chocolate. The work presented in this thesis is aimed at understanding the role played by lecithin and PGPR in modifying the rheology of chocolate by conducting molecular level studies of the surfactant films at the solid/liquid interface relevant to molten chocolate suspensions and providing a structural basis for the observed rheological effects.

Lecithin and PGPR are both amphiphilic molecules that form micellar structures in triglyceride oils. SAXS and SANS studies were conducted for solutions

of lecithin, PGPR and their binary mixtures in GTO (a saturated medium chain triglyceride oil) and TO (an unsaturated long chain triglyceride oil) and are discussed in Chapter 3. These studies provide evidence for an interaction between lecithin and PGPR in the triglyceride oils, and the adsorption of these micellar structures at the solid/liquid interface in chocolate alters the inter-particle interaction which in turn modifies the rheology.

Two model systems were used to understand the solid/liquid interaction in molten chocolate: 65% w/w sucrose in pure triglyceride oils (GTO and TO) suspensions containing 0.8% w/w surfactants which mimic the rheology of molten chocolate and the effect of phospholipid (lecithin and POPC) and polymeric (PGPR) surfactants on the yield stress and high shear viscosity (discussed in Chapter 2); and a planar model system to enable investigations that zoom in at a single solid/liquid interface found in model chocolate suspensions, developed using spin-coated sucrose substrates used in flow cells with triglyceride oil (detailed in Chapter 5).

The adsorption and structure of surfactants at the sucrose/triglyceride interface and the particle-particle correlations in the model chocolate suspensions was investigated using Small Angle Scattering and SESANS, respectively, and is discussed in Chapter 4. The same interfacial structural information was obtained for the surfactant films at a single planar sucrose/triglyceride oil interface using QCM-D (discussed in Chapter 5) and neutron and x-ray reflectivity (discussed in Chapter 6 and 7). Based on these multi-technique studies, a structural mechanism to explain the effect of lecithin and PGPR in modifying the viscosity and yield stress of sucrose/triglyceride oil suspensions, and therefore molten chocolate, is presented in this chapter.

To help unpick the details of the phospholipid and PGPR interactions, structural investigation using small angle scattering and reflectivity were also conducted for for the single component phospholipid, POPC, and its binary mixtures with PGPR, in addition to the multi-component lecithin.

8.2 Structural Model to Explain the Rheological Effect of Surfactants in Chocolate

8.2.1 Role of Surfactants

Contact angle tensiometry studies at planar sucrose/triglyceride oil interface have demonstrated that triglyceride oils wet the sucrose surface. So why are surfactants added to chocolate? In this thesis it has been demonstrated that interaction of the glycerol backbone of the triglycerides with the sucrose interface results in layering of these oil molecules extending up to 10 nm from the interface. QCM-D measurements suggest that this near-interface oriented triglyceride layer has a shear modulus of 1-2 MPa, and can therefore sustain a shear stress. Surface force experiments [124, 125] have also reported layering of oil molecules, such as triolein, toluene, OMCTS and cyclohexane, which can support a finite shear stress. When these layered structures are confined between two interfaces, as would be found between grains of sucrose in a chocolate suspension, the films might be expected to have a significant yield stress (sometimes expressed as viscosity that is orders of magnitude higher than bulk) [126], meaning they will resist flow of the oil. To get the suspensions to flow the sucrose grains need to be separated out of adhesive contact, by application of a stress. This is depicted schematically in Figure 8.1, which shows how excluded volume interactions and inter-particle attraction control the net interaction potential between particles in model chocolate suspensions. The yield stress required to make the suspension flow depends on the net particle-particle interaction, denoted by the solid circles in the schematic. The magnitude of the stress without any surfactants is determined by the magnitude of the adhesion between sucrose grains, which depends on the van der Waals attraction characterised by the sucrose/triglyceride oil/sucrose Hamaker constant and is shown by the solid lines in Figure 8.1. The net attraction between sucrose grains is large giving rise to a large yield stress or a jammed suspension. The addition of surfactants leads to the adsorption of a surfactant film at the sucrose/triglyceride interface which means that the van der Waals attraction is now determined by the smaller surfactant/triglyceride oil/surfactant Hamaker constant [58], depicted by the dashed line (lecithin only case) and dotted line (lecithin + PGPR case), and the excluded volume interaction also shift to higher separation due to the thickness of the interfacial films (denoted by t_{Lec} and t_{LP} in the schematic). Therefore, the suspensions flow at lower applied stresses.

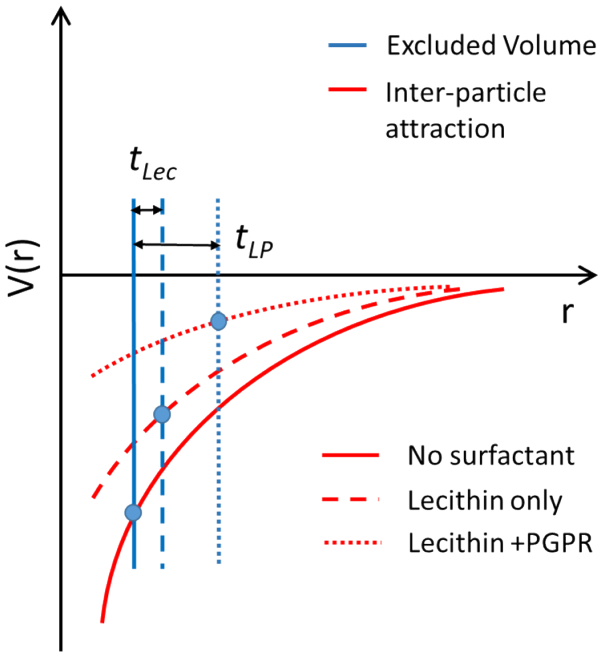

Figure 8.1 *A schematic showing the inter-particle interactions for model chocolate suspensions deconstructed into excluded volume interaction (blue lines) and inter-particle attractions (red lines).* t_{Lec} *and* t_{LP} *denote the thickness of the adsorbed interfacial surfactant film for lecithin only and lecithin + PGPR case. The solid circles represent the net interaction between the particles for the particular suspension.*

8.2.2 Role of Lecithin

Lecithin is the most commonly used surfactant in chocolate and its primary role is to modify the viscosity of molten chocolate. Addition of lecithin at $0.1 - 0.3\%$ (w/w) significantly reduces the viscosity and yield stress of chocolate. However, further addition of lecithin, >0.3% (w/w), increases the yield stress of chocolate. The same effect of addition of lecithin is observed on the rheology of sucrose in triglyceride oil suspensions (model molten chocolate).

Reflectivity studies have shown that lecithin forms compact interfacial films extending $10 - 20$ nm at individual sucrose interfaces that contain an odd number of monolayer equivalents of phospholipids, with the phospholipid head adsorbed at the sucrose interface. For small separations between coated grains, such as occur in frictional sliding, the lecithin film/oil/lecithin film Hamaker constant will determines the van der Waals attraction between the sucrose grains, which is smaller than that for sucrose/oil/sucrose Hamaker constant as depicted by the dashed red line in Figure 8.1. This means that the adhesion, and hence adhesion hysteresis, i.e. the friction, associated with a sliding contact will be less than in the absence of lecithin. The thin compact lecithin film which coats the sucrose grains serves as a molecular ball-bearing that lubricates the sucrose grains, reducing the adhesion and friction between sucrose grains. This reduction in adhesion and friction means the viscosity of the suspensions at high shear rates and the stress required for yielding (flowing) will be reduced.

These lecithin layers have little oil incorporated in them and small angle scattering studies from lecithin solutions in triglyceride oils show formation of inverse core-shell cylindrical micelles which grow in length upon ageing and arrange themselves into hcp structures, which suggests there is still a net van der Waals attraction between lecithin micellar structures. This leads to adhesive interactions between lecithin coated sucrose grains which is also evident in the fractal structure that these grains trace out in triglyceride oil suspensions, evident from the SESANS and the power law exponent of -3 observed for the low q SANS from sucrose in triglyceride oil suspensions. Due to this there is a net adhesive interaction and a yield stress (smaller than in the case with no lecithin) still remains. As more lecithin is added the thickness of the lecithin films at the sucrose interfaces grow, and so the magnitude of the van der Waals attraction between these films across the oil grows, which causes the increase in adhesion and therefore the yield stress grows. Once flowing the high shear viscosity is still determined by the sliding of

the lubricating phospholipid layers between the sucrose grains and hence remains fairly constant beyond complete monolayer coverage ($0.1-0.3\%$ w/w of lecithin).

8.2.3 Role of PGPR

PGPR on the other hand is a polymeric molecule which has a small effect on the viscosity but reduces the yield stress such that at high enough concentrations (2%) the yield stress of the suspension vanishes. The discussion presented here is for $0-0.8\%$ as these are the concentrations which were investigated in this thesis.

PGPR forms inverse core-shell micelles in both GTO and TO with the shells incorporating >50% oil. These micellar structures show no changes upon ageing, suggesting there is little or no attraction between PGPR micelles in triglyceride oil. At the sucrose/triglyceride oil interface PGPR forms extended layers incorporating large amount of oil with total thicknesses in the range of $30-50$ nm, found using QCM-D and reflectivity. This swollen structure leads to a repulsive interaction that pushes the sucrose grains apart out of adhesive contact as is evident from the particle-particle correlation function measured using SESANS from sucrose/triglyceride oil suspensions and the change in the power law scattering of the small angle scattering at low q. This decreases the van der Waals interaction between the sucrose particles, thereby reducing the yield stress of the suspensions. At a single sucrose interface in TO it is clear that a second layer of PGPR aggregates interacts with the first; the mechanism of this attraction is not known, but it could be entanglement of the inverse cylindrical micelles. This suggests that at the interface between two sucrose grains, each bearing a layer of PGPR, one might expect some adhesion to remain and therefore suspensions with PGPR only have a finite yield stress, the magnitude of which is smaller than the lecithin only case due to increased separation and smaller attraction between PGPR layers.

Under high shear the PGPR layer might be expected to undergo a deformation, in which oil is expelled from the layer, and therefore without any added lecithin, PGPR is not as effective in reducing the high shear viscosity.

8.2.4 Combined Effect of Lecithin and PGPR

When lecithin and PGPR are used in combination, lower viscosity and yield stress are observed than for the suspensions containing only lecithin and PGPR respectively. Whilst the viscosity of the suspension is slightly lowered, and approaches the viscosity of lecithin only suspensions at very high shear rates, the yield stress is drastically lowered, such that for 1:1 and 1:3 lecithin to PGPR ratios at a total surfactant concentration of 0.8% w/w, the yield stress vanishes.

As discussed earlier lecithin in triglyceride oil forms micellar structures which, upon ageing, form hcp arrangements capable of sustaining a yield stress in the solution. PGPR incorporates into these micellar structures, disrupting them and dispersing them as individual micelles in the solution. The extent of disruption depends on the PGPR concentration such that some large scale organisation of the micelles is present in 3:1 lecithin to PGPR solutions, but at the same surfactant concentration for a 1:1 lecithin to PGPR mixture no aggregation of the micelles into hcp structures occurs even upon ageing. This suggests that PGPR incorporates into the lecithin micelles, changing the attraction between lecithin micelles into a repulsive interaction.

At a single sucrose interface, the mixture of lecithin and PGPR forms extended films with thicknesses ranging from $30-70$ nm depending on the PGPR fraction in the surfactant mixture with a non-monotonic distribution of lecithin heads. These structures are rationalised as forming from adsorption of the inverse cylindrical micelles of lecthin + PGPR with large amounts of oil entrained in the micelles. Whereas in the lecithin only layers, the inverse cylindrical micelles of lecithin have fused into more bilayer-like structures due to van der Waals attraction, in the mixed lecithin and PGPR layers, the curvature of the lecithin aggregates has been increased retaining the inverse cylindrical micelles. There is greater separation between these phospholipid + PGPR micellar cores than the bilayers found in lecithin brought about by the intercalation of PGPR, which increases the excluded repulsion as depicted by the dotted blue line in Figure 8.1. This observation is more obvious in the case of POPC where Bragg peaks are observed for interfacial lamellar structures, which shift to lower q upon addition of PGPR. This generates an osmotic repulsion within these mixed layers that drastically reduces the attractive interaction between sucrose grains as depicted by the dotted red line in Figure 8.1. This structure leads to a greater separation between the sucrose grains in the model chocolate suspensions. This is indicated by the

finite correlation length and a nearest neighbour bump observed in the particle-particle correlation function measured using SESANS from sucrose in triglyceride oil suspensions stabilised by lecithin and PGPR and the change in the power law exponent observed for low q SANS from these suspensions from -3 to -4. This drastic lowering of inter-particle attraction and creation of sufficient excluded volume between the sucrose grains causes the 3 order of magnitude decrease in the yield stress.

Furthermore, these mixed micelles will not be expelled from the polymer layer upon deformation, so there is a reduction in the high stress viscosity which is now governed by the rolling of these inverse micellar structures instead of sliding between phospholipid layers. At even higher shear stresses the near-sucrose interface phospholipid layer, as evident from the reflectivity studies, controls the viscosity and therefore viscosity of the lecithin only suspensions is obtained.

8.3 Conclusions and Future Outlook

A structural basis to explain the rheology of molten chocolate has been established using simplified model systems and a multi-technique approach. The role of lecithin, PGPR and their combination in modifying the viscosity and yield stress of chocolate has been understood by systematically unpicking various interactions. In these studies lab based techniques and central facilities studies were used together to understand complex rheological behaviour. Lab-based techniques (QCM-D, contact angle) can be traced back to neutron/synchrotron techniques to provide absolute measures of the amount of adsorbed material and its molecular scale distribution. Neutrons and x-ray studies have been of key importance as they provide a means of seeing through otherwise opaque model chocolate samples at the nanoscale.

The surfactants and the triglyceride oils used in these studies are similar: both have polar heads and hydrocarbon chains with varying degree of activity for the sucrose interface and differing capacities to incorporate oil. This makes the use of multiple approaches to understand the system essential. One such handle was the use of two different triglyceride oils: the medium chain saturated GTO and the long chain unsaturated TO, with GTO being less similar to the lecithin and PGPR molecules than TO. This has made two differences apparent: firstly there is greater van der Waals attraction between surfactant layers (lecithin and PGPR)

in TO than in GTO, and secondly the differences between the PGPR structures in the two oils, as discussed in Chapter 7.

The yield stress of sucrose in triglyceride oil suspensions containing lecithin is higher in the case of TO than in GTO, as is the van der Waals attraction between lecithin layers leading to thicker interfacial film. This provides a means of confirming the hypothesis that attractive interaction between phospholipid layers gives rise to the yield stress in sucrose/triglyceride oil suspensions.

The difference between the PGPR structure in the two oils is important in understanding how PGPR behaves depending on the solvent and also what the important features are in terms of rheology modification individually and when used in combination with phospholipids. The near interface structure controls the high shear regime and the far from interface structure determines the low shear regime, which is similar for PGPR in both TO and GTO and so is the rheology. The intermediate regime is different for the two oils where a second layer of PGPR aggregates is present in the case of TO and a polymer brush-like region comprising solvated PGPR micelles is observed for GTO arises again due to the greater attraction between PGPR layers in TO than in GTO. Despite this difference, the interaction of PGPR with phospholipids is similar in both GTO and TO, both in terms of its effect on reducing the yield stress of sucrose/triglyceride oil suspensions and phospholipid solutions, and disrupting the ordered phospholipid structures in solutions and at the sucrose/triglyceride interface. This indicates that the important features of PGPR in terms of reducing the yield stress are its ability to interact with phospholipid layers and its ability to incorporate oil. Therefore, the search for natural replacements for PGPR should take into account three important factors:

1. Interaction with triglyceride oils: Triglyceride oils in general and specifically the ones found in cocoa butter should be a good solvent for the replacement molecule. This will facilitate incorporation of oil in the interfacial layers swelling them which will provide the steric repulsion required to reduce the van der Waals interaction between the solid grains and thereby the yield stress of the suspension.

2. Polarity: The incorporation of PGPR into the phospholipid layers is the mechanism by which significant oil (greater than in the case of lecithin only suspensions) can be entrained in the interfacial surfactant layer. In order to interact with lecithin layers, any replacement molecule should have some

polarity (possibly in between that of lecithin and oil), as otherwise it will not interact with the phospholipid any more than the oil.

3. Polydispersity: Incorporation of PGPR into the phospholipid layers introduces a curvature and disrupts the ordered phospholipid structures. Scattering and reflectivity studies with phospholipids only show that the multi-component nature of lecithin when compared to the single component POPC gives rise to structures with greater curvature and less order (cylindrical micelles instead of lamellar structures). The yield stress for suspensions containing lecithin is also lower than those containing POPC. Therefore, it can be argued that due to multiple length scales in PGPR, the structures formed by the mixture of lecithin (and also POPC) and PGPR are polydisperse and do not pack perfectly allowing more oil to be entrained between the micelles, which is desirable. This suggests any replacement molecule should have polydispersity either by making it multi-component or introducing polydispersity in its polymeric nature.

In addition to the search for a natural replacement for PGPR, there are some ongoing and continuation studies that arise from this work:

- In order to complete the hypothesis presented here, neutron and x-ray reflectivity studies for Lec_{POPC} (50:50 mixture of POPC and triglyceride oil) and Lec_{POPC} + PGPR films at the sucrose/triglyceride interface were carried out and are qualitatively discussed in Chapter 7. Some preliminary fits have been obtained as shown in Figure 8.2 which indicate that both the d-spacing between POPC layers and the number of phospholipid+PGPR layers adsorbed at the sucrose/TO increases as the PGPR fraction of the surfactant mixture is increased. This strongly supports the hypothesis that PGPR incorporates into the phospholipid layers, pushing them apart and also increases the overall thickness of the adsorbed surfactant layers. This results in a steric repulsion between the layers and reduces the van der Waals interaction between sucrose grains, leading to the yield stress of the suspension being lowered. Detailed analysis of this data is ongoing and can provide quantitative information regarding the effect of PGPR on separating the phospholipid layers.

- In addition to looking at single component replacement for lecithin, the effect of multiple head-groups and tail-lengths can be investigated by

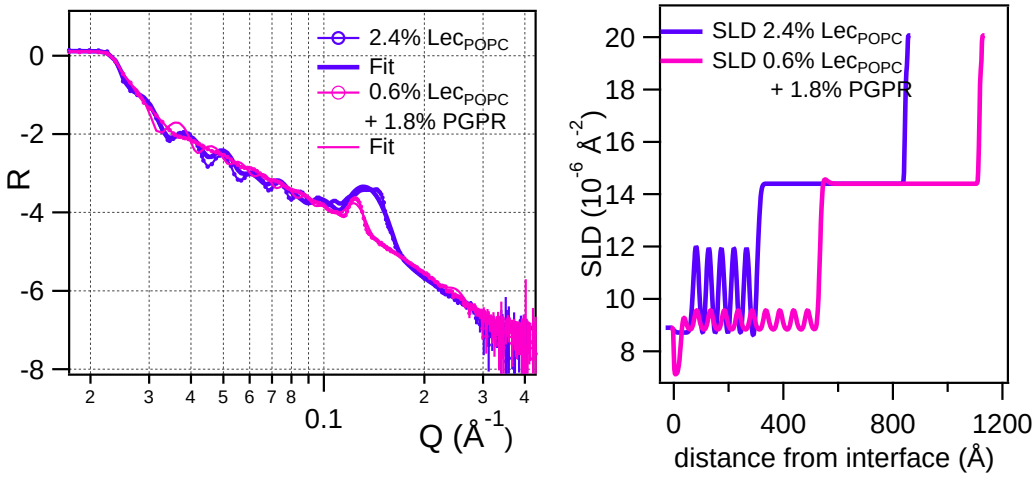

Figure 8.2 *XRR from 2.4% Lec$_{POPC}$ (purple) and 0.6% Lec$_{POPC}$ + 1.8% PGPR (pink) films at the sucrose/TO interface. Left panel: XRR and the corresponding fits using parametrised slab model. Right panel: The corresponding SLD profile.*

carrying out similar scattering and reflectivity studies by replacing lecithin with a mixture of PC + PE lipids (POPC + POPE) and two PC lipids with varying tail lengths (POPC + DMPC). This can provide useful insight into how multi-component surfactant mixtures differ from the single component surfactants.

– This work has endeavoured to understand interfacial surfactant structure and how it impacts the rheology of suspensions. Some inferences have been drawn regarding the impact of shear and confinement on interfacial surfactant structure based on the steady state structure without any applied force. The changes upon the application of stress or under confirmation can be directly measured on the interfacial structure using reflectivity [134, 135], or on particle-particle correlations in a dense suspensions by applying a stress while carrying out SESANS experiments.

Appendix A

Structure and Details of Triglyceride Oils and Surfactants

A.1 Structure of Triglyceride Oils

The chemical structure of deuterated triglyceride oils, TO, TB, TP and GTO is shown below in Figures A.1 and A.2. For the hydrogenated oils the deuterium (labelled as D) in the structure is replaced with with hydrogen (H).

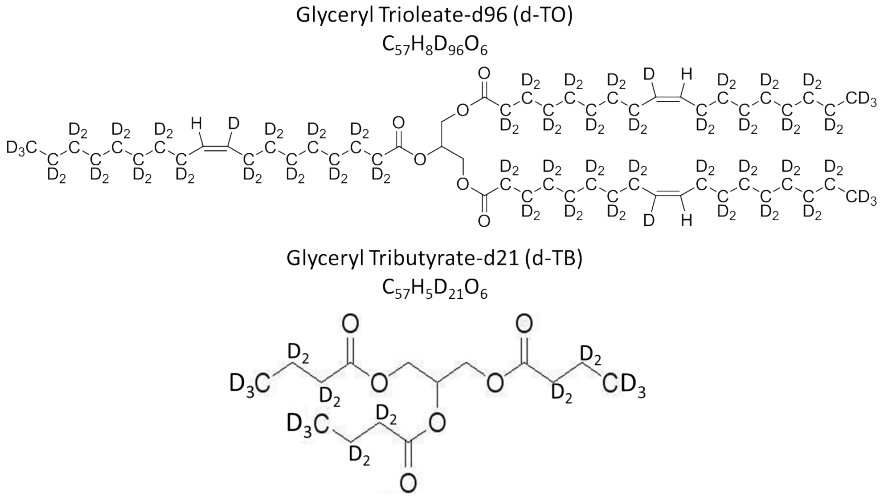

Figure A.1 *Structure of deuterated Glyceryl Trioleate (top) obtained from ANSTO, Australia and deuterated Glyceryl Tributyrate (bottom) obtained from Deuteration Facilities, ISIS, UK*

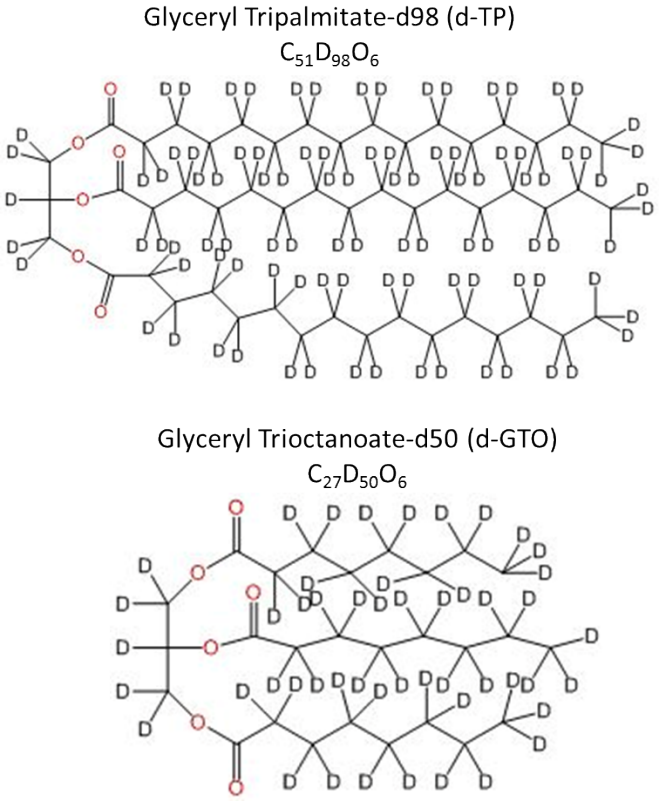

Figure A.2 *Structure of perdeuterated Glyceryl Tripalmitate (top) and perdeuterated Glyceryl Tricotanoate (bottom) obtained from QMX Laboratories, UK*

A.2 Details and Structure of Surfactants

A.2.1 Phospholipids

Lipidomics on Lecithin

Lipidomics data on lecithin sample from Mars, UK showing the top 20 components which are triglycerides, phosphocholine (PC), phosphoethanolamine (PE) and phosphoinositol (PI).

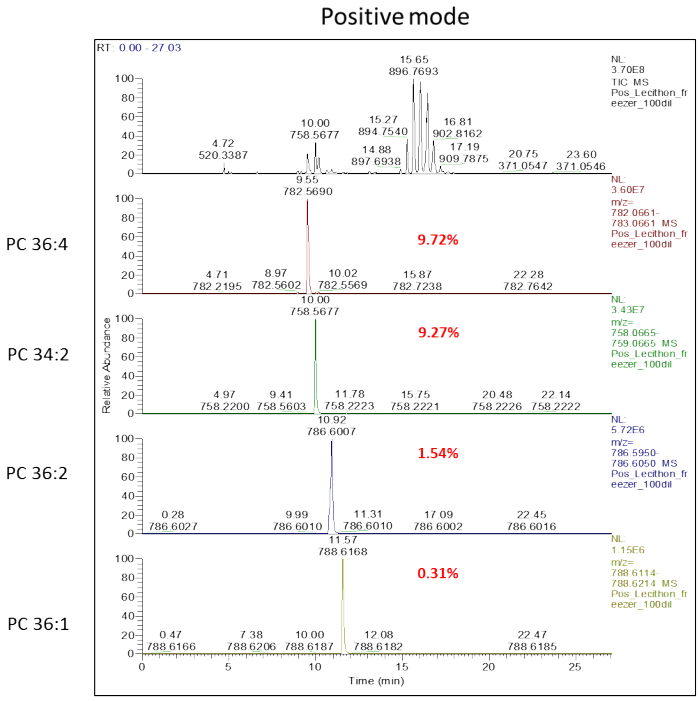

Top 20 lipids

Positive mode	Negative mode
TG(54:6)	PI(34:2)
TG(54:5)	PC(36:4)
TG(54:4)	PC(34:2)
TG(52:4)	PC(36:3)
TG(52:3)	PE(34:2)
TG(54:7)	PE(36:4)
TG(54:3)	PI(36:2)
PC(36:4)	PI(36:4)
TG(52:2)	PC(36:2)
PC(34:2)	PI(34:1)
PC(36:3)	18:1-Glc-Stigmasterol
TG(52:5)	PI(34:3)
TG(54:2)	PI(36:3)
PC(36:2)	PE(36:3)
TG(50:2)	PC(34:1)
TG(54:8)	PC(36:5)
PC(36:1)	LPI 18:2
TG(50:1)	PC(30:1)
PC(36:5)	LPC 18:2
LPC 18:0	LPI 16:0

DG	Diacylglycerols
GSL	Glycosphingolipids
PC	Phosphatidylcholines
PE	Phosphatidylethanolamines
PI	Phosphatidylinositols
ST	Sterols
TG	Triacylglycerols

Figure A.3 *Lipidomics on lecithin sample from Mars Chocolate, UK. Left panel: Positive mode data showing the majority PC components. Right panel: Summary of the top 20 components in positive and negative mode.*

Structure of Phospholipids

The structure for POPC and POPE, which are representative phospholipids for lecithin is shown in Figure A.4. The alkyl chains in lecithin range from saturated and unsaturated 12-18 carbon atoms with the majority being palmitoyl, oleoyl

and linoleoyl. For d31-POPC and d31-POPE, the 31 hydrogen atoms in the palmitoyl chain are replaced with deuterium.

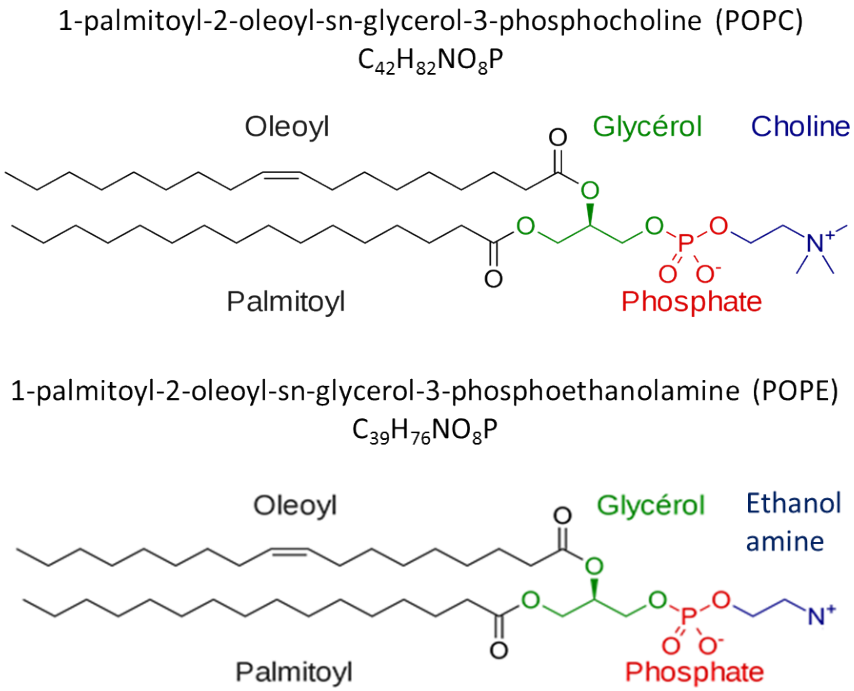

Figure A.4 *Structure of POPC (top) and POPE (bottom) obtained from Avanti Polar Lipids, USA.*

A.2.2 PGPR

Structure of PGPR

PGPR is a polymeric surfactant with the structure shown in Figure A.5 with n and m ranging from 1-6 with peaks at 2, 3 for both.

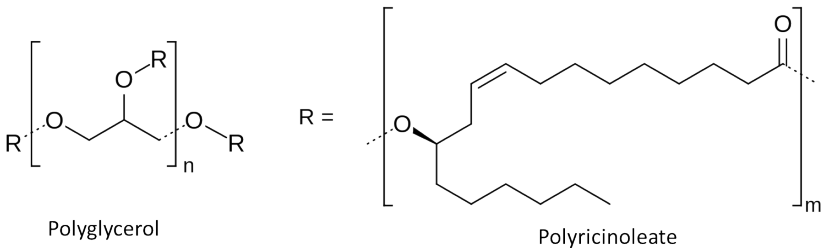

Figure A.5 *Structure of PGPR obtained from Mars Chocolate, UK.*

NMR Studies of PGPR

NMR spectra, ^{1}H and ^{13}C, for PGPR obtained from Mars Chocolate, UK compared to the paper by Orfanakis *et al.* [5]. this suggests multiple species, as observed by Orfanakis *et al.* were present.

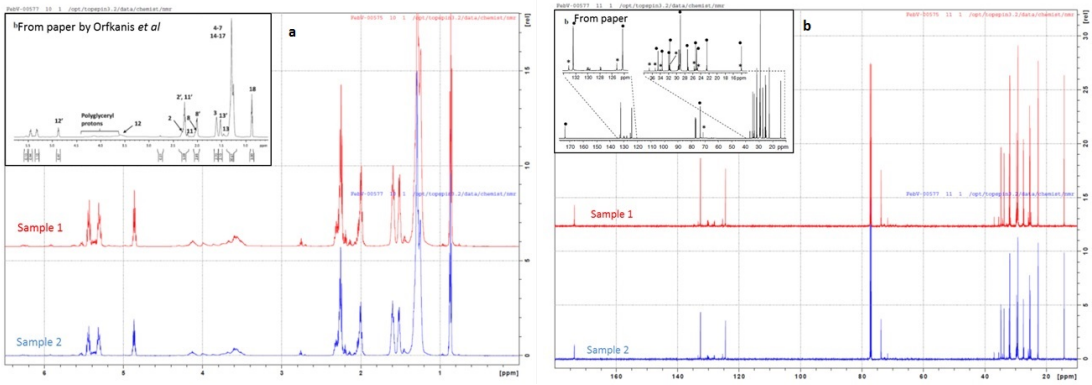

Figure A.6 *Left panel: ^{1}H NMR spectra for two PGPR samples. Right Panel: ^{13}C NMR spectra for two PGPR samples. The inset shows the spectra obtained by Orfanakis et al. [5]*

DOSY NMR was also carried out on the samples (see figure A.7) to get an idea about the diffusion coefficient of the species present in the PGPR sample. The diffusion co-efficient observed using the DOSY experiments gives a radius of ∼2 nm for the species.

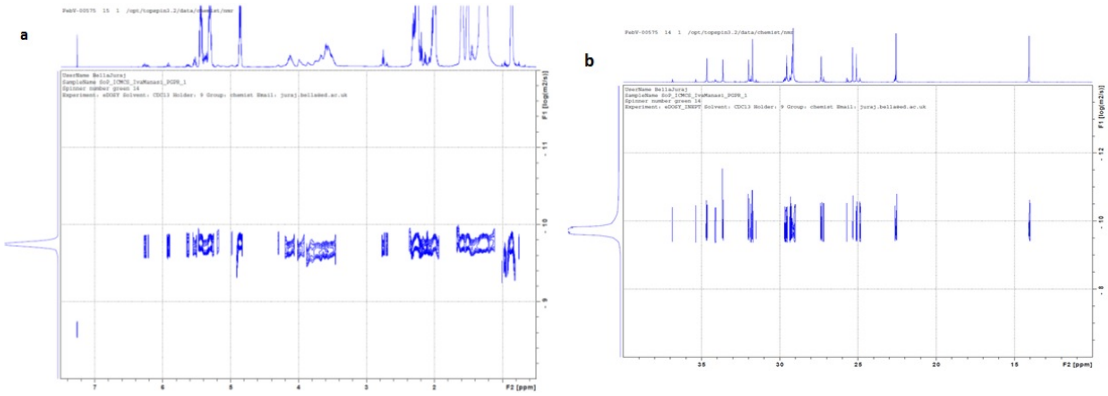

Figure A.7 *Left panel: ^{1}H DOSY NMR spectra for two PGPR samples. Right panel: ^{13}C DOSY NMR spectra for two PGPR samples.*

Appendix B

Beaucage Model Fits to Small Angle Scattering Data from Model Chocolate Suspensions

The model chocolate suspensions comprising sucrose in triglyceride oil were fit to a 2 level Beaucage model described in Section 4.3.2 where the first level describes the adsorbed surfactant layer and the second level describes scattering from the sucrose/triglyceride oil interface and other components in these complex systems.

B.1 Beaucage Model Fits for Small Angle Scattering Data from Sucrose in GTO Suspensions with Lecithin and PGPR

SANS and SAXS from 65% w/w sucrose in d-GTO and h-GTO, respectively, containing 0.8% total surfactant with varying lecithin and PGPR ratios. The fits obtained for the data discussed in Section 4.3.5 are detailed here.

B.1.1 SANS Data for Sucrose in d-GTO Suspensions

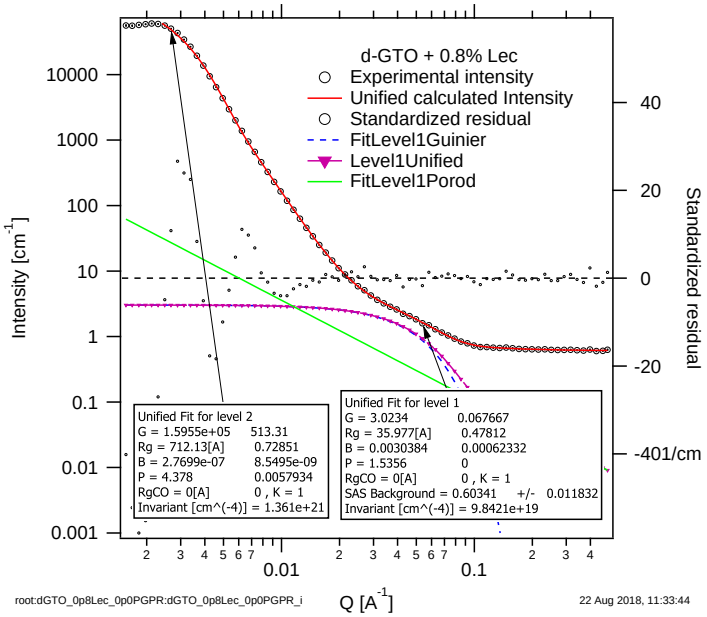

Figure B.1 *SANS for model chocolate, 65% w/w sucrose in d-GTO suspensions, containing 0.8% lecithin.*

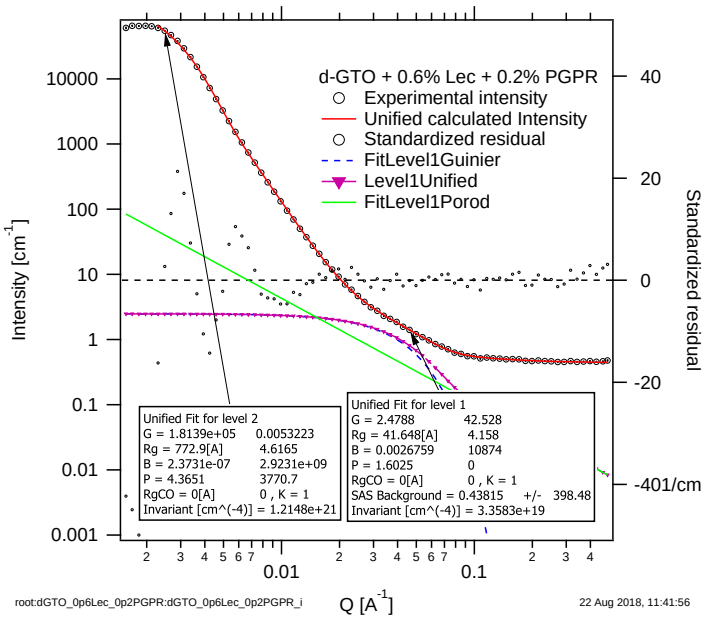

Figure B.2 *SANS for model chocolate, 65% w/w sucrose in d-GTO suspensions, containing 0.6% lecithin + 0.2% PGPR.*

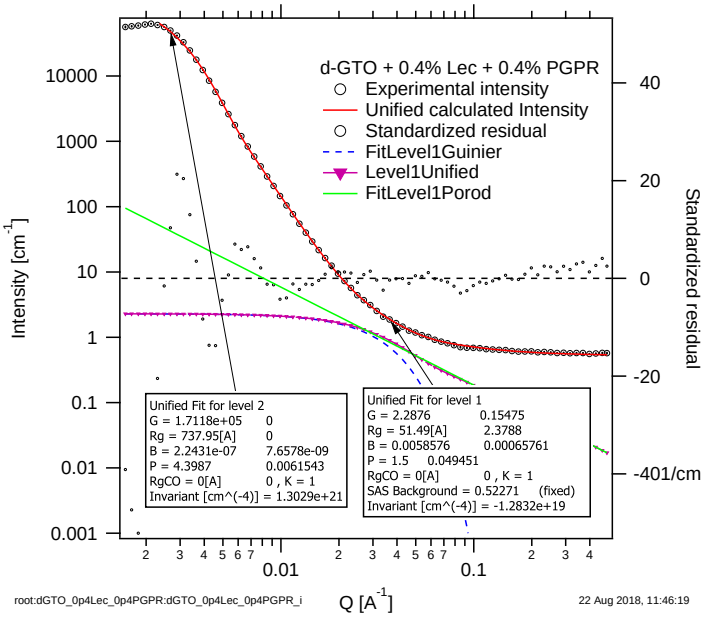

Figure B.3 *SANS for model chocolate, 65% w/w sucrose in d-GTO suspensions, containing 0.4% lecithin + 0.4% PGPR.*

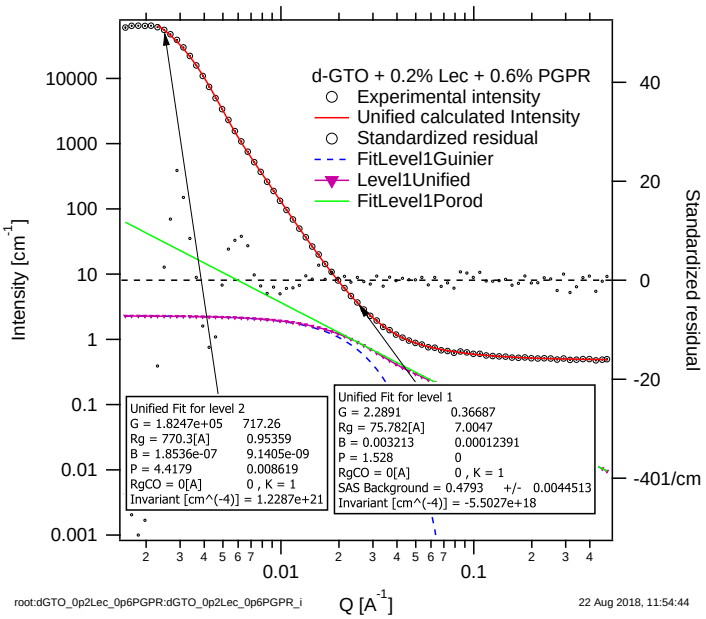

Figure B.4 *SANS for model chocolate, 65% w/w sucrose in d-GTO suspensions, containing 0.2% lecithin + 0.6% PGPR.*

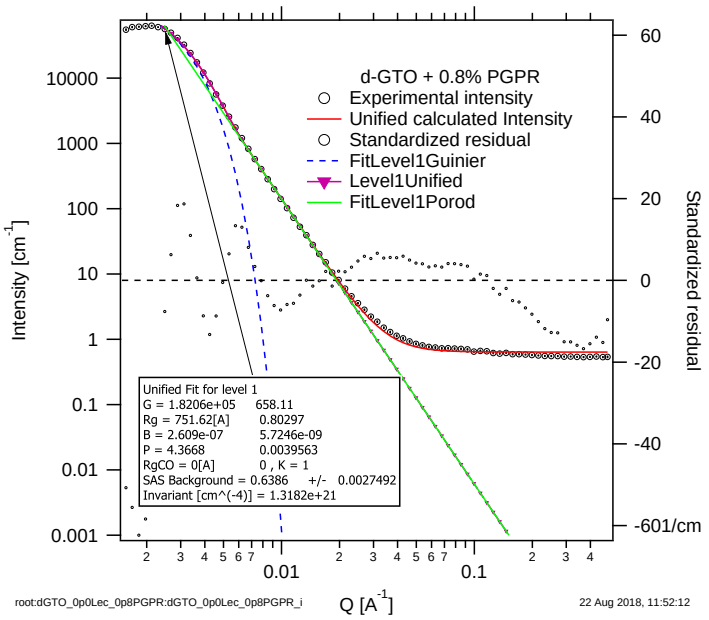

Figure B.5 *SANS for model chocolate, 65% w/w sucrose in d-GTO suspensions, containing 0.8% PGPR.*

B.1.2 SAXS Data for Sucrose in GTO Suspensions

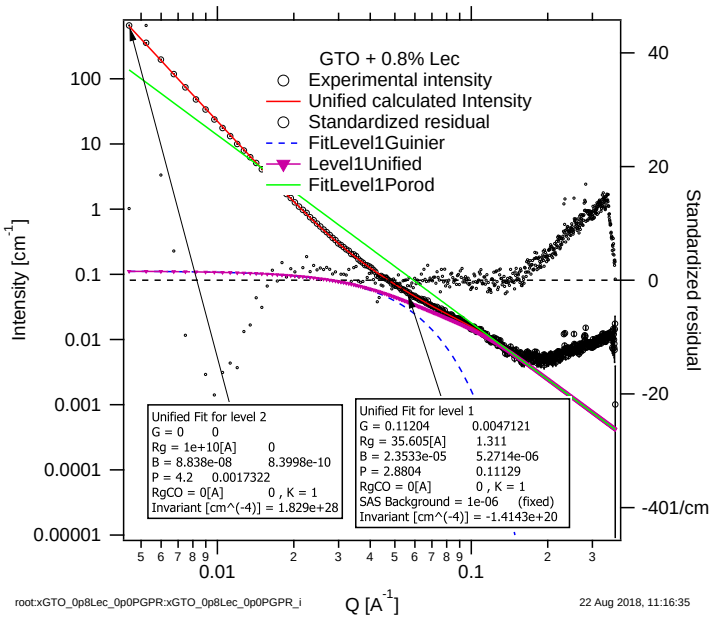

Figure B.6 *SAXS for model chocolate, 65% w/w sucrose in GTO suspensions, containing 0.8% lecithin.*

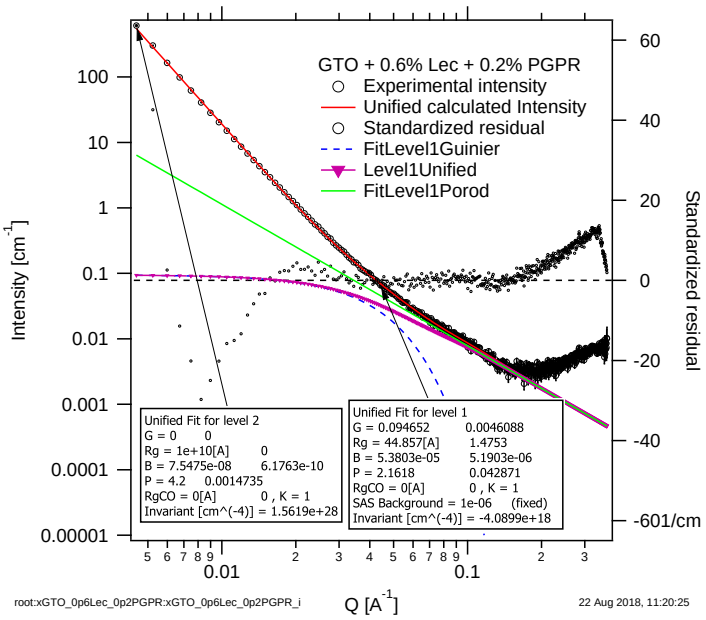

Figure B.7 *SAXS for model chocolate, 65% w/w sucrose in GTO suspensions, containing 0.6% lecithin + 0.2% PGPR.*

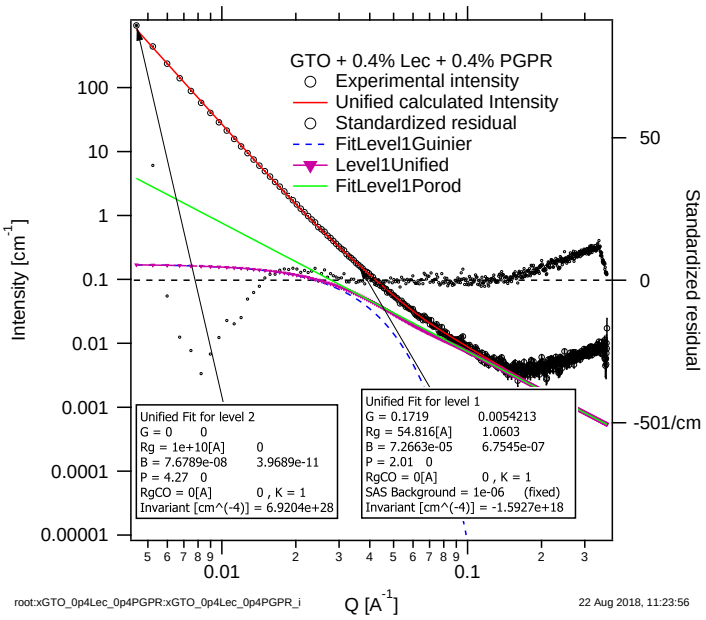

Figure B.8 *SAXS for model chocolate, 65% w/w sucrose in GTO suspensions, containing 0.4% lecithin + 0.4% PGPR.*

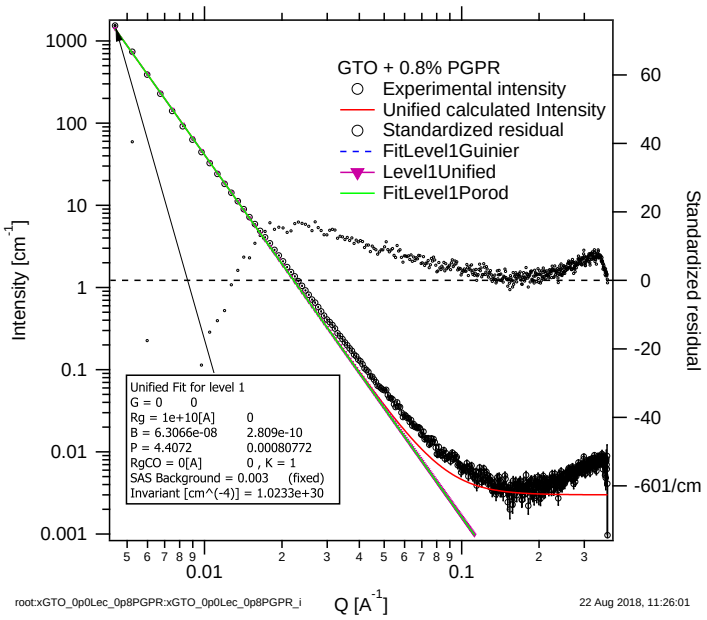

Figure B.9 *SAXS for model chocolate, 65% w/w sucrose in GTO suspensions, containing 0.8% PGPR.*

B.2 Beaucage Model Fits for Small Angle Scattering Data from Sucrose in TO/TP Suspensions with Lecithin and PGPR

SANS and SAXS from 65% w/w sucrose in d-TP and h-TO, respectively, containing 0.8% total surfactant with varying lecithin and PGPR ratios. The fits obtained for the data discussed in Section 4.3.6 are detailed here.

B.2.1 SANS Data for Sucrose in d-TP Suspensions

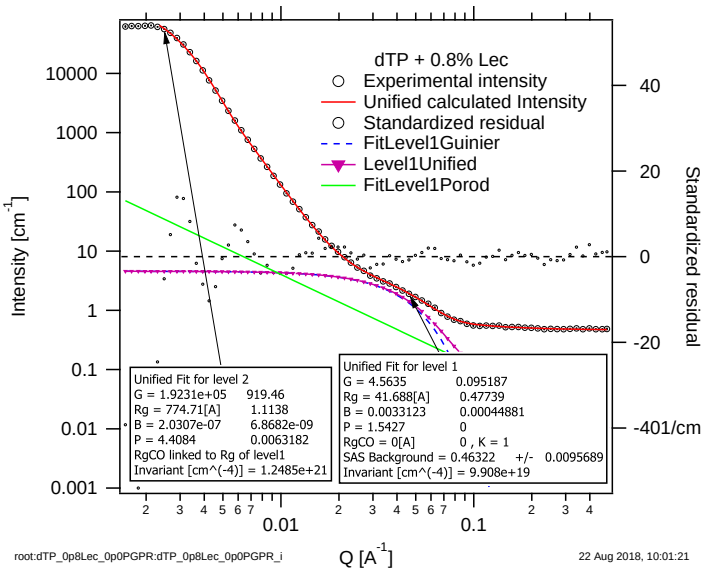

Figure B.10 *SANS for model chocolate, 65% w/w sucrose in d-TP suspensions, containing 0.8% lecithin.*

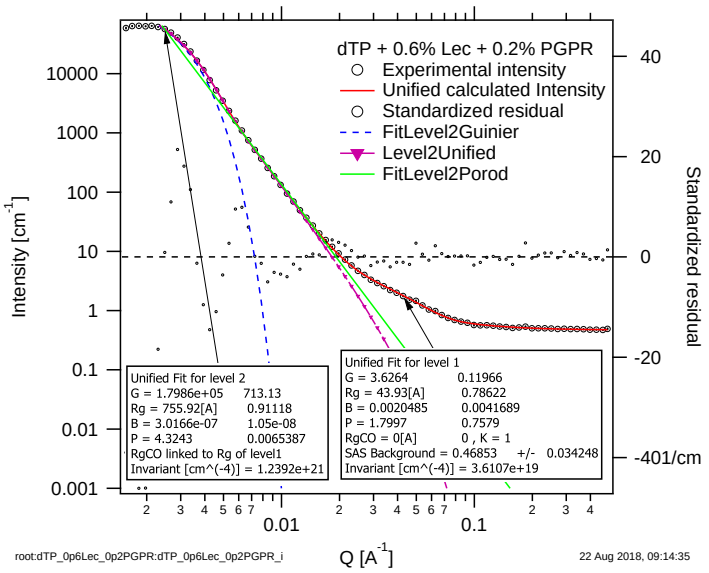

Figure B.11 *SANS for model chocolate, 65% w/w sucrose in d-TP suspensions, containing 0.6% lecithin + 0.2% PGPR.*

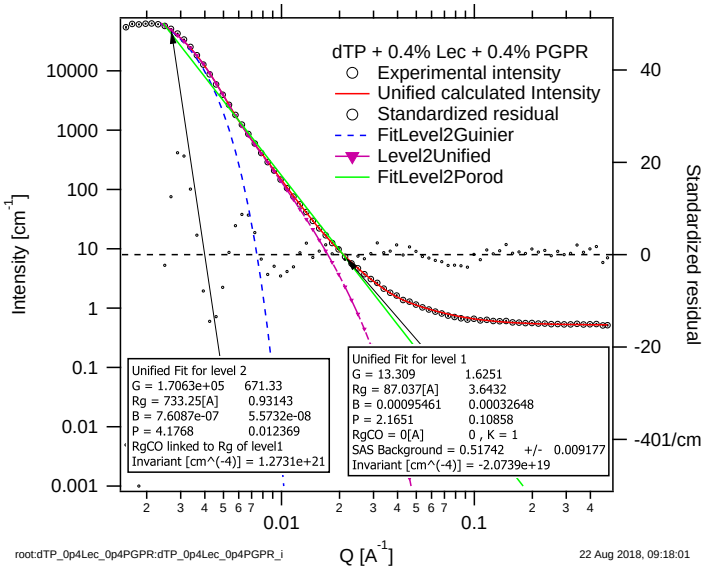

Figure B.12 *SANS for model chocolate, 65% w/w sucrose in d-TP suspensions, containing 0.4% lecithin + 0.4% PGPR.*

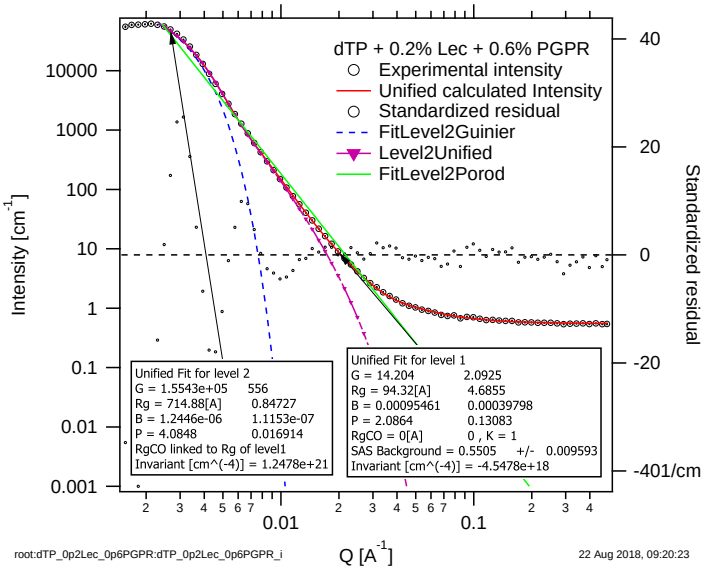

Figure B.13 *SANS for model chocolate, 65% w/w sucrose in d-TP suspensions, containing 0.2% lecithin + 0.6% PGPR.*

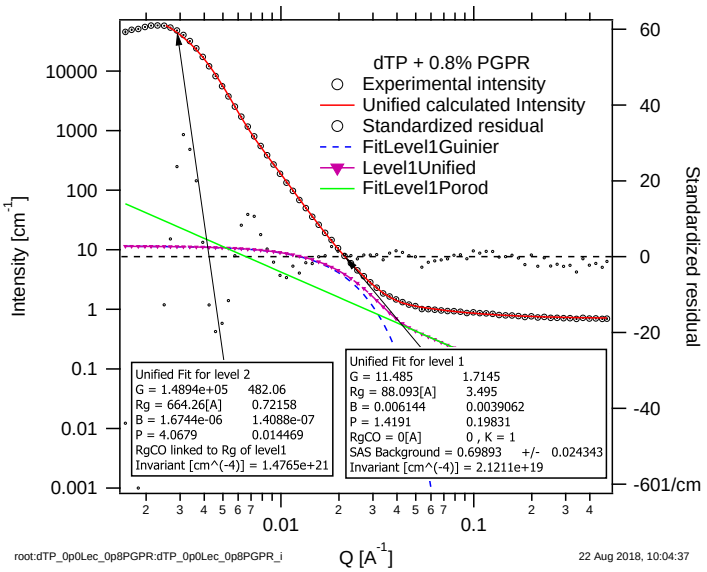

Figure B.14 *SANS for model chocolate, 65% w/w sucrose in d-TP suspensions, containing 0.8% PGPR.*

B.2.2 SAXS Data for Sucrose in TO Suspensions

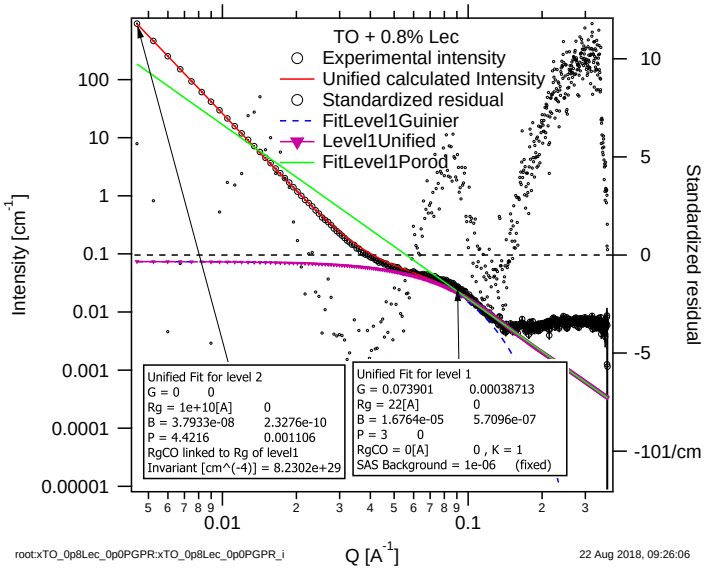

Figure B.15 *SAXS for model chocolate, 65% w/w sucrose in TO suspensions, containing 0.8% lecithin.*

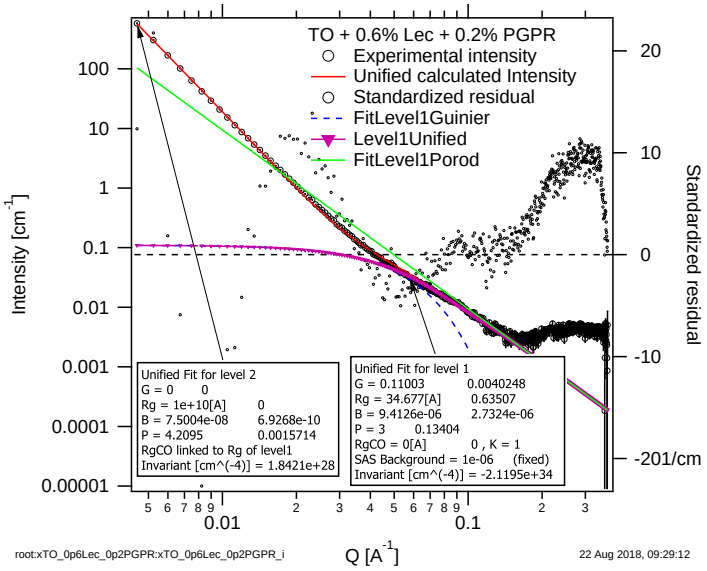

Figure B.16 *SAXS for model chocolate, 65% w/w sucrose in TO suspensions, containing 0.6% lecithin + 0.2% PGPR.*

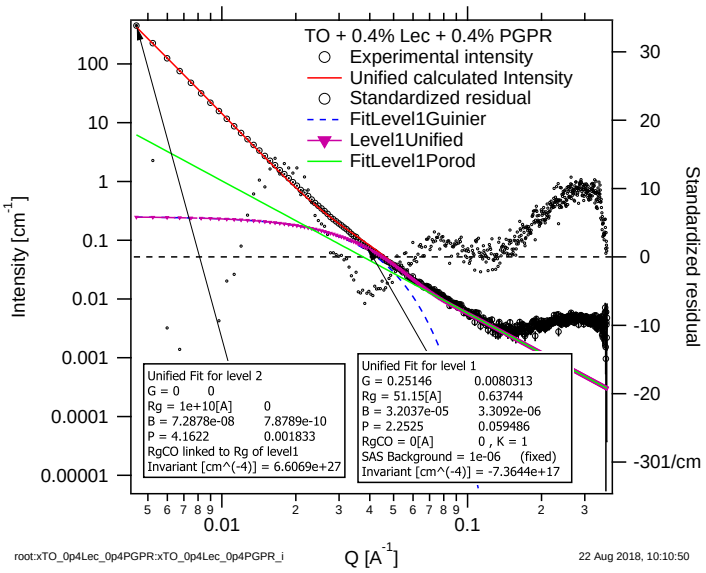

Figure B.17 *SAXS for model chocolate, 65% w/w sucrose in TO suspensions, containing 0.4% lecithin + 0.4% PGPR.*

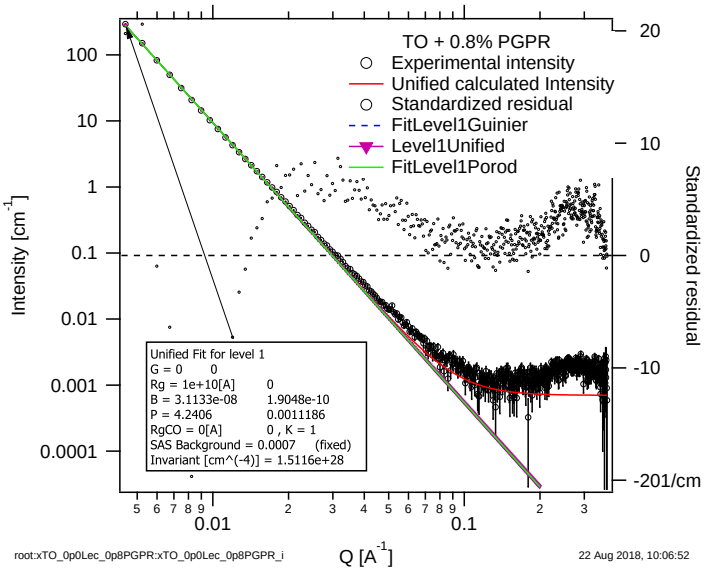

Figure B.18 *SAXS for model chocolate, 65% w/w sucrose in TO suspensions, containing 0.8% PGPR.*

Appendix C

Layering of Triglyceride Oil at Sucrose Interface: MATLAB Code for the SLD Profile

The MATLAB code written to fit the x-ray and neutron reflectivity data measured for triglyceride layering at the sucrose interface based on the analytical model discussed in Section 6.3.2

C.1 MATLAB Code for the X-Ray SLD Profile

This section details the MATLAB code to calculate the SLD profile for x-ray reflectivity where the x-rays are incident from the bulk triglyceride oil phase, followed by the layered triglyceride, sucrose layer, silicon oxide layer and finally the silicon block.

```
1 %% Function to calculate the XRR SLD profile for layered ...
     triglyceride at sucrose interfaces
2 function [output] = SLD_TG_XRR(params, bulk_in, bulk_out, contrast)
3
4 %% Model Parameters
5
6 % Si
7 SLD_si = bulk_out(contrast);        %SLD of Si layer
```

```
8
9  % SiOx
10 sig_siox = params(1);              %Width of Si/SiOx interface
11 SLD_siox = params(2);              %SLD of SiOx layer
12 thick_siox = params(3);            %thickness of SiOx layer
13
14 % Sucrose
15 sig_suc = params(4);               %Width of SiOx/Suc interface
16 SLD_suc = params(5);               %SLD of Suc layer
17 thick_suc = params(6);             %thickness of Suc layer
18
19 % Oil
20 sig_tg = params(7);                %Width of Suc/TG interface
21 L = params(8);                     %length of TG layer
22 r = params(9);                     %number of ordered layers
23 A = params(10);                    %Amplitude of oscillation ...
       from bulk
24 p = params(11);                    %Exponent for oscillations
25 k = params(12);                    %Smearing parameter
26 SLD_TG = bulk_in(contrast);        %Average SLD of TG
27 SLD_TGH = 13.5e-06;                %SLD of TGH
28 SLD_TGT = 7.8e-06;                 %SLD of TGT
29
30 %% Dependent parameters
31
32 % Define the interfaces
33 I_tg = 500;                                %TG/Sucrose Interface
34 I_suc = I_tg + thick_suc;                  %Suc/SiOx Interface
35 I_siox = I_suc + thick_siox;               %SiOx/Si Interface
36 B = (SLD_TG-SLD_TGT)./(SLD_TGH-SLD_TGT); %volume frac of heads ...
       in bulk
37 n_lay = thick_siox+thick_suc+500+(r*L)...
38         +(10*(sig_tg+sig_siox+sig_suc)); %Total length of the ...
              calculated SLD profile
39
40 %% SLD funcions
41
42 %Si
43 vf_si =@(x) (1-erf(-(x-I_siox)./sig_siox))./2;
44 Psi = @(x) SLD_si.*vf_si(x);
45
46 %SiOx
47 vf_siox =@(x) ...
       (erf((x-I_suc)./sig_suc)+erf(-(x-I_siox)./sig_siox))/2;
48 Psiox = @(x) SLD_siox.*vf_siox(x);
```

```
49
50 %Sucrose
51 vf_suc = @(x) (erf((x-I_tg)./sig_tg)+erf(-(x-I_suc)./sig_suc))/2;
52 Psuc = @(x) SLD_suc.*vf_suc(x);
53
54 %Oil
55 vf_tgh = @(x) Poil_XRR((x-I_tg)./L,r,p,L,k,A,B)...
56          +((A-(A.*B)+B).*(erf(-(x-I_tg)./sig_tg)-1)./2);
57 vf_tgt = @(x) 1-(vf_si(x)+vf_siox(x)+vf_suc(x)+vf_tgh(x));
58 P_tgh = @(x) vf_tgh(x).*SLD_TGH;
59 P_tgt = @(x) vf_tgt(x).*SLD_TGT;
60 Poil = @(x) P_tgh(x) + P_tgt(x);
61
62 %Sum of all layers
63 Psum = @(x) Psi(x) + Psiox(x) + Psuc(x) + Poil(x);
64 x = -10:0.1:n_lay;
65
66 %% Plot SLD
67 close all; % closes any open figures
68 figure();
69 plot(x,vf_tgt(x),'m',x,vf_tgh(x),'g', x, vf_suc(x),...
70     'r',x,vf_siox(x),'b',x,vf_si(x),'c');
71 figure();
72 plot(x,Poil(x),'g', x, Psuc(x),'r',x,Psiox(x),'b',x,Psi(x),'c');
73 figure();
74 plot(x,Psum(x),'r');
75
76 %% Output
77 Psum = Psum(x);
78 [output] = [x', Psum'];
```

```
1  %% Function to calculate the volume fraction of triglyceride ...
       head for XRR
2  function vfhead = Poil_XRR(x,r,p,L,k,A,B)
3      foil = @(x,r,p) ...
           A.*(((cos(pi.*x./(1+k.*(abs(x))))+1)./2).^p-(B))...
4                       .*exp(-((x./(1+k.*abs(x))).^2)./r) + B;
5      vfhead(x≤0)= foil(x(x≤0),r,p);
6      vfhead(x≥0)= A-(A.*B)+B;
7  end
```

C.2 MATLAB Code for the Neutron SLD Profile

This section details the MATLAB code to calculate the SLD profile for neutron reflectivity where the neutrons are incident through the silicon block, followed by the silicon oxide layer, sucrose layer, the layered triglyceride and finally the bulk triglyceride oil phase.

```
%% Function to calculate the NR SLD profile for layered ...
    triglyceride at sucrose interfaces
function [output] = SLD_TG_NR(params, bulk_in, bulk_out, contrast)

%% Model Parameters

% Si
SLD_si = bulk_in;                   %SLD of Si layer

% SiOx
sig_siox = params(1);               %Width of Si/SiOx interface
SLD_siox = params(2);               %SLD of SiOx layer
thick_siox = params(3);             %thickness of SiOx layer

% Sucrose
sig_suc = params(4);                %Width of SiOx/Suc interface
SLD_suc = params(5);                %SLD of Suc layer
thick_suc = params(6);              %thickness of Suc layer

% Oil
sig_tg = params(7);                 %Width of Suc/Triglyceride ...
    interface
L = params(8);                      %length of TG
r = params(9);                      %number of ordered layers
A = params(10);                     %Amplitude of oscillation ...
    from bulk
Lh = params(11);                    %Length of head group
k = params(12);                     %Smearing parameter
SLD_TGH = params(13);               %SLD of TGH
SLD_TG = bulk_out;                  %Average SLD of Triglyceride
SLD_TGT = -0.22e-06;                %SLD of TGT

%% Dependent parameters

% Define the interfaces
```

```
I_siox = 50;                                %Si/SiOx Interface
I_suc = I_siox + thick_siox;                %SiOx/Suc Interface
I_tg = I_suc + thick_suc;                   %Suc/Triglyceride Interface
B = (SLD_TG-SLD_TGT)./(SLD_TGH-SLD_TGT); %volume fraction of ...
    heads in bulk
n_lay = thick_siox+thick_suc+500+(r*L)...
        +(10*(sig_tg+sig_siox+sig_suc)); %Total length of the ...
            calculated SLD profile

%% SLD funcions

%Si
vf_si = @(x) (1-erf((x-I_siox)./sig_siox))./2;
Psi = @(x) SLD_si.*vf_si(x);

%SiOx
vf_siox =@(x) ...
    (erf((x-I_siox)./sig_siox)-erf((x-I_suc)./sig_suc))./2;
Psiox = @(x) SLD_siox.*vf_siox(x);

%Sucrose
vf_suc = @(x) (erf((x-I_suc)./sig_suc)-erf((x-I_tg)./sig_tg))/2;
Psuc = @(x) SLD_suc.*vf_suc(x);

%Oil
vf_tgh = @(x) Poil_NR((x-I_tg)./L,r,Lh,L,k,A,B)...
              +((A-(A.*B)+B).*(erf((x-I_tg)./sig_tg)-1)./2);
vf_tgt = @(x) 1-(vf_si(x)+vf_siox(x)+vf_suc(x)+vf_tgh(x));
P_tgh = @(x) vf_tgh(x).*SLD_TGH;
P_tgt = @(x) vf_tgt(x).*SLD_TGT;
Poil = @(x) P_tgh(x) + P_tgt(x);

%Sum of all layers
Psum = @(x)  Psi(x) + Psiox(x) + Psuc(x) + Poil(x);
x = -10:1:n_lay;

%% Plot SLD
close all; % closes any open figures
figure();
plot(x,vf_tgt(x),'m',x,vf_tgh(x),'g', x, vf_suc(x),...
      'r',x,vf_siox(x),'b',x,vf_si(x),'c');
 figure();
plot(x,Poil(x),'g', x, Psuc(x),'r',x,Psiox(x),'b',x,Psi(x),'c');
figure();
plot(x,Psum(x),'r');
```

```
75
76 %% Output
77 Psum = Psum(x);
78 output = [x' Psum'];
```

```
1 %% Function to calculate the volume fraction of triglyceride ...
     head for NR
2 function vfhead = Poil_NR(x,r,p,L,k,A,B)
3     foilNR = @(x,r,p) ...
          A.*((((cos(pi.*x./(1+k.*(abs(x))))+1)./2).^p)-B)...
4                         .*exp(-((x./(1+k.*abs(x))).^2)./r) + B;
5     vfhead(x≥0)= foilNR(x(x≥0),r,p);
6     vfhead(x≤0)= A-(A.*B)+B;
7 end
```

Appendix D

Lecithin At Sucrose/Triglyceride Oil Interface: MATLAB Code for the SLD Profile

The MATLAB code written to fit the neutron and x-ray reflectivity data measured for lecithin films at sucrose interface using the model discussed in Section 7.3.2.

D.1 MATLAB Code for the Neutron SLD Profile

The MATLAB code written to simultaneously fit neutron reflectivity data measured for lecithin thin films at the sucrose/triglyceride oil interface at two contrasts of the triglyceride oil (bulk out phase) using the model discussed in Section 7.3.2. The neutrons are incident through the silicon, followed by the silicon oxide, sucrose, the lecithin layers and finally the bulk triglyceride oil. This code details calculation for a lecithin layer comprising 7 monolayers of phospholipid head and tails which is the case for TO. For GTO, there are 5 monolayers present and the MATLAB code is a cut down version of this code,

```
1 %% Function to calculate the NR SLD profile for 7 lecithin ...
     layers at sucrose/TG interface.
2 function [output] = SLD_lecithin_NR_2contrasts...
3                     (params,bulk_in,bulk_out,contrast)
4
```

```
%Silicon
SLD_si = bulk_in(contrast);

% SiOx
if contrast == 1
 sig_siox = params(1);          %Width of Si/SiOx interface
 SLD_siox = params(2);
 thick_siox = params(3);
 % Sucrose
 sig_suc = params(4);           %Width of SiOx/Suc interface
 SLD_suc = params(5);
 thick_suc = params(6);
 sig_tg = params(7);            %Width of Suc/TG interface
elseif contrast == 2
 sig_siox = params(45);         %Width of Si/SiOx interface
 SLD_siox = params(2);
 thick_siox = params(46);
 % Sucrose
 sig_suc = params(47);          %Width of SiOx/Suc interface
 SLD_suc = params(5);
 thick_suc = params(48);
 sig_tg = params(49);
end

% Oil
SLD_tg = bulk_out(contrast);

% Lecithin layers
SLD_tail = params(8);
SLD_head = params(9);
apm_l1 = params(10);
apm_l2 = params(11);
apm_l3 = params(12);
apm_l4 = params(13);
apm_l5 = params(14);
apm_l6 = params(15);
apm_l7 = params(16);
s_head1 = params(17);
s_tail1 = params(18);
s_head2 = params(19);
s_tail2 = params(20);
s_head3 = params(21);
s_tail3 = params(22);
s_head4 = params(23);
s_tail4 = params(24);
```

```
s_head5 = params(25);
s_tail5 = params(26);
s_head6 = params(27);
s_tail6 = params(28);
s_head7 = params(29);
s_tail7 = params(30);
sig_head1 = params(31);
sig_tail1 = params(32);
sig_head2 = params(33);
sig_tail2 = params(34);
sig_head3 = params(35);
sig_tail3 = params(36);
sig_head4 = params(37);
sig_tail4 = params(38);
sig_head5 = params(39);
sig_tail5 = params(40);
sig_head6 = params(41);
sig_tail6 = params(42);
sig_head7 = params(43);
sig_tail7 = params(44);

%% Fixed parameters
thick_si = 100;
v_tail = 935;                %volume of Lecithin tails
v_head = 321.2;              %volume of Lecithin heads
v_Lecithin = v_tail+v_head; %volume of Lecithin (POPC)
v_tgt = 1470;                %volume of TG tails (= 663 for GTO)
v_tgh = 185.8;               %volume of TG heads
v_tg = v_tgt+v_tgh;          %volume of TG molecules
n_lay=1500;
x=0:1:n_lay;

%%dependent parameters
%thickness of head-tail layers
thick_head1 = (((1-s_head1)*v_head) + ...
    (s_head1*v_tg))./((1-s_head1)*apm_l1);
thick_tail1 = (((1-s_tail1)*v_tail) + ...
    (s_tail1*v_tg))./((1-s_tail1)*apm_l1);
thick_tail2 = (((1-s_tail2)*v_tail) + ...
    (s_tail2*v_tg))./((1-s_tail2)*apm_l2);
thick_head2 = (((1-s_head2)*v_head) + ...
    (s_head2*v_tg))./((1-s_head2)*apm_l2);
thick_head3 = (((1-s_head3)*v_head) + ...
    (s_head3*v_tg))./((1-s_head3)*apm_l3);
```

```
89 thick_tail3 = (((1-s_tail3)*v_tail) + ...
       (s_tail3*v_tg))./((1-s_tail3)*apm_l3);
90 thick_tail4 = (((1-s_tail4)*v_tail) + ...
       (s_tail4*v_tg))./((1-s_tail4)*apm_l3);
91 thick_head4 = (((1-s_head4)*v_head) + ...
       (s_head4*v_tg))./((1-s_head4)*apm_l4);
92 thick_head5 = (((1-s_head5)*v_head) + ...
       (s_head5*v_tg))./((1-s_head5)*apm_l5);
93 thick_tail5 = (((1-s_tail5)*v_tail) + ...
       (s_tail5*v_tg))./((1-s_tail5)*apm_l5);
94 thick_tail6 = (((1-s_tail6)*v_tail) + ...
       (s_tail6*v_tg))./((1-s_tail6)*apm_l6);
95 thick_head6 = (((1-s_head6)*v_head) + ...
       (s_head6*v_tg))./((1-s_head6)*apm_l6);
96 thick_head7 = (((1-s_head7)*v_head) + ...
       (s_head7*v_tg))./((1-s_head7)*apm_l7);
97 thick_tail7 = (((1-s_tail7)*v_tail) + ...
       (s_tail7*v_tg))./((1-s_tail7)*apm_l7);
98
99 %SLD of various head-tail layers
100 SLD_head1 = (s_head1*SLD_tg) + ((1-s_head1)*SLD_head);
101 SLD_tail1 = (s_tail1*SLD_tg) + ((1-s_tail1)*SLD_tail);
102 SLD_tail2 = (s_tail2*SLD_tg) + ((1-s_tail2)*SLD_tail);
103 SLD_head2 = (s_head2*SLD_tg) + ((1-s_head2)*SLD_head);
104 SLD_head3 = (s_head3*SLD_tg) + ((1-s_head3)*SLD_head);
105 SLD_tail3 = (s_tail3*SLD_tg) + ((1-s_tail3)*SLD_tail);
106 SLD_tail4 = (s_tail4*SLD_tg) + ((1-s_tail4)*SLD_tail);
107 SLD_head4 = (s_head4*SLD_tg) + ((1-s_head4)*SLD_head);
108 SLD_head5 = (s_head5*SLD_tg) + ((1-s_head5)*SLD_head);
109 SLD_tail5 = (s_tail5*SLD_tg) + ((1-s_tail5)*SLD_tail);
110 SLD_tail6 = (s_tail6*SLD_tg) + ((1-s_tail6)*SLD_tail);
111 SLD_head6 = (s_head6*SLD_tg) + ((1-s_head6)*SLD_head);
112 SLD_head7 = (s_head7*SLD_tg) + ((1-s_head7)*SLD_head);
113 SLD_tail7 = (s_tail7*SLD_tg) + ((1-s_tail7)*SLD_tail);
114
115 %Interfaces
116 I_siox = thick_si;
117 I_suc = I_siox + thick_siox;
118 I_head1 = I_suc + thick_suc;
119 I_tail1 = I_head1 + thick_head1;
120 I_tail2 = I_tail1 + thick_tail1;
121 I_head2 = I_tail2 + thick_tail2;
122 I_head3 = I_head2 + thick_head2;
123 I_tail3 = I_head3 + thick_head3;
124 I_tail4 = I_tail3 + thick_tail3;
```

```
I_head4 = I_tail4 + thick_tail4;
I_head5 = I_head4 + thick_head4;
I_tail5 = I_head5 + thick_head5;
I_tail6 = I_tail5 + thick_tail5;
I_head6 = I_tail6 + thick_tail6;
I_head7 = I_head6 + thick_head6;
I_tail7 = I_head7 + thick_head7;
I_tg = I_tail7 + thick_tail7;

%%
%Si
vf_si = @(x) (1-erf((x-I_siox)./sig_siox))./2;
Psi = @(x) SLD_si.*vf_si(x);
%SiOx
vf_siox =@(x) ...
    (erf((x-I_siox)./sig_siox)-erf((x-I_suc)./sig_suc))./2;
Psiox = @(x) SLD_siox.*vf_siox(x);
%sucrose
vf_suc = @(x) ...
    (erf((x-I_suc)./sig_suc)-erf((x-I_head1)./sig_head1))/2;
Psuc = @(x) SLD_suc.*vf_suc(x);
%Lecithin layer 1 - head
vf_head1 = ...
    @(x)(erf((x-I_head1)./sig_head1)-erf((x-I_tail1)./sig_tail1))/2;
Phead1 = @(x) SLD_head1.*vf_head1(x);
%Lecithin layer 1 - tail
vf_tail1 = ...
    @(x)(erf((x-I_tail1)./sig_tail1)-erf((x-I_tail2)./sig_tail2))/2;
Ptail1 = @(x) SLD_tail1.*vf_tail1(x);
%Lecithin layer 2 - tail
vf_tail2 = ...
    @(x)(erf((x-I_tail2)./sig_tail2)-erf((x-I_head2)./sig_head2))/2;
Ptail2 = @(x) SLD_tail2.*vf_tail2(x);
%Lecithin layer 2 - head
vf_head2 = ...
    @(x)(erf((x-I_head2)./sig_head2)-erf((x-I_head3)./sig_head3))/2;
Phead2 = @(x) SLD_head2.*vf_head2(x);
%Lecithin layer 3 - head
vf_head3 = ...
    @(x)(erf((x-I_head3)./sig_head3)-erf((x-I_tail3)./sig_tail3))/2;
Phead3 = @(x) SLD_head3.*vf_head3(x);
%Lecithin layer 3 - tail
vf_tail3 = ...
    @(x)(erf((x-I_tail3)./sig_tail3)-erf((x-I_tail4)./sig_tail4))/2;
Ptail3 = @(x) SLD_tail3.*vf_tail3(x);
```

```
%Lecithin layer 4 - tail
vf_tail4 = ...
    @(x)(erf((x-I_tail4)./sig_tail4)-erf((x-I_head4)./sig_head4))/2;
Ptail4 = @(x) SLD_tail4.*vf_tail4(x);
%Lecithin layer 4 - head
vf_head4 = ...
    @(x)(erf((x-I_head4)./sig_head4)-erf((x-I_head5)./sig_head5))/2;
Phead4 = @(x) SLD_head4.*vf_head4(x);
%Lecithin layer 5 - head
vf_head5 = ...
    @(x)(erf((x-I_head5)./sig_head5)-erf((x-I_tail5)./sig_tail5))/2;
Phead5 = @(x) SLD_head5.*vf_head5(x);
%Lecithin layer 5 - tail
vf_tail5 = ...
    @(x)(erf((x-I_tail5)./sig_tail5)-erf((x-I_tail6)./sig_tail6))/2;
Ptail5 = @(x) SLD_tail5.*vf_tail5(x);
%Lecithin layer 6 - tail
vf_tail6 = ...
    @(x)(erf((x-I_tail6)./sig_tail6)-erf((x-I_head6)./sig_head6))/2;
Ptail6 = @(x) SLD_tail6.*vf_tail6(x);
%Lecithin layer 6 - head
vf_head6 = ...
    @(x)(erf((x-I_head6)./sig_head6)-erf((x-I_head7)./sig_head7))/2;
Phead6 = @(x) SLD_head6.*vf_head6(x);
%Lecithin layer 7 - head
vf_head7 = ...
    @(x)(erf((x-I_head7)./sig_head7)-erf((x-I_tail7)./sig_tail7))/2;
Phead7 = @(x) SLD_head7.*vf_head7(x);
%Lecithin layer 7 - tail
vf_tail7 = ...
    @(x)(erf((x-I_tail7)./sig_tail7)-erf((x-I_tg)./sig_tg))/2;
Ptail7 = @(x) SLD_tail7.*vf_tail7(x);

%oil
vf_tg = @(x) (erf((x-I_tg)./sig_tg)+1)/2;
Poil = @(x) SLD_tg.*vf_tg(x);

%volume fraction of heads, tails and oil in Lecihtin layers
vf_h7 = (1-s_head7)*vf_head7(x);
vf_t7 = (1-s_tail7)*vf_tail7(x);
vf_h6 = (1-s_head6)*vf_head6(x);
vf_t6 = (1-s_tail6)*vf_tail6(x);
vf_h5 = (1-s_head5)*vf_head5(x);
vf_t5 = (1-s_tail5)*vf_tail5(x);
vf_h4 = (1-s_head4)*vf_head4(x);
```

```
vf_t4 = (1-s_tail4)*vf_tail4(x);
vf_h3 = (1-s_head3)*vf_head3(x);
vf_t3 = (1-s_tail3)*vf_tail3(x);
vf_h2 = (1-s_head2)*vf_head2(x);
vf_t2 = (1-s_tail2)*vf_tail2(x);
vf_h1 = (1-s_head1)*vf_head1(x);
vf_t1 = (1-s_tail1)*vf_tail1(x);
%total volume fraction of heads and tails in lecithin layer
vf_htotal = vf_h7+vf_h6+vf_h5+vf_h4+vf_h3+vf_h2+vf_h1;
vf_ttotal = vf_t7+vf_t6+vf_t5+vf_t4+vf_t3+vf_t2+vf_t1;

vf_tgf = @(x) 1-(vf_si(x)+vf_siox(x)+vf_suc(x)+vf_htotal+vf_ttotal);

vf_sum = @(x) ...
    vf_si(x)+vf_siox(x)+vf_suc(x)+vf_head7(x)+vf_tail7(x)...
        +vf_head6(x)+vf_tail6(x)+vf_head5(x)+vf_tail5(x)+...
        vf_head4(x)+vf_tail4(x)+vf_head3(x)+vf_tail3(x)+...
        vf_head2(x)+vf_tail2(x)+vf_head1(x)+vf_tail1(x)+vf_tg(x);
Psum = @(x) ...
    Poil(x)+Ptail1(x)+Phead1(x)+Phead2(x)+Ptail2(x)+Ptail3(x)...
        +Phead3(x)+Phead4(x)+Ptail4(x)+Ptail5(x)+Phead5(x)+
        Phead6(x)+Ptail6(x)+Ptail7(x)+Phead7(x)+Psuc(x)+Psiox(x)+Psi(x);

%% Plot SLD and volume fractions
close all; % closes any open figures
figure();
plot(x,Psum(x),'r');
figure();
plot(x,Psi(x),'g',x,Psiox(x),'c',x,Psuc(x),'r',x,Poil(x),'g',...
    x,Ptail1(x),'b',x,Phead1(x),'c',x,Phead2(x),'g',x,Ptail2(x),'r',...
    x,Ptail3(x),'b',x,Phead3(x),'c',x,Phead4(x),'g',x,Ptail4(x),'r',...
    x,Ptail5(x),'b',x,Phead5(x),'c',x,Phead6(x),'g',x,Ptail6(x),'r',...
    x,Ptail7(x),'b',x,Phead7(x),'c');
figure();
plot(x,vf_tg(x),'g',x,vf_tail1(x),'b',x,vf_head1(x),'r',x,vf_head2(x),...
'   b',x,vf_tail2(x),'r',x,vf_tail3(x),'b',x,vf_head3(x),'r',...
    x,vf_head4(x),'b',x,vf_tail4(x),'r',x,vf_tail5(x),'b',...
    x,vf_head5(x),'r',x,vf_head6(x),'b',x,vf_tail6(x),'r',...
    x,vf_tail7(x),'b',x,vf_head7(x),'r');
% figure()
plot(x,vf_htotal,'r',x,vf_ttotal,'b',x,vf_tgf(x),'g')

%% Output
Psum = Psum(x);
output = [x' Psum'];
```

D.2 MATLAB Code for the X-Ray SLD Profile

The MATLAB code written to fit x-ray reflectivity data measured for lecithin thin films at the sucrose/triglyceride oil interface using the model discussed in Section 7.3.2. The x-rays are incident from the triglyceride oil, followed by the lecithin layers, followed by the sucrose, silicon oxide and finally the silicon. This code details calculation for a lecithin layer comprising 7 monolayers of phospholipid head and tails which is the case for TO. For GTO, there are 5 monolayers present and the MATLAB code is a cut down version of the same,

```
1  %% Function to calculate the XRR SLD profile for 7 lecithin ...
       layers at sucrose/TG interface.
2  function [output] = ...
       sld_lecithin_xrr(params,bulk_in,bulk_out,contrast)
3  %Silicon
4  SLD_si = bulk_out;
5  % SiOx
6  sig_siox = params(1);              %width of Si/SiOx interface
7  SLD_siox = params(2);
8  thick_siox = params(3);
9
10 % Sucrose
11 sig_suc = params(4);               %width of SiOx/Suc interface
12 SLD_suc = params(5);
13 thick_suc = params(6);
14
15 % Oil
16 sig_tg = params(7);                %width of Suc/TG interface
17 SLD_tg = bulk_in;
18
19 % Lecithin layers
20 SLD_tail = params(8);
21 SLD_head = params(9);
22 apm_l7 = params(10);
23 apm_l6 = params(11);
24 apm_l5 = params(12);
25 apm_l4 = params(13);
26 apm_l3 = params(14);
27 apm_l2 = params(15);
28 apm_l1 = params(16);
29 s_head7 = params(17);
30 s_tail7 = params(18);
```

```
s_head6 = params(19);
s_tail6 = params(20);
s_head5 = params(21);
s_tail5 = params(22);
s_head4 = params(23);
s_tail4 = params(24);
s_head3 = params(25);
s_tail3 = params(26);
s_head2 = params(27);
s_tail2 = params(28);
s_head1 = params(29);
s_tail1 = params(30);
sig_head7 = params(31);
sig_tail7 = params(32);
sig_head6 = params(33);
sig_tail6 = params(34);
sig_head5 = params(35);
sig_tail5 = params(36);
sig_head4 = params(37);
sig_tail4 = params(38);
sig_head3 = params(39);
sig_tail3 = params(40);
sig_head2 = params(41);
sig_tail2 = params(42);
sig_head1 = params(43);
sig_tail1 = params(44);

%% Fixed parameters
thick_tg = 10*sig_tg;
v_tail = 935;
v_head = 321.2;
v_Lecithin = v_tail+v_head;
v_tgt = 1470;
v_tgh = 185.8;
v_tg = v_tgt+v_tgh;
n_lay=1500;
x=0:1:n_lay;

%%dependent parameters
%thickness of head-tail layers
thick_head7 = (((1-s_head7)*v_head) + ...
    (s_head7*v_tg))./((1-s_head7)*apm_l7);
thick_tail7 = (((1-s_tail7)*v_tail) + ...
    (s_tail7*v_tg))./((1-s_tail7)*apm_l7);
```

```
thick_tail6 = (((1-s_tail6)*v_tail) + ...
    (s_tail6*v_tg))./((1-s_tail6)*apm_l6);
thick_head6 = (((1-s_head6)*v_head) + ...
    (s_head6*v_tg))./((1-s_head6)*apm_l6);
thick_head5 = (((1-s_head5)*v_head) + ...
    (s_head5*v_tg))./((1-s_head5)*apm_l5);
thick_tail5 = (((1-s_tail5)*v_tail) + ...
    (s_tail5*v_tg))./((1-s_tail5)*apm_l5);
thick_tail4 = (((1-s_tail4)*v_tail) + ...
    (s_tail4*v_tg))./((1-s_tail4)*apm_l4);
thick_head4 = (((1-s_head4)*v_head) + ...
    (s_head4*v_tg))./((1-s_head4)*apm_l4);
thick_head3 = (((1-s_head3)*v_head) + ...
    (s_head3*v_tg))./((1-s_head3)*apm_l3);
thick_tail3 = (((1-s_tail3)*v_tail) + ...
    (s_tail3*v_tg))./((1-s_tail3)*apm_l3);
thick_tail2 = (((1-s_tail2)*v_tail) + ...
    (s_tail2*v_tg))./((1-s_tail2)*apm_l2);
thick_head2 = (((1-s_head2)*v_head) + ...
    (s_head2*v_tg))./((1-s_head2)*apm_l2);
thick_head1 = (((1-s_head1)*v_head) + ...
    (s_head1*v_tg))./((1-s_head1)*apm_l1);
thick_tail1 = (((1-s_tail1)*v_tail) + ...
    (s_tail1*v_tg))./((1-s_tail1)*apm_l1);

%SLD of various head-tail layers
SLD_head7 = (s_head7*SLD_tg) + ((1-s_head7)*SLD_head);
SLD_tail7 = (s_tail7*SLD_tg) + ((1-s_tail7)*SLD_tail);
SLD_tail6 = (s_tail6*SLD_tg) + ((1-s_tail6)*SLD_tail);
SLD_head6 = (s_head6*SLD_tg) + ((1-s_head6)*SLD_head);
SLD_head5 = (s_head5*SLD_tg) + ((1-s_head5)*SLD_head);
SLD_tail5 = (s_tail5*SLD_tg) + ((1-s_tail5)*SLD_tail);
SLD_tail4 = (s_tail4*SLD_tg) + ((1-s_tail4)*SLD_tail);
SLD_head4 = (s_head4*SLD_tg) + ((1-s_head4)*SLD_head);
SLD_head3 = (s_head3*SLD_tg) + ((1-s_head3)*SLD_head);
SLD_tail3 = (s_tail3*SLD_tg) + ((1-s_tail3)*SLD_tail);
SLD_tail2 = (s_tail2*SLD_tg) + ((1-s_tail2)*SLD_tail);
SLD_head2 = (s_head2*SLD_tg) + ((1-s_head2)*SLD_head);
SLD_head1 = (s_head1*SLD_tg) + ((1-s_head1)*SLD_head);
SLD_tail1 = (s_tail1*SLD_tg) + ((1-s_tail1)*SLD_tail);

%Interfaces
I_tg = thick_tg;
I_tail1 = I_tg + thick_tail1;
I_head1 = I_tail1 + thick_head1;
```

```
106 I_head2 = I_head1 + thick_head2;
107 I_tail2 = I_head2 + thick_tail2;
108 I_tail3 = I_tail2 + thick_tail3;
109 I_head3 = I_tail3 + thick_head3;
110 I_head4 = I_head3 + thick_head4;
111 I_tail4 = I_head4 + thick_tail4;
112 I_tail5 = I_tail4 + thick_tail5;
113 I_head5 = I_tail5 + thick_head5;
114 I_head6 = I_head5 + thick_head6;
115 I_tail6 = I_head6 + thick_tail6;
116 I_tail7 = I_tail6 + thick_tail7;
117 I_head7 = I_tail7 + thick_head7;
118 I_suc = I_head7 + thick_suc;
119 I_siox = I_suc + thick_siox;
120
121 %%
122 %oil
123 vf_tg = @(x) (1-erf((x-I_tg)./sig_tg))/2;
124 Poil = @(x) SLD_tg.*vf_tg(x);
125 %Lecithin layer 1 - tail
126 vf_tail1 = @(x) ...
       (erf((x-I_tg)./sig_tg)-erf((x-I_tail1)./sig_tail1))/2;
127 Ptail1 = @(x) SLD_tail1.*vf_tail1(x);
128 %Lecithin layer 1 - head
129 vf_head1 = @(x) ...
       (erf((x-I_tail1)./sig_tail1)-erf((x-I_head1)./sig_head1))/2;
130 Phead1 = @(x) SLD_head1.*vf_head1(x);
131 %Lecithin layer 2 - head
132 vf_head2 = @(x) ...
       (erf((x-I_head1)./sig_head1)-erf((x-I_head2)./sig_head2))/2;
133 Phead2 = @(x) SLD_head2.*vf_head2(x);
134 %Lecithin layer 2 - tail
135 vf_tail2 = @(x) ...
       (erf((x-I_head2)./sig_head2)-erf((x-I_tail2)./sig_tail2))/2;
136 Ptail2 = @(x) SLD_tail2.*vf_tail2(x);
137 %Lecithin layer 3 - tail
138 vf_tail3 = @(x) ...
       (erf((x-I_tail2)./sig_tail2)-erf((x-I_tail3)./sig_tail3))/2;
139 Ptail3 = @(x) SLD_tail3.*vf_tail3(x);
140 %Lecithin layer 3 - head
141 vf_head3 = @(x) ...
       (erf((x-I_tail3)./sig_tail3)-erf((x-I_head3)./sig_head3))/2;
142 Phead3 = @(x) SLD_head3.*vf_head3(x);
143 %Lecithin layer 4 - head
```

```
144 vf_head4 = @(x) ...
        (erf((x-I_head3)./sig_head3)-erf((x-I_head4)./sig_head4))/2;
145 Phead4 = @(x) SLD_head4.*vf_head4(x);
146 %Lecithin layer 4 - tail
147 vf_tail4 = @(x) ...
        (erf((x-I_head4)./sig_head4)-erf((x-I_tail4)./sig_tail4))/2;
148 Ptail4 = @(x) SLD_tail4.*vf_tail4(x);
149 %Lecithin layer 5 - tail
150 vf_tail5 = @(x) ...
        (erf((x-I_tail4)./sig_tail4)-erf((x-I_tail5)./sig_tail5))/2;
151 Ptail5 = @(x) SLD_tail5.*vf_tail5(x);
152 %Lecithin layer 5 - head
153 vf_head5 = @(x) ...
        (erf((x-I_tail5)./sig_tail5)-erf((x-I_head5)./sig_head5))/2;
154 Phead5 = @(x) SLD_head5.*vf_head5(x);
155 %Lecithin layer 6 - head
156 vf_head6 = @(x) ...
        (erf((x-I_head5)./sig_head5)-erf((x-I_head6)./sig_head6))/2;
157 Phead6 = @(x) SLD_head6.*vf_head6(x);
158 %Lecithin layer 6 - tail
159 vf_tail6 = @(x) ...
        (erf((x-I_head6)./sig_head6)-erf((x-I_tail6)./sig_tail6))/2;
160 Ptail6 = @(x) SLD_tail6.*vf_tail6(x);
161 %Lecithin layer 7 - tail
162 vf_tail7 = @(x) ...
        (erf((x-I_tail6)./sig_tail6)-erf((x-I_tail7)./sig_tail7))/2;
163 Ptail7 = @(x) SLD_tail7.*vf_tail7(x);
164 %Lecithin layer 7 - head
165 vf_head7 = @(x) ...
        (erf((x-I_tail7)./sig_tail7)-erf((x-I_head7)./sig_head7))/2;
166 Phead7 = @(x) SLD_head7.*vf_head7(x);
167 %sucrose
168 vf_suc = @(x) ...
        (erf((x-I_head7)./sig_head7)-erf((x-I_suc)./sig_suc))/2;
169 Psuc = @(x) SLD_suc.*vf_suc(x);
170 %SiOx
171 vf_siox =@(x) ...
        (erf((x-I_suc)./sig_suc)-erf((x-I_siox)./sig_siox))./2;
172 Psiox = @(x) SLD_siox.*vf_siox(x);
173 %Si
174 vf_si = @(x) (erf((x-I_siox)./sig_siox)+1)./2;
175 Psi = @(x) SLD_si.*vf_si(x);
176
177 %total volume fraction of heads and tails in lecithin layer
178 vf_htotal = vf_h7+vf_h6+vf_h5+vf_h4+vf_h3+vf_h2+vf_h1;
```

```
179 vf_ttotal = vf_t7+vf_t6+vf_t5+vf_t4+vf_t3+vf_t2+vf_t1;
180
181 vf_tgf = @(x) 1-(vf_si(x)+vf_siox(x)+vf_suc(x)+vf_htotal+vf_ttotal);
182
183 vf_sum = @(x) ...
      vf_si(x)+vf_siox(x)+vf_suc(x)+vf_head7(x)+vf_tail7(x)...
184       +vf_head6(x)+vf_tail6(x)+vf_head5(x)+vf_tail5(x)+...
185       vf_head4(x)+vf_tail4(x)+vf_head3(x)+vf_tail3(x)+...
186       vf_head2(x)+vf_tail2(x)+vf_head1(x)+vf_tail1(x)+vf_tg(x);
187 Psum = @(x) ...
      Poil(x)+Ptail1(x)+Phead1(x)+Phead2(x)+Ptail2(x)+Ptail3(x)...
188       +Phead3(x)+Phead4(x)+Ptail4(x)+Ptail5(x)+Phead5(x)+
189       Phead6(x)+Ptail6(x)+Ptail7(x)+Phead7(x)+Psuc(x)+Psiox(x)+Psi(x);
190
191 %% Plot SLD and volume fractions
192 close all; % closes any open figures
193 figure();
194 plot(x,Psum(x),'r');
195 figure();
196 plot(x,Psi(x),'g',x,Psiox(x),'c',x,Psuc(x),'r',x,Poil(x),'g',...
197     x,Ptail1(x),'b',x,Phead1(x),'c',x,Phead2(x),'g',x,Ptail2(x),'r',...
198     x,Ptail3(x),'b',x,Phead3(x),'c',x,Phead4(x),'g',x,Ptail4(x),'r',...
199     x,Ptail5(x),'b',x,Phead5(x),'c',x,Phead6(x),'g',x,Ptail6(x),'r',...
200     x,Ptail7(x),'b',x,Phead7(x),'c');
201 figure();
202 plot(x,vf_tg(x),'g',x,vf_tail1(x),'b',x,vf_head1(x),'r',x,vf_head2(x),...
203 '   b',x,vf_tail2(x),'r',x,vf_tail3(x),'b',x,vf_head3(x),'r',...
204     x,vf_head4(x),'b',x,vf_tail4(x),'r',x,vf_tail5(x),'b',...
205     x,vf_head5(x),'r',x,vf_head6(x),'b',x,vf_tail6(x),'r',...
206     x,vf_tail7(x),'b',x,vf_head7(x),'r');
207 % figure()
208 plot(x,vf_htotal,'r',x,vf_ttotal,'b',x,vf_tgf(x),'g')
209
210 %% Output
211 Psum = Psum(x);
212 output = [x' Psum'];
```

Appendix E

PGPR At Sucrose/Triglyceride Oil Interface: MATLAB Code for the SLD Profile

The MATLAB code written to fit neutron reflectivity data measured for PGPR thin films at the sucrose/triglyceride oil interface using the spline model discussed in Section 7.4.2.

E.1 MATLAB Code for the Neutron SLD Profile

This section details the MATLAB code to calculate the SLD profile for the neutron through the silicon block, followed by the silicon oxide layer, sucrose layer, the polymeric surfactant and finally the bulk triglyceride oil phase.

```
1 %% Function to calculate the NR SLD profile for polymer layer ...
    using splines
2 function [output] = SLD_polymer_NR(params, bulk_in, bulk_out, ...
    contrast)
3 %% Model Parameters
4
5 % Si
6 SLD_si = bulk_in(contrast);
7
8 % SiOx
```

```
sig_siox = params(1);                %Width of Si/SiOx interface
SLD_siox = params(2);
thick_siox = params(3);

% Sucrose
sig_suc = params(4);                 %Width of SiOx/Suc interface
SLD_suc = params(5);
thick_suc = params(6);

% polymer
sig_polymer = params(7);             %Width of Suc/polymer interface
thick_polymer = params(8);           %thickness of polymer layer
sig_tg = params(9);                  %Width of polymer/TG interface
n_points = length(params)-9;
polymer_column = params(10:end);
polymer_column = polymer_column(:);

%oil
SLD_tg = bulk_out(contrast);

%% Dependent parameters
% Define the interfaces
I_siox = 100;                        %Si/SiOx Interface
I_suc = I_siox + thick_siox;         %SiOx/Suc Interface
I_polymer = I_suc + thick_suc;       %Suc/Polymer Interface
I_tg = I_polymer + thick_polymer;    %Polymer/triglyceride interface

%% SLD funcions

%Si
vf_si = @(x) (1-erf((x-I_siox)./sig_siox))./2;
Psi = @(x) SLD_si.*vf_si(x);
%SiOx
vf_siox =@(x) ...
    (erf((x-I_siox)./sig_siox)-erf((x-I_suc)./sig_suc))./2;
Psiox = @(x) SLD_siox.*vf_siox(x);
%Sucrose
vf_suc = @(x) ...
    (erf((x-I_suc)./sig_suc)-erf((x-I_polymer)./sig_polymer))./2;
Psuc = @(x) SLD_suc.*vf_suc(x);
%polymer
Ppolymer = @(x) ...
   PpolymerNR((x-I_polymer),thick_polymer,polymer_column,n_points,..
               SLD_suc,SLD_tg)+ ...
                   SLD_suc.*(erf((x-I_polymer)./sig_polymer)-1)./2 ...
```

```
                    ...
                + SLD_tg.*(-1-erf((x-I_tg)./sig_tg))./2;
vf_tg = @(x) (erf((x-I_tg)./sig_tg)+1)./2;
Poil = @(x) SLD_tg.*vf_tg(x);
%Sum of all layers
Psum = @(x)  Psi(x) + Psiox(x) + Psuc(x) + Ppolymer(x)+Poil(x);

x = -100:1:(thick_siox+thick_suc+thick_polymer)+500;

%% Plot SLD
close all; % closes any open figures
figure();
plot(x,vf_tg(x),'m',x, ...
    vf_suc(x),'r',x,vf_siox(x),'b',x,vf_si(x),'c');
figure();
plot(x,Poil(x),'m',x,Ppolymer(x),'g', ...
    x,Psuc(x),'r',x,Psiox(x),'b',x,Psi(x),'c');
figure();
plot(x,Psum(x),'r');

%%Save polymer layer SLD to convert to volume fraction

assignin('base', 'SLD1',Ppolymer(x));
assignin('base', 'xws1',x);
assignin('base', 'SLD_oil1',Poil(x));
assignin('base', 'Polymer_Interface1',I_polymer)
assignin('base', 'SLD_total1',Psum(x));

%% Output
Psum = Psum(x);
output = [x' Psum'];
```

```
%% Function to calculate the splines for the polymer NR SLD profile
function sld = PpolymerNR(x,thick_polymer,polymer_column, ...
    n_points, SLD_suc,SLD_tg)
     step = thick_polymer/(n_points+1);
     x1 = [0:step:thick_polymer]';
     polymer_y=[SLD_suc ; polymer_column ; SLD_tg];
     f3 = @(x,y,xx) spline(x,y,xx);
     sld(x≥0 & x≤thick_polymer)= f3(x1,polymer_y,x(x≥0 & ...
        x≤thick_polymer));
     sld(x≤0)= SLD_suc;
     sld(x≥thick_polymer)= SLD_tg;
end
```

E.2 MATLAB Code for the X-Ray SLD Profile

This section details the MATLAB code to calculate the SLD profile for the x-rays incident from the bulk triglyceride oil phase, followed by the polymeric surfactant layer, sucrose layer, silicon oxide layer and finally the silicon block.

```
%% Function to calculate the XRR SLD profile for polymer layer ...
    using splines
function [output] = SLD_polymer_XRR(params, bulk_in, bulk_out, ...
    contrast)
%% Model Parameters

% Si
SLD_si = bulk_out(contrast);

% SiOx
sig_siox = params(1);               %Width of Si/SiOx interface
SLD_siox = params(2);
thick_siox = params(3);

% Sucrose
sig_suc = params(4);                %Width of SiOx/Suc interface
SLD_suc = params(5);
thick_suc = params(6);

% polymer
sig_polymer = params(7);            %Width of Suc/polymer interface
thick_polymer = params(8);          %thickness of polymer layer
sig_tg = params(9);
n_points = length(params)-9;
polymer_column = params(10:end);
polymer_column = polymer_column(:);

%oil
SLD_tg = bulk_in(contrast);

%% Dependent parameters
% Define the interfaces
I_tg = 100;                                 %TG/Polymer interface
I_polymer = I_tg + thick_polymer;           %Polymer/Sucrose interface
I_suc = I_polymer + thick_suc;              %Sucrose/SiOx Interface
I_siox = I_suc + thick_siox;                %SiOx/Si Interface

```

```
36
37 %% SLD funcions
38
39 %Si
40 vf_si =@(x) (1-erf(-(x-I_siox)./sig_siox))./2;
41 Psi = @(x) SLD_si.*vf_si(x);
42 %SiOx
43 vf_siox =@(x) ...
       (erf((x-I_suc)./sig_suc)+erf(-(x-I_siox)./sig_siox))/2;
44 Psiox = @(x) SLD_siox.*vf_siox(x);
45 %Sucrose
46 vf_suc = @(x) ...
       (erf((x-I_polymer)./sig_polymer)+erf(-(x-I_suc)./sig_suc))/2;
47 Psuc = @(x) SLD_suc.*vf_suc(x);
48 %Polymer
49 Ppolymer = @(x) ...
       PpolymerXRR((x-I_tg),thick_polymer,polymer_column,n_points,...
50             SLD_suc,SLD_tg) + ...
                  SLD_suc.*(-1-erf((x-I_polymer)./sig_polymer))./2 ...
51             + SLD_tg.*(-1+erf((x-I_tg)./sig_tg))./2;
52 vf_tg = @(x) (1-erf((x-I_tg)./sig_tg))/2;
53 Poil = @(x) SLD_tg.*vf_tg(x);
54 %Sum of all layers
55 Psum = @(x)  Psi(x) + Psiox(x) + Psuc(x) + Ppolymer(x)+Poil(x);
56
57 x = -100:1:(thick_siox+thick_suc+thick_polymer)+500;
58
59 %% Plot SLD
60 close all; % closes any open figures
61 figure();
62 plot(x,vf_tg(x),'m',x, ...
       vf_suc(x),'r',x,vf_siox(x),'b',x,vf_si(x),'c');
63 figure();
64 plot(x,Poil(x),'m',x,Ppolymer(x),'g', ...
       x,Psuc(x),'r',x,Psiox(x),'b',x,Psi(x),'c');
65 figure();
66 plot(x,Psum(x),'r');
67
68 %%Save polymer layer SLD to convert to volume fraction
69
70 assignin('base', 'SLD1',Ppolymer(x));
71 assignin('base', 'xws1',x);
72 assignin('base', 'SLD_oil1',Poil(x));
73 assignin('base', 'Polymer_Interface1',I_polymer)
74 assignin('base', 'SLD_total1',Psum(x));
```

```
75
76 %% Output
77 Psum = Psum(x);
78 output = [x' Psum'];
79
80 %%
81 Psum = Psum(x);
82 [output] = [x', Psum'];
```

```
1  %% Function to calculate the splines for the polymer XRR SLD profile
2  function sld = PpolymerXRR(x,thick_polymer,polymer_column, ...
       n_points, SLD_suc,SLD_tg)
3      step = thick_polymer/(n_points+1);
4      x1 = [0:step:thick_polymer]';
5      polymer_y=[SLD_tg ; polymer_column ; SLD_suc];
6      f3 = @(x,y,xx) spline(x,y,xx);
7      sld(x≥0 & x≤thick_polymer)= f3(x1,polymer_y,x(x≥0 & ...
           x≤thick_polymer));
8      sld(x≤0)= SLD_tg;
9      sld(x≥thick_polymer)= SLD_suc;
10 end
```

Bibliography

[1] R. Pynn. Neutron scatteringa non-destructive microscope for seeing inside matter. In L. Liyuan, R. Rinaldi, and H. Schober, editors, *Introduction to Neutron Scattering*. Springer.

[2] A. K. Ganguli, A. Ganguly, and S. Vaidya. Microemulsion-based synthesis of nanocrystalline materials. *Chem. Soc. Rev.*, 39:474–485, 2010.

[3] A. J. Jackson. Introduction to Small-Angle Neutron Scattering and Neutron Reflectometry. Technical report, NIST Center for Neutron Research.

[4] R. Andersson, L. F. van Heijkamp, I. M. de Schepper, and W. G. Bouwman. Analysis of spin-echo small-angle neutron scatteringmeasurements. *Journal of Applied Crystallography*, 41:868–885, 2008.

[5] A. Orfanakis, E. Hatzakis, K. Kanaki, S. A. Pergantis, A. Rizos, and P. Dais. Characterization of Polyglycerol Polyricinoleate Formulations Using NMR Spectroscopy, Mass Spectrometry and Dynamic Light Scattering. *Journal of the American Oil Chemists' Society*, 90:39–51, 2012.

[6] R. A. L. Jones. *Soft Condensed Matter*. Oxford University Press, 2002.

[7] W. A. Ducker, E .P. Luther, D. R. Clarke, and F. F. Lange. Effect of Zwitterionic Surfactants on InerParticle Force, Rheology, and Particle Packing of Silicon Nitride Slurries. *J. Am. Ceram. Soc.*, 80:575–583, 1997.

[8] F. C. Vernier. *Influence of Emulsifiers on the rheology of chocolate and suspensions of cocoa or sugar particles in oil*. PhD thesis, University of Reading, 1997.

[9] B. Schantz and H. Rohm. Influence of lecithin-PGPR blends on the rheological properties of chocolate. *LWT Food Science and Technology*, 38:41–45, 2004.

[10] E. Blanco, G. L. Hunter, M. Hermes, P. M. Chaikin, and W. C. K. Poon. Particle Dispersion Project - Annual Report 2014. Technical report, School of Physics and Astronomy, University of Edinburgh and Centre for Soft Matter Research, Department of Physics, New York University., 2014.

[11] G. L. Squires. *Introduction to the Theory of Thermal Neutron Scattering.* Cambridge University Press, third edition.. edition, 2012.

[12] J. S. Higgins and H. C. Benoit. *Polymers and Neutron Scattering.* Oxford Science Publications, 1997.

[13] J. Li, P. Rong, and Q. Huang. Characterization of food materials in multiple length scales using small-angle x-ray scattering and nuclear magnetic resonance: principle and applications. In Qingrong Huang, editor, *Nanotechnology in the Food, Beverage and Nutraceutical Industries*, chapter 6, pages 149 – 176. Woodhead Publishing, 2012.

[14] R. Johnson. *Structure and Dynamics: X-ray Diffraction.* University of Oxford, 2011.

[15] V. F. Sears. Neutron scattering lengths and cross sections. *Neutron News*, 3(3):26–37, 1992.

[16] B. T. M. Willis and C. J. Carlile. *Experimental Neutron Scattering.* Oxford University Press, 2009.

[17] Diamond Light Source. URL `https://en.wikipedia.org/wiki/Diamond_Light_Source`.

[18] Rigaku SmartLab X-ray Diffractometer. URL `https://rigaku.com/en/products/xrd/smartlab`.

[19] XENOCS Nano inXider SAXS/WAXS system. URL `http://www.xenocs.com/en/solutions/nano-inxider-saxs-made-easy/`.

[20] R. J. Hunter. *Foundation of Colloidal Science.* Oxford University Press, 1986.

[21] D. H. Everett. *Basic principles of colloidal science* . Cambridge:Royal Society of Chemistry, 1988.

[22] M. Wyart and M. E. Cates. Discontinuous Shear Thickening without Inertia in Dense Non-Brownian Suspensions. *Phys. Rev. Lett.*, 112:098302, 2014.

[23] F. Boyer, E. Guazzelli, and O. Pouliquen. Unifying Suspension and Granular Rheology. *Phys. Rev. Lett.*, 107:188301, 2011.

[24] E. Brown, N. A. Forman, C. S. Orellana, H. Zhang, B. W. Maynor, D. E. Betts, J. M. DeSimone, and H. M. Jaeger. Generality of shear thickening in dense suspensions. *Nature Materials*, 9:220224, 2010.

[25] B. M. Guy, J. A. Richards, D. J. M. Hodgson, E. Blanco, and W. C. K. Poon. A constraint-based approach to granular dispersion rheology. *arXiv:1807.11356*, 2018.

[26] M. A. Rao. Flow and Functional Models for Rheological Properties of Fluid Foods.

[27] K. N. Pham, G. Petekidis, D. Vlassopoulos, S. U. Egelhaaf, W. C. K. Poon, and P. N. Pusey. Yielding behavior of repulsion- and attraction-dominated colloidal glasses. *Journal of Rheology*, 52(2):649–676, 2008.

[28] D. Hugelshofer. *Structural and Rheological Properties of Concentrated Suspensions and Emulsions.* PhD thesis, Swiss Federal Institute of Technology, Zurich, 2000.

[29] G. Arnold, S. Schuldt, Y. Schneider, J. Friedrichs, F. Babick, C. Werner, and H. Rohm. The impact of lecithin on rheology, sedimentation and particle interactions in oil-based dispersions. *Colloids and Surfaces A: Physicochem. Eng. Aspects*, 418:147–156, 2013.

[30] E. Blanco, G. L. Hunter, P. M. Chaikin, and W. C. K. Poon. Particle Dispersion Project - Annual Report 2013. Technical report, School of Physics and Astronomy, University of Edinburgh and Centre for Soft Matter Research, Department of Physics, New York University., 2013.

[31] G. Talbot. Chocolate and cocoa butter - structure and composition. In N. Garti and N. R. Widlak, editors, *Cocoa Butter and Related Compounds*, chapter 1, pages 1–33. AOCS Press, 2012.

[32] L. D. A. Chumpitaz, L. F. Coutinho, and A. J. A. Meirelles. Surface tension of fatty acids and triglycerides. *Journal of Oil & Fat Industries*, 76:379–382, 1999.

[33] E. J. Alameda, V. B. Rodrguez, G. Luzon, M. Fernndez-Serrano, M. Garcia-Roman, D. Vaz, and J. M. Vicaria. Hard-surface cleaning using lipases: Enzymesurfactant interactions and washing tests. *Journal of Surfactants and Detergents*, 10:61–70, 2007.

[34] M. A. Mitsche, L. Wang, and D. M. Small. Adsorption of egg phosphatidylcholine to an air/water and triolein/water bubble interface: Use of the 2-dimensional phase rule to estimate the surface composition of a phospholipid/triolein/water surface as a function of surface pressure. *The Journal of Physical Chemistry B*, 114(9):3276–3284, 2010.

[35] M. Greiner, B. Sonnleitner, M. Mailnder, and H. Briesen. Modeling complex and multi-component food systems in molecular dynamics simulations on the example of chocolate conching. *Food Funct.*, 5:235–242, 2014.

[36] E. Elts M. Kindlein, M. Greiner and H. Briesen. Interactions between phospholipid head groups and a sucrose crystal surface at the cocoa butter interface. *Journal of Physics D: Applied Physics*, 48:384002, 2015.

[37] M. Jerkins, M. Schrter, H. L. Swinney, T. J. Senden, M. Saadatfar, and T. Aste. Onset of mechanical stability in random packings of frictional spheres. *Phys. Rev. Lett.*, 101:018301, 2008.

[38] C. Song, P. Wang, and H. A. Makse. A phase diagram for jammed matter. *Nature*, 453:629632, 2008.

[39] L. E. Silbert. Jamming of frictional spheres and random loose packing. *Soft Matter*, 6:29182924, 2010.

[40] R. Mari and R. Seto. Shear thickening, frictionless and frictional rheologies in non-Brownian suspensions. *Journal of Rheology*, 58:16931724, 2014.

[41] J. Chevalley. Chocolate flow properties. In S. T. Beckett, editor, *Industrial chocolate manufacture and use*. Oxford: Wiley-Blackwell, Oxford, 1999.

[42] S. T. Beckett. Chocolate flow properties. In S. T. Beckett, editor, *Industrial chocolate manufacture and use*. Oxford: Wiley-Blackwell, Oxford, 2009.

[43] T. L. Harris. Surface active lipids in chocolate. *SCI Monograph*, 32:108–122, 1968.

[44] S. I Sugiura, S. Ichikawa, Y. Sano, M. Nakajima, X. Q. Liu, M. Seki, and S. Furusaki. Formation and Characterization of Reversed Micelles Composed of Phospholipids and Fatty Acids. *Journal of Colloid and Interface Science*, 240:566–572, 2001.

[45] P. Rousset, P. Sellappan, and P.. Daoud. Effect of emulsifiers on surface properties of sucrose by inverse gas chromatography. *Journal of Chromatography A*, 969:97–101, 2002.

[46] K. Hashizaki, Y. Sakanishi, S. Yako, H. Tsusaka, M. Imai, H. Taguchi, and Y. Saito. New lecithin organogels from lecithin/polyglycerol/oil systems. *J. Oleo Sci.*, 61:267–275, 2012.

[47] D. I. Svergun, M. H. Koch, P. A. Timmins, and R. P. May. *Small angle X-ray and neutron scattering from solutions of biological macromolecules*, volume 19.

[48] S. King, C. Washington, D. Attwood, C. Booth, S. Mai, Y. W. Yang, and T. Cosgrove. Polymer bristles: a SANS study. *Journal of Applied Crystallography*, 33:664–668, 2000.

[49] A. Guinier and G. Fournet. *Small-angle scattering of X-rays*. Structure of matter series. Wiley, 1955.

[50] I. Livsey. Neutron scattering from concentric cylinders. intraparticle interference function and radius of gyration. *J. Chem. Soc. Faraday Trans. 2*, 83:1445–1452, 1987.

[51] NCNR SANS & USANS Data Reduction and Analysis. URL `https://ncnr.nist.gov/programs/sans/data/red_anal.html`.

[52] Igor Pro 6.3 by Wavemetrics. URL `https://www.wavemetrics.com/order/order_igordownloads6.htm`.

[53] SasView for Small Angle Scattering Analysis. URL `http://sasview.org`.

[54] G. Porod. General theory. In V Glatter and O. Kratky, editors, *Small Angle X-Ray Scattering*. Academic Press, New York.

[55] R. Subramanian, S. Ichikawa, M. Nakajima, T. Kimura, and T. Maekawa. Characterization of phospholipid reverse micelles in relation to membrane processing of vegetable oils. *Eur. J. Lipid Sci. Technol.*, 103:93–97, 2001.

[56] K. Kittipongpittaya, A. Panya, D. J. McClements, and E. A. Decker. Impact of free fatty acids and phospholipids on reverse micelles formation and lipid oxidation in bulk oil. *J. Am. Oil Chem. Soc.*, 91:453–462, 2014.

[57] S. Manjula, I. Kobayashi, and R. Subramanian. Characterization of phospholipid reverse micelles in nonaqueous systems in relation to their rejection during membrane processing. *Food Research International*, 44(4): 925 – 930, 2011.

[58] J. N. Israelachvili. *Intermolecular and Surface Forces*. Academic Press, 2011.

[59] J. Jouhet. Importance of the hexagonal lipid phase in biological membrane organization. *Frontiers in Plant Science*, 4:494, 2013.

[60] R. Nagarajan. Molecular packing parameter and surfactant self-assembly: the neglected role of the surfactant tail. *Langmuir*, 18(1):31–38, 2002.

[61] J. M. Seddon. Structure of the inverted hexagonal (hii) phase, and non-lamellar phase transitions of lipids. *Biochimica et Biophysica Acta (BBA) - Reviews on Biomembranes*, 1031(1):1 – 69, 1990.

[62] S. H. Tung, Y. E. Huang, and S. R. Raghavan. A New Reverse Wormlike Micellar System: Mixtures of Bile Salt and Lecithin in Organic Liquids. *J. Am. Chem. Soc.*, 128:5751–5756, 2006.

[63] J. L. Bradley-Shaw, P. J. Camp, P. J. Dowding, and K. Lewtas. Glycerol Monooleate Reverse Micelles in Nonpolar Solvents: Computer Simulations and Small-Angle Neutron Scattering. *The Journal of Physical Chemistry B*, 119:4321–4331, 2015.

[64] L. K. Shrestha, M. Yamamoto, S. Arima, and K. Aramaki. Charge-free reverse wormlike micelles in nonaqueous media. *Langmuir*, 27:2340–2348, 2011.

[65] R. W. Corkery, D. Rousseau, P. Smith, D. A. Pink, and C. B. Hanna. A case for discotic liquid crystals in molten triglycerides. *Langmuir*, 23(13): 7241–7246, 2007.

[66] D. A. Pink, C. B. Hanna, C. Sandt, A. J. Macdonald, R. Maceachern, R. Corkery, and D. Rousseau. Modeling the solid-liquid phase transition in saturated triglycerides. *The Journal of Chemical Physics*, 132(5):054502 1–11, 2010.

[67] C. Tanford. Micelle shape and size. *The Journal of Physical Chemistry*, 76 (21):3020–3024, 1972.

[68] 3-D structure of Oleic Acid. URL `https://pubchem.ncbi.nlm.nih.gov/compound/oleic_acid`.

[69] F.P. Bowden and D. Tabor. *The Friction and Lubrication of Solids*. Clarendon Press, 2001.

[70] J. Klein, E. Kumacheva, D. Mahalu, D. Perahla, and L. J. Fetters. Reduction of frictional forced between solid surfaces bearing polymer brushes. *Nature*, 370:634636, 1994.

[71] D. Middendorf, A. Juadjur, U. Bindrich, and P. Mischnick. AFM approach to study the function of PGPR's emulsifying properties in cocoa butter based suspensions. *Food Structure*, pages 1–11, 2014.

[72] A. Dedinaite and B. Campbel. Interactions between mica surfaces across triglyceride solution containing phospholipid and polyglycerol polyricinoleate. *Langmuir*, 16:2248–2253, 2000.

[73] J. H. J. Thijssen, A. B. Schofield, and P. S. Clegg. How do (fluorescent) surfactants affect particle-stabilized emulsions? *Soft Matter*, 7(18):7965–7968, 9 2011. ISSN 1744-683X. doi: 10.1039/c1sm05968h.

[74] S. King, P. Griffiths, J. Hone, and T. Cosgrove. SANS from Adsorbed Polymer Layers. *Macromolecular Symposia*, 190(1):33–42, 2002.

[75] G. Beaucage. Approximations Leading to a Unified Exponential/Power-Law Approach to Small-Angle Scattering. *Journal of Applied Crystallography*, 28:717–728, 1995.

[76] G. Beaucage. Small-Angle Scattering from Polymeric Mass Fractals of Arbitrary Mass-Fractal Dimension. *Journal of Applied Crystallography*, 29: 134–146, 1996.

[77] Irena package for analysis of small-angle scattering data. URL `https://usaxs.xray.aps.anl.gov/software/irena`.

[78] P. W. Schmidt. Small-Angle Scattering Studies of Disordered, Porous and Fractal Systems. *Journal of Applied Crystallography*, 24:414–435, 1991.

[79] W. G. Bouwman, J. Plomp, V. O. de Haan, W. H. Kraan, A. A. van Well, K. Habicht, T. Keller, and M. T. Rekveldt. Real-space neutron scattering methods. *Nuclear Instruments and Methods in Physics Research A*, 586: 9–14, 2008.

[80] C. Rehm, J. Barker, W. G. Bouwman, and R. Pynn. DCD USANS and SESANS: a comparison of two neutron scattering techniques applicable for the study of large-scale structures. *Journal of Applied Crystallography*, 46: 354–364, 2013.

[81] E. G. Iashina, E. V. Velichko, M. V. Filatov, W. G. Bouwman, C. P. Duif, A. Brulet, and S. V. Grigoriev. Additive scaling law for structural organization of chromatin in chicken erythrocyte nuclei. *Phys. Rev. E*, 96: 012411, 2017.

[82] C. Fidkowski, M. R. Kaazempur-Mofrad, J. Borenstein, J. P. Vacanti, R. Langer, and Y. Wang. Endothelialized microvasculature based on a biodegradable elastomer. *Tissue Engg.*, 11(1-2):302–309, 2005.

[83] L. E. Scriven. Physics and applications of dip coating and spin coating. *MRS Proceedings*, 121:717, 1988. doi: 10.1557/PROC-121-717.

[84] R. R. L. De Oliveira, D. A. C. Albuquerque, T. G. S. Cruz, F. Yamaji, and F. Leite. *Measurement of the Nanoscale Roughness by Atomic Force Microscopy: Basic Principles and Applications*, pages 147–174. INTECH Open Access Publisher, 2012, London, 2012.

[85] J. Daillant and A. Gibaud. *X-ray and Neutron Reflectivity: Principles and Applications*. Springer, 2009.

[86] W. H. King. Piezoelectric sorption detector. *Analytical Chemistry*, 36(9): 1735–1739, 1964.

[87] QSense E4, Biolin Scientific, . URL `https://www.biolinscientific.com/qsense/instruments/qsense-analyzer`.

[88] G. Sauerbrey. Use of quartz crystals for weighing thin layers and for weighing. *GZ Physics*, 155:206–222, 1959.

[89] D. Sands. *Introduction to crystallography*. Dover classics of science and mathematics. Dover, New York, 1993.

[90] D. K. Sarkar, S. Bera, S.V. Narasimhan, S. Chowdhury, A. Gupta, and K. G. M. Nair. Gixrd and xps investigation of silicidation in ion beam mixed cusi(1 1 1) system. *Solid State Communications*, 107(8):413 – 416, 1998.

[91] C. A. Beevers, T. R. R. Mcdonald, J. H. Robertson, and F. Stern. The crystal structure of sucrose. *Acta Crystallographica*, 5(5):689–690, 1952.

[92] L.A. Girifalco and R.J. Good. A theory for the estimation of surface and interfacial energies. i. derivation and application to interfacial tension. *Journal of Physical Chemistry*, 61(7):904–909, 1957.

[93] Drop Shape Analysis, KRUSS. URL `https://www.kruss-scientific.com/services/education-theory/glossary/drop-shape-analysis/`.

[94] W. van Nieuwenhuyzen. 9 - production and utilization of natural phospholipids. In M. U. Ahmad and X. Xu, editors, *Polar Lipids*, pages 245 – 276. Elsevier, 2015.

[95] D. Johannsmann. Viscoelastic, mechanical, and dielectric measurements on complex samples with the quartz crystal microbalance. *Phys. Chem. Chem. Phys.*, 10:4516–4534, 2008.

[96] M. Rodahl, F. Hook, and B. Kasemo. Qcm operation in liquids: an explanation of measured variations in frequency and q factor with liquid conductivity. (quartz crystal microbalance). *Analytical Chemistry*, 68(13): 2219–2227, 1996.

[97] R. K. Roeder. Chapter 3 - mechanical characterization of biomaterials. In A. Bandyopadhyay and S. Bose, editors, *Characterization of Biomaterials*, pages 49 – 104. Academic Press, Oxford, 2013.

[98] M. V. Voinova, M. Rodahl, M. Jonson, and B. Kasemo. Viscoelastic acoustic response of layered polymer films at fluid-solid interfaces: Continuum mechanics approach. *Physica Scripta*, 59(5):391–396, 1999.

[99] Qtools Software, QSense, . URL `https://web.engr.uky.edu/~cense/Student%20Downloads/QCM%20user/Q-Tools%20Quick%20Start%20Guide.pdf`.

[100] A. Savitzky and M. J. E. Golay. Smoothing and differentiation of data by simplified least squares procedures. *Analytical Chemistry*, 36(8):1627–1639, 1964.

[101] J. M. Wang, Q. X. Huang, Z. Y. Jiang, and K. Tieu. The effects of shear stress on the lubrication performances of oil film of large-scale mill bearing. In *Advances in Abrasive Technology XII*, volume 76 of *Advanced Materials Research*, pages 713–718. Trans Tech Publications, 2009.

[102] J. Iruthayaraj, G. Olanya, and P. Claesson. Viscoelastic properties of adsorbed bottle-brush polymer layers studied by quartz crystal microbalance - dissipation measurements. *Journal Of Physical Chemistry C*, 112(38):15028–15036, 2008.

[103] A. Markidou, W. Y. Shih, and W. H. Shih. Soft-materials elastic and shear moduli measurement using piezoelectric cantilevers. *Review of Scientific Instruments*, 76(6), 2005.

[104] S. X. Liu and J. T. Kim. Application of kevinvoigt model in quantifying whey protein adsorption on polyethersulfone using qcm-d. *Journal of the Association for Laboratory Automation*, 14(4):213–220, 2009.

[105] G. H. Fredrickson, A. Ajdari, L. Leibler, and J. P. Carton. Surface modes and deformation energy of a molten polymer brush. *Macromolecules*, 25 (11):2882–2889, 1992.

[106] M. Campana, A. Teichert, R. Clarke, S.and Steitz, J. R. P. Webster, and A. Zarbakhsh. Surfactant adsorption at the metaloil interface. *Langmuir*, 27(10):6085–6090, 2011.

[107] J. Penfold and R. K. Thomas. The application of the specular reflection of neutrons to the study of surfaces and interfaces. *J. Phys. Condens. Matter*, 2:1369–1412, 1990.

[108] M. Moglianetti, J. R. P. Webster, S. Edmondson, S. P. Armes, and S. Titmuss. A neutron reflectivity study of surfactant self-assembly in weak polyelectrolyte brushes at the sapphirewater interface. *Langmuir*, 27(8): 4489–4496, 2011.

[109] L. R. Griffin, K. L. Browning, C. L. Truscott, L. A. Clifton, and S. M. Clarke. Complete bilayer adsorption of c16tab on the surface of mica using neutron reflection. *The Journal of Physical Chemistry B*, 119(21):6457–6461, 2015.

[110] M. L. Goldberger and Frederick Seitz. Theory of the refraction and the diffraction of neutrons by crystals. *Phys. Rev.*, 71:294–310, 1947.

[111] L. Nevot and P Croce. Characterization of surfaces by grazing reflection of x-rays. application to the study of the polishing of some silicate glasses. *Rev. Phys. Appl.*, 15:761–779, 1980.

[112] A.V. Hughes. RasCAL. URL `https://sourceforge.net/projects/rscl/`.

[113] R. S. Armen, O. D. Uitto, and S. E. Feller. Phospholipid component volumes: Determination and application to bilayer structure calculations. *Biophysical Journal*, 75(2):734 – 744, 1998.

[114] M. Born and E. Wolf. *Principles of Optics*. Pergamon Press, Oxford, Fourth edition, 1970.

[115] D. S. Sivia, W. A. Hamilton, and G. S. Smith. *Bayesian Spectral Analysis of Reflectivity Data*, pages 153–159. Springer Netherlands, Dordrecht, 1991.

[116] A. V. Hughes, F. Ciesielski, A. C. Kalli, L. A. Clifton, T. R. Charlton, M. S. P. Sansom, and J. R. P. Webster. On the interpretation of reflectivity data from lipid bilayers in terms of molecular-dynamics models. *Acta Crystallographica Section D*, 72(12):1227–1240, 2016.

[117] T. Saerbeck, R. Cubitt, A. Wildes, G. Manzin, K. H. Andersen, and P. Gutfreund. Recent upgrades of the neutron reflectometer d17 at ill. *Journal of Applied Crystallography*, 51(2):249–256, 2018.

[118] P. Gutfreund, T. Saerbeck, . Gonzalez, M. A, E. Pellegrini, M. Laver, C. Dewhurst, and R. Cubitt. Towards generalized data reduction on a chopperbased timeofflight neutron reflectometer. *Journal of Applied Crystallography*, 51(3):606–615, 2018.

[119] R. Cubitt, T. Saerbeck, R. A. Campbell, R. Barker, and P. Gutfreund. An improved algorithm for reducing reflectometry data involving divergent

beams or nonflat samples. *Journal of Applied Crystallography*, 48(6):2006–2011, 2015.

[120] M. Nosonovsky. Oil as a lubricant in the ancient middle east. *Tribology Online*, 2(2):44–49, 2007.

[121] H. M. Mobarak, E. Niza Mohamad, H. H. Masjuki, M. A. Kalam, K. A. H. Al Mahmud, M. Habibullah, and A. M. Ashraful. The prospects of biolubricants as alternatives in automotive applications. *Renewable and Sustainable Energy Reviews*, 33:34 – 43, 2014.

[122] J. Klein. Hydration lubrication. *Friction*, 1(1):1–23, 2013.

[123] P. M. Claesson, A. Dedinaite, B. Bergensthl, B. Campbell, and H. Christenson. Interactions between hydrophilic mica surfaces in triolein: triolein surface orientation, solvation forces, and capillary condensation. *Langmuir*, 13(6):1682–1688, 1997.

[124] A. Dedinaite, P. M. Claesson, B. Campbell, and H. Mays. Interactions between modified mica surfaces in triglyceride media. *Langmuir*, 14(19): 5546–5554, 1998.

[125] J. Klein and E. Kumacheva. Simple liquids confined to molecularly thin layers. i. confinement-induced liquid-to-solid phase transitions. *The Journal of Chemical Physics*, 108(16):6996–7009, 1998.

[126] E. Kumacheva and J. Klein. Simple liquids confined to molecularly thin layers. ii. shear and frictional behavior of solidified films. *The Journal of Chemical Physics*, 108(16):7010–7022, 1998.

[127] J. L. Courthaudon, E. Dickinson, and W. W. Christie. Competitive adsorption of lecithin and beta-casein in oil in water emulsions. *Journal of agricultural and food chemistry*, (8):1365–1368, 1991.

[128] E. Dickinson and G. Iveson. Adsorbed films of -lactoglobulin + lecithin at the hydrocarbonwater and triglyceridewater interfaces. *Food Hydrocolloids*, 6(6):533–541, 1993.

[129] I. Scherze, A. Knoth, and G. Muschiolik. Effect of emulsification method on the properties of lecithin and pgpr stabilized waterinoil emulsions. *Journal of Dispersion Science and Technology*, 27(4):427–434, 2006.

[130] S. Mun, Y. Choi, S. J. Rho, C. G. Kang, C. H. Park, and Y. R. Kim. Preparation and characterization of water/oil/water emulsions stabilized by polyglycerol polyricinoleate and whey protein isolate. *Journal of Food Science*, 75(2):E116–E125, 2010.

[131] J. J. Nash and K. A. Erk. Stability and interfacial viscoelasticity of oil-water nanoemulsions stabilized by soy lecithin and tween 20 for the encapsulation of bioactive carvacrol. *Colloids and Surfaces A: Physicochemical and Engineering Aspects*, 517:1–11, 2017.

[132] S. Mettu, C. Wu, and R. R. Dagastine. Dynamic forces between emulsified water drops coated with poly-glycerol-poly-ricinoleate (pgpr) in canola oil. *Journal of Colloid And Interface Science*, 517:166–175, 2018.

[133] Y. G. J. Lau, R. M. Richardson, and R. Cubitt. Smectic order induced at homeotropically aligned nematic surfaces: A neutron reflection study. *The Journal of Chemical Physics*, 124(23):234910, 2006.

[134] R. J. L. Welbourn, F. Bartholomew, P. Gutfreund, and S. M. Clarke. Neutron reflectometry of an anionic surfactant at the solidliquid interface under shear. *Langmuir*, 33(24):5982–5990, 2017.

[135] W. M. de Vos, L. L. E. Mears, R. M. Richardson, T. Cosgrove, R. M. Dalgliesh, and S. W. Prescott. Measuring the structure of thin soft matter films under confinement: A surface-force type apparatus for neutron reflection, based on a flexible membrane approach. *Review of Scientific Instruments*, 83(11), 2012.